

RICE UNIVERSITY

High amplitude response behavior of a linear
oscillator–nonlinear absorber system: Identification, analysis,
and attenuation by using a semi-active absorber in series

by

R. Parker Eason

A THESIS SUBMITTED
IN PARTIAL FULFILLMENT OF THE
REQUIREMENTS FOR THE DEGREE

Doctor of Philosophy

APPROVED, THESIS COMMITTEE:



Andrew J. Dick, Chair
Assistant Professor of Mechanical
Engineering and Materials Science



Marcia K. O'Malley
Associate Professor of Mechanical
Engineering and Materials Science



Satish Nagarajaiah
Professor of Civil Engineering
and Mechanical Engineering

HOUSTON, TEXAS

APRIL 2013

Abstract

High amplitude response behavior of a linear oscillator–nonlinear absorber system: Identification, analysis, and attenuation by using a semi-active absorber in series

by

R. Parker Eason

Auxiliary absorbers provide an effective means to attenuate the vibrations of a structural or mechanical system (the “primary structure”). The simplest auxiliary absorber, a tuned mass damper (TMD), provides reliable narrow-band attenuation but is not robust to the effects of detuning. Strongly nonlinear tuned mass dampers (NTMDs) are capable of wide-band, irreversible energy transfer known as “energy pumping” but can also exhibit high amplitude solutions which significantly amplify the response of the primary structure. Semi-active tuned mass dampers (STMDs) incorporate an actuating element in order to achieve real-time tuning adjustment capability. This thesis presents a global dynamic analysis of the response of a primary structure with an NTMD and then explores the performance of a novel absorber configuration consisting of an NTMD and STMD attached to the primary structure in series. The global dynamic analysis is conducted using a new cell mapping method developed by the author and introduced within the thesis: the parallelized multi-degrees-of-freedom cell mapping (PMDCM) method. The benefits of the additional STMD component are explored for two distinct applications: (1) restoring the performance of a linear TMD which develops a weak nonlinearity due to operation outside

of the intended range or other means, and (2) acting as a safety device to eliminate or minimize convergence to the detached high-amplitude response. In the weakly nonlinear case, the STMD is shown to reduce the effects of the nonlinearity and improve attenuation capability by constraining the motion of the NTMD. In the strongly nonlinear case, the STMD effectively eliminates the complex response behavior and high amplitude solutions which were present in the original system, resulting in a single low amplitude response. Experimental tests using an adjustable-length pendulum STMD verify the numerical results.

Acknowledgments

I would like to first express sincere thanks to my advisor, Dr. Andrew J. Dick. His expansive knowledge in the field of dynamics, keen intuition, and ability to clearly explain complex ideas contributed substantially to my graduate education.

I would like to thank Dr. Satish Nagarajaiah for his ongoing guidance and support of my research. I am especially grateful for his generous donation of experimental resources, without which Chapter 6 could not have been completed. In addition, a thank you to Dr. Marcia K. O'Malley for her contributions as a member of both my master's and doctoral defense committees.

To Jessica, I am especially thankful for the unfaltering love and support over the years. It is a privilege to share my life with such an intelligent and successful woman, and it is to her that I attribute my business acumen, political competence, and steadily-improving vocabulary. I am particularly indebted to her for the selfless sacrifices she has made throughout the final months of my research.

In addition, a thank you to my colleagues, Pooya Ghaderi, Wei Huang, and Yu Liu, for the helpful discussions and daily camaraderie. To the Greenwoods, who have supported my graduate education in many ways and have always treated me as a family member. Also, to my friends, who may never fully understand what I do but will hopefully be quick to forgive me for my absence over the recent months. Finally, a thank you to my family for fostering my technical curiosity as a child and for the ongoing encouragement that helped me get to where I am today.

Contents

Abstract	ii
Acknowledgments	iv
List of Figures	ix
List of Tables	xx
1 Introduction	1
1.1 Auxiliary Vibration Absorbers	3
1.1.1 Tuned Mass Dampers (TMDs)	5
1.1.2 Multiple Tuned Mass Dampers (MTMDs)	8
1.1.3 Nonlinear Tuned Mass Dampers (NTMDs)	10
1.1.4 Active and Semi-Active Tuned Mass Dampers (STMDs)	18
1.2 Numerical Methods	22
1.2.1 Integration and Continuation	22
1.2.2 Cell Mapping	23
1.2.3 Cell State Space Representation	28
2 System Model and Governing Equations	33
3 Weakly Nonlinear Tuned Mass Damper	39
3.1 Effect of Weak Nonlinearity on Performance of TMD	40

3.1.1	Coordinate Transformation	40
3.1.2	Linear Frequency Response	41
3.1.3	Amplitude-Frequency Relationship	43
3.1.4	Effective Frequency Ratio Versus Nonlinearity	44
3.1.5	PN System Response	47
3.2	Series STMD System Performance	51
3.3	TMD/STMD Performance Comparison	57
3.4	Random Excitation	61
3.5	Summary of Results	68
4	A Parallelized Multi-Degrees-of-Freedom Cell Mapping Method	71
4.1	PMDCM Algorithm	72
4.1.1	Initialization	75
4.1.2	Subroutine <i>POPZs</i> — Populate cell array \mathbf{Zs}	75
4.1.3	Subroutine <i>PARIMG</i> — Parallelized image calculation	78
4.1.4	Subroutine <i>SCAN/PROC</i> — Scan and process imaged cells	79
4.1.5	Subroutine <i>POSTSP</i> — Post-scan-and-process	82
4.1.6	Overview	83
4.2	Validation	86
4.2.1	Dynamic model	86
4.2.2	Results	88
4.3	Summary	92
5	Strongly Nonlinear Tuned Mass Damper	93
5.1	System and Environmental Parameter Values	94
5.2	Higher-Frequency Bi-Stable Region, $B_{\omega>1}$	101
5.3	Lower-Frequency Bi-Stable Region, $B_{\omega<1}$	106
5.4	Series STMD System Performance	120

5.5	Summary of Results	129
6	Experimental Validation	134
6.1	Equations of Motion	136
6.2	Constraints	143
6.3	Design and Characterization	145
6.3.1	Primary Structure	146
6.3.2	NTMD	150
6.3.3	STMD	156
6.4	Experimental Results	169
6.5	Summary of Results	191
6.6	Potential Sources of Error	195
6.6.1	Nonlinear Viscous Damping	195
6.6.2	Non-Ideal Excitation	197
6.6.3	Transient Response	198
6.6.4	Component Degradation	198
6.6.5	Sensor Limits	199
6.6.6	Other Error Mechanisms	203
7	Concluding Remarks	204
7.1	Summary of Contributions	205
7.2	Future Work	207
7.2.1	Chaos in the PN System	207
7.2.2	Control Algorithm Development	207
7.2.3	Smart Nonlinear Energy Sink (SNES)	208
7.2.4	Mapping Using a Variable or Adaptive Cell Size	212
7.2.5	Accurate and Efficient Integrity Measure Calculation	212
A	Experimental System Components	218

B Experimental Equipment, Sensors, and Calibration Data	233
B.1 Load Cell	233
B.2 LVDT	234
B.3 Encoder	234
C Selected Code	237
C.1 PMDCM Algorithm	237
C.2 PARIMG Subroutine	243
C.3 SCAN Subroutine	244
C.4 UPDATE Subroutine	246
C.5 CHAOS Subroutine	246
C.6 NEWG Subroutine	246
C.7 OLDG Subroutine	247
C.8 ADDTOG Subroutine	247
C.9 Parallelized EOM	248
C.10 Construct Basins From PMDCM Output	249
C.11 Steady State Solution Information	252
D Analytical Expressions	255
Bibliography	258

List of Figures

1.1	Organizational diagram of various structural vibration attenuation mechanisms. Adapted from Kareem <i>et al.</i> (1999).	4
1.2	Schematic of a tuned mass damper (TMD).	5
1.3	Diagram illustrating examples of passive and semi-active auxiliary absorbers and listing corresponding design configurations for each.	8
1.4	Schematic of a nonlinear tuned mass damper (NTMD).	11
1.5	Schematic illustrating two linear extension springs arranged to produce a geometric nonlinearity.	13
1.6	Frequency-response exhibiting a secondary detached solution branch. Based on the results of Alexander and Schilder (2009).	16
1.7	Schematic of a semi-active tuned mass damper (STMD).	19
1.8	Schematic of the semi-active and independently variable stiffness (SAIVS) device. Adapted from Nagarajaiah and Varadarajan (2005).	20
1.9	A two-dimensional example illustrating the simple cell mapping (SCM) procedure.	26
1.10	Three integrity measures illustrated on the basin portrait of a hypothetical two degrees-of-freedom system.	31
2.1	Schematic of a primary structure with a NTMD and STMD in series.	34

3.1	Detuned frequency ratio versus primary structure amplitude, for $\epsilon_N = 0.02, \gamma_1 = 0.02, \gamma_N = 0.05$	46
3.2	Frequency response of a primary structure attached to a linear absorber with a detuned frequency ratio according to Eqn. (3.23) (solid) compared with the primary structure and NTMD (dashed), $\epsilon_N = 0.02, \gamma_1 = 0.02, \gamma_N = 0.05, \Omega_N = 0.03$	48
3.3	Difference between amplitude of PS attached to an NTMD and amplitude of PS attached to an optimally tuned linear TMD, versus the nonlinear parameter value and excitation frequency.	49
3.4	Primary structure frequency response curves; $\gamma_N = 0.05, F = 1, \Omega = 0.978, \epsilon_N = 0.02, \Omega_N = 0.03$	50
3.5	Contour plot of the primary structure response amplitude versus STMD mass ratio and damping parameter. Force amplitude $F = 0.5$	51
3.6	Primary structure frequency response curves for five mass ratio values, with $\hat{\gamma}_S = 0.02, F = 0.5, \Omega = 0.978, \epsilon_N = 0.02, \Omega_N = 0.03$	53
3.7	Peak resonance time series response for PS, NTMD and STMD for (a) $\epsilon_S = 2 \times 10^{-8}$, (b) $\epsilon_S = 2 \times 10^{-4}$ and (c) $\epsilon_S = 2 \times 10^{-2}; \hat{\gamma}_S = 0.02$	54
3.8	Mass ratio values ϵ_S which minimize the primary structure response amplitude $ q_P $ at each damping parameter value $\hat{\gamma}_S$ and forcing amplitude F	56
3.9	Surface plot showing primary structure response amplitude versus forcing amplitude and frequency for the PS+NTMD system; $\epsilon_S = 1.6 \times 10^{-4}, \hat{\gamma}_S = 0.02$	58
3.10	Surface plot showing primary structure response amplitude versus forcing amplitude and frequency for the PS+NTMD+STMD system; $\epsilon_S = 1.6 \times 10^{-4}, \hat{\gamma}_S = 0.02$	58

3.11	Surface plot showing primary structure response amplitude versus forcing amplitude and frequency for the PS+NTMD+TMD system; $\epsilon_S = 1.6 \times 10^{-4}$, $\hat{\gamma}_S = 0.02$	59
3.12	Primary structure response amplitude versus excitation frequency and STMD stiffness coefficient for (a) $F = 0.1$, (b) $F = 0.5$, (c) $F = 1.0$ and (d) $F = 10.0$; $\epsilon_S = 1.6 \times 10^{-4}$, $\hat{\gamma}_S = 0.02$	60
3.13	Increase or decrease in primary structure response amplitude versus forcing amplitude and frequency from adding an (a) STMD with standard linear tuning, (b) linear TMD and (c) STMD with novel piecewise linear tuning; $\epsilon_S = 1.6 \times 10^{-4}$, $\hat{\gamma}_S = 0.02$. A dashed line separates the positive and negative regions, as labeled. (d) Change in primary structure response amplitude versus frequency at $F = 0.2$ (solid), $F = 0.5$ (dashed) and $F = 0.8$ (dot) for each of the cases shown in (a)-(c). . .	61
3.14	(a) Power spectral density, smoothed (light) and unsmoothed (dark), and (b) time series plot of a seismic-like excitation signal.	63
3.15	Smoothed power spectral density (PSD) of the (a) primary structure and (b) NTMD response. Results presented are from two separate simulations: both using the same excitation signal, the first excluding (dashed) and the second including (solid) the linear TMD attachment in series with the PS and NTMD.	64
3.16	(a) Peak and (b) RMS of the PS response in the time domain for the PNS system with STMD damping parameter $\hat{\gamma}_S = 0.01$ (\circ), 0.02 (\cdot), 0.03 ($*$), 0.04 (\times), and 0.05 ($+$).	66
3.17	Frequency response curves illustrating the performance benefits of the series STMD for harmonic excitation; $\gamma_N = 0.05$, $F = 1$, $\Omega = 0.978$, $\epsilon_N = 0.02$, $\Omega_N = 0.03$	67
4.1	Flowchart illustrating the PMDCM algorithm.	74

4.2	Subroutine <i>POPZs</i> — Populate cell array Zs	76
4.3	Subroutine <i>SCAN/PROC</i> — Scan and process imaged cells.	79
4.4	Subroutine <i>POSTSP</i> — Post-scan-and-process operations.	82
4.5	A two-dimensional example illustrating the processing order within the (a) multi-degrees-of-freedom cell mapping (MDCM) method, and (b) parallelized multi-degrees-of-freedom cell mapping (PMDCM) method with $N_s = 3$	84
4.6	Schematic of the “spring-pendulum”: a two degrees-of-freedom system consisting of a point mass attached to a spring and sliding on a massless pendulum.	87
4.7	Basin portraits produced by using the (a) grid-of-starts (GOS) method, (b) MDCM method, (c) PMDCM method with $N_s = 10$, and (d) PMDCM method with $N_s = 100$	89
4.8	Computation time versus number of cells in subspace S for the PMDCM method with various N_s values and the MDCM method.	91
5.1	Estimated regions of parameter space that meet the criteria noted in the legend from an initial study.	98
5.2	Characteristic frequency-response profile for the (a) primary structure and (b) NTMD illustrating the two bi-stable regions in the PN system response; $\Omega = 0, \hat{\gamma}_N = 0.002, \Omega_N = 0.09, F = 0.35, \phi = 0$. Limit point (\diamond) and torus (\circ) bifurcation points are marked.	100
5.3	Frequency-response of (a) primary structure and (b) NTMD within $B_{\omega>1}$ using numerical continuation (solid/dashed) and numerical inte- gration (\cdot); $\Omega = 0, \hat{\gamma}_N = 0.002, \Omega_N = 0.09, F = 0.35, \phi = 0$	103

5.4	Characteristic Σ^{12} basin portrait for the $B_{\omega>1}$ region; $\omega = 1.8, \Omega = 0, \hat{\gamma}_N = 0.002, \Omega_N = 0.09, F = 0.35, \phi = 0$. Dashed circle is used for size reference, its radius equal to integrity measure normalization radius, $R = 26.3$	104
5.5	Location of the Floquet multipliers of the safe (\circ) and constraint ($+$) attractors in the complex plane, relative to the unit circle.	105
5.6	Phase portrait of the (a) primary structure and (b) NTMD response illustrating the stable (solid) and unstable (dashed) attractors.	107
5.7	Frequency-response of (a) primary structure and (b) NTMD $B_{\omega<1}$ using numerical continuation (solid/dashed) and numerical integration (\cdot); $\Omega = 0, \hat{\gamma}_N = 0.002, \Omega_N = 0.09, F = 0.35, \phi = 0$	109
5.8	Convergence study illustrating integrity measures versus resolution.	110
5.9	Characteristic basin portrait in the (a) Σ^{12} and (b) Σ^{34} planes illustrating the LIM, IF and IIM $^\pm$ integrity measures. Dashed circle is used for size reference, its radius equal to integrity measure normalization radius, $R = 26.3$	112
5.10	(a) Basin portrait and (b) corresponding q_1 time series at five points (i-v); $\Omega = 0, \hat{\gamma}_N = 0.002, \Omega_N = 0.09, F = 0.41, \phi = \pi/2$	113
5.11	Erosion profiles illustrating the four integrity measures versus excitation magnitude at the frequencies corresponding to the midpoint and peak of $B_{\omega<1}$	115
5.12	Appearance of a new stable Period-1 (P-1) solution which acts as a strong attractor; $\Omega = 0, \hat{\gamma}_N = 0.002, \Omega_N = 0.09, F = 0.65$. Limit point (\diamond) and branch point ($+$) bifurcation points are marked.	117
5.13	(a) Separation between two nearby trajectories versus time and (b) largest Lyapunov exponent versus initial position of primary oscillator, $q_i = 0$ for $i = 2, 3, 4$	119

5.14	Frequency-response of the primary structure within the PNS system at six STMD mass ratio values as labeled in (a)–(e); $\Omega = 0, \hat{\gamma}_N = 0.002, \Omega_N = 0.09, F = 0.35, \phi = 0$. Limit point (\diamond) and torus (\circ) bifurcation points are marked.	121
5.15	Frequency-response of the NTMD within the PNS system at six STMD mass ratio values as labeled in (a)–(e); $\Omega = 0, \hat{\gamma}_N = 0.002, \Omega_N = 0.09, F = 0.35, \phi = 0$. Limit point (\diamond) and torus (\circ) bifurcation points are marked.	122
5.16	Frequency-response of the STMD within the PNS system at six STMD mass ratio values as labeled in (a)–(e); $\Omega = 0, \hat{\gamma}_N = 0.002, \Omega_N = 0.09, F = 0.35, \phi = 0$. Limit point (\diamond) and torus (\circ) bifurcation points are marked.	123
5.17	Frequency-response of the PN system (thin) and of the PNS system with $\epsilon_S = 1 \times 10^{-3}$ (thick); $\Omega = 0, \hat{\gamma}_N = 0.002, \Omega_N = 0.09, F = 0.35, \phi = 0$	124
5.18	Bifurcation diagram illustrating the disappearance of the high amplitude solution at an STMD mass ratio of $\epsilon_S = 2 \times 10^{-4}$, at a frequency of $\omega = 0.85$	125
5.19	Basin of attraction versus the primary structure initial position and velocity for the series STMD system with $\epsilon_S =$ (a) 1×10^{-6} , (b) 1×10^{-5} , (c) 1×10^{-4} , (d) 1×10^{-3} , (e) 1×10^{-2} and (f) 1×10^{-1} , $\Omega = 0$. Phase portraits for the low and high amplitude solutions are superimposed.	127
5.20	Primary structure response (a) and excitation (b) versus time with STMD deactivated (blue) and STMD activated (green) as an impulse-like force is applied to the structure.	129

5.21	Primary structure response (a) and excitation (b) versus time illustrating a high-to-low amplitude transition corresponding to a change between STMD deactivated (OFF) and STMD activated (ON). . . .	130
6.1	Schematic illustration of the experimental test setup: (a) side and (b) front view.	135
6.2	Linear spring component consisting of a 5 in (13 cm) tempered steel compression spring welded to two telescoping steel housing pieces. . .	147
6.3	Load measured in the primary spring versus displacement of the primary structure relative to the base.	148
6.4	Primary structure displacement versus time (solid) and the corresponding local minima (\times) and maxima (\bigcirc) of decaying free oscillations. .	149
6.5	Spring rate required to achieve desired nonlinear coefficient (based on number of parallel springs) versus nominal spring length. Markers indicate spring rate and length properties of the purchased spring (\bigcirc) other available springs (\times).	152
6.6	Experimental test setup for primary structure and NTMD (PN System): (a) side and (b) top view.	154
6.7	Applied load versus deflection of the NTMD component (solid) and a third-order least squares approximation (dashed) indicating the linear and nonlinear spring rate coefficients.	155
6.8	NTMD displacement versus time (solid) and the corresponding local minima (\times) and maxima (\bigcirc) of the decaying free oscillations. . . .	157
6.9	Effective STMD mass versus total rod length for a pendulum mass of 3.64 lb (solid), 3.67 lb (dashed), and 3.70 lb (dash-dot).	159

6.10	Natural frequency of the STMD versus total rod length for auxiliary torsional stiffness $k_{tor} = 0$ (solid), 0.292 lb-ft/rad (dashed), 0.555 lb-ft/rad (dash-dot), and 0.909 lbf-ft/rad (dotted). The horizontal dashed line represents the natural frequency required to satisfy the design constraint.	161
6.11	Auxiliary torsion spring rate versus total rod length required to satisfy the design constraint.	162
6.12	Linear range of the pendulum versus clamp offset distance at $k_{tor} = 0.682$ ft-lbf/rad.	163
6.13	Photo of the (a) adjustable-length pendulum STMD and (b) STMD attached in series with the NTMD.	164
6.14	Applied moment versus angular displacement of the STMD pendulum component (solid) with zero added mass ($m_p = 0$) and a first-order least squares approximation (dashed) indicating the torsional spring rate k_{tor}	166
6.15	Natural frequency of the STMD versus effective length of the pendulum rod based on numerical predictions using the characterized torsion spring rate of $k_{tor}^* = 1.24$ ft-lbf/rad (solid), experimental data (\circ), and the numerical approximation best-fit to the experimental data by using a value of $k_{tor} = 1.6$ ft-lbf/rad (dashed).	167
6.16	STMD lateral displacement versus time (solid) and the corresponding local minima (\times) and maxima (\circ) of the decaying free oscillations.	168
6.17	Frequency response of the primary structure for the PN system at four excitation amplitudes: (a) $X_g = 0.04$ in, (b) $X_g = 0.05$ in, (c) $X_g = 0.06$ in, and (d) $X_g = 0.07$ in. NTMD mass ratio $\epsilon_N = 6.0\%$	171

6.18	Frequency response of the NTMD for the PN system at four excitation amplitudes: (a) $X_g = 0.04$ in, (b) $X_g = 0.05$ in, (c) $X_g = 0.06$ in, and (d) $X_g = 0.07$ in. NTMD mass ratio $\epsilon_N = 6.0\%$	172
6.19	Frequency response of the primary structure for the PN system illustrating the hysteresis in the amplitudes of the experimental system obtained during a low-to-high frequency sweep (black arrows) and a high-to-low frequency sweep (red arrows).	173
6.20	Force response of the primary structure for the PN system at four excitation frequencies: (a) $\Omega_g = 0.77$, (b) $\Omega_g = 0.85$, (c) $\Omega_g = 0.90$, and (d) $\Omega_g = 0.95$. NTMD mass ratio $\epsilon_N = 6.0\%$	175
6.21	Force response of the NTMD for the PN system at four excitation frequencies: (a) $\Omega_g = 0.77$, (b) $\Omega_g = 0.85$, (c) $\Omega_g = 0.90$, and (d) $\Omega_g = 0.95$. NTMD mass ratio $\epsilon_N = 6.0\%$	176
6.22	Time series response of the (a) base excitation, (b) primary structure, and (c) NTMD illustrating an abrupt transition from a low to high amplitude solution resulting from a small impulse applied to the primary structure at $t = 0$	178
6.23	Force response of the primary structure for the PN system (numerical: solid/dashed, experimental: (\bigcirc)) compared with the PNS system (numerical: dash-dot, experimental: (\times)) at four excitation frequencies: (a) $\Omega_g = 0.71$, (b) $\Omega_g = 0.77$, (c) $\Omega_g = 0.82$, and (d) $\Omega_g = 0.85$. Total mass ratio in each system is 7.4%	180
6.24	Force response of the NTMD for the PN system (numerical: solid/dashed, experimental: (\bigcirc)) compared with the PNS system (numerical: dash-dot, experimental: (\times)) at four excitation frequencies: (a) $\Omega_g = 0.71$, (b) $\Omega_g = 0.77$, (c) $\Omega_g = 0.82$, and (d) $\Omega_g = 0.85$. Total mass ratio in each system is 7.4%	181

6.25	Force response of the STMD for the PNS system at four excitation frequencies: (a) $\Omega_g = 0.71$, (b) $\Omega_g = 0.77$, (c) $\Omega_g = 0.82$, and (d) $\Omega_g = 0.85$. Total mass ratio is 7.4%.	182
6.26	Frequency response of the primary structure for the PN system (numerical: solid/dashed, experimental: (\bigcirc)) compared with the PNS system (numerical: dash-dot, experimental: (\times)) at four excitation amplitudes: (a) $X_g = 0.04$ in, (b) $X_g = 0.05$ in, (c) $X_g = 0.06$ in, and (d) $X_g = 0.07$ in. Total mass ratio in each system is 7.4%.	184
6.27	Frequency response of the NTMD for the PN system (numerical: solid/dashed, experimental: (\bigcirc)) compared with the PNS system (numerical: dash-dot, experimental: (\times)) at four excitation amplitudes: (a) $X_g = 0.04$ in, (b) $X_g = 0.05$ in, (c) $X_g = 0.06$ in, and (d) $X_g = 0.07$ in. Total mass ratio in each system is 7.4%.	185
6.28	Frequency response of the STMD for the PNS system at four excitation amplitudes: (a) $X_g = 0.04$ in, (b) $X_g = 0.05$ in, (c) $X_g = 0.06$ in, and (d) $X_g = 0.07$ in. Total mass ratio is 7.4%.	186
6.29	Time series response of the excitation and each component in the PN system as the excitation amplitude is gradually increased, decreased, then held constant.	188
6.30	Time series response of the excitation and each component in the PNS system as the excitation amplitude is gradually increased, decreased, then held constant.	189
6.31	Time series response of the excitation and each component in the PNS system with the pendulum motion constrained for $t < 0$ to deactivate the STMD and free for $t \geq 0$, activating the STMD and attenuating the response.	192

6.32	Mechanism used to fix the displacement of the STMD, consisting of a dowel pin inserted through the pendulum rod into a bracket which is clamped to the pendulum mount.	193
6.33	Frequency response of the primary structure for the PN system highlighting the effects of PS damping in the numerical results with the experimental data.	196
6.34	Loose ball bearings observed under the NTMD, indicating degradation of the linear bearing components.	199
6.35	Wear within the STMD component due to contact between the torsional spring attachment and mounting plate.	200
6.36	Failure of one of the six welds in the linear spring component discovered upon completion of the experimental tests.	201
6.37	Angular displacement signal versus time corresponding to the dowel pin experiment, with no offset correction.	202
7.1	Schematic illustration of the proposed smart nonlinear energy sink (SNES) system.	209
7.2	Elliptical path followed by the spring end posts as the rotation angle θ is increased in the proposed SNES system.	210
7.3	An example of the smooth transition from an essentially nonlinear to a linear force-deflection profile as the post rotation angle θ is increased in the proposed SNES system.	211
7.4	Illustration of a targeted algorithm used to accurately and efficiently calculate the local integrity measure (LIM).	213
7.5	Three examples of proposed output plots from a targeted algorithm used to accurately and efficiently calculate the local integrity measure (LIM).	216

A.1	CAD illustration of the full experimental setup from the (a) top and (b) side view. Labels denote system components.	219
A.2	CAD illustration of adjustable-length pendulum (STMD) assembly. Labels denote system components.	220
B.1	Applied load versus load cell output voltage, and best fit line indicating calibration coefficient.	234
B.2	Applied displacement versus LVDT output voltage, and best fit line indicating calibration coefficient.	235
B.3	Rotation angle of the STMD pendulum versus encoder output voltage, and best fit line indicating calibration coefficient.	236

List of Tables

4.1	Efficiency and accuracy benefits of the PMDCM method compared to the MDCM method.	90
5.1	Four sets of parameter values for which the erosion profiles are constructed.	101
6.1	Summary of design constraints for the experimental system based on physical limitations of space, size, and frequency.	146
6.2	Experimental system parameters (dimensional).	169
6.3	Experimental system parameters (non-dimensional).	170

Chapter 1

Introduction

A recurring challenge in the design of structures and mechanical systems is the effective attenuation of vibrations resulting from excitation due to internal imbalance, external loading, or other mechanisms. When it is not possible to isolate a system from the source of excitation or to adjust system parameter values to be less susceptible to resonant vibration, an auxiliary absorber may be beneficial. In the present thesis, the response of two systems under harmonic and random excitation are compared: (1) a linear primary structure coupled with a nonlinear auxiliary absorber, and (2) a linear primary structure coupled with a nonlinear auxiliary absorber and a semi-active absorber in series. The purpose of the semi-active component is to minimize the effective nonlinearity of the nonlinear absorber by limiting its amplitude without over-constraining the motion.

Various methods including the use of auxiliary absorbers have been incorporated in similar systems to effectively minimize the influence of a cubic hardening stiffness. For example, Lim *et al.* determined the conditions to minimize the nonlinear effects in an ultrasonic cutting system modeled as a two degrees-of-freedom Duffing oscillator [1]. Narayanan and Jayaraman numerically demonstrated that an auxiliary absorber could be used to eliminate the chaotic response regimes of a Duffing

oscillator subjected to harmonic excitation [2]. Sun *et al.* found that an STMD and NTMD coupled in parallel with a Duffing oscillator can more efficiently attenuate the vibrations of a nonlinear structure than an STMD component alone [3].

The main results are classified into two cases based on the nonlinear absorber parameter values used in the simulations: weak nonlinearity and strong nonlinearity. Each case is meant to address a distinct application. The *weak nonlinearity* represents the case where a linear auxiliary absorber has developed a small hardening nonlinearity due to component degradation, operation outside of the intended linear range, or other means. The effect of the nonlinearity in this case is to detune the linear absorber which compromises its attenuation capability. The *strong nonlinearity* represents a nonlinear absorber that is capable of “energy pumping”, the recently discovered phenomenon of irreversible, wide-band energy transfer to the absorber. In addition to the favorable behavior resulting from the nonlinearity in this case, high amplitude solutions can also coexist. The semi-active component is therefore proposed as a means to eliminate or minimize convergence to the high amplitude solutions. In each case, the response behavior of the primary structure and nonlinear absorber is characterized, then the performance of the primary structure, nonlinear absorber, and semi-active absorber is evaluated.

In the remainder of this chapter, a literature review of relevant auxiliary absorbers is presented and the various numerical methods used within the thesis are discussed. The system model, governing equations of motion, and non-dimensionalization procedure are described in the following chapter. The case of weak nonlinearity is presented in the third chapter. An analytical expression describing the effective detuning of the absorber attributed to the nonlinear terms is first derived, then numerical methods are used to determine the steady-state performance of the series system using the semi-active component and using a passive absorber component for harmonic and random excitation. In the fourth chapter, a novel cell mapping algorithm used for

the efficient global analysis of multiple degrees-of-freedom systems is developed and validated. The case of the strong nonlinearity is presented in the fifth chapter. An initial study is first presented in order to determine appropriate parameter values, then numerical continuation, numerical integration, and cell-mapping methods are used to identify a family of newly-discovered periodic solutions and conduct a global analysis of the primary structure and nonlinear absorber system. The response of the primary structure, nonlinear absorber, and semi-active absorber is then studied by using the same methods. In the sixth chapter, experimental tests are used to verify some of the key results from the strong nonlinearity case. A summary of contributions and a discussion of suggested future work is presented in the final chapter.

1.1 Auxiliary Vibration Absorbers

In the design of structural and mechanical systems operating in a dynamic environment, whether through internal motion, external loading, or other means, it is often desired to minimize the motion in the system. For many simple systems where the engineer or designer maintains a reasonable degree of control over the parameters, excessive vibrations can be easily avoided by either (1) taking measures to reduce the excitation or isolate the system from the excitation, (2) adjusting the mass or the stiffness of the system is such that its natural frequency is far from the expected dominant frequency of any source of excitation, or (3) incorporating damping elements to dissipate energy.

In some systems, however, sufficient attenuation cannot be achieved using straightforward methods. External excitation sources may be uncontrollable, the range of achievable mass and stiffness values may be limited due to physical or financial constraints, and the intrinsic damping in some structures or mechanical systems may be too low to provide significant dissipation of oscillations [4]. In this case, an auxiliary

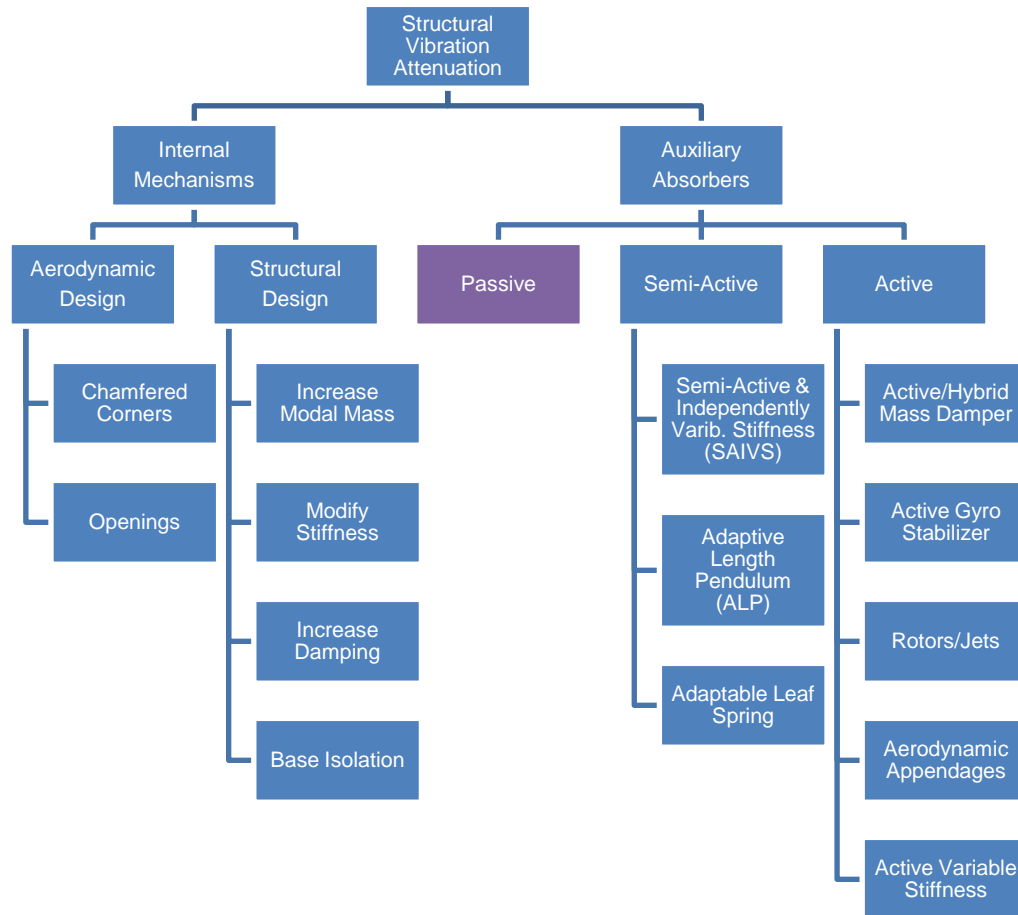


Figure 1.1: Organizational diagram of various structural vibration attenuation mechanisms. Adapted from Kareem *et al.* (1999).

absorber can provide an effective alternative method of attenuating vibrations.

Figure 1.1 presents a diagram illustrating the various mechanisms used to attenuate structural vibrations, as an example. On the largest scale, the mechanisms have been divided into two broad categories: internal mechanisms and auxiliary absorbers. Internal mechanisms, as they have been categorized here, refer to revising elements of the current design to tend towards more favorable response characteristics. Auxiliary absorbers, on the other hand, refer to separate structures which are installed in order to reduce the response in the original structure, denoted hereafter as the *primary structure* (PS).

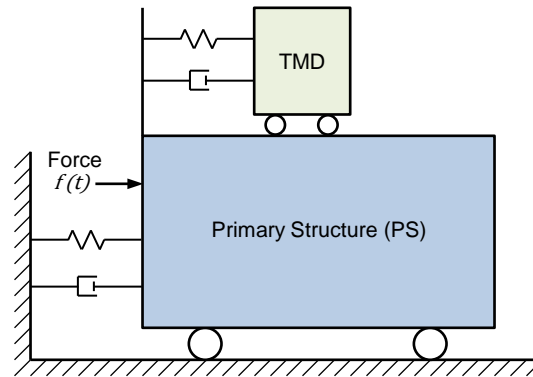


Figure 1.2: Schematic of a tuned mass damper (TMD).

This section provides an overview of the relevant types of auxiliary vibration absorbers in order to allow for a better understanding of the context of the present thesis. The design characteristics and historical development of tuned mass dampers are first discussed, followed by multiple tuned mass dampers, nonlinear tuned mass dampers, and semi-active tuned mass dampers.

1.1.1 Tuned Mass Dampers (TMDs)

The most simple auxiliary absorber is known of the *tuned mass damper* (TMD), which consists of a small mass coupled to the primary structure with a linear stiffness and a linear damping element, as illustrated in Fig. 1.2. The natural frequency of the TMD is tuned to the natural frequency of the primary structure or another frequency of significance. In the neighborhood of this *tuning frequency* (or *tuning ratio* as expressed relative to the natural frequency of the primary structure) vibration is attenuated as a result of the inertial forces from the TMD oscillating out of phase with the primary structure.

The first documented auxiliary absorber implementation came from the transactions of the Royal Institution of Naval Architects in 1883 [5]. At the time, new ship

designs allowed for more robustness against damage but resulted in a larger meta-centric height, causing the ships to be more prone to oscillations. An absorber was created by using a system of compartments partially filled with water, such that the rolling of the ship resulted in the transfer of water between the chambers. Although the mechanics of the absorber were not yet fully understood, the author explained the absorption concept as similar to the ship’s crew running from side to counteract the motion. The geometry of the connections between the chambers was designed so the flow of the water would lag behind the rolling oscillations of the ship, effectively “tuning” the absorber device. The Architects’ absorber was successfully implemented in multiple ships, and the corresponding experimental results showed a successful reduction of rolling motion.

In 1911, Hermann Frahm patented the “device for damping vibrations of bodies”, which is commonly identified as the first tuned mass damper [6]. Frahm identified many potential applications of the device, including the attenuation of oscillations in ships, machinery, aircrafts, and structures. Various absorber configurations including single and multiple *degrees-of-freedom* (DOF) linear oscillators, pendulums, and continuous elements were proposed within the patent, each of which influenced independent research studies over the following decades (*e.g.* [7, 8, 9, 10]).

The first thorough study describing the dynamics of a primary structure coupled with a TMD is often attributed to a paper by Ormondroyd and Den Hartog in 1928 [7]. Using analytical and numerical methods, the authors investigated the influence of the TMD damping ratio using various damping mechanisms and discussing the practicality of each. By observing changes to the frequency-response of the system, it was determined that non-zero damping in the primary structure resulted in a wider suppression bandwidth and a decrease in the resonant peak of each mode, with the tradeoff of allowing for a small non-zero PS oscillation amplitude at the tuning frequency. Many of the analytical expressions derived in Ref. [7] were published in

the first edition of Den Hartog's *Mechanical Vibrations*, which to the present day is widely regarded as the key classical reference on tuned mass dampers [11]. Analytical expressions describing the optimum TMD damping ratio were later presented by Brock [12] and published in the following edition of *Mechanical Vibrations*.

Over the following decades, numerous efforts to optimize the TMD design parameters (*i.e.* mass, tuning ratio, and damping ratio) with respect to various performance measures and excitation conditions were presented. Crandall and Mark determined the optimum design parameters using broadband random excitation, which were similar to those recommended for harmonic forcing [13]. The results of this work were extended by Wirsching and Campbell, who analytically demonstrated that a small TMD was capable of reducing the vibration amplitudes of two mid-rise buildings subjected to broadband random excitation [14]. Jacquot and Hoppe studied the optimum design parameters in order to achieve attenuation for wide-band harmonic excitation [15]. Warburton determined the optimum parameters to minimize a number of different response measures for various harmonic and random excitation conditions [16]. Sadek *et al.* conducted an optimization in order to minimize the response of the first two modes of a structure to random excitation, and demonstrated that the TMD consistently reduced vibration amplitudes in numerical simulations of multi-story buildings subjected to load data obtained from real seismic time-histories [17].

The optimum absorber parameters described in the aforementioned and related works serve as an important tool for the evaluation of alternative configurations and as a starting point for real-world design implementations. In a recent publication, a practical method to evaluate the expected performance of one or more absorbers attached to a structure is presented [18]. Within the proposed method, the frequency response of a real-world structure—obtained analytically or experimentally—can be used to derive the frequency response of the structure coupled with an absorber. As a result, a considerable amount of time in the design process is saved compared with

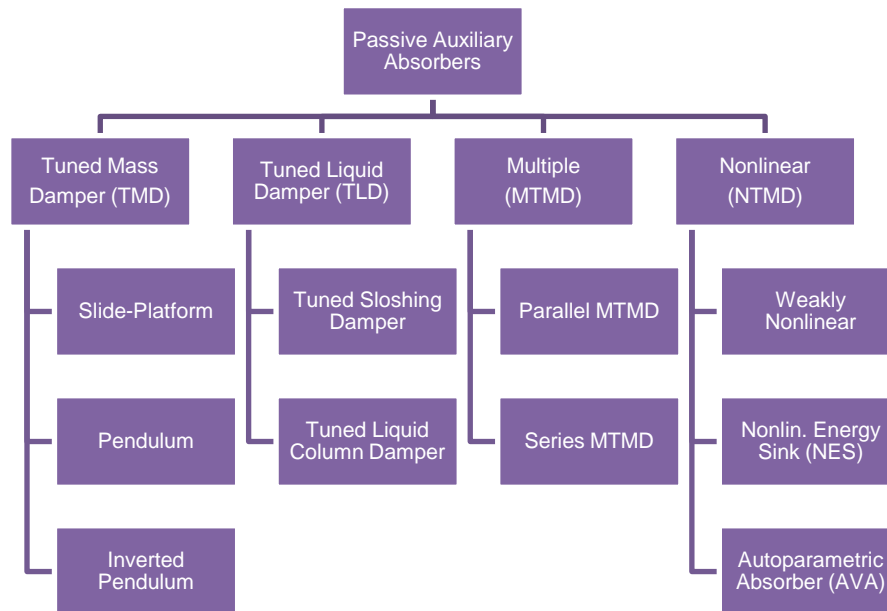


Figure 1.3: Diagram illustrating examples of passive and semi-active auxiliary absorbers and listing corresponding design configurations for each.

finite element analysis or other methods.

The behavior of the linear TMD is now well understood, based on a collection of related work spanning more than a century [19]. Numerous variations of Frahm’s original designs have been developed over the years, as well as many other novel designs. A diagram illustrating some of the most notable passive auxiliary absorber configurations is displayed in Fig. 1.3. Details regarding the implementation of these and other absorber configurations in civil structures worldwide are presented in Ref. [4].

1.1.2 Multiple Tuned Mass Dampers (MTMDs)

Multiple tuned mass damper (MTMD) is a general term used to describe a system consisting of one or more auxiliary vibration absorbers coupled to a primary structure. As the name suggests, the multiple absorbers are typically TMDs, although the term

“MTMD” has been used to denote systems of other absorber variants. The idea of using multiple absorbers to attenuate one or more modes of a structure has been around for nearly as long as the original TMD, discussed *e.g.* in Ormondroyd and Den Hartog’s classic publication [7].

Numerous configurations of MTMDs have been proposed over the years in order to achieve a variety of performance improvements. Srinivasan considered an MTMD system consisting of two parallel absorbers with equal mass: a TMD with viscous damping and an undamped TMD [8]. The proposed MTMD system was shown to be capable of producing an “undamped anti-resonance”, that is, zero primary structure response amplitude at the tuning frequency. The MTMD system therefore completely attenuated the response at the tuning frequency similar to the result produced by an undamped TMD, but with a dissipative element present in the system. Unfortunately, Srinivasan’s MTMD suffered from one of the same drawbacks as the TMD: a narrow effective bandwidth of attenuation, outside of which the primary structure response becomes amplified.

Gupta and Chandrasekaran used numerical integration to study the response of a linear oscillator with multiple damped TMDs tuned to different natural frequencies to loading prescribed by a time history from the 1952 Taft earthquake [20]. The authors concluded that the configuration was not well-suited to attenuate seismic loading. Manikanahally and Crocker conducted analytical and experimental studies using multiple tuned mass dampers to successfully attenuate numerous resonant peaks in a continuous mass-loaded beam [21, 22]. The behavior of multiple liquid dampers (MTLD) all tuned to a single natural frequency of a primary structure was studied by Sun *et. al.* Performance benefits were observed to be similar to a single tuned mass damper [23]. Igusa and Xu examined the performance of a primary oscillator with a large number of tuned mass dampers attached in parallel, each tuned to a different natural frequency equally spaced within a predetermined range [24].

If many dampers with closely spaced natural frequencies were added to a primary structure, the effect was demonstrated to be qualitatively similar to increasing the damping of the structure. When optimally tuned, Igusa and Xu's MTMD system was demonstrated to outperform a single TMD in the neighborhood of the primary resonance, providing a more evenly distributed frequency response.

More recently, an MTMD system consisting of two absorbers arranged in a series configuration, as opposed to parallel, has been studied. Zuo and Nayfeh used modern control methods to optimize the parameters of the series MTMD to attenuate vibrations resulting from harmonic and random excitation [25]. The authors observed that a single mode could be attenuated more effectively using a series MTMD than using a linear TMD or parallel MTMD system, and noted that the performance could be further improved by using negative damping. Zuo expanded upon these results in a later work, determining that the series MTMD system could provide equal or greater wide-band attenuation than other single or multiple absorbers, but with a smaller total mass ratio [26]. Tang and Zuo then compared the performance of the passive series MTMD system to two other MTMD configurations: a passive TMD in series with a semi-active viscous damper, and a passive TMD in series with an active TMD [27, 28]. Both devices were demonstrated to outperform the passive series MTMD and the authors discussed the added potential benefit of using the semi-active viscous damper within the system as an energy harvesting device [27]. Semi-active and active devices will be discussed in Section 1.1.4.

1.1.3 Nonlinear Tuned Mass Dampers (NTMDs)

Auxiliary vibration absorbers consisting of one or more stiffness elements with nonlinear force-displacement characteristics are known as *nonlinear tuned mass dampers* (NTMDs). A schematic illustration of an NTMD coupled with a primary structure is presented in Fig. 1.4. A red arrow is used to denote the nonlinear stiffness ele-

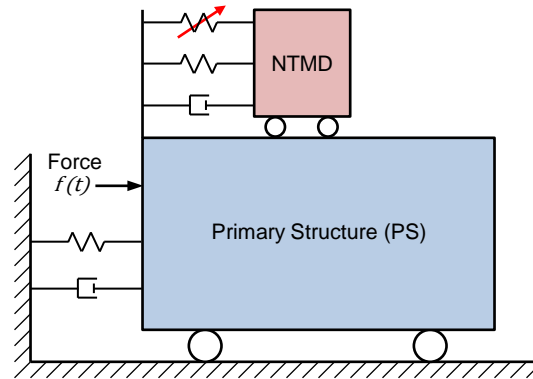


Figure 1.4: Schematic of a nonlinear tuned mass damper (NTMD).

ment. The motivation driving much of the early NTMD research was to widen the suppression bandwidth—the range of frequencies surrounding the tuning frequency within which the primary structure’s response is attenuated. Roberson determined the optimum design parameters for an NTMD with a linear and a cubic stiffness element under wide-band harmonic excitation [29]. The NTMD was successfully demonstrated to provide a larger suppression bandwidth than a linear TMD, with the best performance obtained by using a negative cubic coefficient, *i.e.* a softening system.

An NTMD with a hyperbolic sine nonlinearity was studied the following year by Pipes [30]. Analytical results showed that Pipes’ NTMD reduced the gradient of the resonant peaks in the frequency domain at the expense of introducing harmonic components of the excitation signal into the system response. Other reports of improvements in the suppression bandwidth by using nonlinear absorbers included Arnold [31], Kojima and Saito [32], Soom and Lee [33], Rice and McCraith [34], and Jordanov and Cheshankov [35]. The self-proclaimed first “practical” nonlinear absorber study was conducted by Hunt and Nissen, who considered a softening NTMD constructed from back-to-back Belleville washers, accounting for the effects of energy

dissipation [36].

The conclusions among these studies were similar: (1) an NTMD can be used to produce a wider suppression bandwidth than a linear TMD, (2) a softening nonlinearity generally outperforms a hardening nonlinearity, and (3) little to no benefit is observed outside of the suppression bandwidth. Some authors were also aware of an additional drawback: that nonlinear systems are capable of complex response behavior including multiple coexisting solutions [30, 34]. For example, Nayfeh *et al.* used the method of multiple scales to identify multiple solutions of an NTMD system resulting from an internal resonance between the various modes [37].

Arguably, the most significant potential of the NTMD was not realized until more recently when the energy pumping phenomenon was discovered. *Energy pumping* refers to the rapid and irreversible transfer of energy between two oscillators, the theory of which is rooted in Nayfeh and others' analytical studies of the energy transfer between nonlinear normal modes [38, 39]. Energy pumping is achieved by using a strongly nonlinear TMD with a force-displacement profile most commonly defined by a cubic nonlinearity with zero (*essential nonlinearity*) or near-zero linear stiffness. Figure 1.5 illustrates an example of a geometric configuration using two linear extension springs to produce an essential nonlinearity that exhibits a cubic force-displacement in a third-order approximation. In the particular case of a non-linearizable stiffness, the system is known as a *nonlinear energy sink* (NES) [40]. In the present thesis, both will be referred to as an *NTMD* (or the *strongly nonlinear system*) for consistency, without distinguishing between the case of a zero or near-zero linear stiffness component.

Much of the early energy pumping research was focused on the attenuation capability of an NTMD for transient loading, whereas later studies identified steady-state benefits. The first numerical simulation of transient energy transfer between nonlinear normal modes was by Gendelman in 2001 [41]. Along with his colleagues, Gendelman

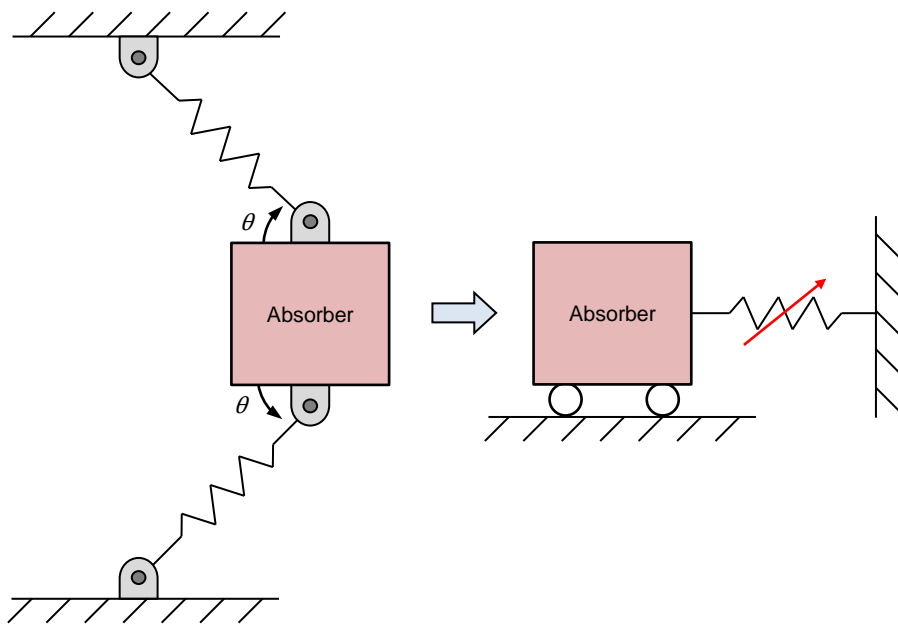


Figure 1.5: Schematic illustrating two linear extension springs arranged to produce a geometric nonlinearity.

expanded on this initial work by presenting a thorough explanation of the dynamics governing the transient energy transfer later the same year [42, 43, 44]. A real-world application was considered by Gourdon and Lamarque, who used numerical simulations to determine the response of two structures coupled with nonlinear absorbers to random excitation representing an earthquake [45]. The authors identified that the non-linearizable characteristic of the absorber allowed it to attenuate wide-band transient vibrations in each of the modes of the structure.

In Refs. [41, 42, 43, 44, 45], the nonlinear oscillator was *grounded*, meaning that nonlinear coupling in the absorber was with respect to a fixed inertial reference frame and that the coupling between the structure and absorber was linear. This configuration poses obvious design challenges since absorbers in civil applications are most commonly installed at the top of tall structures [4]. Gourdon *et al.* studied the response of a linearized low-rise building model with an *ungrounded* NTMD to harmonic, transient, and random excitation using numerical and experimental methods [46]. The authors' unique contribution was the experimental verification of the energy pumping phenomenon for an ungrounded system.

The steady-state benefits of the strongly nonlinear NTMD were first identified by Jiang *et al.* in 2003 [47]. The authors studied the response of a single-DOF primary structure with a grounded NTMD to harmonic excitation using analytical, numerical, and experimental methods. Irreversible energy transfer from the primary structure to the NTMD was observed over a wide range of frequencies which was maximized by using lighter damping in the system, particularly in the NTMD. The results, however, were not universally well-received. Malatkar and Nayfeh refuted the findings of Jiang *et al.*, arguing that they were not able to reproduce the original authors' numerical evidence of energy pumping using a similar grounded NTMD, but did locate regions where the response may be amplified [48]. The authors continued to reiterate their individual viewpoints in a series of rebuttal publications [49, 50].

In 2006, Gourdon *et al.* identified a quasi-periodic response regime in the neighborhood of a 1:1 resonance between the primary structure and NTMD experimentally by using an analogous electrical circuit [51]. Within this region, the primary structure response is attenuated much more efficiently than using a linear TMD with the same mass. The authors then followed with a more rigorous analytical study of the quasi-periodic response in this region, which came to be known as the *strongly modulated response* (SMR) regime [52, 53]. A complementary analysis of the Hamiltonian dynamics of the energy pumping phenomenon and optimization of the parameter values was presented by Quinn *et al.* [54] and Sapsis *et al.* [55]. Other potential applications of the strongly nonlinear NTMD were proposed by Starosvetsky and Gendelman, such as a means to prevent a van der Pol oscillator from exhibiting a limit cycle response [56].

It is well-known that nonlinear systems are capable of complex response behavior such as harmonic, combination, and internal resonances, and the coexistence of multiple stable solutions [38, 57]. Throughout the development of the strongly nonlinear NTMD, many researchers focused their efforts on characterizing the potential drawbacks due to the nonlinear effects in such a system. Shaw *et al.* identified potentially destructive instabilities due to the excitation of a combination resonance at the mean of the linearized natural frequencies of the primary structure and nonlinear absorber [58]. Jiang *et al.* numerically and experimentally confirmed the presence of multiple coexisting stable solutions in the authors' aforementioned work [47].

Alexander and Schilder located a family of detached solutions while using numerical continuation techniques to optimize the NTMD parameter values [59]. A *detached solution* is identified as a closed-loop solution branch in the frequency-response of a system, as illustrated in Fig. 1.6. The results showed that of the two resonance peaks in a characteristic PS and absorber response, the NTMD does attenuate the amplitude of the higher-frequency peak but that the lower-frequency peak become detached

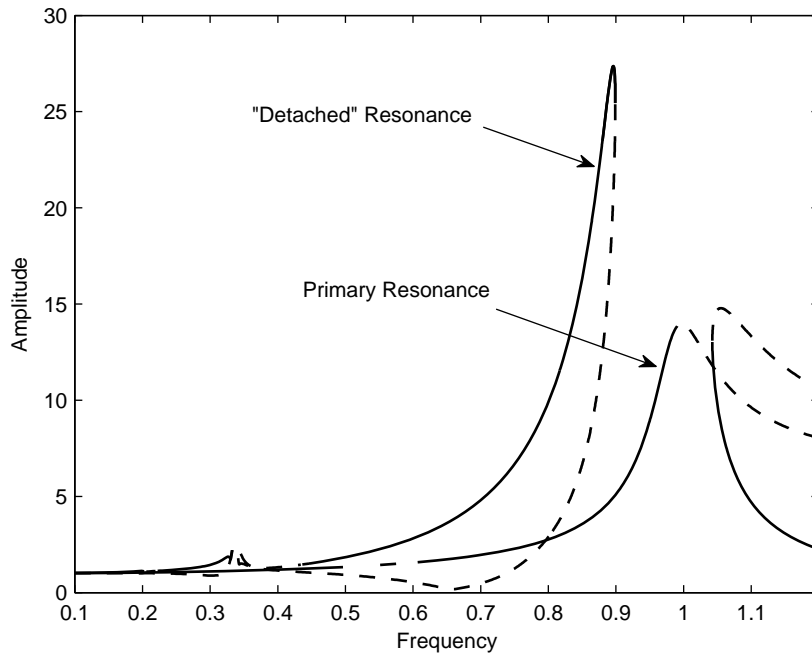


Figure 1.6: Frequency-response exhibiting a secondary detached solution branch. Based on the results of Alexander and Schilder (2009).

and is not attenuated. The authors noted that the approximate analytical techniques used in many previous works may not positively identify all solution branches, and that numerical continuation methods are better suited for the analysis. Based on the coexistence of the high amplitude detached solutions over a large region of parameter space, the authors concluded that an NTMD is not likely to outperform a linear TMD.

Gatti *et al.* conducted an analytical and numerical [60] and an experimental [61] analysis of the formation of detached resonance curves in a related system consisting of an nonlinear oscillator coupled with a linear oscillator. The system was meant to model a nonlinear test structure attached to a shaker so the mass of the nonlinear oscillator was kept small enough that the inertia of the nonlinear oscillator would not affect the linear oscillator. The system was therefore not representative of a nonlinear absorber. The authors' identified that detached resonance curves could

be formed inside the main solution branch—forming what the authors’ denoted as a “bubble” type curve—as well as outside. In another related system consisting of a grounded NTMD and linear primary structure, Savadkoohi *et al.* illustrated evidence of chaotic behavior in the transient response [62]. Similar behavior was also identified within Malatkar and Nayfeh’s contribution [48].

Few methods to reduce or eliminate the influence of the high amplitude coexisting solutions in the strongly nonlinear NTMD system have yet been proposed. In their concluding remarks, Alexander and Schilder suggested that semi-active control may be useful in order to influence the system to exhibit the low amplitude response [59]. Starosvetsky and Gendelman envisioned a semi-active hydraulic damper with a system of valves which they modeled as a piecewise-quadratic viscous damper [56]. Using numerical and analytical methods, the authors demonstrated that the device was capable of eliminating the detached resonance under certain conditions.

Other nonlinear absorber configurations include the *autoparametric vibration absorber* (AVA), which consists of an auxiliary mass coupled to the primary structure in such a way that the motion of the structure changes the stiffness of the absorber and that the motion of the absorber acts back on the structure simultaneously. The potential of using a parametrically coupled mass as an absorber in this way was realized by Haxton and Barr, although the authors admitted that the system was not practical for implementation in its current state [63]. Cartmell and Lawson were later able to improve the performance of the autoparametric vibration absorber by supplementing a degree of computer control [64]. A comprehensive review of the AVA would be beyond the scope of this thesis, so the interested reader is directed to contributions such as Hatwal *et al.* [65], Oueini *et al.* [66], and Vyas *et al.* [67] for more details.

1.1.4 Active and Semi-Active Tuned Mass Dampers (STMDs)

In addition to passive auxiliary absorbers, active, hybrid, and semi-active absorbers have also been developed. In an active system, the absorber mass is coupled to the primary structure using an actuator component. A closed-loop control algorithm is used to determine the output signal to the actuator based on the response of the structure [68]. The concept of using an active control system to attenuate structural vibrations is attributed to a 1972 publication by Yao [69]. The following year, Morrison and Karnop proposed an active absorber which consisted only of the actuating component and mass, with no stiffness or damping elements in the absorber. Later, Lund proposed an active absorber which utilizes stiffness and damping elements similar to the TMD in addition to the actuating component [70], which was followed by a study of the control strategy optimization for the active absorber by Chang and Soong [71]. The first structural implementation of an active absorber system was in Tokyo, Japan in 1989, and was later documented in publications by Kobori *et al.* [72] and Ikeda *et al.* [73]. Active vibration absorbers, now commonly referred to as *active mass dampers* (AMD) have consistently been demonstrated to outperform passive TMDs, with the significant tradeoff of requiring a constant power source.

Hybrid mass damper (HMD) is a term used to describe vibration absorbers with passive and active components [74]. The control systems in HMD systems are often designed for two separate modes of operation, passive and active, in order to utilize the performance benefits of active control when necessary and to conserve power otherwise [68]. Active-passive composite tuned mass dampers consist of a passive TMD and an AMD attached to the primary structure in a series configuration [75, 76]. For a review of active and hybrid vibration absorber systems and for more details regarding the implementation of active structural systems, the reader is referred to Spencer and Nagarajaiah [74], Spencer and Sain [68], Housner *et al.* [77], and Nishitani and Inoue *et al.* [78].

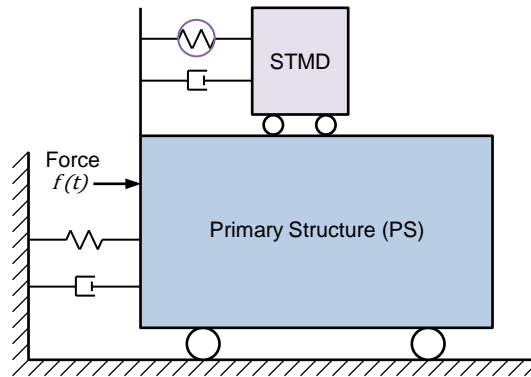


Figure 1.7: Schematic of a semi-active tuned mass damper (STMD).

Semi-active or “*smart*” *tuned mass dampers* (STMDs), schematically illustrated in Fig. 1.7, are auxiliary absorbers which incorporate a variable stiffness or variable damping element. STMDs, like AMDs and HMDs, rely on closed-loop feedback control and are able to outperform passive absorbers. However, since the power source in an STMD is used to modify the configuration of a variable element rather than to directly impart a force to control the system, the power requirements of an STMD system are significantly less than for an AMD or HMD. An STMD can be classified by the variable element used. Examples of *variable damping* devices include variable orifice dampers [79], magnetorheological (MR) fluid dampers [68], and variable-friction dampers [80, 81]. *Variable stiffness* devices include a pneumatic spring modulated by adjusting the pressure in the air chamber [82], an adjustable compound leaf-spring [83], and the semi-active continuously and independently variable stiffness device [84].

The model of the STMD used within this thesis is based on the *semi-active continuously and independently variable-stiffness* (SAIVS) device developed by Nagarajaiah and patented in 2000 [84]. A schematic illustration of the SAIVS device is presented in Fig. 1.8, adapted from Nagarajaiah and Varadarajan [85]. A linear electromechan-

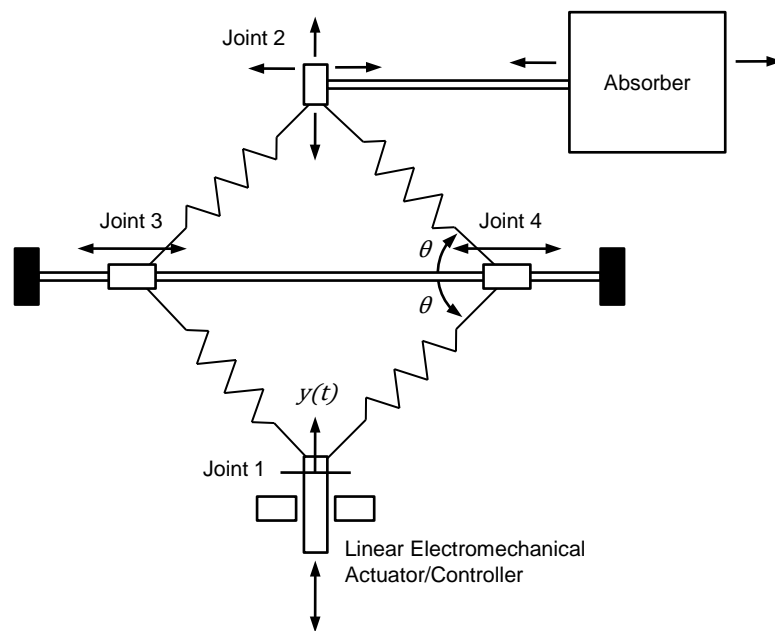


Figure 1.8: Schematic of the semi-active and independently variable stiffness (SAIVS) device. Adapted from Nagarajaiah and Varadarajan (2005).

ical actuator is used to directly apply a vertical displacement to Joint 1, resulting in a horizontal displacement of Joints 3 and 4 along the fixed rod and a vertical displacement of Joint 2. The linear actuator therefore modifies the angle θ of the parallelogram composed of four linear springs, which changes the resultant force of the springs acting on the horizontal displacement of the absorber. This configuration allows for the smooth and continuous adjustment of the absorber stiffness over a wide range of values [86].

In order to attenuate vibrations using the SAIVS STMD, the real-time frequency content of the response or excitation is characterized and the natural frequency of the STMD is tuned to the dominant frequency. Various characterization and control methods have been explored throughout the development of the SAIVS device. Early efforts utilized the Hilbert transform [87] and empirical mode decomposition [88]. A characterization method using the *short time Fourier transform* (STFT) was then developed [85], and a corresponding control algorithm was introduced [89]. A summary of the characterization and control methods for the SAIVS STMD is presented by Nagarajaiah [90].

The SAIVS STMD has been demonstrated analytically, numerically and experimentally to outperform passive tuned mass dampers, achieving similar performance to an active tuned mass damper with significantly less operational power and increased robustness [85, 88, 90]. Effective and robust performance has been demonstrated for various types of excitation [89], and for various structures including base-isolated bridges [91] and buildings [92]. Experimental tests conducted include base-isolated [93, 94] and multi-story 1:10 scale model structures [90].

More recently, Nagarajaiah and Pasala developed the *adaptive length pendulum* (ALP) device [95]. The ALP consists of a pendulum absorber, the natural frequency of which can be adjusted smoothly and continuously in real-time by controlling the length of the pendulum. Mechanisms that can be used to adjust the length of a

pendulum include shape memory alloy and electromechanical actuators. Nagarajaiah and Pasala experimentally verified the performance of the ALP device with each mechanism by using a scaled model of a two-story structure [95].

1.2 Numerical Methods

This section presents an overview of the numerical methods used within the present thesis. A brief summary of numerical integration and continuation techniques is first given. A literature review of the various cell mapping methods is then presented, followed by an introduction to the theory and applications of cell state space representation. Finally, the integrity measures which will be used to express the results of the global analysis in Chapter 5 are described.

1.2.1 Integration and Continuation

With the exception of the analytical results derived in Chapter 3 and the experimental results obtained in Chapter 6, the results in this thesis are obtained by using numerical integration, numerical continuation, and cell mapping methods. Numerical integration is a common technique used to determine the time domain response of initial value problems. First, differential equations of an arbitrary order are transformed to a system of first-order equations by using elementary methods. Given a set of initial conditions, a trajectory is then determined from a weighted average of current and predicted future derivatives by evaluating the differential equations. For the simulations within the present thesis, the fourth-order Runge-Kutta algorithm is used.

Numerical integration can be used to accurately reproduce the time-series behavior of a dynamic system. Integration methods are, however, inefficient for parametric studies such as a frequency-response or force-response plot due to the time required

for the transient behavior to decay at each step within the plot. Furthermore, in order to identify the various attractors in the case of multiple coexisting solutions, the particular initial conditions leading to each attractor must be determined, often by trial-and-error.

In order to overcome these limitations, AUTO bifurcation and continuation software is used [96, 97]. The AUTO software utilizes a number of algorithms based on the problem definition, most notably for the present research the *pseudo-arclength continuation method*. The pseudo-arclength continuation method is a predictor-corrector method. In order to initialize the algorithm, a grid of state values over one response period is determined by using analytical methods or numerical integration results, representing the initial solution. Then, given a pre-selected parameter and starting direction, a solution branch is traced by an iterative process of modifying the parameter value, predicting the resulting steady-state trajectory, and refining the prediction by using a convergence algorithm such as the Newton-Raphson method. Continuation methods can be used to efficiently and accurately trace stable and unstable solution branches with respect to a predetermined control parameter. Continuation methods are especially useful in the analysis of nonlinear systems due to the complex and often unpredictable response behavior. Additionally, the pseudo-arclength method provides the unique ability to trace folding solution branches.

1.2.2 Cell Mapping

Nonlinear dynamic systems are capable of exhibiting complex and interesting response characteristics. One common nonlinear response feature is the coexistence of multiple stable attractors. In order to better understand the system dynamics and be able to more accurately predict the expected response behavior, it is important to (1) identify the amplitude and stability of each attractor, and (2) identify the size and distribution of the *basins* associated with each attractor (*i.e.* the set of all initial

conditions converging to the attractor) [98].

Determining the amplitude and stability of each attractor identifies what response behavior is possible in a given system. This information can be obtained by constructing a frequency-response plot using numerical [96] or approximate analytical [57] techniques. Characterizing the basins of attraction identifies the conditions which produce each type of response behavior. This analysis is important since a direct correlation exists between the size and distribution of the basins and the structural integrity of the dynamic system [99, 100]. Unfortunately, basin construction typically requires significant computational resources and therefore is often not performed in practice. Furthermore, no comparable analytical techniques exist [101]. In the remainder of this section, the various methods used to identify the basins of attraction are described.

The most straightforward method used to determine the basins of attraction is the *grid of starts* (GOS), also referred to as *integration of a grid of points* (IGP). In this method, *basin portraits*—two-dimensional cross sections illustrating the basin distribution—are constructed by numerically integrating response trajectories from a grid of initial conditions. The length of the numerical integrations must be such that the transient behavior decays sufficiently to allow for identification of the steady-state response resulting from each initial condition. In addition to the conceptual simplicity and ease of implementation of the GOS, the method provides near-zero error, its accuracy limited only by the accuracy of the numerical integration [102]. However, the computational cost of the GOS method is high, especially for higher-dimensional systems and parametric studies. Regardless, GOS remains as one of the most widely used global analysis tools (see for example [103], and references within).

Cell mapping methods can provide an accurate approximation of the basins of attraction using a fraction of the computing resources of GOS and can be better suited for analyzing random excitation [104, 105, 106]. The first cell mapping method

was Hsu's *simple cell mapping* (SCM), which became the basis for many cell mapping methods developed in the following years [104]. The key characteristic of cell mapping methods is that continuous state space is approximated by a discrete array of cells known as *cell state space*. By conducting a short-time integration from the center of each cell within the array and identifying the cell containing the endpoint of the trajectory, a cell-to-cell map is created which completely describes the dynamics of the system. In addition to illustrating the basins of attraction, the map can also be used to quickly synthesize long-term trajectories.

Figure 1.9 illustrates the SCM procedure for a hypothetical two-dimensional system. The cell state space consists of a group of cells numbered from 1–30 and a *sink cell* used to identify the destination of all trajectories mapping outside the group of cells. The thick square indicates a 3×3 region in which the basin portrait will be constructed. In a real analysis, a resolution of 101×101 or more is typically used. Note that the total number of mapped cells is much larger than the number of cells in the portrait region in order to capture trajectories that may exit and reenter the region. After cells 1–13 have been processed, the cell number to which each maps is indicated by an arrow (\rightarrow). Dashed arrows labeled (a–d) illustrate the next four steps, each representing a trajectory initiated from the center of the respective cell and integrated forward over a short time interval.

The SCM method was demonstrated to drastically reduce computation times for single degree-of-freedom systems when compared with the GOS. However, a few shortfalls of the method were also identified. Error propagation was possible due to the inconsistency between the endpoint of a trajectory segment within a cell and the start of the subsequent trajectory segment using the centerpoint method [107]. Hsu argued that accurate results could be obtained using a sufficiently small cell size, noting that similar roundoff errors are experienced during any numerical integration or experimental data collection due to the finite precision of computers and sensors [104].

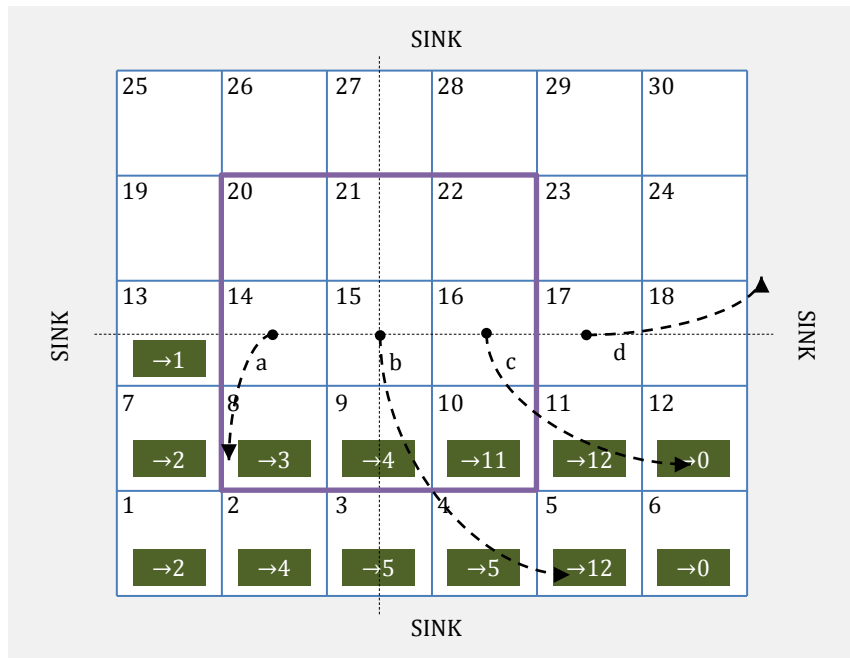


Figure 1.9: A two-dimensional example illustrating the simple cell mapping (SCM) procedure.

Room for improvement was also identified when dealing with chaotic systems or basins with fractal boundaries. Due to the finite number of states that exist within the SCM method, the means for identifying chaotic behavior is limited to assuming that any response which has not repeated in a predetermined number of steps is chaotic. In order to overcome this limitation, Hsu *et al.* developed the *generalized cell mapping* (GCM) method [108, 109]. The GCM method is more computationally expensive than the SCM method, but provides a probabilistic analysis of the system that is more efficient than other iterative numerical procedures necessary to produce comparable results [101, 103].

The *interpolated cell mapping* (ICM) method was later introduced by Tongue and Gu [103, 107] and gained popularity due to its increased accuracy over SCM, particularly at lower resolutions (*e.g.* [110, 111]). As the name suggests, ICM uses interpolative methods to more accurately reproduce long-term trajectories. For low-dimensional systems, no marginal increase in computational cost of ICM over SCM is encountered. However, interpolations become complicated for higher-dimensional systems, diminishing the efficiency of the method [102].

Other cell mapping methods were developed in the following years. *Tensor product interpolated cell mapping* (TPICM) uses a more complex mapping process to achieve higher-order accuracy than ICM at the expense of additional CPU cost [112]. *Multiple mapping* (MM) also demonstrates increased accuracy over ICM, particularly in regions of cell state space where nearby trajectories diverge quickly. MM results in only marginal gains in run time over ICM compared to the gains associated with TPICM [113]. *Modified interpolated cell mapping* (MICM) reduces the run time from that of ICM by providing additional instructions allowing for early termination of the iterative procedures in the ICM method [102]. Other modifications to the SCM and ICM methods allow for the study of bifurcations under parameter variations [114] and application to discontinuous systems [115].

Among these methods, however, the problem remained that efficiency benefits over the GOS method were lost for higher-dimensional systems. The cause of the poor scaling capability of cell mapping methods to date was that in order for a basin portrait to be constructed, the mapping of each cell in the N -dimensional cell state space must be determined, resulting in an exponential increase in number of cells to map when increasing the system dimension.

The *multi-degrees-of-freedom cell mapping* (MDCM) method, developed in [116, 117, 115] and applied in [118, 119], overcomes this limitation. The MDCM method uses a coordinate numbering convention for each cell which imposes no intrinsic limit on the size of cell state space. Therefore, even for a system with an arbitrarily large number of dimensions, the only cells that must be processed are those in a two-dimensional subspace corresponding to the basin portrait and the cells encountered in each subsequent trajectory leading to the attractor.

The technique of only processing certain cells if they are encountered in a previous map is what allows the MDCM method to scale efficiently to larger-dimensional systems. However, the sequential nature of the process limits the ability to utilize parallel computing resources within the algorithm. This dichotomy forms the motivation for the parallelized multi-degrees-of-freedom cell mapping (PMDCM) method, a variant of the MDCM method where the algorithm is restructured in order to utilize parallel processing resources and further improve efficiency benefits.

1.2.3 Cell State Space Representation

A summary of the mathematical construction of cell state space and the basic MDCM procedure is provided as follows. All equations in this section are adapted from [115].

For a system of N first-order differential equations described by Eq. (1.1),

$$\dot{x}_i = F_i(x_1, \dots, x_N; t), \quad i = 1, \dots, N, \quad (1.1)$$

cell state space is constructed by partitioning continuous state space into a discretized region of cells. Each cell \mathbf{z} is uniquely identified by N indices, $\mathbf{z} = [z_1, \dots, z_N]$, $z_i \in \mathbb{Z}$. The cell spacing h_i is consistent in each dimension such that for each cell centered at

$$c_i = h_i z_i, \quad i = 1, \dots, N, \quad (1.2)$$

the cell boundaries contain all states within

$$(z_i - 1/2)h_i \leq x_i \leq (z_i + 1/2)h_i, \quad i = 1, \dots, N. \quad (1.3)$$

In order to construct a basin portrait of the region described by

$$\Omega' = \{\mathbf{x} \in \mathbb{R}^N \mid x_i^{(l)} \leq x_i \leq x_i^{(u)}, i = 1, 2 \wedge x_i = 0, i = 3, \dots, N\}, \quad (1.4)$$

a two-dimensional subset S of cell state space is defined,

$$S = \{\mathbf{z} \in \mathbb{Z}^N \mid z_i^{(l)} \leq z_i \leq z_i^{(u)}, i = 1, 2 \wedge z_i = 0, i = 3, \dots, N\}, \quad (1.5)$$

where $z_i^{(l)}$ and $z_i^{(u)}$, $i = 1, 2$ indicate the cells at the lower and upper limit of the subspace, respectively. Thus, S consists of a total of M cells,

$$M = (1 + z_1^{(u)} - z_1^{(l)})(1 + z_2^{(u)} - z_2^{(l)}). \quad (1.6)$$

Basin portraits are constructed by conducting a series of numerical integrations spanning a short-time duration in order to determine the cell z_i^* which contains the endpoint x_i^* of each trajectory,

$$z_i^* = \text{int}(x_i^*/h_i + 1/2), \quad (1.7)$$

where $\text{int}(X)$ indicates rounding to the largest integer less than or equal to X .

The MDCM procedure starts by initiating a trajectory from the center of one of the cells within S . If the cell within which the trajectory ends z_i^* has not already been processed, a new trajectory is initiated from the center of z_i^* . This sequence is repeated until a trajectory ends within a cell which has already been processed, indicating periodic behavior. The current sequence is then terminated and a new trajectory is initiated from the next cell in S until all cells have been processed. For a detailed description of the MDCM method, the reader is encouraged to refer to the referenced texts [115].

Integrity Measures

Basin portraits provide a useful illustration of the strength of various attractors, representing the dynamical integrity of a system. At least two distinct regions are illustrated in each portrait: the safe basin and the constraint basin. The *safe basin*, denoted by \mathcal{A}_∞ , represents the set of all initial conditions that converge to a “safe solution” possessing favorable response characteristics. In this case, the safe solution is defined by a steady-state response amplitude below a threshold value. The *constraint basin*, \mathcal{C}_∞ , represents the set of initial conditions that converge to a solution above the threshold value. In some cases, multiple safe or constraint basins are illustrated in a single portrait in order to distinguish between regions converging to specific attractors.

When the results from a large number of basin portraits are to be summarized, as is the case in the present study, it becomes necessary to concisely identify key characteristics of the portraits using scalar *integrity measures*. Plotting the integrity measures versus excitation magnitude forms the *erosion profiles*, an important tool used to compare the structural integrity of a system [100]. In the present work, four scalar integrity measures are used: the *global integrity measure* (GIM), *local integrity measure* (LIM) and *impulsive integrity measure* (IIM) developed by Soliman and

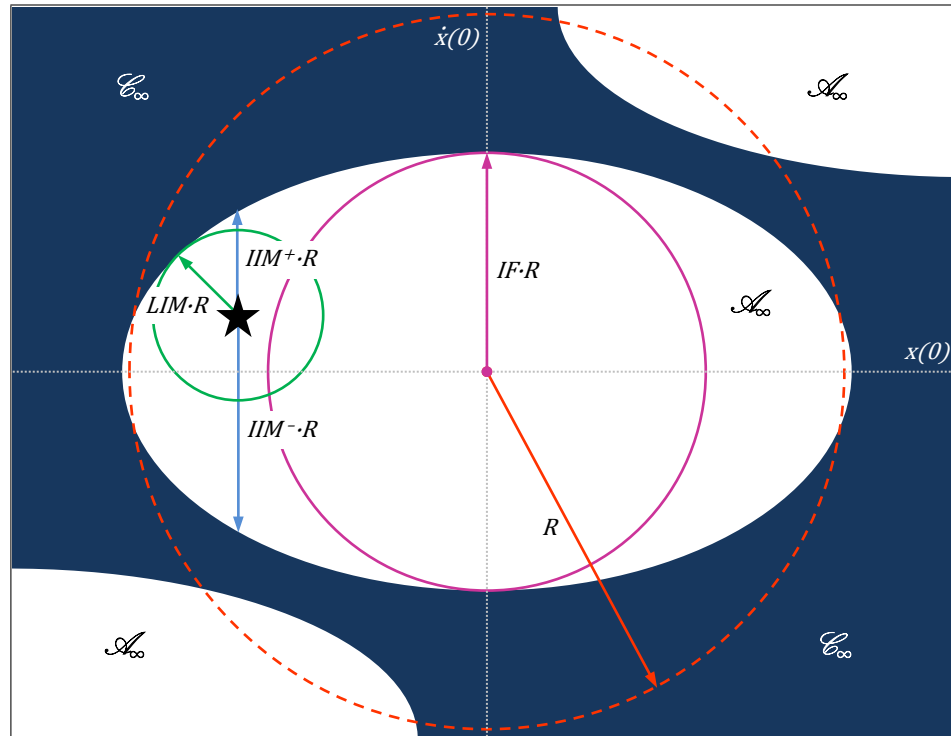


Figure 1.10: Three integrity measures illustrated on the basin portrait of a hypothetical two degrees-of-freedom system.

Thompson in 1989 [120], and the *integrity factor* (IF), introduced by Lenci and Rega in the last decade [121]. In general, $\text{GIM} \geq \text{IF} \geq \text{IIM} \geq \text{LIM}$. Figure 1.10 illustrates three of the integrity measures superimposed on the basin portrait of a hypothetical two-DOF system. The basin portrait consists of a disjoint safe basin (white) and a constraint basin (shaded). The safe attractor is denoted with a star.

The global integrity measure and the local integrity measure are two of the most commonly used integrity measures in this type of global analysis [120]. The GIM is defined as the normalized hyper-volume of the safe basin \mathcal{A}_∞ . In a two-dimensional system, the GIM therefore represents the area of \mathcal{A}_∞ normalized by a reference area (*e.g.* the area within the circle of radius R). The LIM is a much more conservative measure, defined as the normalized radius of the largest hyper-sphere (circle in two dimensions) that is centered on the safe attractor and entirely contained within the safe basin. A direct correlation therefore exists between the LIM and the stability of

the safe attractor with regard to its robustness to perturbations.

Also directly correlated to the stability of the safe attractor is the impulsive integrity measure. Recalling that an ideal impulse is defined as an instantaneous change in velocity, the IIM is defined as the normalized distance from the safe attractor to the boundary of \mathcal{C}_∞ in the direction of a generalized coordinate corresponding to a velocity. The IIM corresponding to an impulse in the positive direction is denoted by IIM^+ , and in the negative direction by IIM^- . The measure IIM^\pm is used to indicate the minimum of the two impulse integrity measures.

The integrity factor was introduced as an alternative to the GIM in order to account only for the compact part of the safe basin. The IF is defined as the normalized radius of the largest hyper-sphere (circle in two dimensions) that can be completely contained within the safe basin and therefore provides a more conservative integrity estimation than the GIM when dealing with disjoint basins or fractal or entangled boundaries.

Chapter 2

System Model and Governing Equations

A schematic of the three degrees-of-freedom system consisting of a primary structure (PS), nonlinear tuned mass damper (NTMD) and semi-active tuned mass damper (STMD) is presented in Fig. 2.1. The mass of the primary structure, NTMD and STMD are M , m_N and m_S , respectively. Parameters c_1 , c_N and c_S represent the viscous damping coefficients for each of the three structures.

The restoring force of the primary structure is represented by a simple linear spring, with stiffness k_1 . The restoring force of the nonlinear tuned mass damper consists of one linear and one cubic term, as described by Eqn. (2.1).

$$f_N = k_M(x_1 - x_N) + \alpha_N(x_1 - x_N)^3. \quad (2.1)$$

The stiffness coefficient of the STMD k_S is tuned such that the natural frequency of the STMD is equal to the excitation frequency, $\omega_S = \omega_f$. In a real-world application, the stiffness tuning would be achieved by a feedback control system which monitors the structural response, calculates the dominant frequency of the excitation or response, and adjusts the stiffness accordingly; for example, using the algorithms

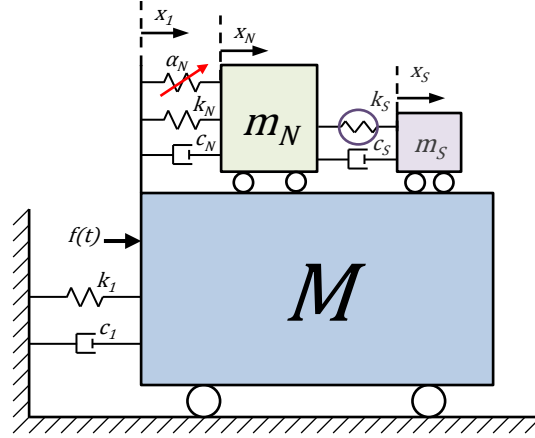


Figure 2.1: Schematic of a primary structure with a NTMD and STMD in series.

developed in [90]. Clearly, some time delay between a change in the excitation and the corresponding stiffness adjustment in the STMD is inevitable, however, such time delay does not cause any deterioration of performance [90]. Therefore, to provide an initial evaluation of the attenuation capability of the system considered in the present study, the stiffness tuning of the STMD is assumed to be instantaneous with respect to changes in the excitation.

The equations of motion are derived from the Euler-Lagrange equations for the system by using standard methods which can be found in vibrations textbooks (i.e. [122, 123]). The cubic-coupled terms in the resulting equations resemble those in other systems such as [46] and [1], for example. The equations of motion for the 3-DOF system is expressed in dimensional form as,

$$\hat{\mathbf{M}}\ddot{\mathbf{x}}(t) + \hat{\mathbf{C}}\dot{\mathbf{x}}(t) + \hat{\mathbf{K}}\mathbf{x}(t) + \hat{\mathbf{n}}(\mathbf{x}(t)) = \hat{\mathbf{g}}(t), \quad (2.2)$$

where,

$$\mathbf{x}(t) = \begin{Bmatrix} x_P(t) \\ x_N(t) \\ x_S(t) \end{Bmatrix}, \quad (2.3)$$

$$\hat{\mathbf{M}} = \begin{bmatrix} M & 0 & 0 \\ 0 & m_N & 0 \\ 0 & 0 & m_S \end{bmatrix}, \quad (2.4)$$

$$\hat{\mathbf{C}} = \begin{bmatrix} c_1 + c_N & -c_N & 0 \\ -c_N & c_N + c_S & -c_N \\ 0 & -c_S & c_N \end{bmatrix}, \quad (2.5)$$

$$\hat{\mathbf{K}} = \begin{bmatrix} k_1 + k_N & -k_N & 0 \\ -k_N & k_N + k_S & -k_S \\ 0 & -k_S & k_S \end{bmatrix}, \quad (2.6)$$

$$\hat{\mathbf{n}}(\mathbf{x}(t)) = \begin{Bmatrix} \alpha_N (x_1(t) - x_N(t))^3 \\ \alpha_N (x_N(t) - x_1(t))^3 \\ 0 \end{Bmatrix}, \quad (2.7)$$

$$\hat{\mathbf{g}}(t) = \begin{Bmatrix} f \sin(\omega_f t) \\ 0 \\ 0 \end{Bmatrix}. \quad (2.8)$$

Multiplying both sides of the equation by the inverse of $\hat{\mathbf{M}}$ gives,

$$\mathbf{I}\ddot{\mathbf{x}}(t) + \hat{\mathbf{M}}^{-1}\hat{\mathbf{C}}\dot{\mathbf{x}}(t) + \hat{\mathbf{M}}^{-1}\hat{\mathbf{K}}\mathbf{x}(t) + \hat{\mathbf{M}}^{-1}\hat{\mathbf{n}}(\mathbf{x}(t)) = \hat{\mathbf{M}}^{-1}\hat{\mathbf{g}}(t), \quad (2.9)$$

where the inverse is simply,

$$\hat{\mathbf{M}}^{-1} = \begin{bmatrix} 1/M & 0 & 0 \\ 0 & 1/m_N & 0 \\ 0 & 0 & 1/m_S \end{bmatrix}, \quad (2.10)$$

and $\mathbf{I} = \hat{\mathbf{M}}^{-1}\hat{\mathbf{M}}$, where it is noted that $\mathbf{I}\ddot{\mathbf{x}}(t) = \ddot{\mathbf{x}}(t)$. In order to non-dimensionalize with respect to time, the following substitution is made,

$$t = \frac{\tau}{\omega_1}, \quad (2.11)$$

and therefore

$$\frac{d}{dt} = \omega_1 \frac{d}{d\tau}, \quad \frac{d^2}{dt^2} = \omega_1^2 \frac{d^2}{d\tau^2}. \quad (2.12)$$

In order to non-dimensionalize with respect to length, a characteristic length L is chosen and the new non-dimensional length coordinates $\mathbf{y}(\tau)$ are defined as

$$\mathbf{y}(\tau) = \frac{\mathbf{x}(\tau)}{L}. \quad (2.13)$$

Substituting Eqns. (2.11)–(2.13) into Eqn. (2.9) results in

$$\omega_1^2 L \mathbf{y}''(\tau) + \omega_1 L \hat{\mathbf{M}}^{-1} \hat{\mathbf{C}} \mathbf{y}'(\tau) + L \hat{\mathbf{M}}^{-1} \hat{\mathbf{K}} \mathbf{y}(\tau) + L^3 \hat{\mathbf{M}}^{-1} \hat{\mathbf{n}}(\mathbf{y}(\tau)) = \hat{\mathbf{M}}^{-1} \hat{\mathbf{g}}(\tau), \quad (2.14)$$

where

$$\hat{\mathbf{g}}(\tau) = \begin{Bmatrix} f \sin\left(\frac{\omega_f}{\omega_1} \tau\right) \\ 0 \\ 0 \end{Bmatrix}. \quad (2.15)$$

After dividing both sides of the equation by $\omega_1^2 L$, the following variables are sub-

stituted,

$$\begin{aligned}
c_1/M &= 2\gamma_1\omega_1, & c_N/m_N &= 2\gamma_N\omega_2, & c_S/m_S &= 2\gamma_S\omega_S, \\
\omega_1 &= \sqrt{k_1/M}, & \omega_2 &= \sqrt{k_N/m_N}, & \omega_N &= \sqrt{\alpha_N/m_N}, \\
\omega_S &= \sqrt{k_S/m_S}, & \epsilon_N &= m_N/M, & \epsilon_S &= m_S/M, \\
\Omega &= \omega_2/\omega_1, & \Omega_N &= \omega_N L/\omega_1, & \Omega_S &= \omega_S/\omega_1, \\
\omega &= \omega_f/\omega_1, & F &= f/k_1 L = f/(\omega_1^2 M).
\end{aligned} \tag{2.16}$$

As illustrated in Fig. 2.1, the system model incorporates a constant damping coefficient between the NTMD and STMD. However, the stiffness tuning of the STMD modulates its natural frequency ω_S which in turn influences the STMD damping ratio according to Eqn. (2.16). For this reason, the non-dimensional STMD damping parameter is introduced, $\hat{\gamma}_S$. Compared with the actual damping ratio of the STMD, γ_S —the value of which changes with the STMD stiffness—the STMD damping parameter is defined as $\hat{\gamma}_S = c_S/2\omega_1 m_S = \gamma_S \Omega_S$, such that $\hat{\gamma}_S = \gamma_S$ when the STMD is tuned to the natural frequency of the primary structure, $\omega_S = \omega_1$. This notation is used to maintain consistency by allowing the damping ratio of the STMD to be expressed in a similar non-dimensionalized form as the primary structure damping ratio γ_1 . Since the value of γ_S always appears as a coefficient of Ω_S within the equations of motion, the ω_S terms drop out and therefore the damping term is indeed constant. Due to the near-zero and zero-valued linear tuning ratios used in Chapter 5, it is also helpful to introduce a constant damping coefficient for the NTMD. In a similar manner, the NTMD damping parameter is defined within Chapter 5 as $\hat{\gamma}_N = c_N/2\omega_1 m_N = \gamma_N \Omega$.

After simplifying, the following expression is obtained, non-dimensionalized with respect to time and length,

$$\mathbf{y}''(\tau) + \mathbf{C}\mathbf{y}'(\tau) + \mathbf{K}\mathbf{y}(\tau) + \bar{\mathbf{n}}(\mathbf{y}(\tau)) = \bar{\mathbf{g}}(\tau), \tag{2.17}$$

where,

$$\mathbf{C} = \begin{bmatrix} 2\gamma_1 + 2\gamma_N\Omega\epsilon_N & -2\gamma_N\Omega\epsilon_N & 0 \\ -2\gamma_N\Omega & 2\gamma_N\Omega + 2\hat{\gamma}_S\frac{\epsilon_S}{\epsilon_N} & -2\hat{\gamma}_S\frac{\epsilon_S}{\epsilon_N} \\ 0 & -2\hat{\gamma}_S & 2\hat{\gamma}_S \end{bmatrix}, \quad (2.18)$$

$$\mathbf{K} = \begin{bmatrix} 1 + \Omega^2\epsilon_N & -\Omega^2\epsilon_N & 0 \\ -\Omega^2 & \Omega^2 + \Omega_S^2\frac{\epsilon_S}{\epsilon_N} & -\Omega_S^2\frac{\epsilon_S}{\epsilon_N} \\ 0 & -\Omega_S^2 & \Omega_S^2 \end{bmatrix}, \quad (2.19)$$

$$\bar{\mathbf{n}}(\mathbf{x}(\tau)) = \begin{bmatrix} \Omega_N^2\epsilon_N (x_1(\tau) - x_N(\tau))^3 \\ \Omega_N^2 (x_N(\tau) - x_1(\tau))^3 \\ 0 \end{bmatrix}, \quad (2.20)$$

$$\bar{\mathbf{g}}(\tau) = \begin{bmatrix} F \sin(\omega\tau) \\ 0 \\ 0 \end{bmatrix}. \quad (2.21)$$

Finally, a new non-dimensional coordinate system $\mathbf{q}(\tau)$ is introduced in order to express the ratio of the system response with the static response amplitude $|\mathbf{y}^{st}|$ —the amplitude of each coordinate at $\omega \approx 0$ —as

$$\mathbf{q}(\tau) = \frac{\mathbf{y}(\tau)}{|\mathbf{y}^{st}|}. \quad (2.22)$$

The fully non-dimensionalized equations of motion are therefore expressed as

$$\mathbf{q}''(\tau) + \mathbf{C}\mathbf{q}'(\tau) + \mathbf{K}\mathbf{q}(\tau) + \mathbf{n}(\mathbf{q}(\tau)) = \mathbf{g}(\tau). \quad (2.23)$$

The two degrees-of-freedom form of Eqn. (2.23) is obtained by eliminating the third row and column of all arrays and removing terms related to the STMD.

Chapter 3

Weakly Nonlinear Tuned Mass Damper

In this chapter, the performance of a system consisting of a linear primary system, a tuned mass damper with a “weak” nonlinear stiffness, and a semi-active tuned mass damper in series is explored. In this case, the designation of “weak” is used to indicate a nonlinear parameter value large enough to compromise attenuation capability but not large enough to produce the complex nonlinear phenomena which will be presented in Chapter 5. The system considered in the present chapter is *not* meant to correspond an absorber that is intentionally designed with weakly nonlinear characteristics in order to increase the suppression bandwidth (*e.g.* [29, 30, 34, 36]). The results in this chapter are intended to address the problem of an optimally tuned linear TMD which has developed an unintended hardening nonlinearity as a result of degradation of components, operation outside of the intended linear range, or by other means.

First, the response of the two-DOF system consisting of the primary structure (PS) and NTMD—referred to hereafter as the *PN system*—is characterized. In the next section, the results of a parametric study of the STMD parameters that minimize

the PS response in the three-DOF system consisting of the PS, NTMD and STMD in series—hereafter referred to as the *PNS system*—are presented. The performance benefits from the STMD are compared with that of a linear TMD added in a similar configuration in the following section. Then, the performance of the PNS system under random excitation is evaluated. A summary of results is presented in the final section.

3.1 Effect of Weak Nonlinearity on Performance of TMD

In this section, it is demonstrated how a weak cubic nonlinearity detunes a vibration absorber and consequently reduces its attenuation capability. Analytical equations are derived describing the amount of detuning versus the system parameters. First, a coordinate transformation is introduced in order to decouple the stiffness matrix for compatibility with the perturbation methods. Then, the Laplace Transform is used to obtain a solution of the linearized equations of motion. In the following section, the frequency-amplitude relationship of the nonlinear response is approximated using the Method of Multiple Scales. The amplitudes calculated for the linear system are then combined with the nonlinear amplitude-frequency relationship to obtain an expression for the detuned absorber frequency ratio. Finally, the results derived from the analytical approximations are presented and compared with the results of numerical simulations.

3.1.1 Coordinate Transformation

In present form, Eqn. (2.23) is not suitable for use in the Method of Multiple Scales due to the linear stiffness coupling between the two degrees of freedom, which appears as off-diagonal terms in the \mathbf{K} matrix. However, the linear stiffness can be easily

decoupled by expressing the equation in terms of the modal coordinates. Since this section is focused only on the behavior of the PN system without the third degree-of-freedom introduced by the STMD, the two-DOF form of Eqn. (2.23) is used, obtained by eliminating the third row and column of all arrays and removing terms related to the STMD.

The modal coordinate system $\mathbf{z}(\tau) = \{z_1(\tau), z_2(\tau)\}^T$ is introduced by defining

$$\mathbf{y}(\tau) = \mathbf{P}\mathbf{z}(\tau), \quad (3.1)$$

where \mathbf{P} is the matrix composed of the eigenvectors of \mathbf{K} . Substituting Eqn. (3.1) into Eqn. (2.23) and pre-multiplying by the inverse of \mathbf{P} , denoted by \mathbf{P}^{-1} , we obtain,

$$\mathbf{z}''(\tau) + \mathbf{P}^{-1}\mathbf{C}\mathbf{P}\mathbf{z}'(\tau) + \mathbf{P}^{-1}\mathbf{K}\mathbf{P}\mathbf{z}(\tau) + \mathbf{P}^{-1}\tilde{\mathbf{n}}(\mathbf{z}(\tau)) = \mathbf{P}^{-1}\mathbf{g}(\tau), \quad (3.2)$$

By defining the new matrices $\tilde{\mathbf{C}} = \mathbf{P}^{-1}\mathbf{C}\mathbf{P}$ and $\tilde{\mathbf{K}} = \mathbf{P}^{-1}\mathbf{K}\mathbf{P}$, and vectors $\tilde{\mathbf{n}}(\mathbf{z}(\tau)) = \mathbf{P}^{-1}\tilde{\mathbf{n}}(\mathbf{z}(\tau))$ and $\tilde{\mathbf{g}}(\tau) = \mathbf{P}^{-1}\mathbf{g}(\tau)$, the equations of motion are expressed more concisely as

$$\mathbf{z}''(\tau) + \tilde{\mathbf{C}}\mathbf{z}'(\tau) + \tilde{\mathbf{K}}\mathbf{z}(\tau) + \tilde{\mathbf{n}}(\mathbf{z}(\tau)) = \tilde{\mathbf{g}}(\tau), \quad (3.3)$$

Equation 3.3 represents the matrix form of the equations of motion expressed in terms of the non-dimensional modal coordinates $\mathbf{z}(\tau)$. The stiffness matrix $\tilde{\mathbf{K}}$ is diagonal, indicating that the linear stiffness is decoupled. The composition terms in each matrix is explicitly described in Appendix D.

3.1.2 Linear Frequency Response

By ignoring the vector of nonlinear terms $\tilde{\mathbf{n}}(\mathbf{z}(\tau))$ in Eqn. (3.3), the linear form of the equations of motion in the modal coordinate system—that is, the resulting equations in the case of $\Omega_N = 0$ —can be expressed as

$$z_1''(\tau) + 2\gamma_{11}z_1'(\tau) + 2\gamma_{12}z_2'(\tau) + \omega_{11}^2z_1(\tau) = g(\tau), \quad (3.4)$$

$$z_2''(\tau) + 2\gamma_{21}z_1'(\tau) + 2\gamma_{22}z_2'(\tau) + \omega_{22}^2z_2(\tau) = -g(\tau). \quad (3.5)$$

The damping and natural frequency parameters γ_{ij} and ω_{ii} , $i, j = 1, 2$, are each functions of the system parameters $\gamma_1, \gamma_N, \Omega$, and ϵ_N , and are obtained by comparing the form of Eqns. (3.4) and (3.5) with the explicit formulation of the equations of motion given in Appendix D. By transforming Eqns. (3.4)–(3.5) into the Laplace domain, a straightforward solution can be obtained by algebraic manipulation (see, *e.g.* [122]). The Laplace Transform $\mathcal{L}[\cdot]$ of the coordinates, their derivatives, and the forcing function are defined as

$$\mathcal{L}[z_i(\tau)] = Z_i(s), \quad (3.6)$$

$$\mathcal{L}[z_i'(\tau)] = sZ_i(s) - z_i(0), \quad (3.7)$$

$$\mathcal{L}[z_i''(\tau)] = s^2Z_i(s) - sz_i(0) - z_i'(0), \quad (3.8)$$

$$\mathcal{L}[g(\tau)] = G(s), \quad (3.9)$$

where s is a complex frequency parameter. Taking the Laplace Transform of both sides of Eqns. (3.4)–(3.5) and rearranging results in

$$(s^2 + 2\gamma_{11}s + \omega_{11}^2)Z_1(s) + (2\gamma_{12}s)Z_2(s) = G(s), \quad (3.10)$$

$$-(2\gamma_{21}s)Z_1(s) - (s^2 + 2\gamma_{22}s + \omega_{22}^2)Z_2(s) = -G(s). \quad (3.11)$$

Further manipulation yields the input-output equations describing the amplitude of each coordinate relative to the forcing function,

$$\frac{Z_1(s)}{G(s)} = \frac{s^2 + 2s(\gamma_{12} + \gamma_{22}) + \omega_{22}^2}{-4s^2\gamma_{12}\gamma_{21} + 2s\gamma_{11}(s^2 + 2s\gamma_{22} + \omega_{22}^2) + (s^2 + \omega_{11}^2)(s^2 + 2s\gamma_{22} + \omega_{22}^2)}, \quad (3.12)$$

$$Z_2(s) = - \left(\frac{s^2 + 2(\gamma_{11} + \gamma_{21})s + \omega_{11}^2}{s^2 + 2(\gamma_{12} + \gamma_{22})s + \omega_{22}^2} \right) Z_1(s). \quad (3.13)$$

The amplitudes of the modal coordinates at a given frequency ω are obtained by substituting $s = j\omega$ into Eqns. (3.12)–(3.13) and taking the complex magnitude of the result.

3.1.3 Amplitude-Frequency Relationship

In order to estimate the amplitude-frequency relationship resulting from the nonlinearity, a nonlinear form of Eqn. (3.3) is again used. The equations of motion are now expressed as

$$z_1'' + \omega_{11}^2 z_1 = -2\gamma_{11} z_1' + \alpha_{11} z_1^3 + \alpha_{12} z_1^2 z_2 + \alpha_{13} z_1 z_2^2 + \alpha_{14} z_2^3, \quad (3.14)$$

$$z_2'' + \omega_{22}^2 z_2 = -2\gamma_{22} z_2' + \alpha_{21} z_1^3 + \alpha_{22} z_1^2 z_2 + \alpha_{23} z_1 z_2^2 + \alpha_{24} z_2^3, \quad (3.15)$$

where the explicit notation of the time-dependence of the coordinates (τ) has been dropped in the interest of space.

Equations (3.14)–(3.15) represent the free response of the nonlinear system in terms of the modal coordinates. The off-diagonal damping terms γ_{12} and γ_{21} from Eqn. (3.3) are assumed to have a negligible influence on the amplitude-frequency relationship, so they have been ignored. Again, the coefficients γ_{ii} and α_{ij} , $i = 1, 2, j = 1, \dots, 4$, are functions of the system parameters $\gamma_1, \gamma_N, \Omega, \epsilon_N$, and Ω , and are obtained by comparing the form of the equations with those in Appendix D.

The form of Eqns. (3.14)–(3.15) is similar to that of the two degrees-of-freedom system studied by Nayfeh and Mook [38]. Based on the results of the Method of Multiple Scales analysis presented in Ref. [38], the first-order approximate solution can be expressed as

$$z_1(\tau) \approx a_{10} \cos((\omega_{11} + \theta_{11}(a_{10}, a_{20}))\tau + \theta_{10}), \quad (3.16)$$

$$z_2(\tau) \approx a_{20} \cos((\omega_{22} + \theta_{22}(a_{10}, a_{20}))\tau + \theta_{20}), \quad (3.17)$$

where the frequency parameters θ_{11} and θ_{22} are expressed as functions of the response amplitudes a_{10} and a_{20} as

$$\theta_{11}(a_{10}, a_{20}) = \frac{3\alpha_{11}}{8\omega_{11}}a_{10}^2 + \frac{\alpha_{13}}{4\omega_{11}}a_{20}^2, \quad (3.18)$$

$$\theta_{22}(a_{10}, a_{20}) = \frac{3\alpha_{24}}{8\omega_{22}}a_{20}^2 + \frac{\alpha_{22}}{4\omega_{22}}a_{10}^2. \quad (3.19)$$

3.1.4 Effective Frequency Ratio Versus Nonlinearity

It follows from Eqns. (3.16)–(3.17) that the free-response frequencies of the PN system in the decoupled modal coordinate system are

$$\bar{\omega}_{11}(a_{10}, a_{20}) = \omega_{11} + \frac{3\alpha_{11}}{8\omega_{11}}a_{10}^2 + \frac{\alpha_{13}}{4\omega_{11}}a_{20}^2, \quad (3.20)$$

$$\bar{\omega}_{22}(a_{10}, a_{20}) = \omega_{22} + \frac{3\alpha_{24}}{8\omega_{22}}a_{20}^2 + \frac{\alpha_{22}}{4\omega_{22}}a_{10}^2. \quad (3.21)$$

In the case of zero nonlinearity, $\Omega_N = 0$, all α_{ij} terms become zero and the response frequency of each modal coordinate is equal to the corresponding natural frequency. Otherwise, the free-response frequencies are increased, demonstrating that

the nonlinear terms have effectively detuned the natural frequencies.

Equations (3.20)–(3.21) present an approximate expression describing the relationship between the response frequency and amplitude of the PN system with a weak nonlinearity in the modal coordinate system. In order to return to the original coordinate system, the detuned stiffness matrix $\bar{\mathbf{K}}$ is defined by replacing the diagonal terms in $\tilde{\mathbf{K}}$ by their detuned counterparts (Eqns. (3.20)–(3.21)) and reversing the coordinate transformation procedure described in Section 3.1.1,

$$\bar{\mathbf{K}} = \mathbf{P} \begin{bmatrix} \bar{\omega}_{11}^2 & 0 \\ 0 & \bar{\omega}_{22}^2 \end{bmatrix} \mathbf{P}^{-1}, \quad (3.22)$$

Since $K_{(2,2)} = \Omega^2$, the effect of the nonlinear parameter Ω_N on the tuning ratio Ω can be determined from the corresponding element in $\bar{\mathbf{K}}$. The detuned frequency ratio $\bar{\Omega}$ is therefore defined as a function of the response amplitudes as,

$$\bar{\Omega}(a_{10}, a_{20}) = \left(\frac{P_{(1,1)}\bar{\omega}_{22}(a_{10}, a_{20})^2 - P_{(1,2)}\bar{\omega}_{11}(a_{10}, a_{20})^2}{P_{(1,1)} - P_{(1,2)}} \right)^{1/2}. \quad (3.23)$$

A direct relationship between $\bar{\Omega}$ and Ω_N is then obtained by using the amplitudes for the corresponding linear system calculated from Eqns. (3.12)–(3.13) and the optimum tuning ratio $\Omega = (1 + \epsilon_N)^{-1}$ defined in Ref. [124] to calculate the detuned natural frequencies in Eqns. (3.20)–(3.21) and substitute into Eqn. (3.23). Figure 3.1 illustrates the detuned frequency ratio $\bar{\Omega}$ versus the primary structure amplitude. The vertical dashed line marks the optimum tuning ratio based on the mass of the absorber. As the nonlinear coefficient increases from zero—acting as an optimally tuned linear TMD ($\bar{\Omega} = \Omega = 0.9804$)—to $\Omega_N = 0.03$, the detuned frequency ratio increases to $\bar{\Omega} = 2.16$, resulting in a corresponding increase to the primary structure amplitude.

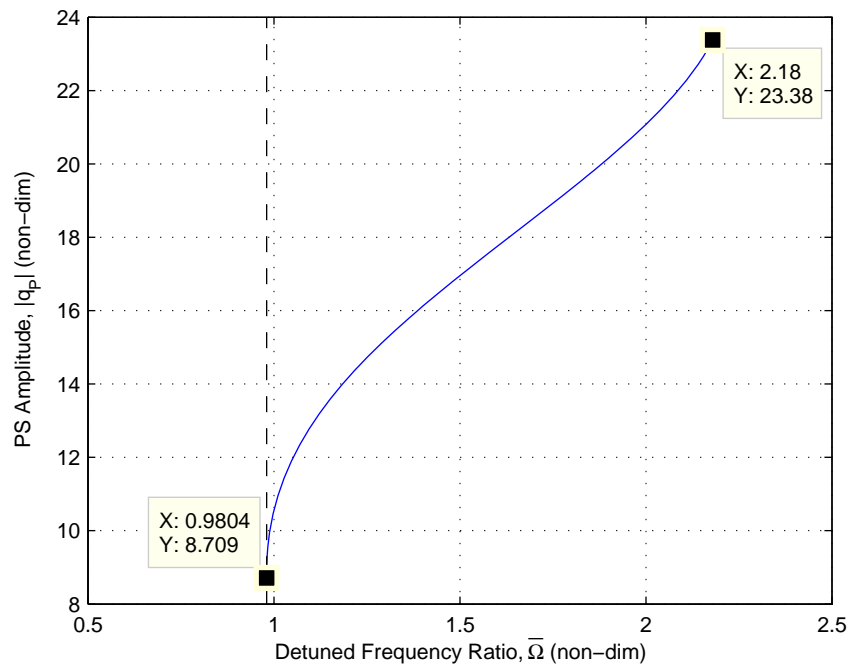


Figure 3.1: Detuned frequency ratio versus primary structure amplitude, for $\epsilon_N = 0.02$, $\gamma_1 = 0.02$, $\gamma_N = 0.05$.

3.1.5 PN System Response

In Fig. 3.2, the frequency response of the PN system using a nonlinear parameter value of $\Omega_N = 0.03$ is compared with the frequency response of a primary structure coupled with a linear absorber that is detuned according to the analytical relation given in Eqn. (3.23). The damping ratios $\gamma_1 = 0.02$ and $\gamma_N = 0.05$, mass ratio $\epsilon_N = 0.02$, and excitation magnitude $F = 1$ correspond to realistic values according to Refs. [14, 59]. The frequency and amplitude of the primary resonance peak obtained using the analytical relations are within 0.3% and 1.5% of the values obtained by directly integrating the nonlinear equations. This example verifies that the increase in the peak amplitude of the primary structure in the PN system due to a weak cubic stiffness nonlinearity can be accurately represented by a linear TMD that has been detuned according to Eqn. (3.23). All subsequent results presented in this chapter will be obtained using numerical integration of the nonlinear equations of motion.

Figure 3.3 illustrates how the attenuation capability of the NTMD is reduced as the nonlinear parameter is increased. The shading indicates the difference between the amplitude of the primary structure attached to the NTMD (the PN system) and the amplitude of the primary structure attached to an optimally tuned linear TMD (the PT system), *i.e.* $|q_P|^{(PN)} - |q_P|^{(PT)}$. Dashed lines and ‘ \pm ’ markers are used to distinguish between positive and negative regions for grayscale printing. A small nonlinear component two orders of magnitude less than that of the linear coefficient significantly decreases the effectiveness of the NTMD, as indicated by the dark (red) shading in the neighborhood of $\omega = 1$.

The frequency-response of the PN system and of the PT system are compared with the frequency-response of the primary structure alone in Fig. 3.4. The nonlinear coefficient is $\Omega_N = 0.03$, therefore the difference between the PN and PT response corresponds to the data forming the top row of Fig. 3.3. In this plot, the effect of the weak nonlinearity on the primary structure response is more clearly observed.

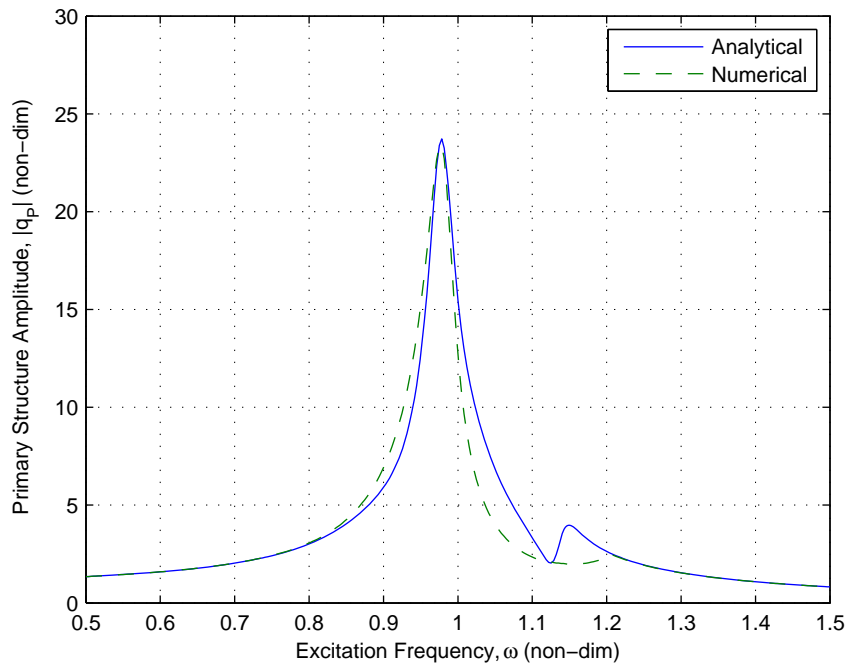


Figure 3.2: Frequency response of a primary structure attached to a linear absorber with a detuned frequency ratio according to Eqn. (3.23) (solid) compared with the primary structure and NTMD (dashed), $\epsilon_N = 0.02$, $\gamma_1 = 0.02$, $\gamma_N = 0.05$, $\Omega_N = 0.03$.

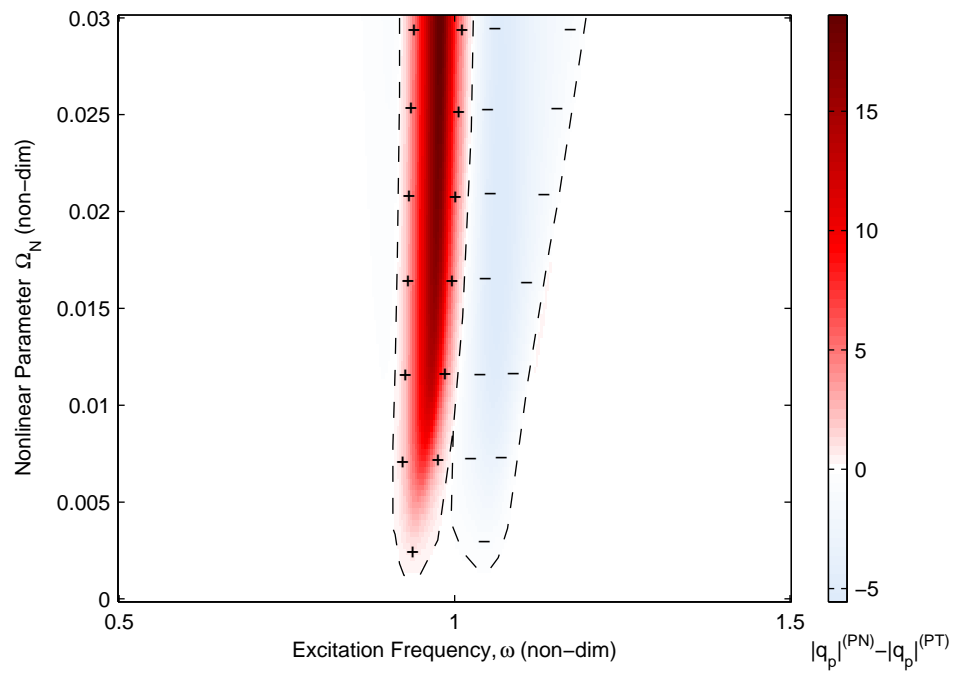


Figure 3.3: Difference between amplitude of primary structure attached to an NTMD and amplitude of primary structure attached to an optimally tuned linear TMD, versus the nonlinear parameter value and excitation frequency.

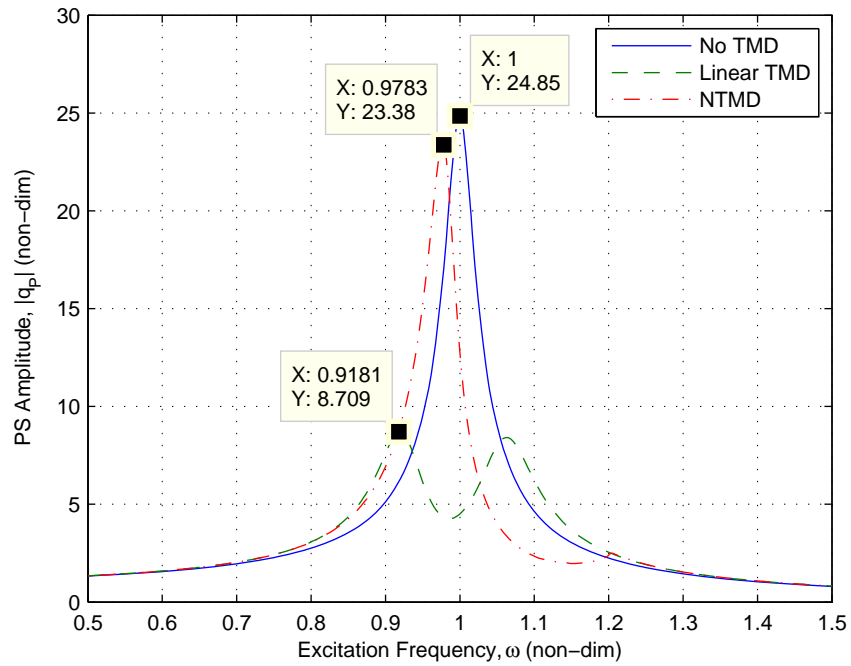


Figure 3.4: Primary structure frequency response curves; $\gamma_N = 0.05$, $F = 1$, $\Omega = 0.978$, $\epsilon_N = 0.02$, $\Omega_N = 0.03$.

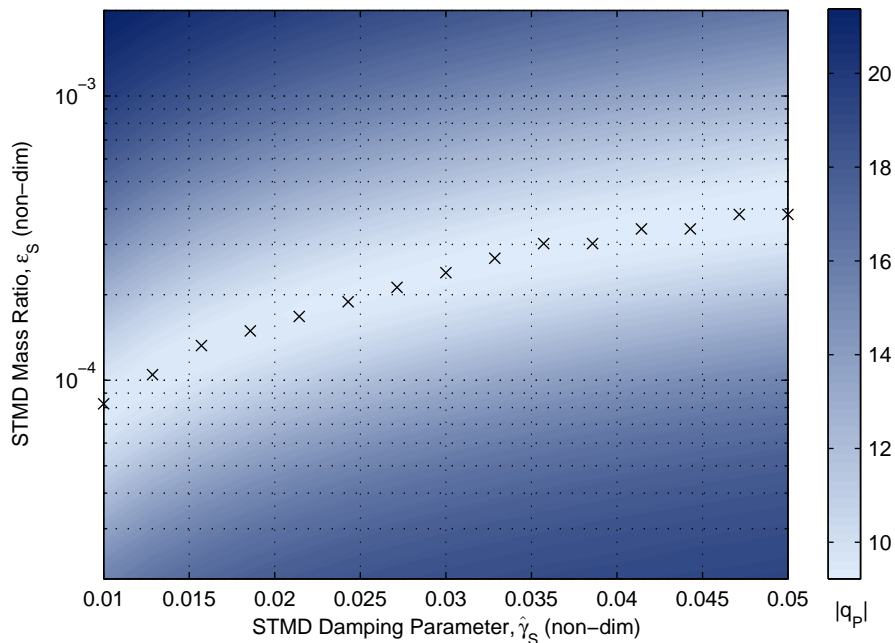


Figure 3.5: Contour plot of the primary structure response amplitude versus STMD mass ratio and damping parameter. Force amplitude $F = 0.5$.

The peak primary structure response amplitude in the PN system is $|q_P| = 23.4$, which is more than double the amplitude corresponding to the optimum linear TMD, $|q_P| = 8.71$. The peak response amplitude in the PN system is close to that of the primary structure alone, $|q_P| = 24.9$, indicating that the detuning resulting from the nonlinearity renders the absorber almost completely ineffective.

3.2 Series STMD System Performance

An STMD is now added in series with the primary structure and NTMD to form the PNS system and the attenuation capability is studied using a variety of different STMD configurations. Figure 3.5 is a contour plot illustrating the peak response amplitude of the primary structure $|q_P|$ (shading) versus STMD mass ratio ϵ_S and STMD damping parameter $\hat{\gamma}_S$. The corresponding data is obtained from 40 values of

the STMD mass ratio ϵ_S between 2×10^{-5} and 2×10^{-3} (logarithmic spacing) and 15 values of the damping parameter $\hat{\gamma}_S$ between 0.01 and 0.05 (linear spacing). Since the mass ratio ϵ_S represents the mass of the STMD relative to the primary structure ($\epsilon_S = m_S/M$) these values correspond to STMD mass values of 0.002% to 0.2% of the primary structure, respectively, which are 0.1% to 10% of the mass of the NTMD since $\epsilon_N = 2 \times 10^{-2}$.

In order to determine the parameters which most effectively attenuate the primary structure's response, the element containing the minimum value from each vector of peak amplitudes corresponding to a single damping parameter value (columns in Fig. 3.5) is located. The corresponding STMD mass ratio which results in the smallest peak response amplitude is identified as the optimum mass ratio and is marked with an '×'. When the mass of the STMD is significantly above or below the optimum value, the benefit of the STMD is diminished. For the most effective attenuation using the STMD, it is therefore recommended to select mass and damping values according to the curve formed by the '×' markers, hereafter referred to as the *design curve*.

The effect of the STMD on the frequency response of the primary structure is illustrated in Fig. 3.6. Three separate line styles are used to distinguish between three cases: STMD mass ratio value is (a) below design curve recommendation from Fig. 3.5 (dash-dot), (b) at recommended value (solid), and (c) above recommended value (dashed). In Fig. 3.6, two curves each are displayed for cases (a) and (c) so that the behavior in extreme cases can be examined in addition to reasonable but non-optimal values. Time series response plots for each of the three components in the PNS system are presented in Fig. 3.7 for the same three cases: STMD mass ratio (a) too low, (b) optimized, and (c) too high.

When the mass ratio is many orders of magnitude less than the optimum value ($\epsilon_S = 2 \times 10^{-8}$), the frequency response curve qualitatively resembles that of the pri-

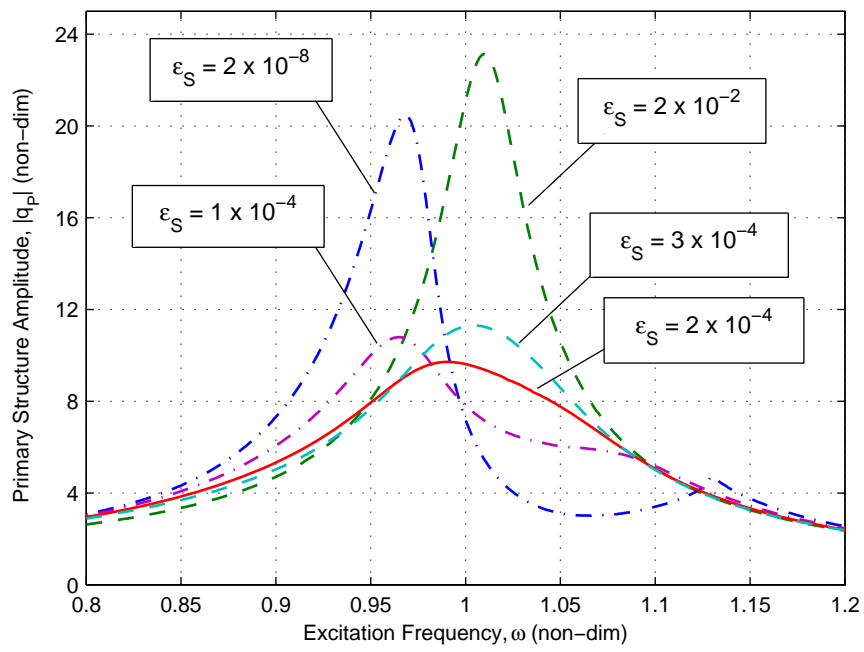


Figure 3.6: Primary structure frequency response curves for five mass ratio values, with $\hat{\gamma}_S = 0.02$, $F = 0.5$, $\Omega = 0.978$, $\epsilon_N = 0.02$, $\Omega_N = 0.03$.

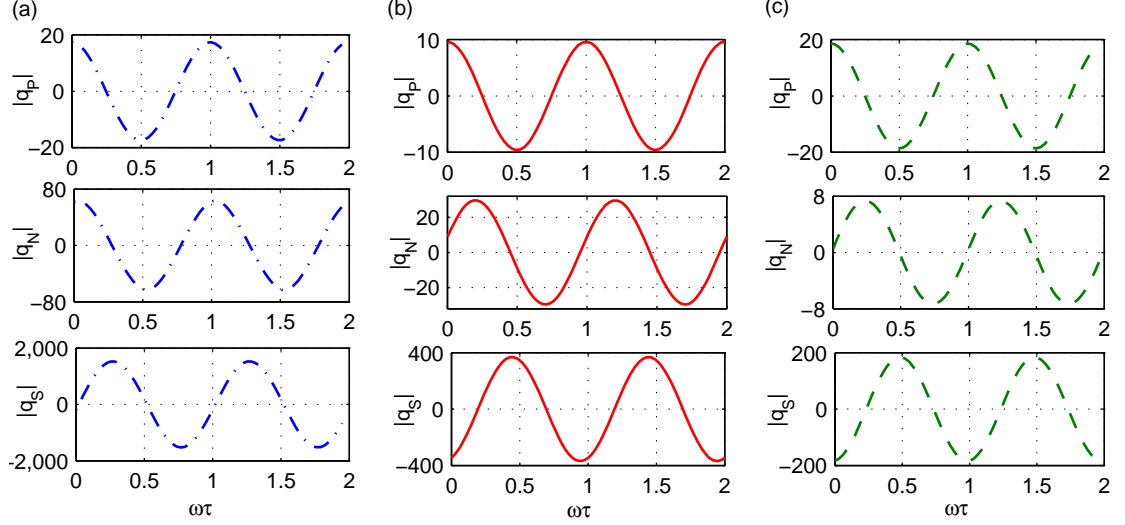


Figure 3.7: Peak resonance time series response for PS, NTMD and STMD for (a) $\epsilon_S = 2 \times 10^{-8}$, (b) $\epsilon_S = 2 \times 10^{-4}$ and (c) $\epsilon_S = 2 \times 10^{-2}$; $\hat{\gamma}_S = 0.02$.

mary structure and NTMD alone, suggesting a negligible influence from the STMD. At the resonant peak producing the maximum amplitude, the primary structure and NTMD are oscillating in phase with the STMD out of phase by $-\pi/2$ radians, supporting this conclusion. When the mass of the STMD is optimized ($\epsilon_S = 2 \times 10^{-4}$), the peak response amplitude is minimized and the NTMD and STMD oscillate with phases of $-\pi/2$ and $-\pi$ radians relative to the primary structure, respectively. In this manner the STMD opposes the motion of the primary structure at the most prominent resonant state, removing enough energy from the NTMD to confine its displacements to an approximately linear region. At higher STMD mass ratios, however, the effect of the STMD reduces the displacement of the NTMD to the extent that its effect on the primary structure is diminished. The maximum response amplitude of the primary structure in this case increases proportional to the mass ratio. By comparing the response curves resulting from the mass ratio values that are $\pm 50\%$ of the optimum value ($\epsilon_S = 3 \times 10^{-4}$ and 1×10^{-4} , Fig. 3.6), it is observed that favorable attenuation is still achieved within a wide range of non-optimum STMD mass ratio values.

It is important to note the large response amplitudes of the STMD, in each case one to two orders of magnitude higher than the NTMD and primary structure. The velocity of the STMD is expected to increase as its mass is reduced, which corresponds to the observed increase in the response amplitude. When selecting the mass ratio of the STMD, a tradeoff therefore exists between attenuation capability and space required to accommodate the STMD displacements, well illustrated in Figs. 3.6 and 3.7. The series STMD absorber is therefore a more viable option when the displacement of the primary structure is expected to be small. For example, to reduce the primary structure response amplitude to 5 cm would require space to accommodate an STMD amplitude of 2 m. Investigations into the geometric nonlinear effects due to large stroke of STMD by Yan *et al.* found that the geometric nonlinearity of the SAIVS device does not produce unsatisfactory effects as long as the frequency is close to 1 [125]. Furthermore, in order to avoid an unnecessarily large SAIVS device it may be possible to adjust the control algorithm to compensate for the geometric nonlinearity inherent in the design of the SAIVS device for large displacements (see Fig. 1.8).

The peak primary structure response amplitude is now studied for different combinations of the three parameters ϵ_S , $\hat{\gamma}_S$ and F to determine the influence of the excitation magnitude on the optimum parameter values. For each $\hat{\gamma}_S$ and F , a datapoint is plotted at the mass ratio ϵ_S corresponding to the smallest peak response amplitude, forming the design curve. This is the same procedure used in Fig. 3.5, but the contour shading is omitted in the present figure in order to allow for plotting multiple curves. The results are presented in Fig. 3.8. Note that the curve corresponding to $F = 0.5$ is the same data as that which was presented in Fig. 3.5. For reference, a non-dimensional excitation magnitude of $F = 0.6$ represents excitation with the intensity of a seismic event, $F = 0.35$ represents excitation with half the intensity of a seismic event, and $F = 2.5$ represents the “worst case scenario” excita-

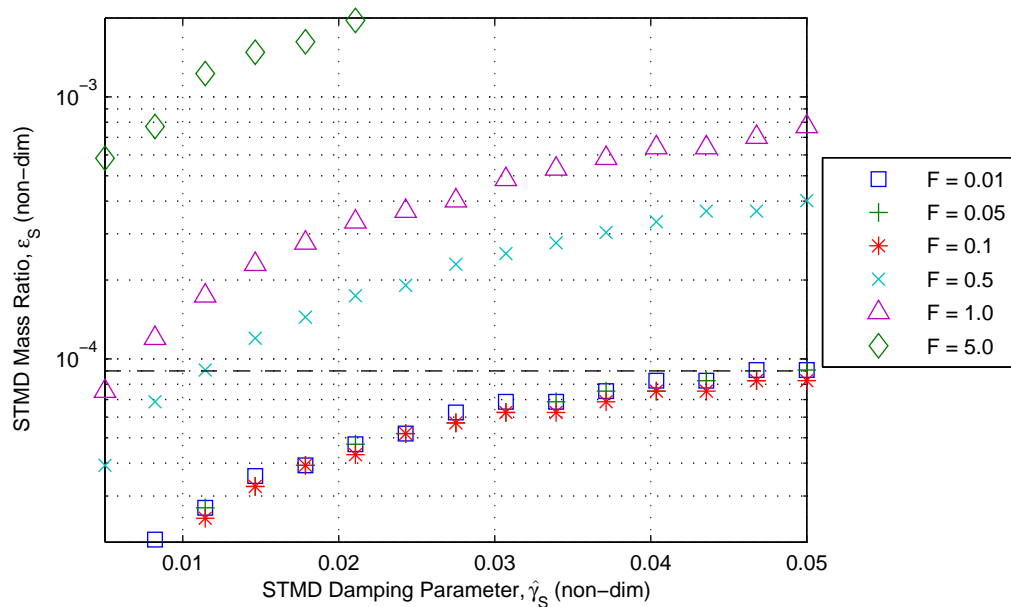


Figure 3.8: Mass ratio values ϵ_S which minimize the primary structure response amplitude $|q_P|$ at each damping parameter value $\hat{\gamma}_S$ and forcing amplitude F .

tion from a seismic event. These values are based on the procedure used in Ref. [59] to determine the magnitude of harmonic excitation signals to match the intensity of a seismic event.

The optimum STMD parameter values are similar for $F = 0.01, 0.05, \text{ and } 0.1$, but for higher amplitudes $F = 0.5, 1.0, \text{ and } 5.0$ the optimum parameters values are specific to the particular forcing amplitude. It is important to note that these results do not infer that an STMD designed with optimum parameters for a specific forcing amplitude will not be effective at attenuating vibrations at a different forcing amplitude. The performance of the series STMD could be further improved by incorporating a semi-active viscous damping element which would allow for optimal parameter values to be realized over a range of excitation magnitudes, as illustrated by the dashed line within Fig. 3.8. The effectiveness of an STMD over a range of forcing amplitudes will be further demonstrated in the following section.

3.3 TMD/STMD Performance Comparison

A well-known drawback of the linear TMD is the region outside of its bandwidth of suppression where the TMD acts as a vibration amplifier [11]. By modulating the stiffness such that the STMD is always tuned to the dominant response frequency, the STMD has been demonstrated to outperform a linear TMD as a standalone absorber [89]. In this section, the performance of the PNS system is compared to a new system where the STMD has been replaced by a linear tuned mass damper with equal mass and damping parameter values (the *PNT system*) to determine whether similar benefits can be realized.

The primary structure response amplitude as a function of excitation magnitude and frequency is illustrated in Figs. 3.9, 3.10, and 3.11 for the three systems: the PN system, the PNS system, and the PNT system, respectively. A significant reduction in the PS response amplitude at the primary resonance $\omega = 0.98$ is observed using both the STMD and linear TMD. However, the primary structure motion is attenuated more effectively by the STMD in the neighborhood of this resonance. In other words, the semi-active tuning capability extends the benefit of the second absorber to a wider frequency range.

By comparing the frequency response between Figs. 3.10 and 3.11 for $\omega > 1$, the linear TMD is observed to outperform the STMD. However, the STMD is not limited to a specific tuning of $\Omega_S = \omega$ as was presented in Fig. 3.10. Rather, the versatile design of the STMD allows for implementation of any arbitrary tuning desired. In order to determine the most effective tuning, the primary structure response amplitude versus excitation frequency and STMD stiffness coefficient Ω_S for four different forcing levels is examined, as shown in Fig. 3.12. It is observed that tuning to $\Omega_S = \omega$, marked by a dashed line in each panel, does not minimize the response at all frequencies. Specifically, this tuning appears to be the most effective for $\omega < 1$, but less effective above this range. In order to compensate, an alternate piecewise

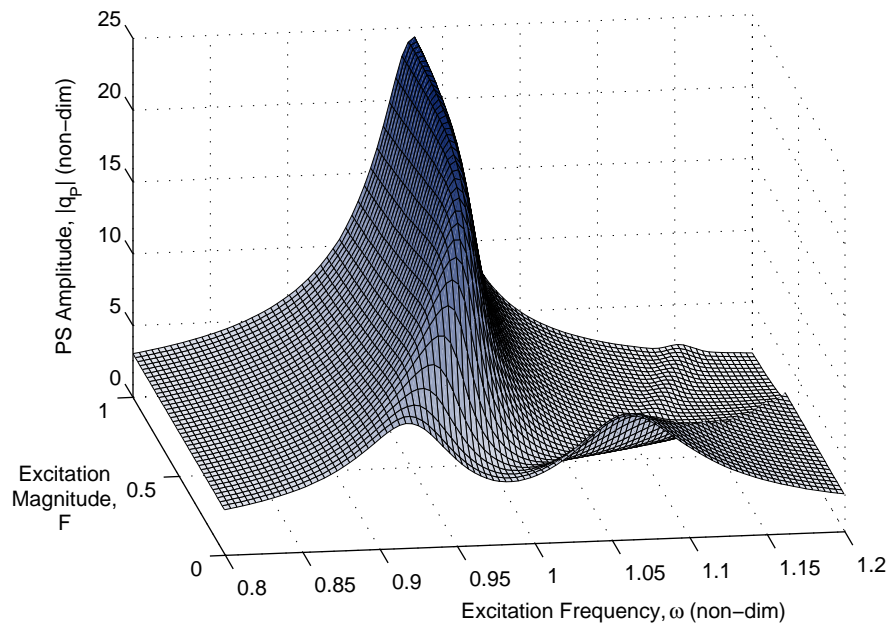


Figure 3.9: Surface plot showing primary structure response amplitude versus forcing amplitude and frequency for the PS+NTMD system; $\epsilon_S = 1.6 \times 10^{-4}$, $\hat{\gamma}_S = 0.02$.

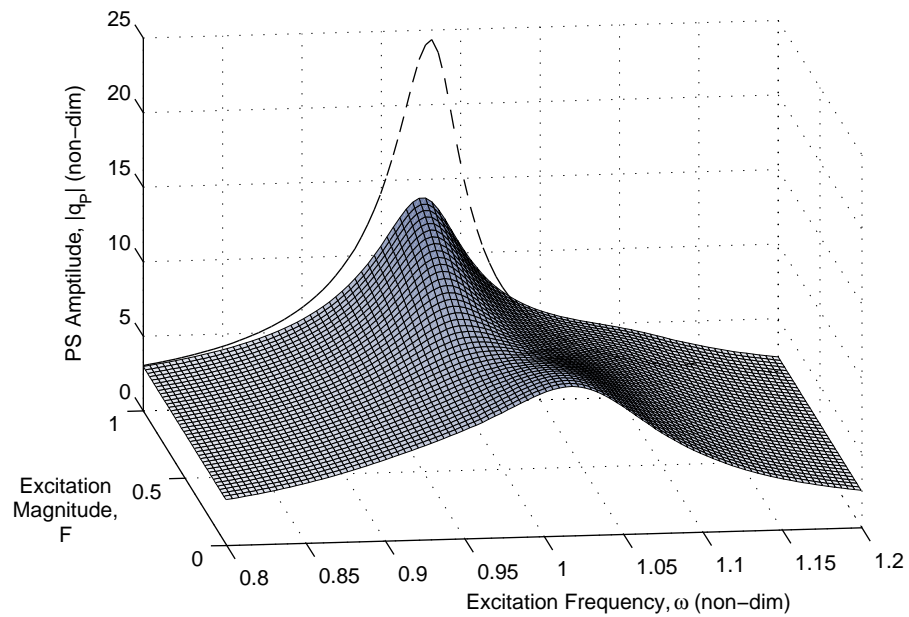


Figure 3.10: Surface plot showing primary structure response amplitude versus forcing amplitude and frequency for the PS+NTMD+STMD system; $\epsilon_S = 1.6 \times 10^{-4}$, $\hat{\gamma}_S = 0.02$.

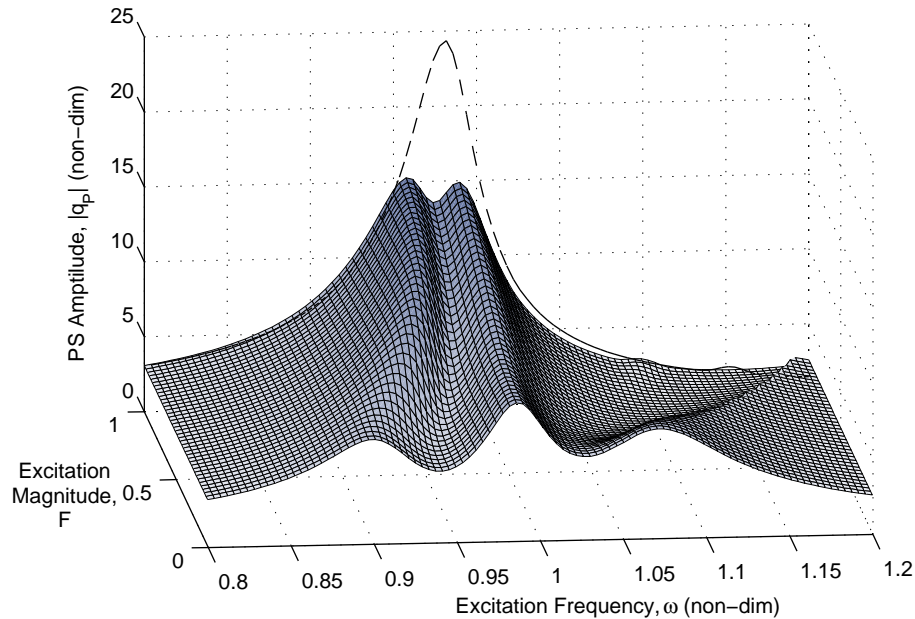


Figure 3.11: Surface plot showing primary structure response amplitude versus forcing amplitude and frequency for the PS+NTMD+TMD system; $\epsilon_S = 1.6 \times 10^{-4}$, $\hat{\gamma}_S = 0.02$.

linear tuning is proposed: $\Omega_S = \omega$ for $\omega < 1$, and $\Omega_S = 1$ for $\omega \geq 1$ —marked by a dotted line in Fig. 3.12. This tuning therefore allows the benefits of the STMD to be realized at lower frequencies, and effectively acts as a linear TMD at higher frequencies. This configuration has the additional benefit of requiring even less power than the power requirements of a standard STMD, as no adjustments are required of the STMD stiffness tuning device for frequencies above $\omega = 1$.

The performance using this proposed piecewise linear tuning scheme is compared with the performance using a simple linear tuning scheme and using a linear TMD. The primary structure response amplitude of a system using an (a) STMD with standard linear tuning, (b) linear TMD and (c) STMD with novel piecewise linear tuning, expressed relative to the response of the PN system, is illustrated in Fig. 3.13. Two dimensional plots are presented in Fig. 3.13(d) to more clearly illustrate the data within (a–c) at forcing amplitudes of $F = 0.2$ (solid), $F = 0.5$ (dashed), and

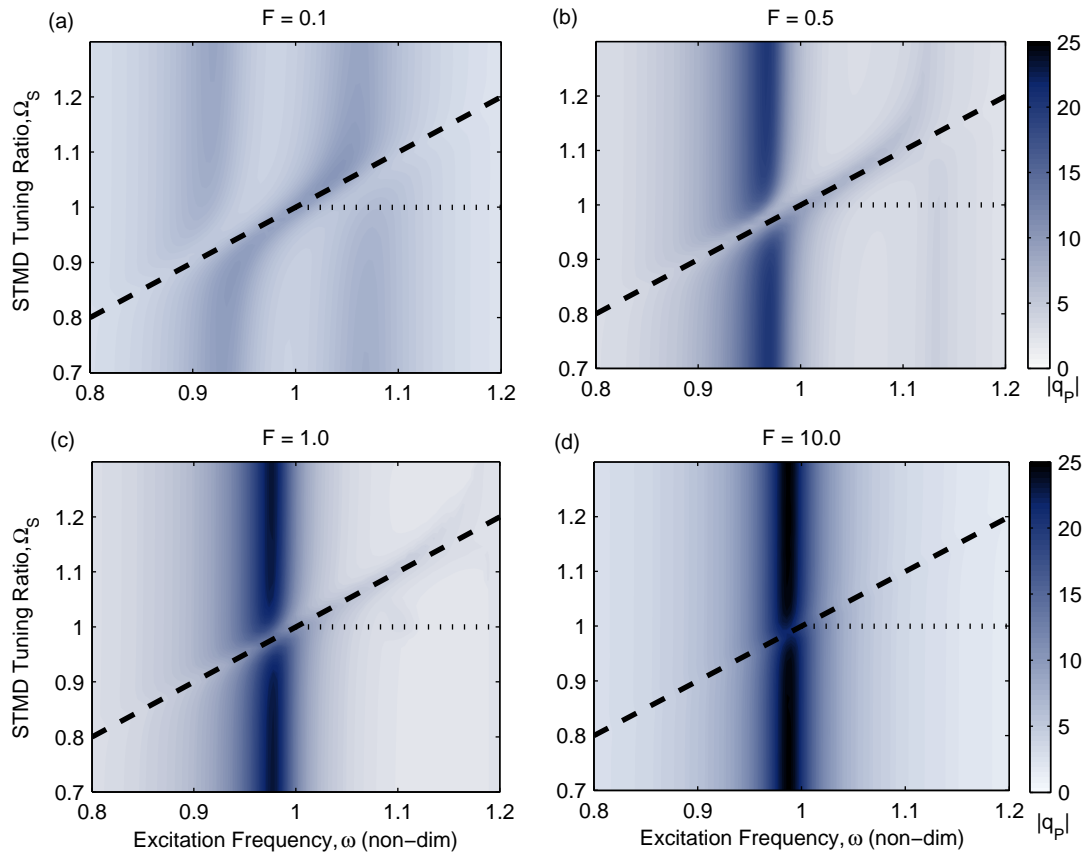


Figure 3.12: Primary structure response amplitude versus excitation frequency and STMD stiffness coefficient for (a) $F = 0.1$, (b) $F = 0.5$, (c) $F = 1.0$ and (d) $F = 10.0$; $\epsilon_S = 1.6 \times 10^{-4}$, $\hat{\gamma}_S = 0.02$.

$F = 0.8$ (dot). The shading represents the difference between the amplitude of the PNS or PNT system and the amplitude of the PN system, $\Delta|q_P| = |q_P|^{(PNS/PNT)} - |q_P|^{(PN)}$. A wide band decrease in response amplitude around $\omega = 0.978$ and a small increase in response amplitude above $\omega = 1$ is observed for the standard linear STMD tuning, agreeing with Fig. 3.10. A narrow band decrease in response amplitude is observed around $\omega = 0.98$ using the linear TMD, with a significantly smaller response amplitude increase at higher frequencies. The STMD with piecewise linear tuning combines the best aspects of these two systems, exhibiting wide band response amplitude reductions around $\omega = 0.98$ and minimal response increases for higher excitation frequencies.

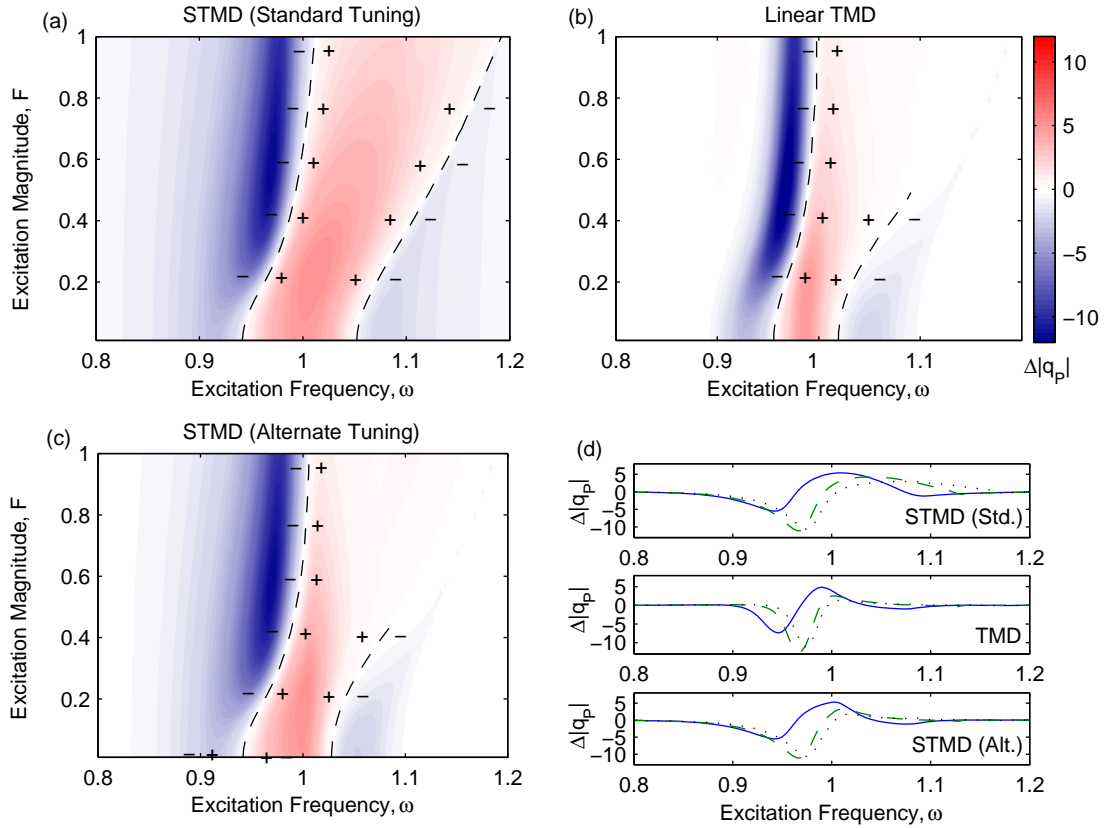


Figure 3.13: Increase or decrease in primary structure response amplitude versus forcing amplitude and frequency from adding an (a) STMD with standard linear tuning, (b) linear TMD and (c) STMD with novel piecewise linear tuning; $\epsilon_S = 1.6 \times 10^{-4}$, $\hat{\gamma}_S = 0.02$. A dashed line separates the positive and negative regions, as labeled. (d) Change in primary structure response amplitude versus frequency at $F = 0.2$ (solid), $F = 0.5$ (dashed) and $F = 0.8$ (dot) for each of the cases shown in (a)-(c).

3.4 Random Excitation

Harmonic excitation was used in Sections 3.1–3.3 in order to provide an unbiased evaluation of the system response. Of course, real-world systems may experience a variety of loading conditions. The excitation produced by an unbalance in rotating machinery may be approximately harmonic with small modulations in frequency or amplitude, whereas the excitation produced by wind or seismic motion acting on a civil structure is often random in nature. The response of the PNS system under random excitation is therefore studied in this section in order to provide a more complete

evaluation of the system performance. Since the attenuation of civil structures has been a strong motivation driving vibration absorber research, a random signal with seismic-like characteristics is used.

It is noted that the tuning ratio of the STMD is fixed at $\Omega_S = 1$ for all simulations in this section, so that the natural frequency of the STMD equals the expected average dominant response frequency of the primary structure. This allows the dynamics of the interaction between the system components to be isolated from the influence of other factors. The alternative of tuning the STMD in real-time to the actual dominant response frequency would require more development of the control system and is therefore beyond the scope of this thesis. The STMD therefore behaves as a linear TMD, but will still be referred to as an STMD for the purpose of consistency, with the understanding that the results would accurately approximate the behavior of an STMD with ideal tuning.

The autoregressive moving average (ARMA) method is used to generate a random excitation signal with a seismic-like frequency distribution. The ARMA method is an iterative method which generates a random signal using a combination of white noise deviates and previous values of the signal, described in detail in Refs. [126, 127, 128, 129]. The prescribed frequency distribution is the Kanai-Tajimi spectrum, a commonly used seismic spectrum approximation [59, 130, 131],

$$g(\omega) = \frac{\omega_g^4 + (2\zeta_g\omega_g\omega)^2}{(\omega_g^2 - \omega^2)^2 + (2\zeta_g\omega_g\omega)^2} K. \quad (3.24)$$

The Kanai-Tajimi spectrum is non-dimensionalized to ensure compatibility with the equations of motion by following the procedure used in Chapter 2. The free parameters are then set to $\zeta_g = 0.34$, $K = 0.05$ and $\Omega_g = 1$, where $\Omega_g = \omega_g/\omega_1$ [59]. The damping ratio ζ_g corresponds to that of a rock site, the spectrum level K is selected such that force magnitudes $|F(\tau)_{max}| < 1$ and the frequency parameter is selected to represent the worst case scenario where the natural frequency of the ground

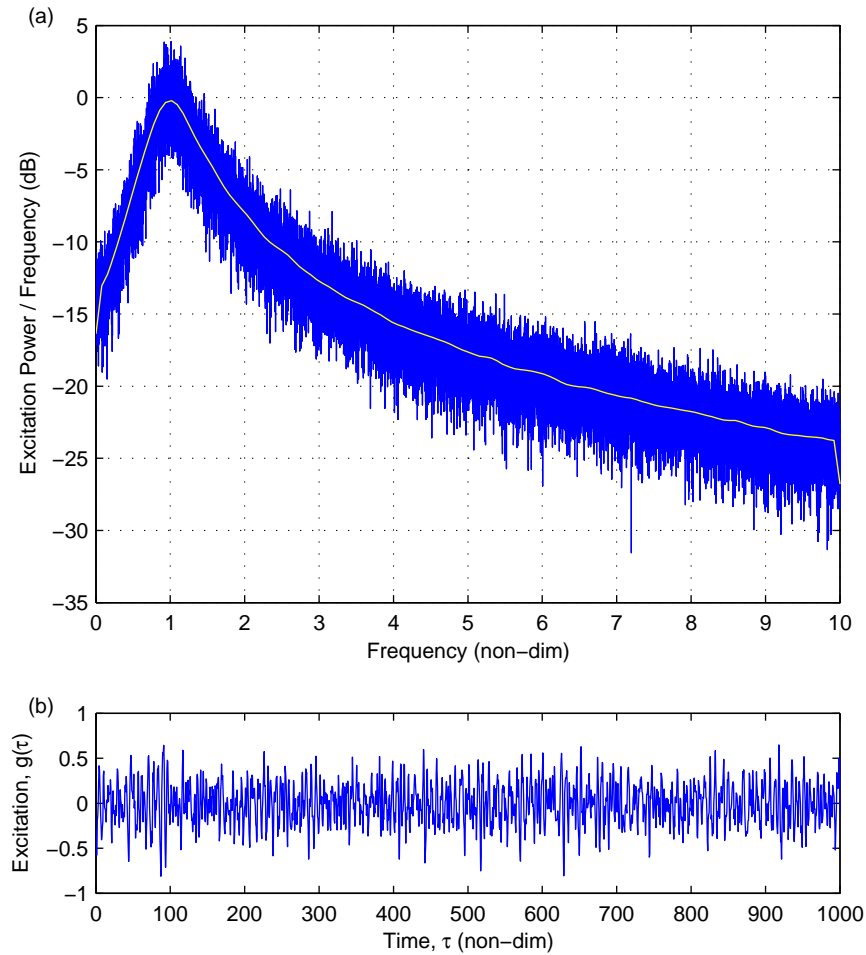


Figure 3.14: (a) Power spectral density, smoothed (light) and unsmoothed (dark), and (b) time series plot of a seismic-like excitation signal.

ω_g matches the natural frequency of the structure.

Since the variation of only a single parameter is considered while the other system parameters are held fixed, only a single simulation is needed to provide a sufficient understanding of the behavior. A random excitation signal is synthesized with a total length of $\tau = 2\pi \times 10^4$, which is determined to be sufficiently long to produce smooth and repeatable response characteristics in the frequency domain. Figure 3.15 illustrates (a) the smoothed Welch power spectral density (PSD) plot of the excitation signal and (b) a time series plot displaying a portion of the excitation signal.

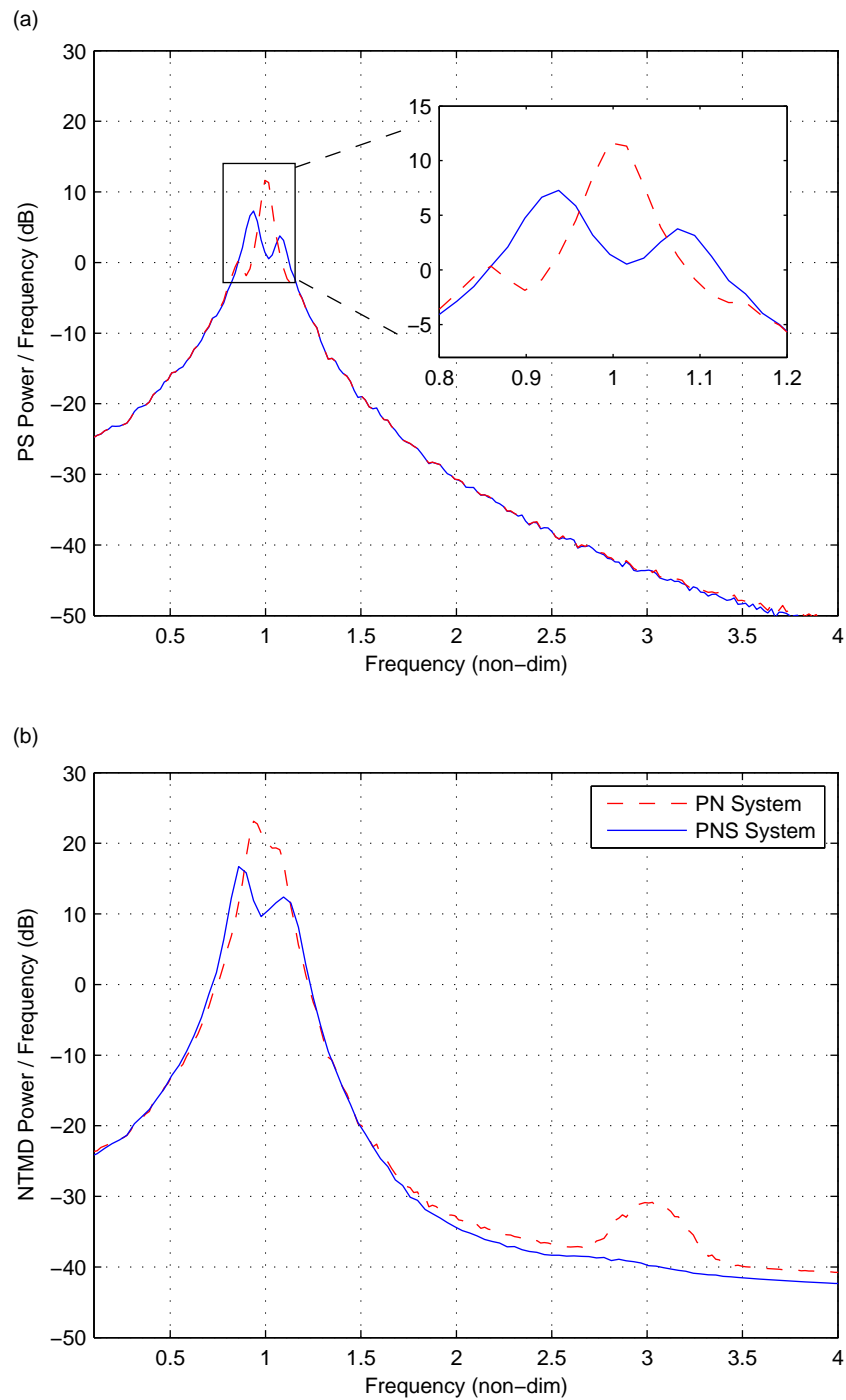


Figure 3.15: Smoothed power spectral density (PSD) of the (a) primary structure and (b) NTMD response. Results presented are from two separate simulations: both using the same excitation signal, the first excluding (dashed) and the second including (solid) the linear TMD attachment in series with the PS and NTMD.

The PSD plots of the (a) primary structure and (b) NTMD response resulting from the random excitation signal are displayed in Fig. 3.15. Within the plots, dashed curves denote the results corresponding to the two-DOF PN reference system and solid curves denote the 3-DOF PNS system. The PSD of the STMD component is not shown here and simply displays a resonant peak at a non-dimensional frequency of $\omega = 1$.

It is observed in Fig. 3.15(b) that the addition of the STMD eliminates the NTMD's superharmonic resonance at $\omega = 3$, decreasing the NTMD power from -31 to -40 dB. The elimination of the superharmonic resonance indicates that the STMD component has minimized the effect of the nonlinearity by limiting the motion of the NTMD. In addition, the STMD reduces the peak power of the primary structure from 11.6 to 7.3 dB and of the NTMD from 23.1 to 16.7 dB (Figs. 3.15(a) and 3.15(b), respectively). These reductions verify that even under random excitation, the attenuation capability of an absorber detuned by a stiffening nonlinearity can be improved by adding a small STMD in series.

Additional simulations are conducted in order to study the response using various parameter values and the random excitation signal illustrated in Fig. 3.14. Figure 3.16 displays the (a) peak and (b) RMS of the primary structure's time domain response versus the STMD mass ratio ϵ_S for $F = 0.35$. Curves representing five different STMD damping parameter values, $\hat{\gamma}_S = \{0.01, \dots, 0.05\}$ are compared with lines denoting the response of the primary structure only (solid), primary structure and optimally tuned linear TMD (dashed), and primary structure and NTMD (dash-dot). The correlation between the STMD mass ratio which minimizes the response and the STMD damping parameter agrees with the results obtained using harmonic excitation and presented in Fig. 3.5.

It is observed in Fig. 3.16(a) that the addition of a small STMD component with a mass on the order of 0.1% of the primary structure and a damping parameter of $\hat{\gamma}_S =$

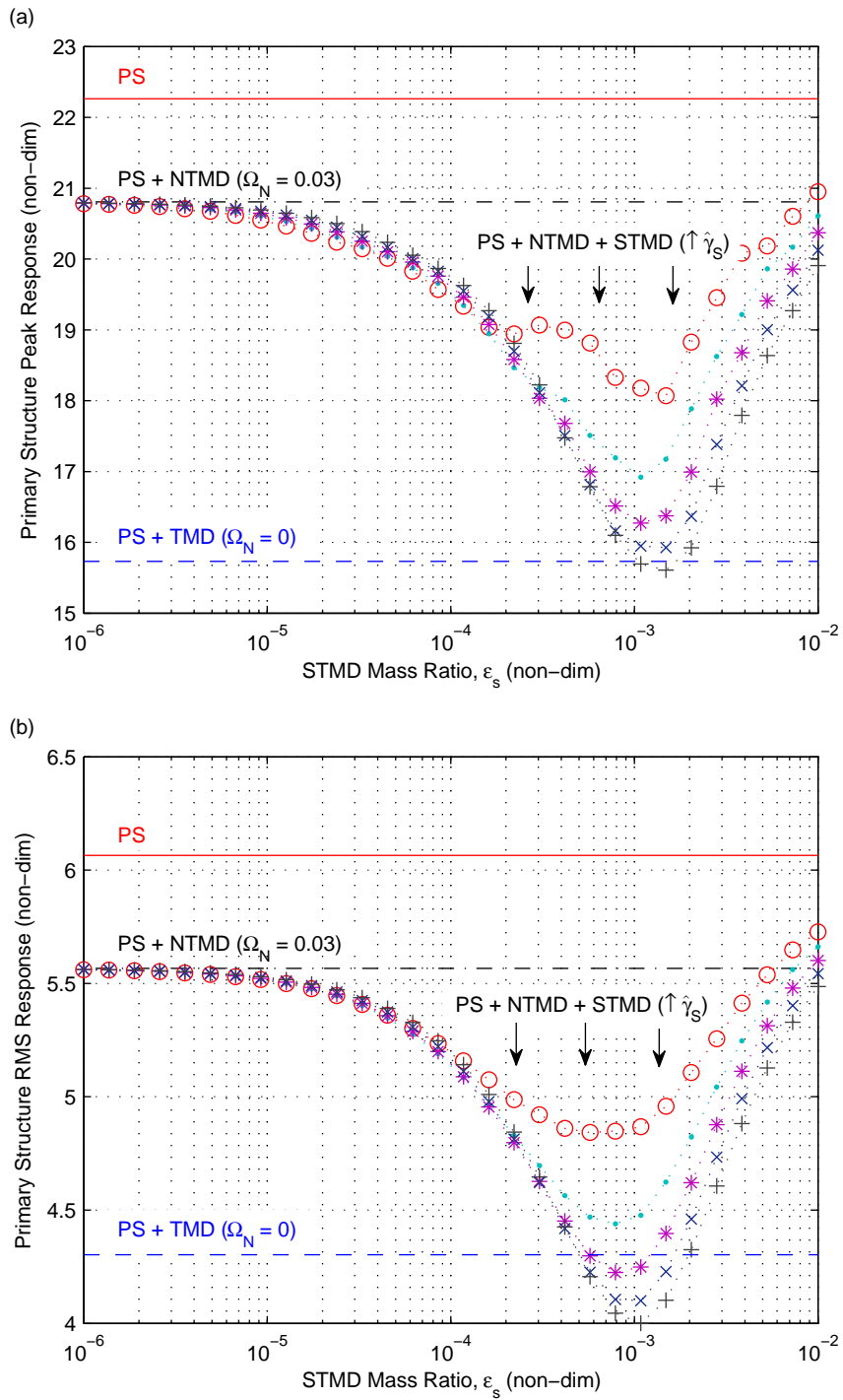


Figure 3.16: (a) Peak and (b) RMS of the PS response in the time domain for the PNS system with STMD damping parameter $\hat{\gamma}_s = 0.01$ (\circ), 0.02 (\cdot), 0.03 ($*$), 0.04 (\times), and 0.05 ($+$).

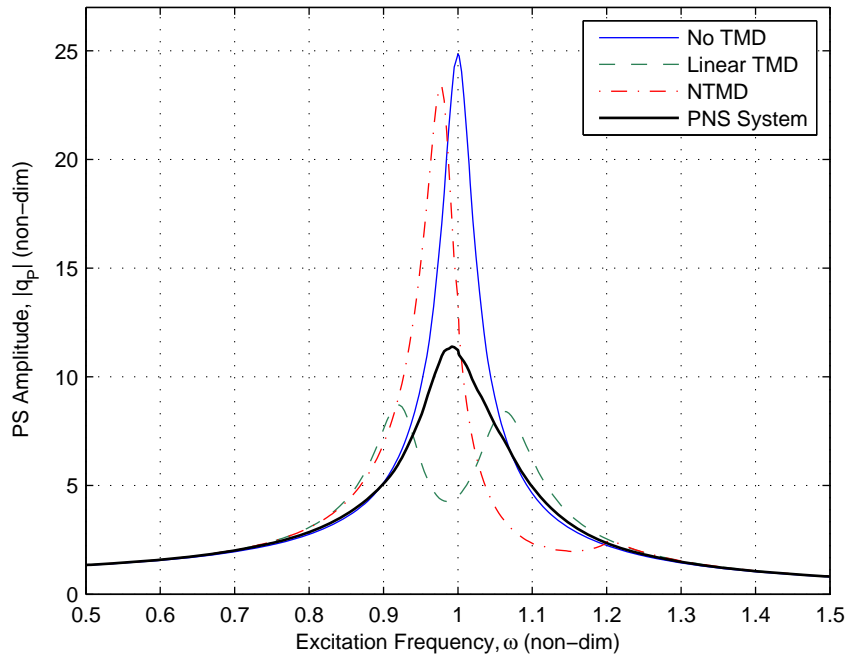


Figure 3.17: Frequency response curves illustrating the performance benefits of the series STMD for harmonic excitation; $\gamma_N = 0.05$, $F = 1$, $\Omega = 0.978$, $\epsilon_N = 0.02$, $\Omega_N = 0.03$.

0.05 can reduce the peak amplitude from 20.8 to 15.6. The resulting peak amplitude is similar to that of the primary structure with an optimally tuned TMD. From Fig. 3.16(b), it is observed that the effect of the STMD component is a reduction in the RMS response from 5.57 to 4.00, resulting in an RMS value significantly lower than that achieved with the optimum TMD. These results demonstrate the effectiveness of the STMD at improving the attenuation capability of the NTMD under random excitation. Furthermore, it is noted that all $\hat{\gamma}_S$ and $\epsilon_S \leq 0.05$ result in a favorable PNS response over that of the PN system, reducing RMS and peak response amplitudes even if the optimum values of the mass and damping parameters are not used.

3.5 Summary of Results

In this chapter, the performance of a three degrees-of-freedom system (the PNS system) consisting of a linear primary structure (PS), tuned mass damper with a “weak” cubic stiffening nonlinearity (NTMD), and semi-active tuned mass damper (STMD) is compared with the response of the two-degrees of freedom consisting only of the PS and NTMD (the PN system), and a two-degrees of freedom system consisting of the PS and optimally tuned linear TMD (the PT system). In this case, the nonlinearity is strong enough to detune the absorber and compromise the system performance, but weak enough that the response does not exhibit the complex nonlinear phenomena such as multiple solutions which will be explored in Chapter 5. The following conclusions are made:

- The correlation between the nonlinear coefficient and the primary structure (PS) peak amplitude can be accurately described by using analytical techniques including the Method of Multiple Scales and the Laplace Transform. The key mechanism attributed to the peak amplitude increase was the detuning of the linear frequency ratio which occurs as a result of the amplitude-frequency relationship introduced by the nonlinearity (Fig. 3.1). For a nonlinear coefficient of $\Omega_N = 0.03$ —two orders of magnitude less than the linear coefficient—the peak PS amplitude increases to more than 250% of the response corresponding to an optimum TMD, within 6% of the PS response amplitude with no absorber (Fig. 3.4).
- Adding an STMD in series with the NTMD can limit the motion of the NTMD to an approximately linear range, improving the attenuation capability and resulting in a response similar to a highly-damped single-DOF oscillator with a peak response amplitude in the neighborhood of an optimally tuned linear TMD (Fig. 3.17).

- The optimum STMD mass and damping parameter values are a function of the excitation magnitude (Figs. 3.5–3.8). Higher excitation magnitudes produce a larger PS response, resulting in a larger frequency detuning of the absorber and requiring a larger STMD mass ratio to counteract. An additional semi-active damping element would provide the ability to adjust to different excitation amplitudes.
- If the STMD mass ratio value is multiple orders of magnitude larger than the optimum value, it is possible to limit the motion of the NTMD enough that the effect of both absorbers on the primary structure is negligible (Fig. 3.6). However, for a mass ratio value within at least $\pm 50\%$ of the design curve, the peak amplitude and RMS of the PS response in the frequency domain are similar to the optimum value. This demonstrates that the attenuation performance of the PNS system is robust to reasonable variations from the optimum parameter values.
- The straightforward method of tuning the fundamental frequency of the STMD to the excitation frequency provided a wider-band frequency-response amplitude reduction, but an increase in PS response amplitude at some frequencies above the primary resonance when compared with a passive linear tuned mass damper (Figs. 3.9–3.11). Improved performance was demonstrated using an alternate STMD tuning scheme: maintaining the simple linear tuning below the fundamental frequency of the primary structure and using a constant stiffness for higher excitation frequencies such that the fundamental frequency of the STMD is equal to the PS fundamental frequency (Fig. 3.12). This piecewise linear tuning combines the performance benefits of the STMD and passive linear mass damper and further reduces the power requirements (Fig. 3.13).
- The performance benefits achieved by adding the STMD component were ver-

ified using a random excitation signal with seismic-like frequency characteristics (Fig. 3.14). The elimination of the NTMD superharmonic at three times the fundamental frequency (Fig. 3.15(b)) provides evidence that the STMD has minimized the nonlinear effects. The STMD is demonstrated to reduce the peak and RMS response amplitudes in the time domain for all mass ratios less than $\epsilon_S = 0.05$ (Fig. 3.16). At the optimum mass ratio, the PNS system achieved a peak response amplitude similar to the PT system and an RMS amplitude less than the PT system.

The results within this thesis demonstrate that adding a small STMD to a vibration absorber that has developed a small nonlinearity due to operation outside of the intended range, degradation of components, or other means can increase the attenuation of the primary structure. Optimum attenuation can be achieved using an STMD with a mass three to four orders of magnitude less than the primary structure. It is therefore believed that adding a small series STMD may be a practical, cost-efficient alternative to repairing the absorber in an attempt to remove the nonlinearity or replacing the absorber with a new linear TMD or full-scale STMD.

Chapter 4

A Parallelized

Multi-Degrees-of-Freedom Cell

Mapping Method

Few numerical tools are well suited to efficiently analyze the global dynamics of higher-dimensional systems. The multi-degrees-of-freedom cell mapping method (MDCM), discussed in Section 1.2.2, is one exception that is capable of processing higher-dimensional systems much more efficiently than other common methods. One unfortunate drawback of the MDCM method, however, is that the sequential nature of the algorithm limits its ability to utilize the parallel computing resources available in modern machines.

In this chapter, the *parallelized multi-degrees-of-freedom cell mapping* (PMDCM) method is introduced. The PMDCM method preserves the key operations of the MDCM method but introduces a restructured algorithm which allows multiple mapping steps to be calculated in parallel. In the first section, the PMDCM algorithm and corresponding subroutines are described in detail. The efficiency and accuracy of the PMDCM method is illustrated in the following section by analyzing a two

degrees-of-freedom system. In the final section, a brief summary is presented. A MATLAB script providing an example of the PMDCM method can be found in the Appendix.

4.1 PMDCM Algorithm

In this section, key parameters are first defined and an overview of the PMDCM algorithm is presented. Then, the various subroutines are described. Finally, a summary of the key differences between the MDCM and PMDCM methods is given.

Many of the parameters within the PMDCM method are similar to those used within the MDCM method but of higher-dimension than their counterparts. Other parameters are unique to the PMDCM algorithm. Key parameters used within the PMDCM algorithm are as follows, where $\mathbb{M}(R, C)$ is used to indicate an $R \times C$ matrix and \mathbb{N} represents the set of natural numbers:

- M : Number of cells in subset S , $M \in \mathbb{N}$,
- N : Dimension of the dynamic system, $N \in \mathbb{N}$,
- $Nper$: User-defined number of excitation periods corresponding to the length of each numerical integration $Nper \in \mathbb{N}$,
- MAX : User-defined maximum number of steps in each sequence $MAX \in \mathbb{N}$,
- \mathbf{Z} : Array containing all cells in subset S , $\mathbf{Z} \in \mathbb{M}(M, N)$,
- ri : Index of the smallest valued row in \mathbf{Z} that has not been processed, $ri \in \mathbb{N}$,
- Ns : User-defined number of sequences to simultaneously process, $Ns \in \mathbb{N}$,
- \mathbf{Zs} : Array of cells to simultaneously process, $\mathbf{Zs} \in \mathbb{M}(Ns, N)$,
- Npc : Number of processed cells, $Npc \in \mathbb{N}$,

- Ng : Number of periodic groups, $Ng \in \mathbb{N}$,
- \mathbf{pc} : Ordered array containing all processed cells, $\mathbf{pc} \in \mathbb{M}(Npc, N)$,
- \mathbf{g} : Vector of group numbers corresponding to each processed cell in \mathbf{pc} , $\mathbf{g} \in \mathbb{Z}^{Npc}$,
- \mathbf{Ks} : Number of cells in each sequence, $\mathbf{Ks} \in \mathbb{N}^{Ns}$,
- \mathbf{Ls} : Longest trajectory within each sequence, $\mathbf{Ls} \in \mathbb{N}^{Ns}$,
- \mathbf{inds} : Array indicating all cells in each processing sequence by storing an index corresponding to the cell location in \mathbf{pc} , $\mathbf{inds} \in \mathbb{M}(Ns, \max(\mathbf{Ks}(r)))$,
- \mathbf{op} : Vector indicating open rows of \mathbf{Zs} , $\mathbf{op} \in \mathbb{Z}^R, 0 \leq R \leq Ns$.

The number of simultaneous sequences Ns has the greatest impact on total run time. Specifying $Ns = 1$ results in a process similar to the MDCM method, producing identical results but with greater overhead cost. Values of $Ns > 1$ utilize simultaneous processing, reducing the total run time. In general, larger values of Ns result in greater efficiency gains at the expense of larger memory requirements. In practice, it is recommended to set Ns to a value which balances the desired efficiency and available memory.

The number of excitation periods per step $Nper$ is, in general, initially set to 1 and then increased up to 10–20 if slow convergence is experienced due to low damping, for example. A common value for the maximum number of steps is $MAX = 20$. The reader is directed to the supporting literature for the full details regarding appropriate values for these parameters [115].

A flowchart illustrating the PMDCM algorithm is presented in Fig. 4.1. After initialization, a loop containing four subroutines forms the main body of the algorithm: (1) *POPZs*: populating open locations in the \mathbf{Zs} array with cells from \mathbf{Z} , (2) *PARIMG*: simultaneously imaging the cells contained in \mathbf{Zs} , (3) *SCAN/PROC*:

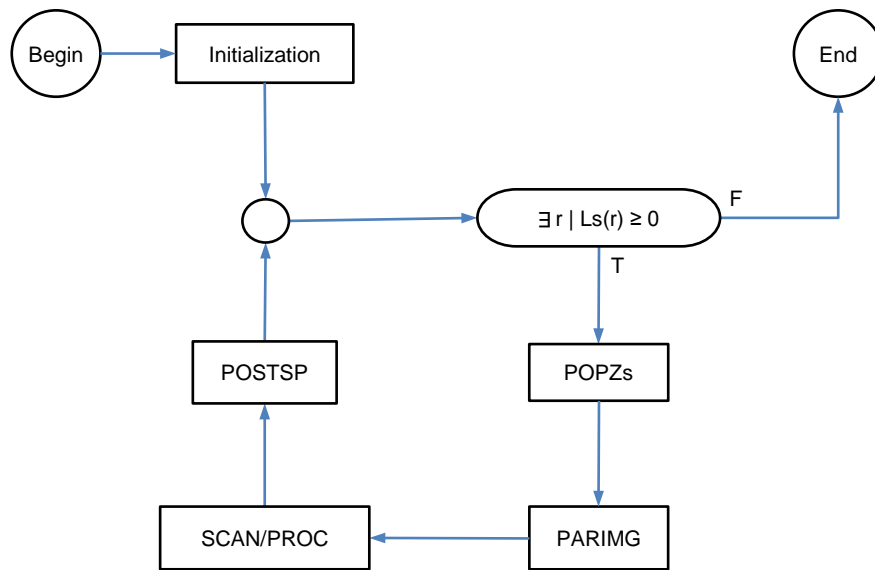


Figure 4.1: Flowchart illustrating the parallelized multi-degrees-of-freedom cell mapping (PMDCM) algorithm.

scanning **pc** and processing each of the image cells and (4) *POSTSP*: identifying completed sequences in order to determine open locations in **Zs** where new sequences can be initiated.

4.1.1 Initialization

In order to initialize the algorithm, the following steps are performed:

- $Ng := 0$,
- $ri := 1$,
- $\mathbf{op} := [1, \dots, Ns]$,
- $\mathbf{Ls} := \mathbf{0}$,
- $\mathbf{Ks} := \mathbf{0}$,
- $Nchaos := 0$.

The first two steps indicate that no periodic groups have yet been identified and that processing will begin with the first row of **Z**. If multiple subsets S are to be studied by importing **pc** and **g** arrays from previous runs, the initial value of Ng must be adjusted to reflect the number of groups already identified in the imported arrays.

At this point, array **Zs**—the list of Ns cells to simultaneously process—is empty. The assignment $\mathbf{op} := [1, \dots, Ns]$ is used to indicate that all rows from 1 to Ns are open. The last statement assigns an initial value of zero to all elements in **Ls** so the conditional statement following initialization is true, leading to subroutine *POPZs*.

4.1.2 Subroutine *POPZs* — Populate cell array **Zs**

In this subroutine, array **Zs** is populated by assigning cell values from **Z** starting at row ri to each open location listed in **op**. The subroutine is diagrammed in Fig. 4.2.

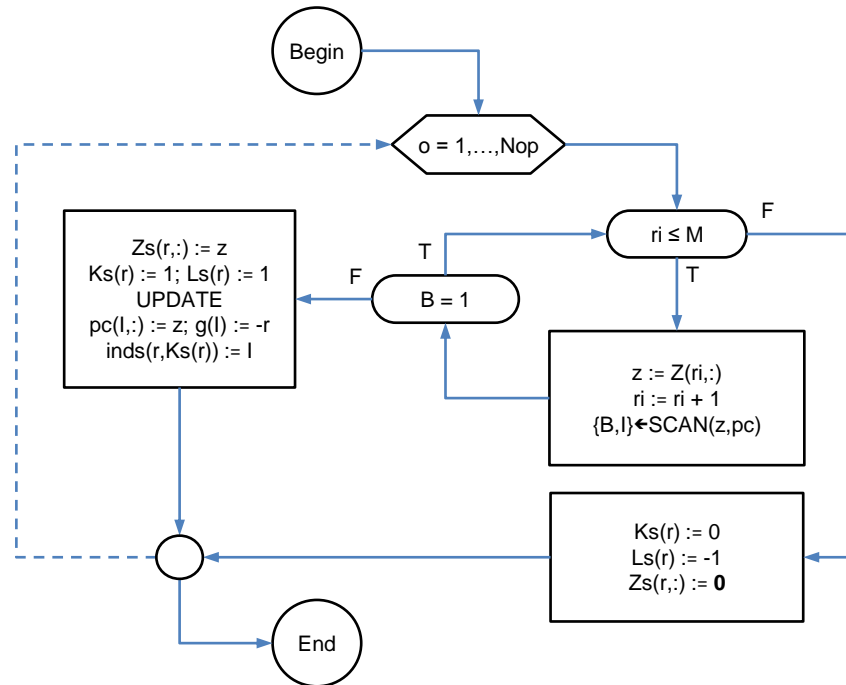


Figure 4.2: Subroutine *POPZs* — Populate cell array \mathbf{Zs} .

If every row of \mathbf{Zs} contains a sequence in-process then \mathbf{op} is an empty set, subroutine *POPZs* performs no operations and the algorithm continues with the next subroutine. Otherwise, if unprocessed cells remain in \mathbf{Z} ($ri \leq M$), the following operations are performed for all $o = 1, \dots, Nop$, where Nop is the number of elements in vector \mathbf{op} and $r := \mathbf{op}(o)$. The notation (r) is used to denote the r^{th} scalar element in a vector and $(r, :)$ to denote the row vector corresponding to row r in an array.

- $\mathbf{z} := \mathbf{Z}(ri, :)$,
- $ri := ri + 1$,
- $\{B, I\} \leftarrow \text{SCAN}(\mathbf{z}, \mathbf{pc})$.

The first two steps assign the cell indices located in row ri of array \mathbf{Z} to a temporary variable, \mathbf{z} , and increment ri . The third step calls the *SCAN* subroutine from the MDCM method, a process which scans array \mathbf{pc} for cell \mathbf{z} and returns a binary

value B indicating whether \mathbf{z} does ($B = 1$) or does not ($B = 0$) exist in \mathbf{pc} and a row index I , as defined in Ref. [115] and presented in Appendix C.

These steps are repeated until $B = 0$, indicating that cell \mathbf{z} has not already been processed, or until eventually $ri > M$, indicating that there are no remaining cells from \mathbf{Z} to process. In the case of $B = 0$, the following steps are performed:

- $\mathbf{Zs}(r, :) := \mathbf{z}$,
- $\mathbf{Ks}(r) := 1$,
- $\mathbf{Ls}(r) := 1$,
- *UPDATE*,
- $\mathbf{pc}(I, :) := \mathbf{z}$,
- $\mathbf{g}(I) := -r$,
- $\mathbf{inds}(r, \mathbf{Ks}(r)) := I$,

First, the cell indices stored in the temporary variable \mathbf{z} are assigned to open row r of \mathbf{Zs} . Element r is set to unity in vectors \mathbf{Ks} and \mathbf{Ls} to indicate the start of a new sequence. Then, subroutine *UPDATE* (see Appendix C) is called to rearrange \mathbf{pc} and \mathbf{z} is added to an open location in \mathbf{pc} . The group number corresponding to the cell is assigned as $-r$, indicating that the cell is currently under processing in the r^{th} sequence. In the final step, the index corresponding to the location of cell \mathbf{z} in \mathbf{pc} is recorded at the corresponding step in the r^{th} sequence in \mathbf{inds} .

The loop is terminated after the last open location has been assigned, $o = \text{Nop}$. However, in the case where $ri \leq M$ is not satisfied—indicating that all cells in \mathbf{Z} have been processed—a different set of steps are followed for all remaining loop iterations:

- $\mathbf{Zs}(r) := \mathbf{0}$,

- $\mathbf{Ks}(r) := 1$,
- $\mathbf{Ls}(r) := -1$.

The first two steps are helpful for troubleshooting, to ensure that no unprocessed cells remain in \mathbf{Zs} after the algorithm is finished. The last step assigns the particular value of -1 to row r in \mathbf{Ls} , used to indicate that no subsequent images are required of this row but also that \mathbf{Zs} should not be repopulated.

4.1.3 Subroutine *PARIMG* — Parallelized image calculation

The purpose of the *PARIMG* subroutine is to determine the “image” of each cell \mathbf{z} within \mathbf{Zs} , meaning the cell containing the endpoint of a trajectory segment initiated from the center of cell \mathbf{z} . This is similar to the *IMG* subroutine within the MDCM method, however, in the PMDCM method multiple images are calculated simultaneously. Accomplishing multiple numerical integrations in parallel is what allows the PMDCM method to operate in much less total run time.

In order to calculate the image of each cell in \mathbf{Zs} , the system described by Eqn. (1.1) is treated instead as a set of identical, uncoupled systems in parallel. The equations of motion therefore become,

$$\begin{aligned} \dot{\mathbf{x}}^1 &= \mathbf{F}^1(\mathbf{x}^1; t), \\ &\vdots \\ \dot{\mathbf{x}}^{Ns} &= \mathbf{F}^N(\mathbf{x}^{Ns}; t), \end{aligned} \tag{4.1}$$

where $\mathbf{x}^k = [x_1^k, \dots, x_N^k]^T$ and $\mathbf{F}^k = [F_1^k, \dots, F_N^k]^T$, $k = 1, \dots, Ns$. Superscript T indicates the vector transpose.

Numerical integrations are performed by starting from a vector of initial conditions

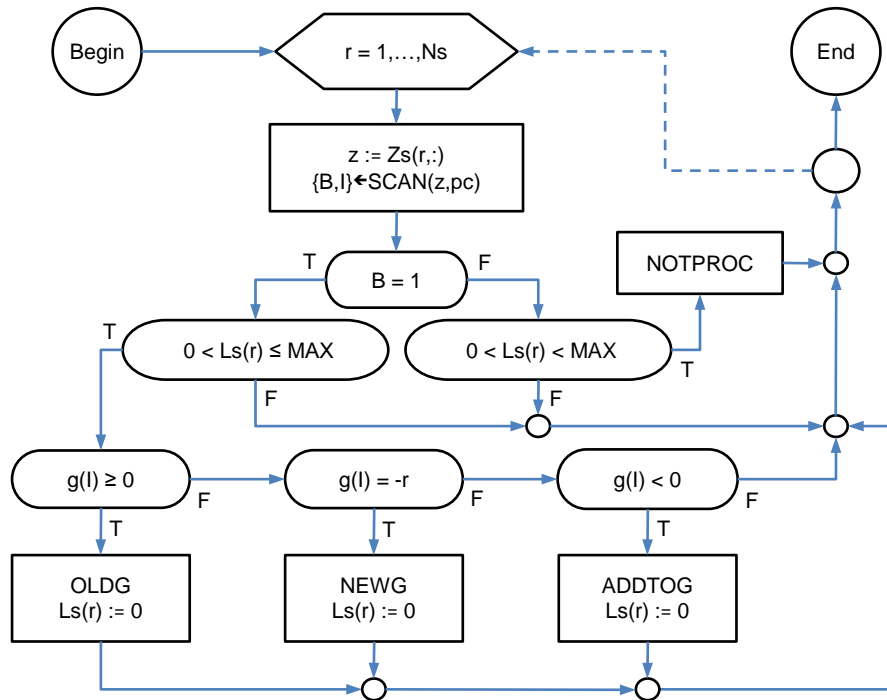


Figure 4.3: Subroutine *SCAN/PROC* — Scan and process imaged cells.

$IC = [\mathbf{c}^1, \dots, \mathbf{c}^{Ns}]$, where $\mathbf{c}^k \in \mathbb{R}^N$ is the vector of coordinates of the center of cell $\mathbf{Zs}(k, :)$ according to Eq. (1.2), and $IC \in \mathbb{R}^{N \cdot Ns}$. The image cells are then determined from the endpoint of the trajectory using Eq. (1.7).

4.1.4 Subroutine *SCAN/PROC* — Scan and process imaged cells

At this point, array \mathbf{Zs} now contains Ns image cells obtained by the previous subroutine. In this subroutine, illustrated in Fig. 4.3, each cell in \mathbf{Zs} is individually scanned and processed.

For each row r —corresponding to a particular sequence, the following steps are performed,

- $\mathbf{z} := \mathbf{Zs}(r, :)$,

- $\{B, I\} \leftarrow \text{SCAN}(\mathbf{z}, \mathbf{pc})$.

The first step assigns the cell stored in row r of \mathbf{Zs} to a temporary variable \mathbf{z} . Then, subroutine *SCAN* is called, returning a value of $B = 1$ if \mathbf{z} exists in \mathbf{pc} (if the cell has already been processed or is under processing) or $B = 0$ if not, and a variable I corresponding to a row in \mathbf{pc} .

If cell \mathbf{z} has not been processed ($B = 0$) and if $0 < \mathbf{Ls}(r) < \text{MAX}$ is satisfied, indicating that the sequence has not been discontinued nor reached the maximum allowed length, the following steps are performed—denoted within the flowchart by shorthand *NOTPROC*:

- *UPDATE*,
- $\mathbf{Ks}(r) := \mathbf{Ks}(r) + 1$,
- $\mathbf{Ls}(r) := \mathbf{Ls}(r) + 1$.
- $\mathbf{pc}(I, :) := \mathbf{z}$,
- $\mathbf{g}(I) := -r$,
- $\mathbf{inds}(r, \mathbf{Ks}(r)) := I$,

In the first two steps above, \mathbf{pc} is updated and cell \mathbf{z} is added to the ordered array. The corresponding group number is updated, indicating that the cell is under processing in sequence r . Array \mathbf{inds} is updated, providing a connection between the current step in the sequence and the location of the corresponding cell in \mathbf{pc} . Then, the values of $\mathbf{Ks}(r)$ and $\mathbf{Ls}(r)$ are incremented, indicating that another cell has been added to the current sequence and to the current trajectory.

On the other hand, if cell \mathbf{z} has already been processed ($B = 1$) and if $0 < \mathbf{Ls}(r) \leq \text{MAX}$ is satisfied, indicating that the sequence has not been discontinued nor exceeded the maximum allowed length, three cases are possible:

(P1) Trajectory maps to a predetermined trajectory that has already been completed, $\mathbf{g}(I) \geq 0$:

- *OLDG*,
- $\mathbf{Ls}(r) := 0$.

Subroutine *OLDG* from the MDCM method is called, updating the group number of all cells in the current sequence with the group number of \mathbf{z} (see Appendix C). The corresponding row of \mathbf{Ls} is set to zero to indicate that the sequence has been completed and a new sequence can be started in this row.

(P2) Current trajectory repeats itself, $g(I) = -r$:

- *NEWG*,
- $\mathbf{Ls}(r) := 0$.

Subroutine *NEWG* from the MDCM method is called, updating the group number of all cells in the current sequence with a new group number (see Appendix C). The corresponding row of \mathbf{Ls} is set to zero to indicate that the sequence has been completed and a new sequence can be started in this row.

(P3) Trajectory maps to another trajectory that is in progress, $\mathbf{g}(I) < 0$:

- *ADDG*,
- $\mathbf{Ls}(r) := 0$.

This case—the intersection of two independent sequences, both under-processing—is unique to the PMDCM method. Subroutine *ADDG* appends all cells from sequence r to the sequence corresponding to $\mathbf{g}(I)$. Within the subroutine \mathbf{Ks} is increased according to the number of cells that have been added, but \mathbf{Ls} is not modified, since the length of the original trajectory corresponding to $g(I)$ has not been changed. Row r

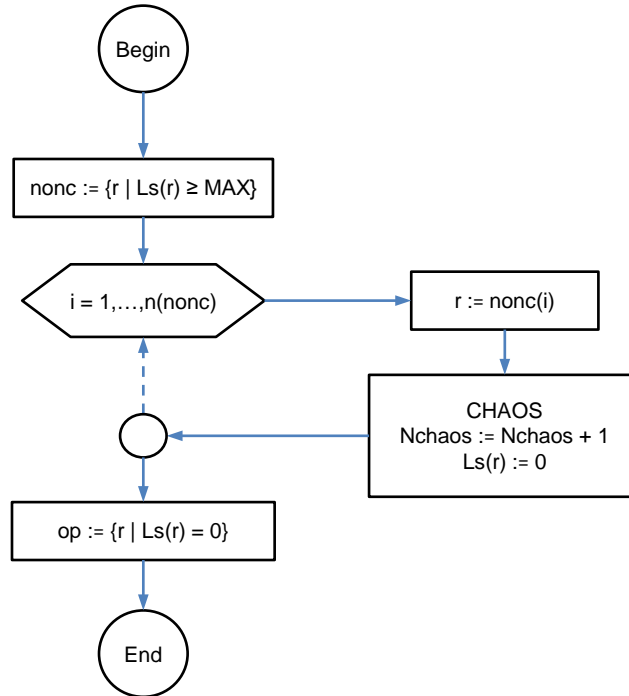


Figure 4.4: Subroutine *POSTSP* — Post-scan-and-process operations.

of \mathbf{Ls} is then set to zero to indicate that the sequence has been completed and a new sequence can be started in this row.

Subroutine *ADDG* is as follows:

- for $c = 1, \dots, \mathbf{Ks}(r)$,
- $\mathbf{inds}(-\mathbf{g}(I), \mathbf{Ks}(r) + c) := \mathbf{inds}(r, c)$,
- $\mathbf{g}(\mathbf{inds}(r, c)) := \mathbf{g}(I)$,
- end,
- $\mathbf{Ks}(-\mathbf{g}(I)) := \mathbf{Ks}(-\mathbf{g}(I)) + \mathbf{Ks}(r)$.

4.1.5 Subroutine *POSTSP* — Post-scan-and-process

Figure 4.4 illustrates the *POSTSP* subroutine. The subroutine accomplishes two things. First, the length of each sequence is checked and those longer than the

user-specified MAX are labeled as chaos and marked as completed. Second, the rows corresponding to all completed sequences are identified in preparation for the following subroutine, *POPZs*.

The first step, $nonc := \{r \in \mathbb{N} \mid \mathbf{Ls}(r) \geq MAX\}$, creates a vector $nonc$ containing row numbers that correspond to sequences which have exceeded the maximum user-specified length, MAX . At each row that exceeds the MAX length, $r = nonc(i), i = 1, \dots, n(nonc)$ where $n(X)$ represents the number of elements in X , the following steps are performed,

- *CHAOS*,
- $Nchaos = Nchaos + 1$,
- $\mathbf{Ls}(r) := 0$

The first step executes the *CHAOS* subroutine (see Appendix C), the main tasks of which are to add cell \mathbf{z} to the \mathbf{pc} array and to assign a value of zero to the group number of all cells in the current sequence, denoting that the cells lead to a chaotic attractor [115]. The total number of chaotic sequences $Nchaos$ is then incremented, and the counter \mathbf{Ls} reset to indicate that the sequence has been completed.

In the final step of the subroutine, $\mathbf{op} := \{r \in \mathbb{N} \mid \mathbf{Ls}(r) = 0\}$, the vector \mathbf{op} is updated. Vector \mathbf{op} now contains a list of all rows in \mathbf{Zs} to be repopulated based on the indication given by a value of $\mathbf{Ls}(r) = 0$.

4.1.6 Overview

There are two main differences between the PMDCM algorithm and the MDCM algorithm. The first is the order in which cells are imaged and processed. The MDCM algorithm is a sequential process, alternating between imaging and scanning/processing to construct one trajectory sequence at a time. In the PMDCM method, a set

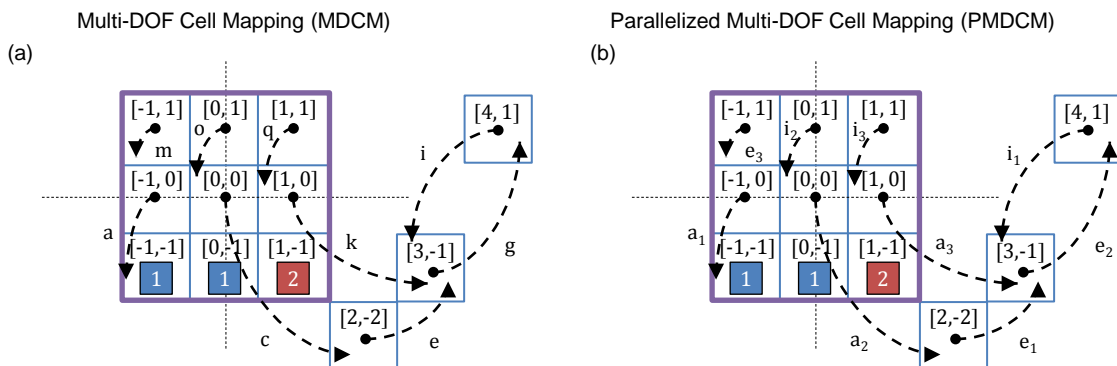


Figure 4.5: A two-dimensional example illustrating the processing order within the (a) multi-degrees-of-freedom cell mapping (MDCM) method, and (b) parallelized multi-degrees-of-freedom cell mapping (PMDCM) method with $N_s = 3$.

of images are calculated in parallel, then each is scanned and processed individually, thus creating a set of trajectory sequences. The parallel imaging is accomplished by using an augmented set of governing equations in parallel, significantly reducing the total run time. Many variables from the MDCM method were modified in order to account for the multiple trajectories in PMDCM, most being higher-dimensional representations of their MDCM counterparts.

The second main difference is the necessary *ADDG* subroutine. Since multiple trajectory sequences are being simultaneously processed within the PMDCM method, it is possible for two trajectories to intersect before either reaches a periodic attractor. The *ADDG* subroutine addresses this problem by appending the cells from the intersecting sequence to the intersected sequence.

Figure 4.5 illustrates both of these differences and their effect on the processing order between the (a) MDCM and (b) PMDCM method with $N_s = 3$. The thick square indicates a 3×3 subset S of cell state space in a hypothetical two-dimensional system. Assume that the three cells on the bottom row have already been processed, mapping to periodic groups g_1 , g_1 , and g_2 , respectively. Dashed lines illustrate the

trajectories in each of the imaging steps, with the order of steps indicated by the accompanying letters. Subscripts indicate steps performed simultaneously. Omitted letters correspond to scanning and processing steps.

In the MDCM method, shown in Fig. 4.5(a), the imaging step and the scanning and processing step alternate throughout the procedure. Trajectory (a) ends within an already-processed cell belonging to g_1 , so in step (b) the designation of g_1 is added to cell $[-1, 0]$. Trajectory (c) is followed by processing step (d), which identifies that (c) ends in an un-processed cell. Trajectories (e), (g), and (i) follow, in between which processing steps (f) and (h) add the corresponding cells to the current trajectory. In step (j), it is determined that the current sequence repeats itself, so each cell in the sequence is labeled as g_3 , a new group. Trajectories (k), (o), and (q) map to completed sequences, so in the respective processing steps (l), (p) and (r) each are labeled accordingly. Trajectory (m) maps to itself, and therefore in step (n) a new periodic group g_4 is formed.

In the PMDCM method, shown in Fig. 4.5(b), multiple simultaneous imaging steps are followed by sequential scanning and processing steps. Trajectories (a_1, a_2, a_3) are calculated in parallel and together constitute the first step. In step (b) it is determined that (a_1) ends within an already-processed cell belonging to g_1 , so the designation of g_1 is added to cell $[-1, 0]$. Steps (c) and (d) identify that (a_2) and (a_3) both map to new cells that have not yet been processed. Trajectories (e_1, e_2, e_3) are then calculated in parallel, followed by the corresponding processing steps: in step (f), since (e_1) ends within a cell under-processing in a different sequence, cells $[0, 0]$ and $[2, -2]$ are added to the intersected sequence; step (g) identifies that (e_2) maps to a new, not yet processed cell; in step (h), since (e_3) maps to itself, a new periodic group g_3 is formed. Trajectories (i_1, i_2, i_3) are the final image, and in processing steps (j), (k), and (l) the cells corresponding to each are assigned to g_4 .

In this basic example, end result from both methods is similar. However, due to

the differences in processing order between the MDCM and PMDCM methods coupled with the small errors introduced by the center point approximation, identical results are not expected. A small amount of disagreement is typical, particularly at fractal basin boundaries where it is known that many cell mapping methods experience reduced accuracy. These errors are minimized by decreasing the cell size. In the following section, it is demonstrated that in addition to the efficiency benefits, the accuracy of the PMDCM method is also improved over the MDCM method.

4.2 Validation

In this section, results obtained by using the PMDCM method are compared with those by the MDCM method. First, the governing equations of a dynamic system are described. Then, the basin portraits obtained using each of the methods are presented and the efficiency benefits of the PMDCM method are discussed.

4.2.1 Dynamic model

A two degrees-of-freedom planar spring-pendulum system is used to compare the cell mapping methods, as illustrated in Fig. 4.6. This particular system was selected due to its mechanical simplicity, academic familiarity, and the availability of relevant published results. A detailed analysis of the basin portraits of the spring-pendulum system was presented by Alasty and Shabani using the GOS method [132].

The governing equations for the spring-pendulum system with periodic force and moment excitation are presented in Eqns. (4.2)–(4.3), adapted from [132].

$$\ddot{x} + c_1\dot{x} + \omega_1^2x - (1+x)\dot{\phi}^2 + \omega_2^2(1-\cos\phi) = F\cos(\Omega t), \quad (4.2)$$

$$(1+x)^2\ddot{\phi} + c_2\dot{\phi} + 2(1+x)\dot{x}\dot{\phi} + \omega_2^2(1+x)\sin\phi = M\cos(\Omega t), \quad (4.3)$$

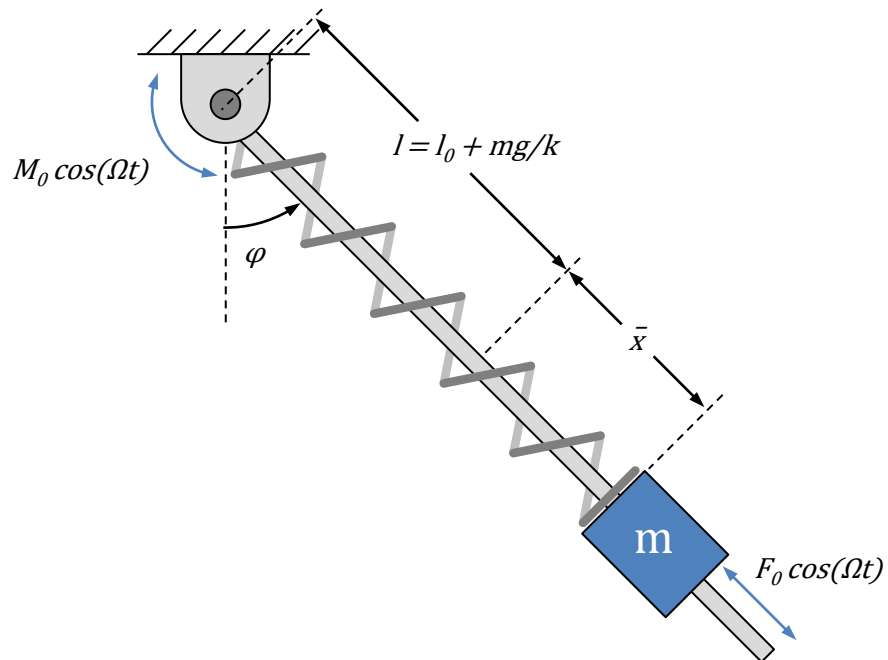


Figure 4.6: Schematic of the “spring-pendulum”: a two degrees-of-freedom system consisting of a point mass attached to a spring and sliding on a massless pendulum.

where the following substitutions have been made:

$$F = F_0/ml, \quad M = M_0/ml^2, \quad (4.4)$$

$$\omega_1^2 = k/m, \quad \omega_2^2 = g/l, \quad (4.5)$$

$$c_1 = \bar{c}_1/m, \quad c_2 = \bar{c}_2/m, \quad (4.6)$$

$$x = \bar{x}/l, \quad l = l_0 + mg/k. \quad (4.7)$$

Parameters F_0 and M_0 indicate the amplitude of the harmonic force and moment loading, respectively. The respective natural frequencies of the spring-mass and the pendulum are denoted by ω_1 and ω_2 . Parameters c_1 and c_2 represent the damping coefficients of the linear and angular motion. The non-dimensional displacement of the mass from static equilibrium and the vertical angle of the pendulum are given by x and ϕ , respectively. Note that the variables used to denote parameters in the present chapter are defined independently of their meaning elsewhere in the thesis.

4.2.2 Results

Basin portraits are constructed for the case of operation near the pendulum resonance, $\Omega \approx \omega_2$, with zero force loading, $F = 0$. Internal resonance is encouraged by tuning the resonant frequency of the mass to $\omega_1 = \omega_2/2$. Excitation magnitude and damping parameter values are set to $M = 0.00087$ and $c_1 = c_2 = 0.005$, respectively, consistent with Ref. [132].

Figure 4.7 illustrates basin portraits constructed by using the (a) GOS method, (b) MDCM method, (c) PMDCM method with $N_s = 10$, and (d) PMDCM method with $N_s = 100$. The resolution of each portrait is 201×201 . Black and white shading is used to denote the basins which converge to attractors at $a_2 = 0.035$ and $a_2 = 0.195$, respectively, where a_2 is the amplitude of the pendulum. Data points within the GOS

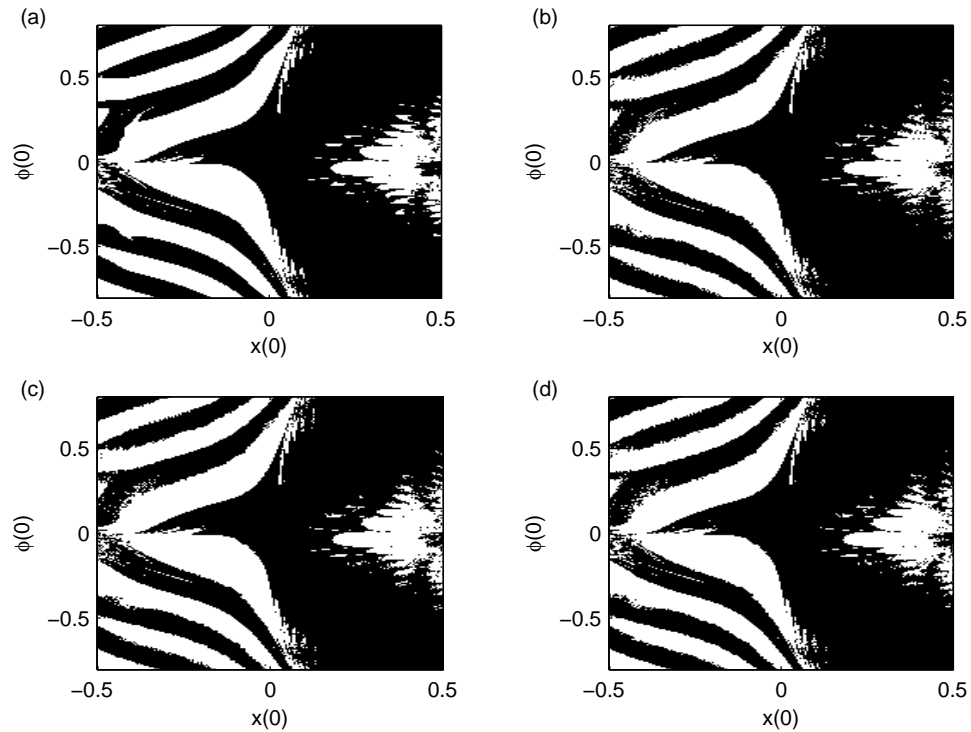


Figure 4.7: Basin portraits produced by using the (a) grid-of-starts (GOS) method, (b) MDCM method, (c) PMDCM method with $N_s = 10$, and (d) PMDCM method with $N_s = 100$.

method are measured after 1000 excitation periods, which is determined to be long enough for the transient behavior to decay and therefore represents the “true” basin portrait. All features from the GOS portrait are observed in the MDCM and PMDCM method, with only minor discrepancies noted at the basin boundaries, particularly in the fractal regions. The portrait constructed using the PMDCM method with $N_s = 1$ is identical to the MDCM results and is therefore not shown here.

Table 4.1 provides a concise accuracy and efficiency comparison between the MDCM and PMDCM methods. Total run time and percentage of the run time required by the MDCM method are indicated by τ and $\Delta\tau$, respectively. The total run time was clocked using the internal timers within MATLAB. For reference, the total run time using the GOS method was approximately one order of magnitude larger than with the MDCM method. Simulations were conducted on a Dell Optiplex

Table 4.1: Efficiency and accuracy benefits of the PMDCM method compared to the MDCM method.

Algorithm	τ	$\Delta\tau$	N_ϵ	N_ϵ/N_T	ΔGIM
MDCM	10,049s	100.0%	1,236	3.05%	0.11%
PMDCM $_{ N_s=1}$	14,206s	141.4%	1,236	3.05%	0.11%
PMDCM $_{ N_s=10}$	2,415s	24.0%	1,124	2.78%	0.09%
PMDCM $_{ N_s=100}$	678s	6.7%	1,110	2.75%	0.04%

760 with an Intel Core2 Quad CPU processor, Q9650 @ 3 GHz with 4 MB RAM. Number of error cells N_ϵ represents the number of cells in the portrait indicating convergence to a different attractor than the “true” GOS results. Number of error cells as a percentage of the total cells is indicated by N_ϵ/N_T . The error in the *global integrity measure* (GIM) when compared to the value calculated using the GOS method is represented by ΔGIM . The global integrity measure indicates the percentage of total cells which converge to a specific attractor, in this case $a_2 = 0.035$ (black). A detailed description of the GIM and other integrity measures commonly used in this type of analysis can be found in [120].

When only one sequence is processed at a time in the PMDCM method, $N_s = 1$, the PMDCM method produces identical results to the MDCM method with 3.05% cell-by-cell error and 0.11% error in the integrity measure. In this case the total run time is increased by 41% due to the additional overhead required to implement the PMDCM method. However, the benefits of the PMDCM method are realized for $N_s = 10$ and $N_s = 100$ which reduce the total run time by 76% and 93%, respectively. For comparison, the total run time using the GOS method is about 1×10^5 seconds.

It is also noted that the errors are decreased as the number of cells processed in parallel is increased, with the error in the integrity measure for $N_s = 100$ less than half of the error for the MDCM method. The more cells that are processed at a time in the PMDCM method, the greater the likelihood of a cell in S being processed

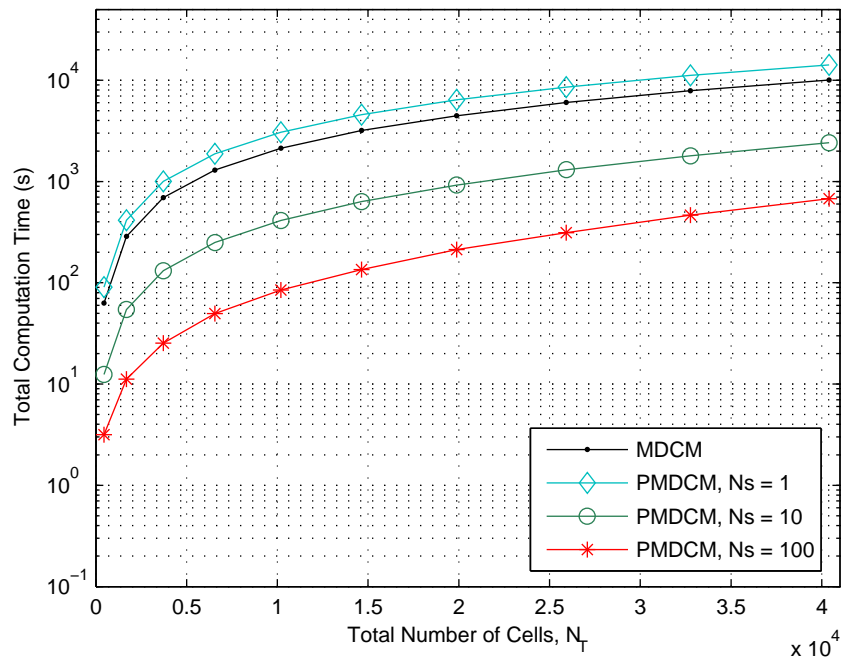


Figure 4.8: Computation time versus number of cells in subspace S for the PMDCM method with various N_s values and the MDCM method.

as the first cell in a new sequence rather than processed when encountered within another sequence. Since small truncation errors accumulate as a sequence progresses, the accuracy of the predicted steady state behavior resulting from a cell in S is greater when the sequence starts with S . These errors are most prominent at fractal basin boundaries such as those illustrated in Fig. 4.7.

Figure 4.8 illustrates the total run time required versus the number of cells in the subset S . Consistent with the results from Table 4.1, an increase in run time is observed for PMDCM with $N_s = 1$ over MDCM due to the additional overhead within the algorithm. However, for all array sizes run times are drastically reduced as N_s is increased. Diminishing returns and eventually computer memory limitations are experienced for values of $N_s \gg 100$.

4.3 Summary

In this chapter, the parallelized multi-degrees-of-freedom cell mapping (PMDCM) method was introduced. The PMDCM method uses the same underlying theory and operations as the MDCM method to conduct the analysis, but employs a significantly restructured algorithm which allows for the use of parallel computing. The PMDCM algorithm loops through four main subroutines until all cells have been processed: (1) assigning unprocessed cells to available locations in an auxiliary array, (2) determining the image of each cell in the auxiliary array by simultaneous numerical integration, (3) scanning and processing each image cell individually, and (4) identifying non-converging and completed sequences and denoting the corresponding locations in the auxiliary array as available.

A two-dimensional planar spring-pendulum system was used to evaluate the accuracy and speed of the new method. Results obtained using the PMDCM method were compared to those obtained using the MDCM method and the “true” solution produced with the GOS method. Using a quad-core processor, the PMDCM method (100 simultaneous integrations) reduced total run time by 93% while also reducing the integrity measure error from 0.11% to 0.04%, when compared to the MDCM method.

The PMDCM method is believed to be the most efficient numerical tool available for the global dynamic analysis of multiple degrees-of-freedom (MDOF) systems. The PMDCM method improves upon the benefits for mapping MDOF systems demonstrated by the MDCM method by more efficiently utilizing parallel computing resources and significantly reducing run time. Further improvement of the performance benefits of the PMDCM method over the MDCM method are expected as the number of available processors increases. The PMDCM method imposes no intrinsic limitation on the number of dimensions of a system, making the method suitable for the analysis of virtually any dynamic system.

Chapter 5

Strongly Nonlinear Tuned Mass Damper

Strongly nonlinear tuned mass dampers have been shown to possess some unique benefits when used as passive vibration absorbers. Specifically, these devices are capable of irreversible energy transfer known as energy pumping, which takes place in a quasi-periodic regime in the neighborhood of the primary resonance. It has been shown, however, that within certain regions in the frequency domain away from the primary resonance, multiple stable solutions coexist [59, 61]. Hereafter, these regions are referred to as *bi-stable regions* as long as two or more stable solutions coexist.

Two main bi-stable regions are generally present in the primary structure and NTMD (the PN system) response—one above and one below the primary resonance frequency. Within these regions, the lower-amplitude solution is the main branch to which the system will typically converge when starting from a state of rest. The higher-amplitude solution occurs as a result of the nonlinearity folding and distorting the two resonance peaks present in the linear absorber response. The magnitude of the higher-amplitude solutions generally exceeds the peak response achievable by using a linear TMD, therefore negating the benefit of the NTMD and potentially

damaging the primary structure. Within this chapter, all additional solutions identified within these bi-stable regions will be referred to as either a “low amplitude” or “high amplitude” solution, a distinction which will be clarified in the following section.

The two key contributions of the research presented in this chapter are (1) to characterize the existence and strength of the coexisting solutions in the PN system and (2) to demonstrate a means to eliminate convergence to the high amplitude solution by adding a small STMD component (the PNS system). The existence and magnitude of some of the period one solutions within the bi-stable regions have been identified in previous works (*e.g.* [3, 59, 61]), but some additional solutions (attractors) as well as the basins which indicate the relative strength of each attractor have not yet been studied. Key concepts in this chapter such as basins, integrity measures, and erosion profiles are explained in detail in Section 1.2.3.

In the first section, an initial study is performed to determine the regions of parameter space within which the NTMD is capable of outperforming a linear TMD but where multiple solutions are also present. The attractors and corresponding basins and integrity measures for the higher-frequency and lower-frequency bi-stable regions are identified in the second and third sections, respectively. In the fourth section, the benefits of adding a small STMD component are demonstrated. A summary of the results is presented in the final section.

5.1 System and Environmental Parameter Values

The response of the PN system is a function of five system parameters: ϵ_N , γ_1 , $\hat{\gamma}_N$, Ω , and Ω_N , and two environmental parameters: F and ω . The first challenge is therefore to determine a small number of design and environmental parameter value combinations for which to construct a meaningful set of erosion profiles. The

recent literature on strongly nonlinear absorbers and energy sinks provides various examples of parameter values at which the energy pumping phenomenon can be observed [46, 59]. The focus of the present study, however, is to study the system response using not necessarily the *optimum* or *idealized* parameter values but rather using values in the neighborhood of the optimum values for which multiple stable solutions can be observed by using a reasonable range of initial conditions. First, realistic limits for the value of each of the parameter are defined, then a preliminary numerical study is used to identify parameter value combinations that result in the desired behavior.

Following the example of a related study [59], a mass ratio value of $\epsilon = 0.1$ is used, representing an approximate upper limit of the largest absorber that would be installed in a structure. Structural damping is commonly approximated by a ratio of 2% or 5%, so the primary damping ratio of $\gamma_1 = 0.02$ is used [14]. Similarly, NTMD damping ratio values of $\gamma_N \in \{0, 0.02, 0.05\}$ are considered, where the ideal case of zero-damping has been included as a lower limit. It is noted that small damping values such as these are commonly targeted to maximize energy transfer to the absorber. The value of the NTMD damping coefficient $\hat{\gamma}_N$ will be selected based on the results of this preliminary study.

The linear stiffness parameter is varied from $\Omega \in [0, 1]$, with the lower limit representing an essentially nonlinear absorber and the upper limit bounded by the natural frequency of the primary structure. Following again the nonlinear absorber design process used to achieve energy pumping in [59], the nonlinear stiffness parameter is expected to be on the order of $\Omega_N \approx 0.1$ or less, so the range of values $\Omega_N \in [0, 0.5]$ is selected. Initial simulations using values up to $\Omega_N = 2$ verified that no favorable response behavior at higher nonlinear levels have been overlooked.

Three representative values for the excitation magnitude parameter are considered, $F \in \{0.35, 0.6, 2.5\}$. The first, $F = 0.35$, represents a seismic event that is

approximately half of the expected strength. Most importantly, this value matches that used to produce some of the key results in [59] within which the detached resonance is illustrated. The second, $F = 0.6$, is used to denote the “most-likely” case. The largest magnitude value, $F = 2.5$, represents the “worst-case” scenario where the dominant frequency of the seismic event corresponds to the natural frequency of the primary structure. Each of these scalar values was calculated by taking the root-mean-squared value of the frequency-dependent excitation magnitude over $\omega \in [0, 2]$ for the Kanai-Tajimi event described in [59].

In order for the erosion profiles constructed in the following subsection to be most useful, sets of parameter values must be located that produce a response which meets the following two criteria:

1. Multiple stable solutions coexist (bi-stable regions) within the range of “expected” operating conditions as defined by the environmental parameters.
2. The NTMD outperforms an optimally tuned linear TMD when considering *only* the safe attractor (low amplitude solution branch) in each bi-stable region.

The first condition is a necessary criterion in order to be able to construct the erosion profiles, which exist only when more than one stable solution is present. The second condition ensures that the erosion profiles will be useful, since the end goal of the present and related research is to determine whether an NTMD can be developed which outperforms an optimally tuned linear TMD. In this context, if an NTMD does not satisfy the second condition then it provides no practical value and therefore its corresponding erosion profile is of no interest. Two performance measures: (1) peak amplitude and (2) RMS of the frequency-response are used as efficient methods to determine whether an NTMD with the given parameter values outperforms an optimally-tuned linear TMD. The second criterion is satisfied if either of the two measures indicates favorable performance over the TMD when only the safe attractor

(low amplitude solution branch) of the PS response in the PN system is considered. The safe attractor is determined by slowly increasing the excitation magnitude from zero-valued initial conditions, following the procedure in Ref. [120].

A numerical algorithm is developed to scan the parameter space in order to identify a rough estimate of the regions that meet these two criteria. For each of the nine combinations of γ_N and F , a grid of 30×30 Ω and Ω_N values is constructed, spanning the domain of each parameter. At each point (Ω, Ω_N) within each grid, numerical integration is used to synthesize a solution at each of 50 excitation frequencies $\omega \in [0.5, 1.5]$ and 30 initial conditions $q_1(0) \in [0, 35]$, $q_i(0) = 0$ for $i = 2, 3, 4$. This range and resolution of initial conditions is determined to be sufficient to identify the presence of multiple solutions by examining a single-dimensional cross section of the basin, and is later verified by examining the basins constructed in the final part of this section. The set of amplitudes $|q_1|$ calculated from each solution at the combinations of ω and $q_1(0)$ are used to determine which, if any, of the above criteria are met by the point (Ω, Ω_N) .

Figure 5.1 illustrates the results of the parameter space scan. Each subplot represents a combination of γ_N and F , as indicated by the respective row and column labels. Light (yellow) shading indicates that only the first criterion is satisfied at the given point, medium (red) shading indicates that only the second criterion is satisfied and dark (black) shading indicates that both of the criteria are satisfied, providing the *region of interest*. The absence of shading indicates that neither of the criteria is satisfied.

Two general trends are observed from the results presented in Fig. 5.1. First, the area of the region of interest decreases and shifts toward lower values of Ω_N as the excitation magnitude increases. This confirms intuition that the effective nonlinearity is directly proportional to both the nonlinear stiffness and excitation magnitude, and also indicates that the system is less robust to detuning of the linear or nonlinear

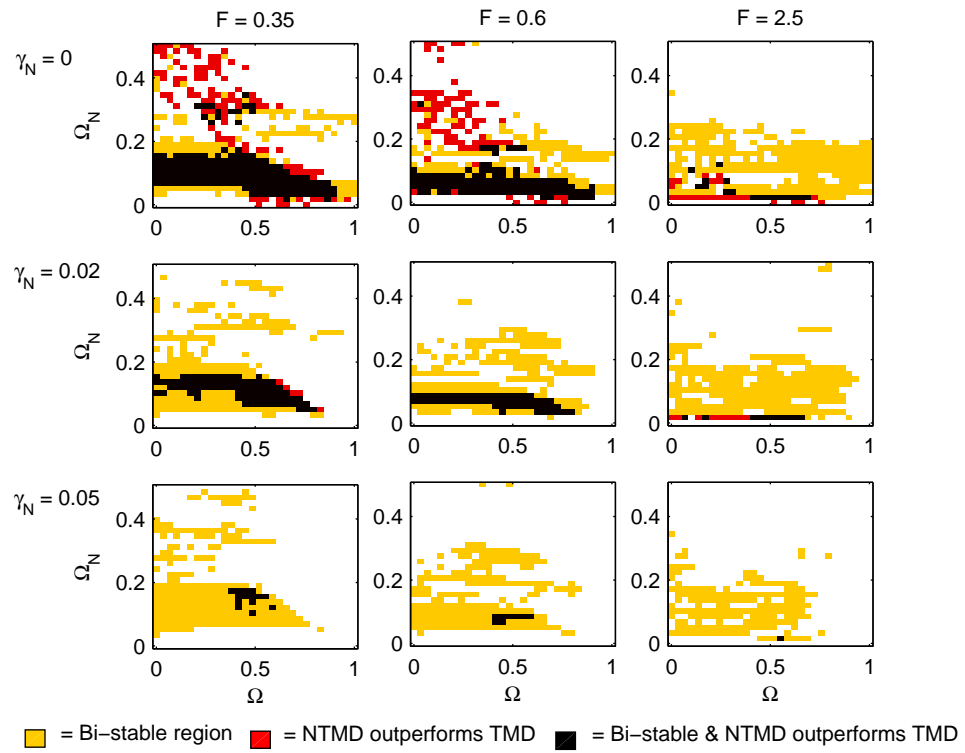


Figure 5.1: Estimated regions of parameter space that meet the criteria noted in the legend from an initial study.

stiffness at larger excitation magnitudes. Second, larger NTMD damping ratio values correlate with a smaller region of interest and a shift toward larger values of Ω . This suggests that the damping in an NTMD should be kept as small as possible.

The regions of interest estimated in Fig. 5.1 are refined by examining frequency-response plots constructed using numerical continuation techniques at a number of points in each grid. In general, the frequency-response profiles within the regions of interest follow a characteristic trend, illustrated in Fig. 5.2. The Period-1 solutions depicted in Fig. 5.2 were also observed by Alexander and Schilder, who studied the profile changes that occurred for various parameter values [59]. In this most general case two bi-stable regions exist, indicated by $B_{\omega < 1}$ and $B_{\omega > 1}$.

The higher-frequency bi-stable region, denoted hereafter as $B_{\omega > 1}$, is observed for $\omega \in [1.4, 3.4]$ in the present example. In general, for larger values of Ω_N the magnitude of the upper solution branch decreases and the limit point bifurcation at the upper bound of the region shifts right, increasing the width of the region. With the exception of the zero-NTMD damping case, smaller values of Ω also result in a rightward shift of the limit point bifurcation. The integrity of the low amplitude solution within $B_{\omega > 1}$ is determined to be significantly higher than in the lower-frequency region, $B_{\omega < 1}$, and therefore the main focus of this paper is on the integrity of solutions in $B_{\omega < 1}$. A brief overview of the behavior within $B_{\omega > 1}$ is presented in Section 5.2.

The lower-frequency bi-stable region $B_{\omega < 1}$ is observed for $\omega \in [0.6, 0.9]$ in the present example. Initial results reveal that depending on the initial conditions either the lower-amplitude (safe solution) or higher-amplitude (constraint solution) branch could dominate the system response. Therefore, the present study is focused on determining the erosion profiles within $B_{\omega < 1}$. These results are presented in Section 5.3.

Results are obtained at two key excitation frequencies within $B_{\omega < 1}$, denoted ω_m and ω_p . The first, ω_m , corresponds to the midpoint of the bi-stable region bounded by the torus bifurcation of the safe solution at the lower limit and by the limit point

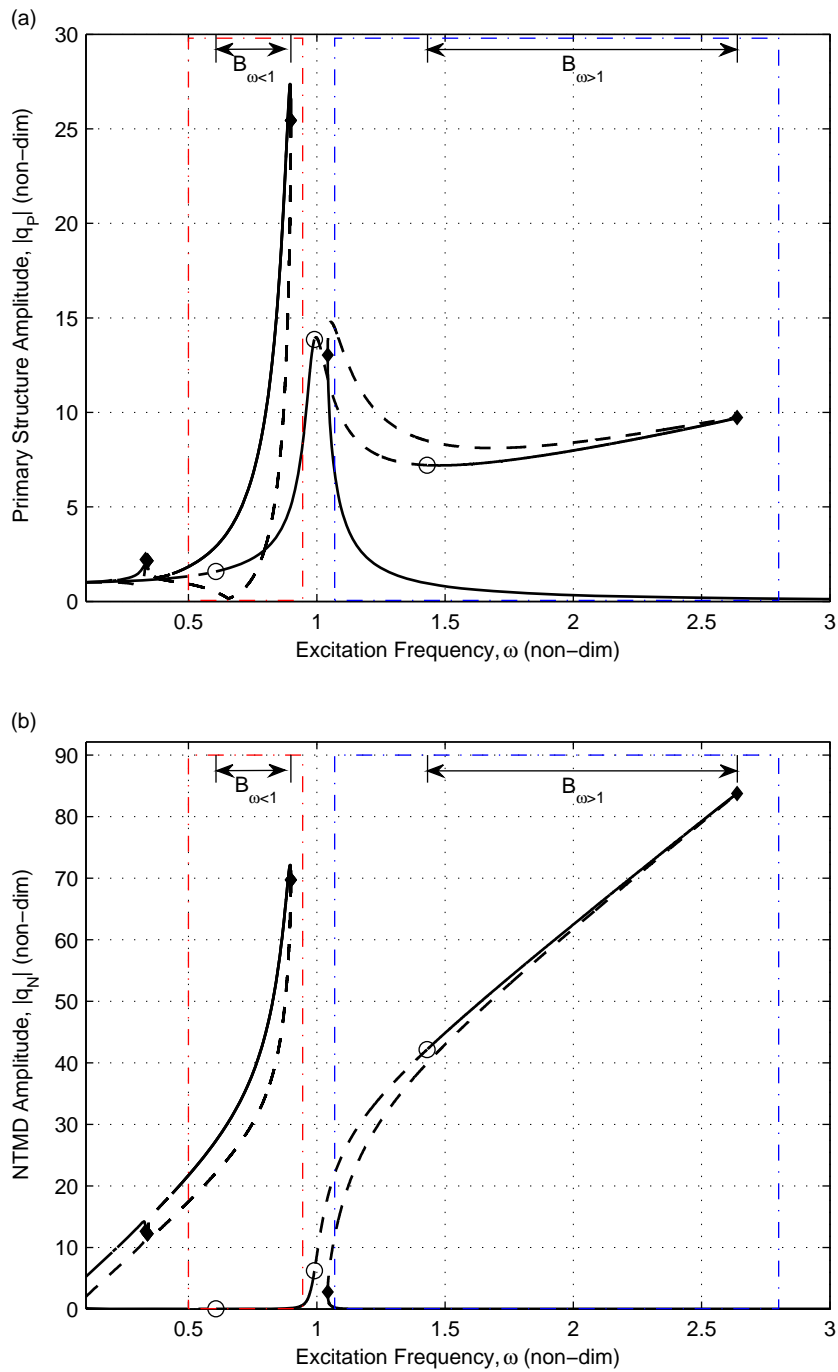


Figure 5.2: Characteristic frequency-response profile for the (a) primary structure and (b) NTMD illustrating the two bi-stable regions in the PN system response; $\Omega = 0, \hat{\gamma}_N = 0.002, \Omega_N = 0.09, F = 0.35, \phi = 0$. Limit point (\diamond) and torus (\circ) bifurcation points are marked.

Table 5.1: Four sets of parameter values for which the erosion profiles are constructed.

ϵ	γ_1	Ω	$\hat{\gamma}_N$	Ω_N
0.1	0.02	0	0	0.06
0.1	0.02	0	0.002	0.09
0.1	0.02	0.1	0	0.06
0.1	0.02	0.1	0.002	0.09

bifurcation of the constraint solution at the upper limit. The second, ω_p , is the frequency corresponding to the peak amplitude of the constraint solution.

Table 5.1 lists the four sets of system parameter values from which the erosion profiles are constructed. In order to examine both an ideal case and a realistic case, the four sets are combinations of zero and non-zero values of $\hat{\gamma}_N$ and Ω . When $\Omega = 0$ the system represents an essentially nonlinear absorber, or “nonlinear energy sink”. Frequency response profiles indicate that larger linear stiffness values decrease the width of the bi-stable region, so a small value, $\Omega = 0.1$, is selected in order to focus on a case where the influence of the high amplitude response is more significant. The NTMD damping parameter value $\hat{\gamma}_N = 0.002$ corresponds to a 2% damping ratio at $\Omega = 0.1$. The value of the nonlinear parameter Ω_N is 0.06 for zero NTMD damping and 0.09 for $\hat{\gamma}_N = 0.002$, to correspond with the location of the center of the region of interest depicted in Fig. 5.1, which shifts according to γ_N .

5.2 Higher-Frequency Bi-Stable Region, $B_{\omega>1}$

Figure 5.3 illustrates the frequency-response within the $B_{\omega>1}$ region for (a) the primary structure amplitude $|q_1|$ and (b) the NTMD amplitude $|q_3|$. The axis limits in Fig. 5.3 correspond to the blue dash-dot rectangle surrounding $B_{\omega>1}$ within Fig. 5.2. The stable and unstable solution branches identified using numerical continuation techniques are drawn using solid and dashed lines, respectively. Steady-state am-

plitudes obtained using numerical integration for $q_1(0) \in [-200, 0]$, $q_i(0) = 0$ for $i = 2, 3, 4$ are presented as black dots.

In addition to the Period-1 ($P-1$) curves illustrated in Fig. 5.2, a Period-3 branch and two smaller branches, Period-5 and Period-2 are observed. To the knowledge of the author, these higher-period branches have not been identified in previous literature. Each of the additional branches was initially identified in the results obtained from numerical integration. The steady-state solution was then used as a starting point for numerical continuation. Continuations were not always successful; most often the continuation methods failed to converge when initialized from results near $\omega \approx 1$, possibly due to remaining transient behavior or a long-period, near-quasiperiodic response.

A characteristic basin portrait for $B_{\omega > 1}$ in the Σ^{12} plane is presented in Fig. 5.4. The excitation frequency is $\omega = 1.8$, near the center of the bi-stable region. Basins corresponding to three stable attractors are clearly observed, agreeing with the three branches shown in Fig. 5.3(a): $P-1^{(1)}$, $P-3$, and $P-1^{(2)}$. Basin \mathcal{A}_∞^1 (black) corresponding to the lowest amplitude solution $|q_1| = 0.4$ ($P-1^{(1)}$), consists of a compact central region (radius = 15, IF ≈ 0.57) surrounded by a larger region where \mathcal{A}_∞^1 and \mathcal{A}_∞^2 (grey), corresponding to $|q_1| = 1.6$ ($P-3$), are intermixed. The constraint basin \mathcal{C}_∞ (white), represents an amplitude of $|q_1| = 7.7$ ($P-1^{(2)}$) consists of a relatively small area and is not encountered until a radius of 46.8, corresponding to an integrity factor of IF = 1.78 as indicated by a comparison with the reference circle (dashed). The radius of the reference circle is 26.3, which is the normalization radius that will be determined from the results of the global analysis given in Section 5.3.

The trend throughout $B_{\omega > 1}$ is well represented by Fig. 5.4. It takes a much higher amount of energy than in $B_{\omega < 1}$ to transition the primary structure into a potentially harmful high amplitude response. Even in the event of a large impact, the primary oscillator would be more likely to settle to a safe, low amplitude response due to the

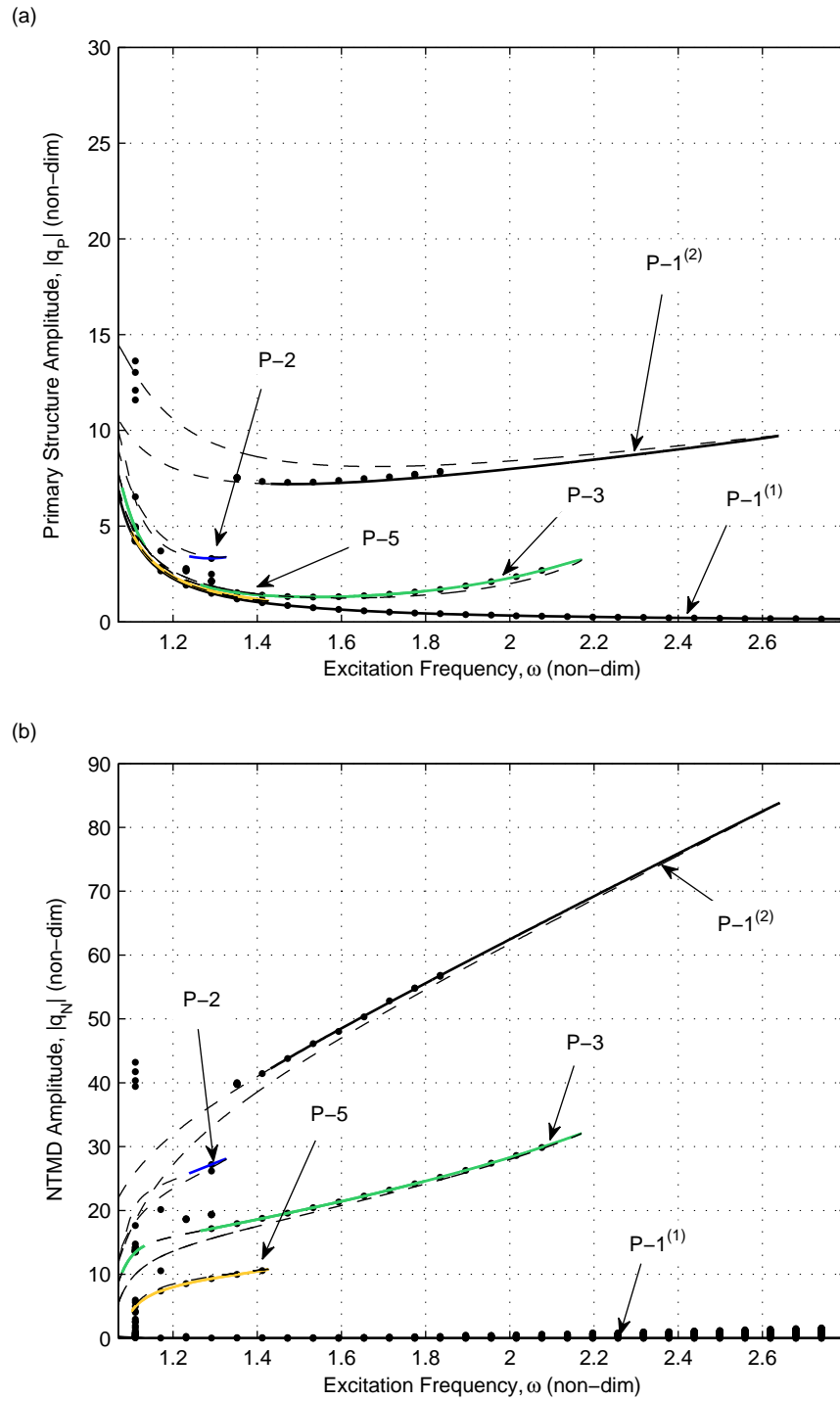


Figure 5.3: Frequency-response of (a) primary structure and (b) NTMD within $B_{\omega>1}$ using numerical continuation (solid/dashed) and numerical integration (\cdot); $\Omega = 0$, $\hat{\gamma}_N = 0.002$, $\Omega_N = 0.09$, $F = 0.35$, $\phi = 0$.

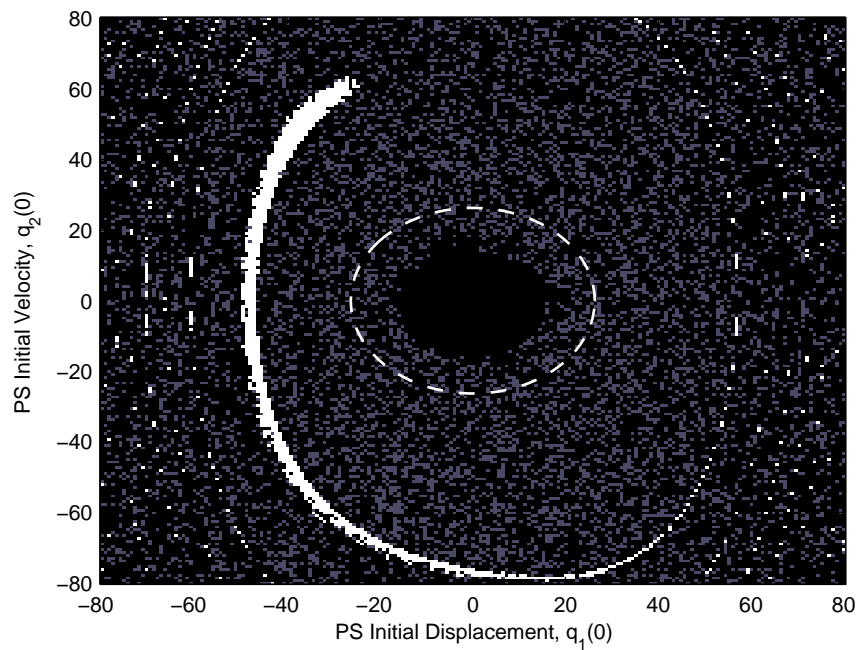


Figure 5.4: Characteristic Σ^{12} basin portrait for the $B_{\omega>1}$ region; $\omega = 1.8$, $\Omega = 0$, $\hat{\gamma}_N = 0.002$, $\Omega_N = 0.09$, $F = 0.35$, $\phi = 0$. Dashed circle is used for size reference, its radius equal to integrity measure normalization radius, $R = 26.3$.

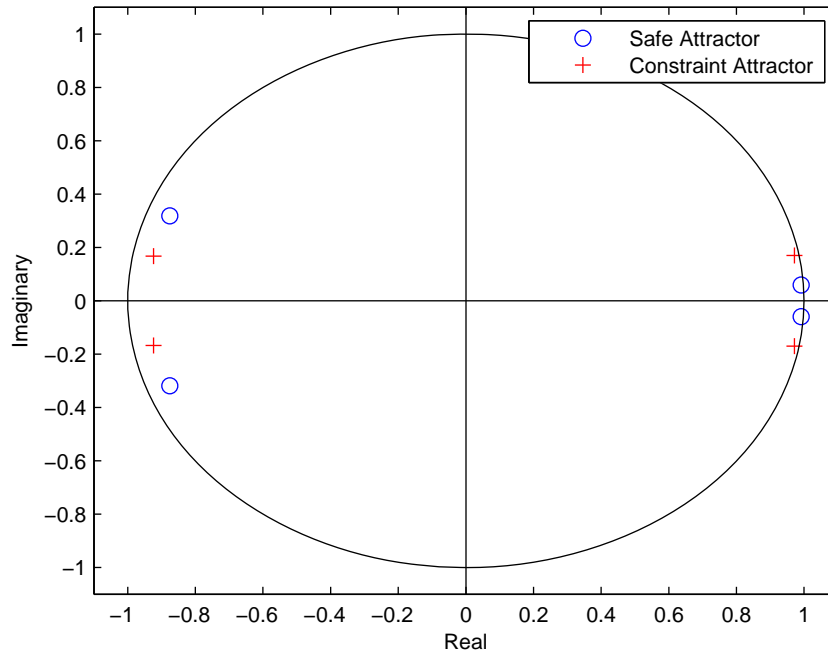


Figure 5.5: Location of the Floquet multipliers of the safe (\circ) and constraint ($+$) attractors in the complex plane, relative to the unit circle.

narrowness of the constraint basin. Similarly, if the primary oscillator were to settle to a high amplitude response, a small perturbation could return the system to the low amplitude state.

In order to identify the mechanism responsible for the high integrity of the safe attractor within the $B_{\omega>1}$ region, the results from a Floquet analysis are compared with phase portraits of the coexisting stable and unstable attractors. *Floquet analysis* is a numerical method where the response of the system to small perturbations from the periodic attractors is studied in order to determine the *Floquet multipliers*, quantitative measures of the local stability of the attractors. Details regarding Floquet theory and the analysis procedure can be found in nonlinear dynamics texts such as Ref. [57].

The results of a Floquet analysis of the stable attractors at $\omega = 1.8$ are illustrated in Fig. 5.5. The system parameters correspond to those from Figs. 5.3 and 5.4. All

Floquet multipliers of the safe (\circ) and constraint ($+$) attractors lie within the unit circle, indicating that the attractors are asymptotically stable. However, all multipliers are located near the unit circle, which indicates that the local stability of both the safe and constraint attractors is weak. Figure 5.6 illustrates the corresponding phase portraits of the (a) primary structure and (b) NTMD response, displaying both the stable (solid) and unstable (dashed) attractors. Note that the NTMD displacement and velocity of the safe attractor is near-zero and therefore is difficult to observe in Fig. 5.6(b). The phase portraits and the results of the Floquet analysis suggest the mechanism responsible for the high integrity of the safe attractor within the $B_{\omega>1}$ region. Although the Floquet analysis indicates that the *local* stability of the safe and constraint attractors is weak and of similar strength, the unstable solution is located in close proximity to the stable constraint attractor in phase space. The proximity of the unstable solution (a “repellor”) to the constraint attractor is believed to strongly influence the *global* stability of the safe attractor. A more thorough study of this behavior is reserved for future work.

5.3 Lower-Frequency Bi-Stable Region, $B_{\omega<1}$

The frequency-response of the system within $B_{\omega<1}$ is illustrated in Fig. 5.7. The axis limits in Fig. 5.7 correspond to the red dash-dot rectangle surrounding $B_{\omega<1}$ within Fig. 5.2. The two Period-1 solution branches originally introduced in Fig. 5.2, $P-1^{(1)}$ and $P-1^{(2)}$, are depicted here in black. Additionally, a set of detached higher-period solution branches are superimposed in color. Again, the black dots represent steady-state amplitudes obtained using numerical integration over a range of initial conditions in $q_1(0) \in [-200, 0]$, $q_i(0) = 0$ for $i = 2, 3, 4$ for each ω . By comparing the results obtained by numerical integration with those by continuation, we see that the majority of the solution branches have been identified with both methods. However,

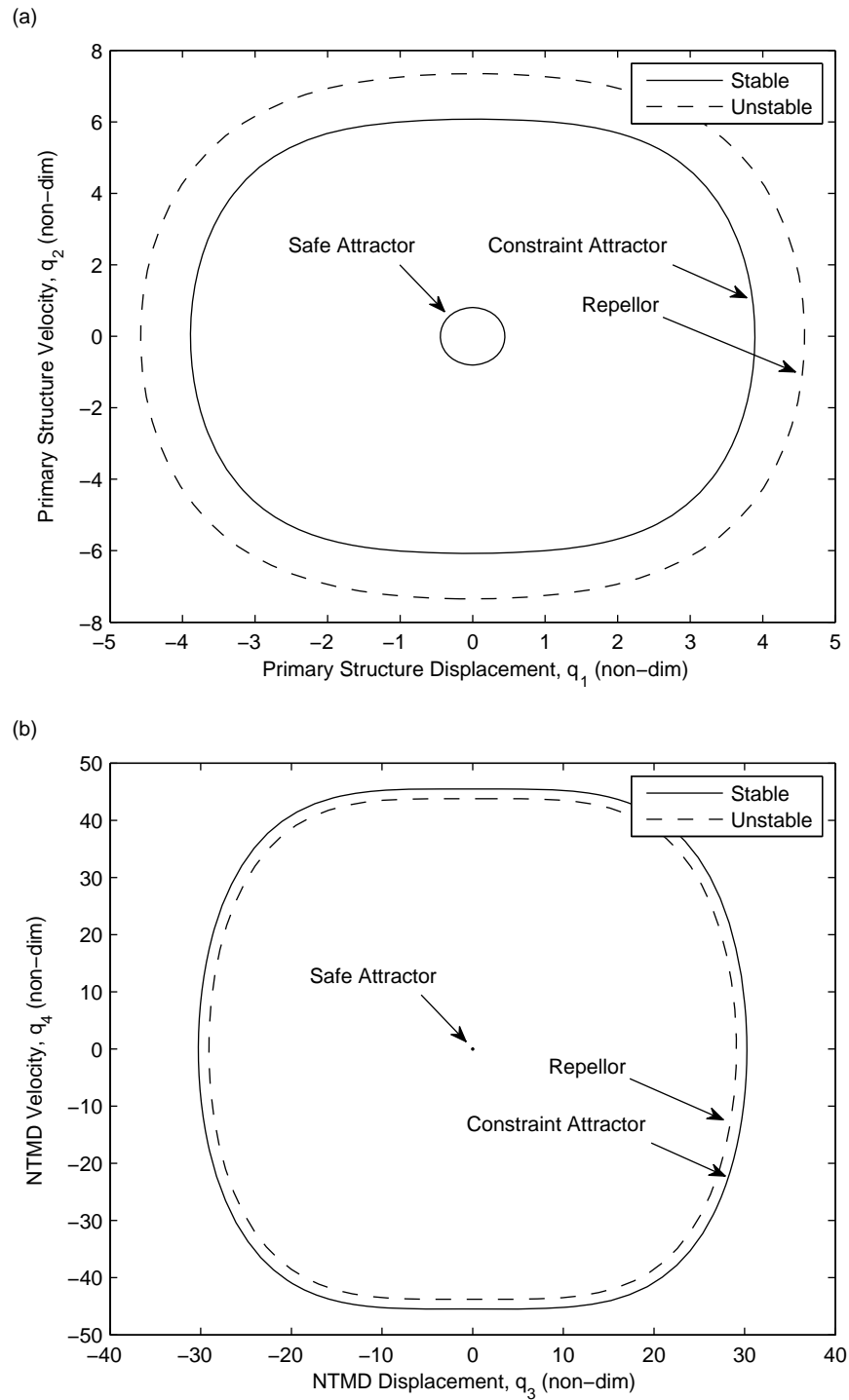


Figure 5.6: Phase portrait of the (a) primary structure and (b) NTMD response at $\omega = 1.8$ illustrating the stable (solid) and unstable (dashed) attractors.

certain branches could not be verified with the continuation methods due to their close proximity to other solutions, low stability, or other factors preventing numerical convergence.

While the higher-period branches do introduce a variety of new and interesting non-zero NTMD response amplitudes in this region, all primary structure amplitude values remain in the neighborhood of the original Period-1 branches, $P-1^{(1)}$ and $P-1^{(2)}$. Since the end goal is to attenuate the primary structure at the expense of NTMD motion anyway, the primary structure amplitude remains the focus, and therefore the distinct separation between the amplitude of the safe and constraint Period-1 branches is used to define the safe basin \mathcal{A}_∞ and conversely, the constraint basin \mathcal{C}_∞ . Within the global analysis, the safe basin is defined as,

$$\mathcal{A}_\infty := \{ \mathbf{q}^0 \mid |q_1|_{\mathbf{q}(0)=\mathbf{q}^0} \geq 1.5|q_1|_{\mathbf{q}(0)=\mathbf{0}} \}, \quad (5.1)$$

where \mathbf{q}^0 represents the vector of initial conditions and $\mathbf{0}$ represents the zero vector. Both automated and manual quality checks are also used to ensure that transient behavior has sufficiently decayed and that each point is added to the correct basin.

In order to calculate the erosion profiles for each of the four parameter value combinations $(\hat{\gamma}_N, \Omega)$, a series of 576 two-dimensional basin portraits are constructed using the PMDCM method. Based on the results of a convergence test, presented in Fig. 5.8, it is determined that a resolution of 101^2 is sufficient to estimate the value of each integrity measure within $\pm 1\%$ of its true value. Limits for the Σ^{12} and Σ^{34} portraits are set to $q_i^0 \in [-30, 30]$, $i = 1, 2$, and $q_i^0 \in [-60, 60]$, $i = 3, 4$, respectively, such that the range is large enough to capture the compact part of the safe basin for the lowest forcing cases.

Since each basin portrait displays a 2-D cross-section of a 4-D hyper-space, the particular choice of the two fixed IC values, (*i.e.* q_f^0 , $f \neq a, b$ in portrait Σ^{ab}) influences the portrait itself. In order to provide a general measure of integrity without the bias

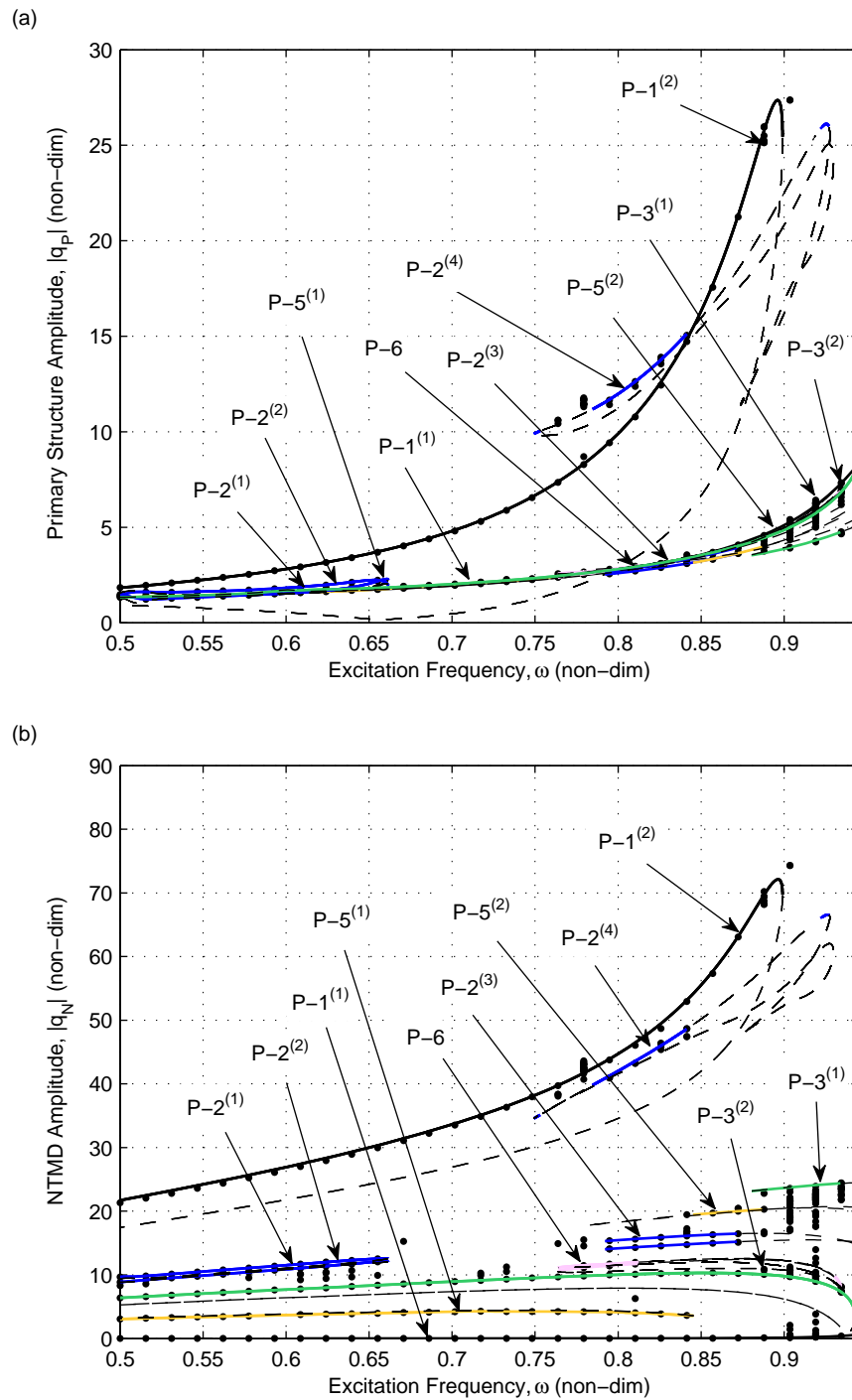


Figure 5.7: Frequency-response of (a) primary structure and (b) NTMD $B_{\omega < 1}$ using numerical continuation (solid/dashed) and numerical integration (\cdot); $\Omega = 0$, $\hat{\gamma}_N = 0.002$, $\Omega_N = 0.09$, $F = 0.35$, $\phi = 0$.

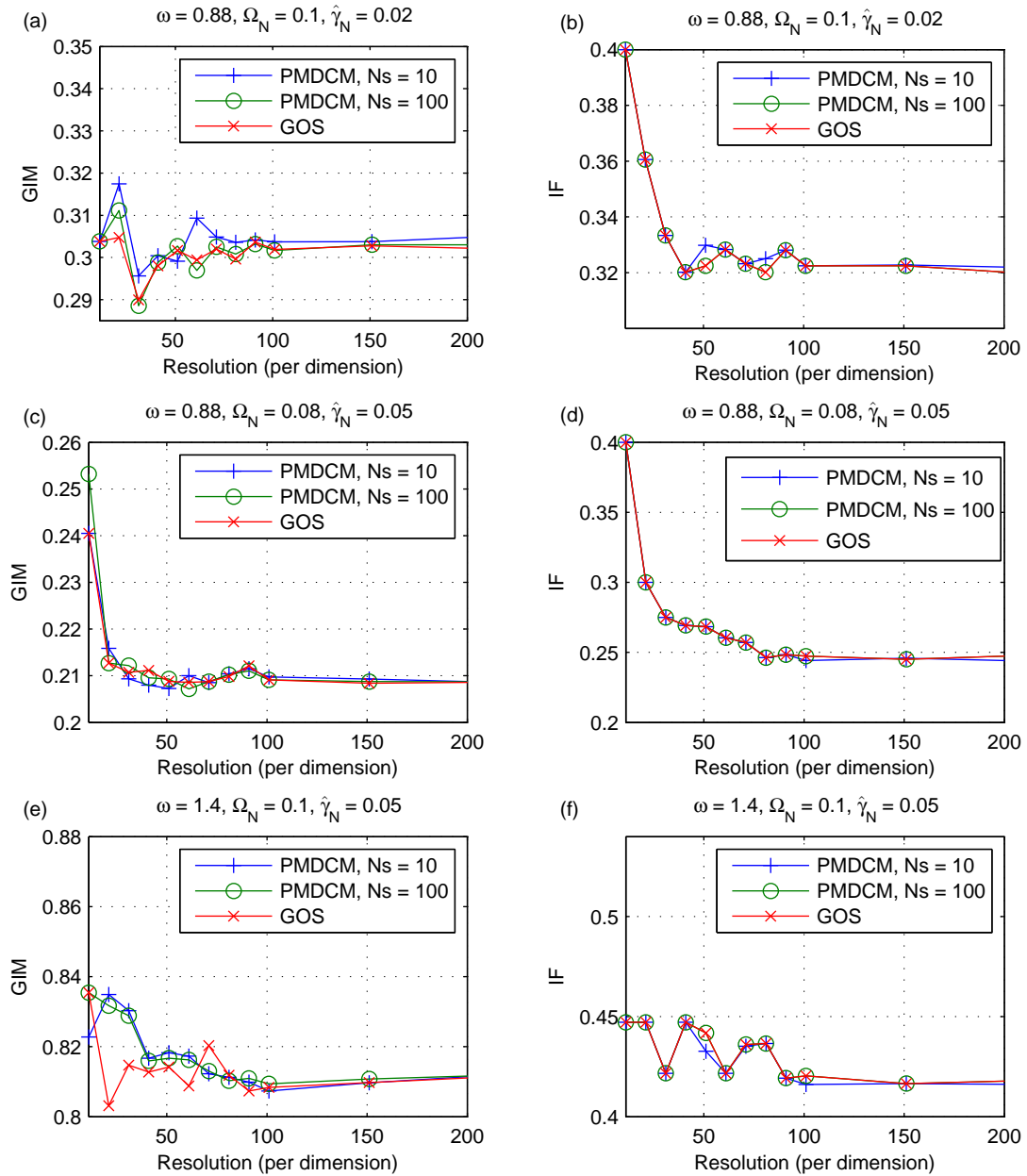


Figure 5.8: Convergence study illustrating key integrity measures versus resolution.

of defining the two fixed ICs at a specific point on a trajectory, the GIM and IF are calculated from basins with $q_f^0 = 0$. The LIM and IIM, on the other hand, specifically relate to the position of the attractor within the portrait and therefore meaningful values of these measures can only be calculated using portraits intersected by the safe attractor [100]. These measures are calculated in the present study by taking the minimum integrity values calculated from each of eight planes intersected by the low amplitude Period-1 attractor, evenly spaced over the period T at $\tau = 0, T/8, \dots, 7T/8$. All integrity measures represent the minimum value calculated from each of four phase offsets $\phi = \{0, \pi/2, \pi, 3\pi/2\}$ and two portrait planes Σ^{12} and Σ^{34} [100].

Figure 5.9 illustrates the characteristic basin portrait in the (a) Σ^{12} and (b) Σ^{34} planes. Black and white shading denotes the safe basin \mathcal{A}_∞ and the constraint basin \mathcal{C}_∞ , respectively. In this example, $\Omega = 0, \hat{\gamma}_N = 0.002, \Omega_N = 0.09, F = 0.35$ and $\phi = 0$. The basin portraits intersect the periodic attractor (*) at $\mathbf{q} = [-2.81, -3.63, 0.07, 0.09]$. The size of the smallest circle represents the LIM, with a radius drawn from the attractor to the closest point belonging to \mathcal{C}_∞ . Vertical dashed lines drawn between the attractor and the closest point in \mathcal{C}_∞ in the positive and negative directions illustrate the IIM^+ and IIM^- , respectively. The larger solid circle represents the IF, calculated by using the center of area of \mathcal{A}_∞ as an initial guess and using a numerical iterative method of enlarging and translating a circle until the space is filled. The dashed circle is for reference, its radius of 26.3 corresponding to the value used to normalize the integrity measures.

Figure 5.10(b) illustrates five response time series (i–v) corresponding to each of the initial conditions marked in the basin portrait presented in Fig. 5.10(a). Parameters for the basin portrait are identical to Fig. 5.9(a) with the exception of the phase offset, which here is $\phi = \pi/2$ in order to obtain more variation between basins on the $q_1(0)$ axis. The time series results verify the accuracy of the basin portrait

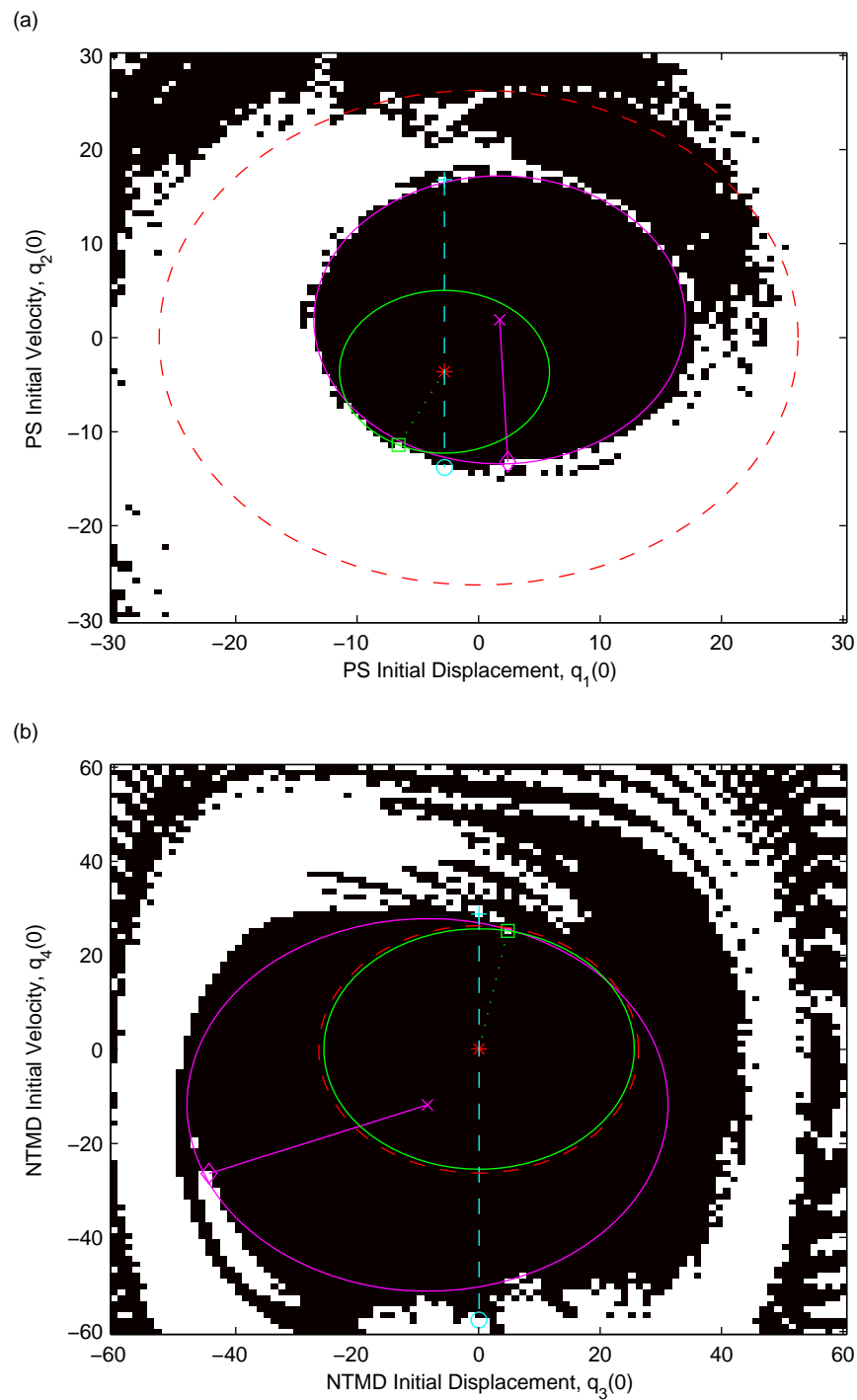


Figure 5.9: Characteristic basin portrait in the (a) Σ^{12} and (b) Σ^{34} planes illustrating the LIM, IF and IIM^\pm integrity measures. Dashed circle is used for size reference, its radius equal to integrity measure normalization radius, $R = 26.3$.

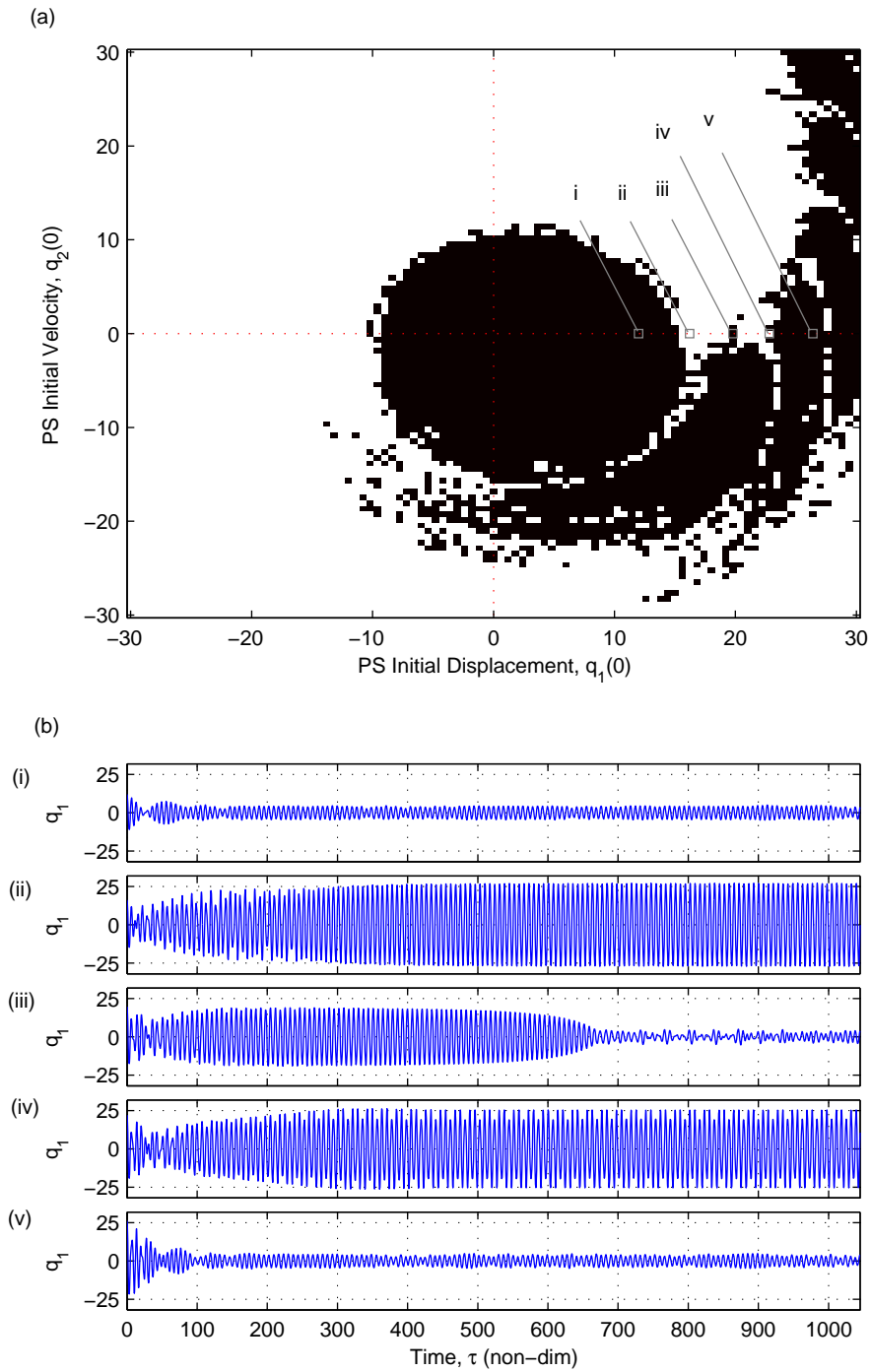


Figure 5.10: (a) Basin portrait and (b) corresponding q_1 time series at five points (i-v); $\Omega = 0$, $\hat{\gamma}_N = 0.002$, $\Omega_N = 0.09$, $F = 0.41$, $\phi = \pi/2$.

constructed using the PMDCM method, and help to better illustrate the transient behavior.

Given the four parameter combinations $(\hat{\gamma}_N, \Omega)$, two frequencies ω_m and ω_p , four phase offsets ϕ , two portrait planes Σ and nine fixed parameter combinations (including zero plus eight trajectory intersection points), a total of 576 basin portraits are constructed. Since each basin portrait represents the steady state behavior resulting from 101^2 different initial conditions, the erosion profiles effectively summarize the behavior of over 5.9×10^6 possible response trajectories.

The erosion profiles summarizing the results of the global analysis are presented in Fig. 5.11. Each row corresponds to one of the four integrity measures versus excitation magnitude parameter F . Zero damping and $\hat{\gamma}_N = 0.002$ are denoted by (\circ) and $(+)$, and zero linear stiffness and $\Omega = 0.1$ by solid and dashed lines, respectively. The normalization radius is $R = 26.3$, selected such that the largest IF value is unity. As expected, the integrity steadily decreases as the excitation magnitude increases. For excitation parameter values $F > 0.85$ all integrity measures are approximately zero, indicating that the system will always converge to the high amplitude constraint solution.

The first conclusion regarding the erosion profiles is that the two configurations with zero damping consistently exhibit 20–40% higher integrity than those with a small amount of damping. In addition, the zero-damping configurations maintain positive integrity for 25–45% larger excitation magnitude than the corresponding non-zero configurations. This indicates that when the NTMD is undamped, the primary oscillator is more likely to exhibit a low amplitude response and is more robust to impact loads. While it is impossible to truly obtain zero damping in a real-world design, it is recommended that the nonlinear absorber damping be as close to zero as possible to attain the best integrity.

Secondly, the small linear stiffness coefficient $\Omega = 0.1$ introduces no significant

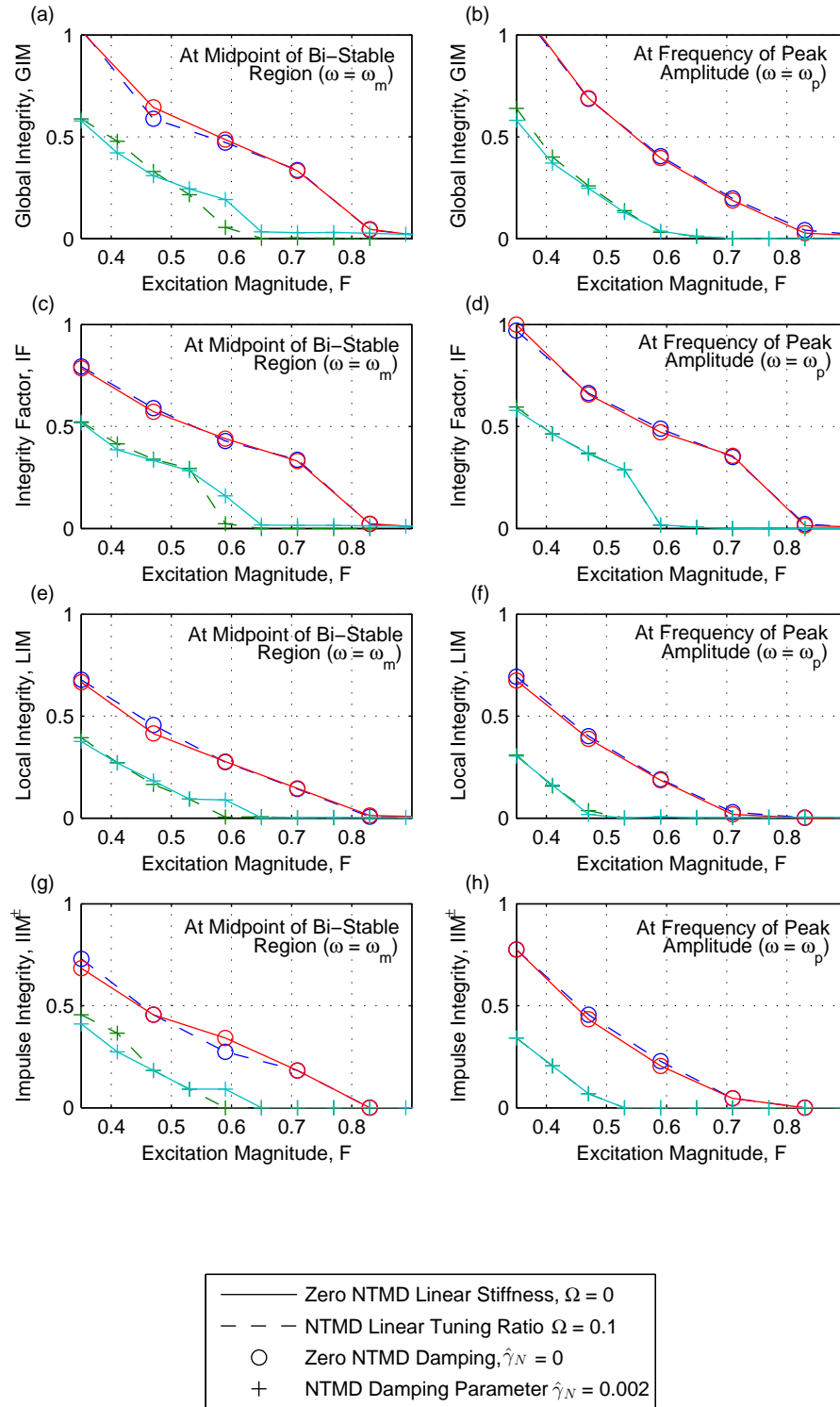


Figure 5.11: Erosion profiles illustrating the four integrity measures versus excitation magnitude at the frequencies corresponding to the midpoint and peak of $B_{\omega < 1}$.

change to the erosion profiles, as illustrated by comparing the dashed and solid lines in Fig. 5.11. Although the linear stiffness component may adversely affect other performance considerations such as transient behavior, the present study finds no evidence that a small linear stiffness component will affect the system integrity. Therefore, if a small linear stiffness component produces other favorable response characteristics, it can be added to the system without significantly impacting the integrity.

By comparing erosion profiles between the midpoint ω_m and peak ω_p of $B_{\omega < 1}$ using the GIM and IF integrity measures, we note that the integrity is consistently higher at ω_p . This observation seems to validate the intuition that because a larger separation exists between the amplitudes of the safe and constraint solutions at ω_p than at ω_m , reaching the constraint solution would require more energy and therefore the integrity would be higher at ω_p . However, examining the LIM and IIM $^\pm$ integrity measures, we observe the opposite trend—that the integrity is lower ($\hat{\gamma}_N = 0.002$) or at best unchanged ($\hat{\gamma}_N = 0$) for ω_p when compared with ω_m . These results indicate that although both the total hyper-volume and the size of the compact center of the safe basin increase as the frequency increases from ω_m to ω_p , the trajectory of the safe attractor moves no farther away from the constraint basin boundary. Therefore, the safe solution of the system is no more robust to perturbations at the most potentially harmful frequency ω_p than at ω_m .

Perhaps the most unexpected observation is that the safe basin integrity is completely eliminated in all four cases for $F > 0.85$. By examining the various frequency-response profiles, we see that the complete loss of integrity correlates with a bifurcation initiating at the peak of the constraint solution, as illustrated in Fig. 5.12. In this bifurcation, the original constraint solution $P-1^{(2)}$ becomes unstable, but simultaneously another stable constraint solution $P-1^{(3)}$ is created. The stability change and existence of an additional stable branch in this region was also identified by [59], but the implications of this new branch on the global dynamics were not studied. Even

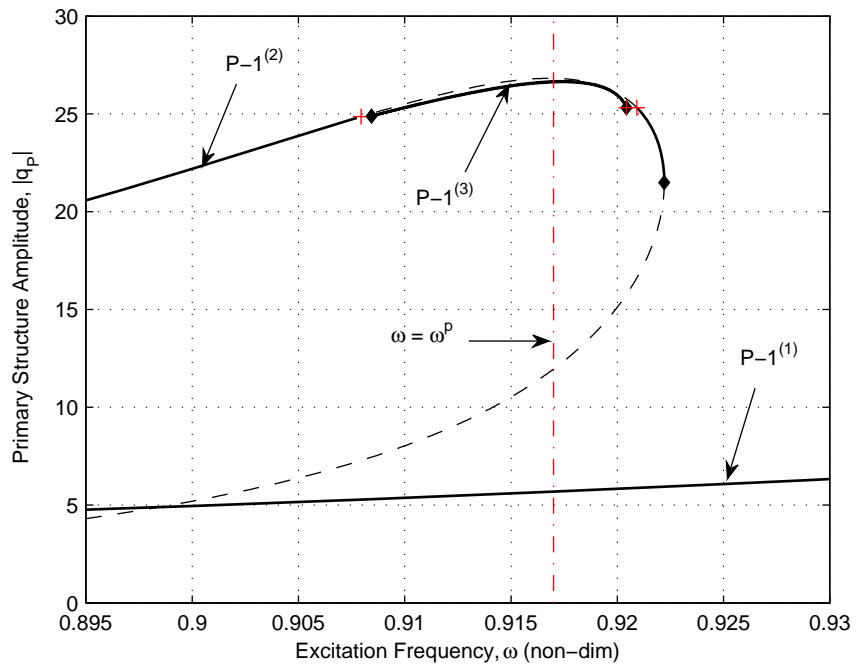


Figure 5.12: Appearance of a new stable Period-1 (P-1) solution which acts as a strong attractor; $\Omega = 0$, $\hat{\gamma}_N = 0.002$, $\Omega_N = 0.09$, $F = 0.65$. Limit point (\diamond) and branch point (+) bifurcation points are marked.

though the original safe solution $P-1^{(1)}$ is still present and stable, the new constraint solution is a strong attractor to which all initial conditions converge.

As a final note, recall from the higher-period curves identified in Figs. 5.3 and 5.7 that the PN system is capable of exhibiting a Period-3 response, which is a characteristic of systems that are capable of exhibiting chaotic behavior. Although the intent of the present study has been fulfilled, further evidence of chaotic response behavior in the PN system will be shared with the intention of motivating further investigations.

The distance between two trajectories initially separated by $d = 1 \times 10^{-10}$ is plotted as a function of time in Fig. 5.13(a). Parameter values are chosen to correspond to conditions where chaos-like behavior is observed by using $\omega = 1.1$, $\mathbf{q}^0 = [34, 0, 0, 0]$, $\gamma_N = 0.05$, $\Omega = 0.1$, $\Omega_N = 0.1$, $F = 0.35$. The plot illustrates a textbook example of exponential divergence followed by eventual saturation at $\tau \approx 250$. The largest Lyapunov exponent is positive, displayed adjacent to the curve. Both are known characteristics of chaotic systems [57].

By examining the value of the largest Lyapunov exponent λ versus the primary structure initial condition q_1^0 in Fig. 5.13(b), it is observed that in the central region of the basin—for low q_1^0 values—the Lyapunov exponent is negative, indicating the absence of chaotic behavior. Above some threshold value however, in this case $q_1^0 \geq 29$, λ becomes positive. Therefore, for larger values of initial energy, it is important to consider that the present system is capable of exhibiting chaotic behavior. Chaotic behavior has been identified in a system consisting of a linear oscillator and a *grounded* essentially nonlinear absorber [48, 62], but to the knowledge of the author it has not been identified in a system with an ungrounded NTMD.

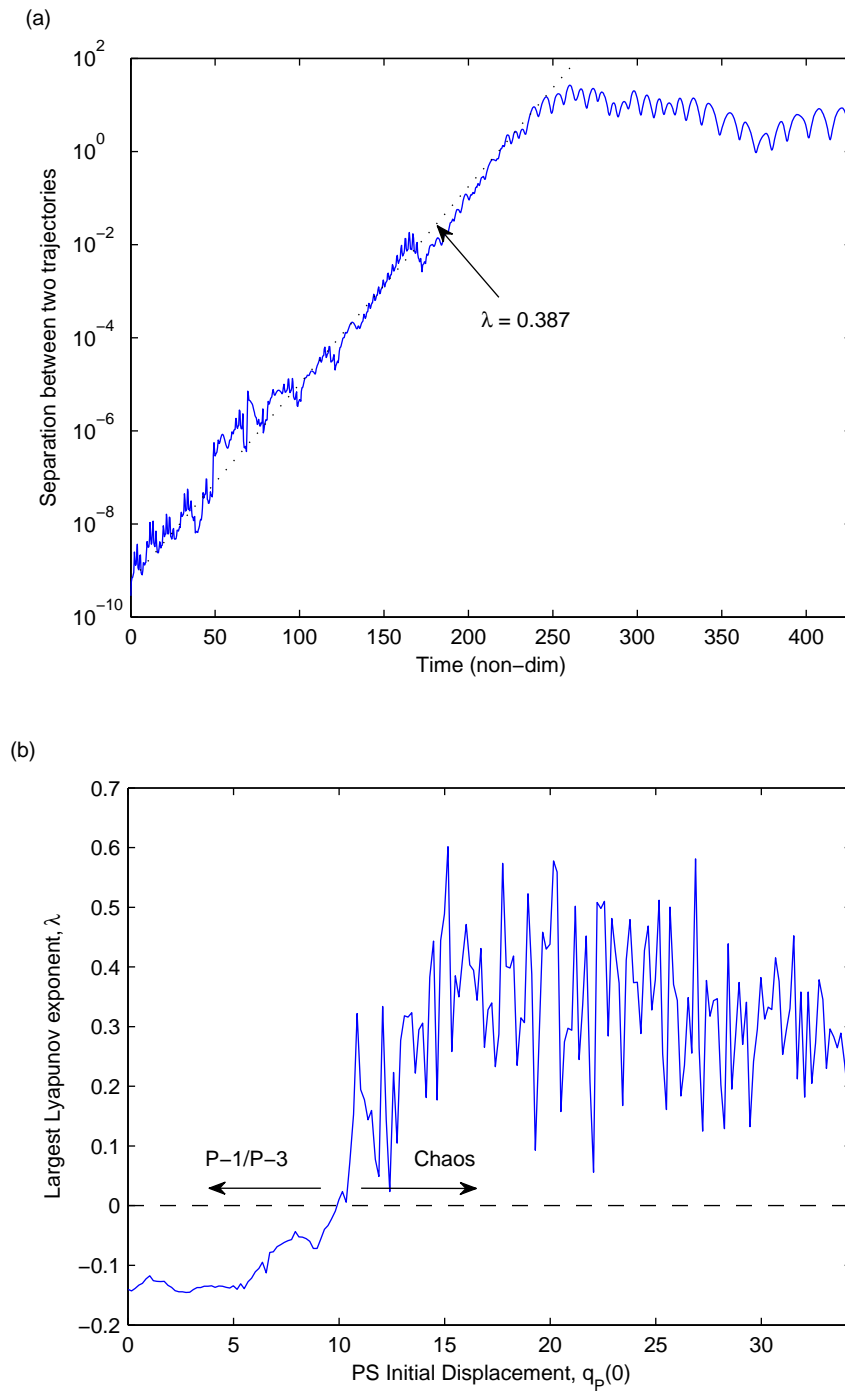


Figure 5.13: (a) Separation between two nearby trajectories versus time and (b) largest Lyapunov exponent versus initial position of primary oscillator, $q_i = 0$ for $i = 2, 3, 4$.

5.4 Series STMD System Performance

In this section, the performance of the three degrees-of-freedom system consisting of the primary structure, NTMD, and STMD (the PNS system) is compared with the performance of the reference system (the PN system) presented in Sections 5.2 and 5.3. These results will illustrate the benefit of adding the small STMD component to the strongly nonlinear system.

Figures. 5.14, 5.15, and 5.16 illustrate the frequency-response of the primary structure, NTMD, and STMD, respectively, for the PNS system at six STMD mass ratio values in increasing orders of magnitude from $\epsilon_S = 1 \times 10^{-7}$ (panel (a), 0.00001% of the mass of the PS) to $\epsilon_S = 1 \times 10^{-2}$ (panel (f), 1% of the mass of the PS). System parameter values are: $\Omega = 0$, $\hat{\gamma}_N = 0.002$, $\Omega_N = 0.09$, $F = 0.35$, $\hat{\gamma}_S = 0.02$, allowing for direct comparison with the response of the PN system presented in Figs. 5.2, 5.3, and 5.7. Again, stable and unstable Period-1 solutions are denoted by solid and dashed curves, respectively. Note that the range of the dependent axis in Fig. 5.16 is modified to account for the large variation in response magnitude between panels.

The effect of the STMD is subtle at the smallest mass ratio, $\epsilon_S = 1 \times 10^{-7}$, decreasing the range of the $B_{\omega>1}$ region as shown in Fig. 5.14(a). At increasing orders of magnitude of ϵ_S , panels (b)–(d), the range of the $B_{\omega>1}$ region continues to decrease along with the peak response magnitude within the $B_{\omega<1}$ region. At a value of $\epsilon_S = 1 \times 10^{-3}$ and larger, panels (e) and (f), both bi-stable regions have been eliminated. At the highest value shown: $\epsilon_S = 1 \times 10^{-2}$, panel (f), the response is qualitatively similar to that of the primary structure with no absorbers.

The results presented in Figs. 5.14, 5.15, and 5.16 indicate that by using an STMD with a mass of 0.1% that of the primary structure ($\epsilon_S = 1 \times 10^{-3}$), the primary structure will exhibit a simple and predictable response. Away from the primary resonance, ($\omega \leq 0.9$ and $\omega \geq 1.1$) the primary structure response amplitude matches that of the safe, low amplitude Period-1 attractor observed in the PN system. To

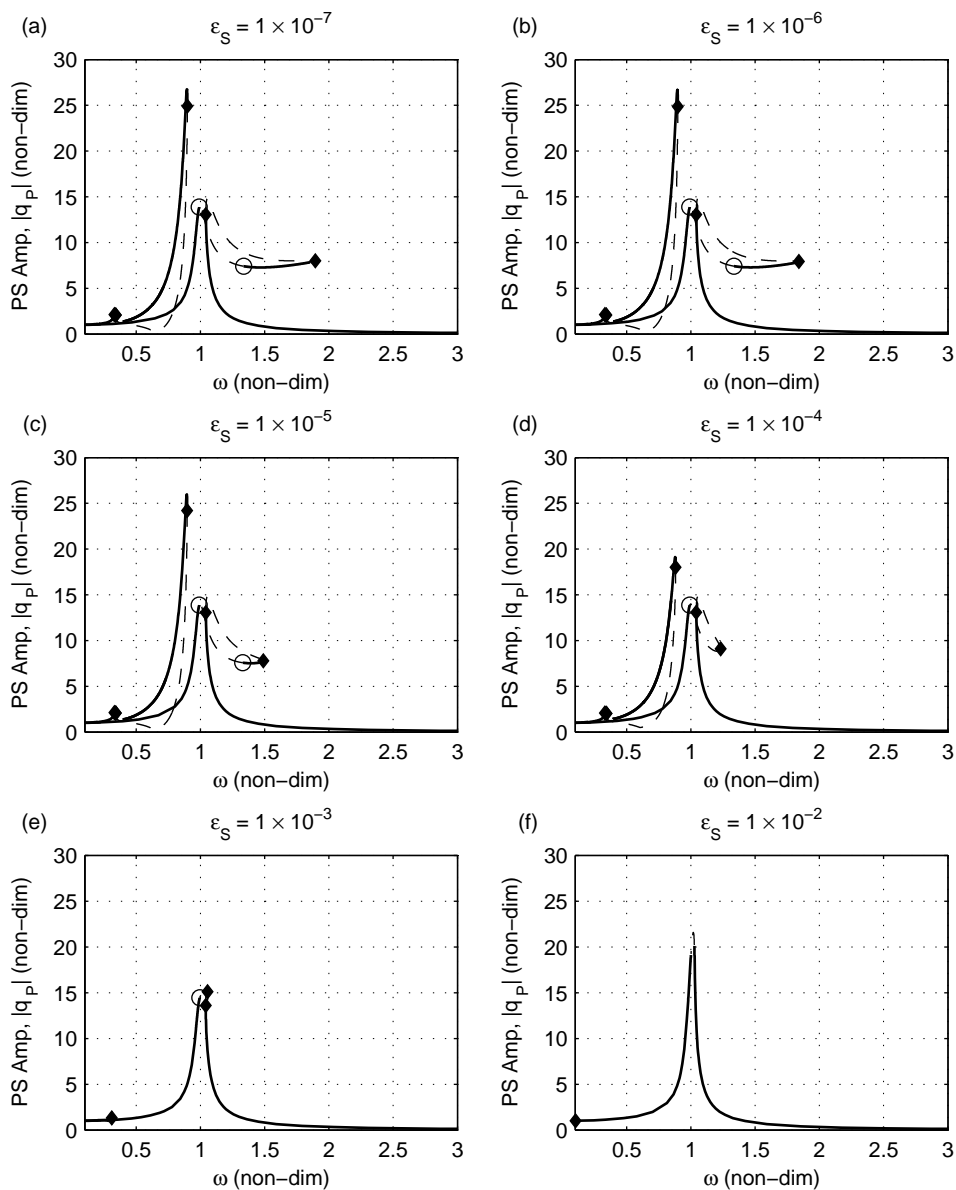


Figure 5.14: Frequency-response of the primary structure within the PNS system at six STMD mass ratio values as labeled in (a)–(e); $\Omega = 0$, $\hat{\gamma}_N = 0.002$, $\Omega_N = 0.09$, $F = 0.35$, $\phi = 0$. Limit point (\diamond) and torus (\circ) bifurcation points are marked.

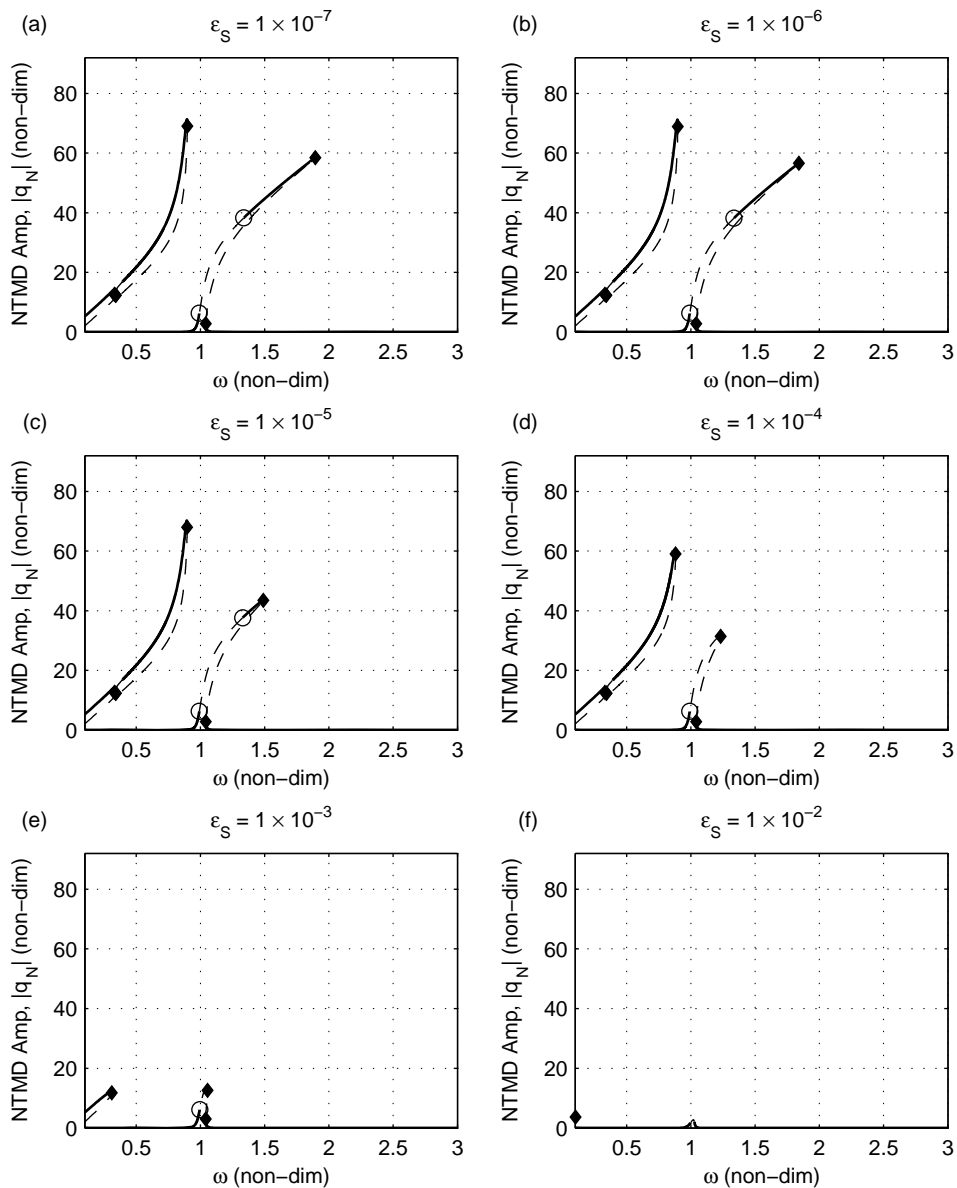


Figure 5.15: Frequency-response of the NTMD within the PNS system at six STMD mass ratio values as labeled in (a)–(e); $\Omega = 0$, $\hat{\gamma}_N = 0.002$, $\Omega_N = 0.09$, $F = 0.35$, $\phi = 0$. Limit point (\diamond) and torus (\circ) bifurcation points are marked.

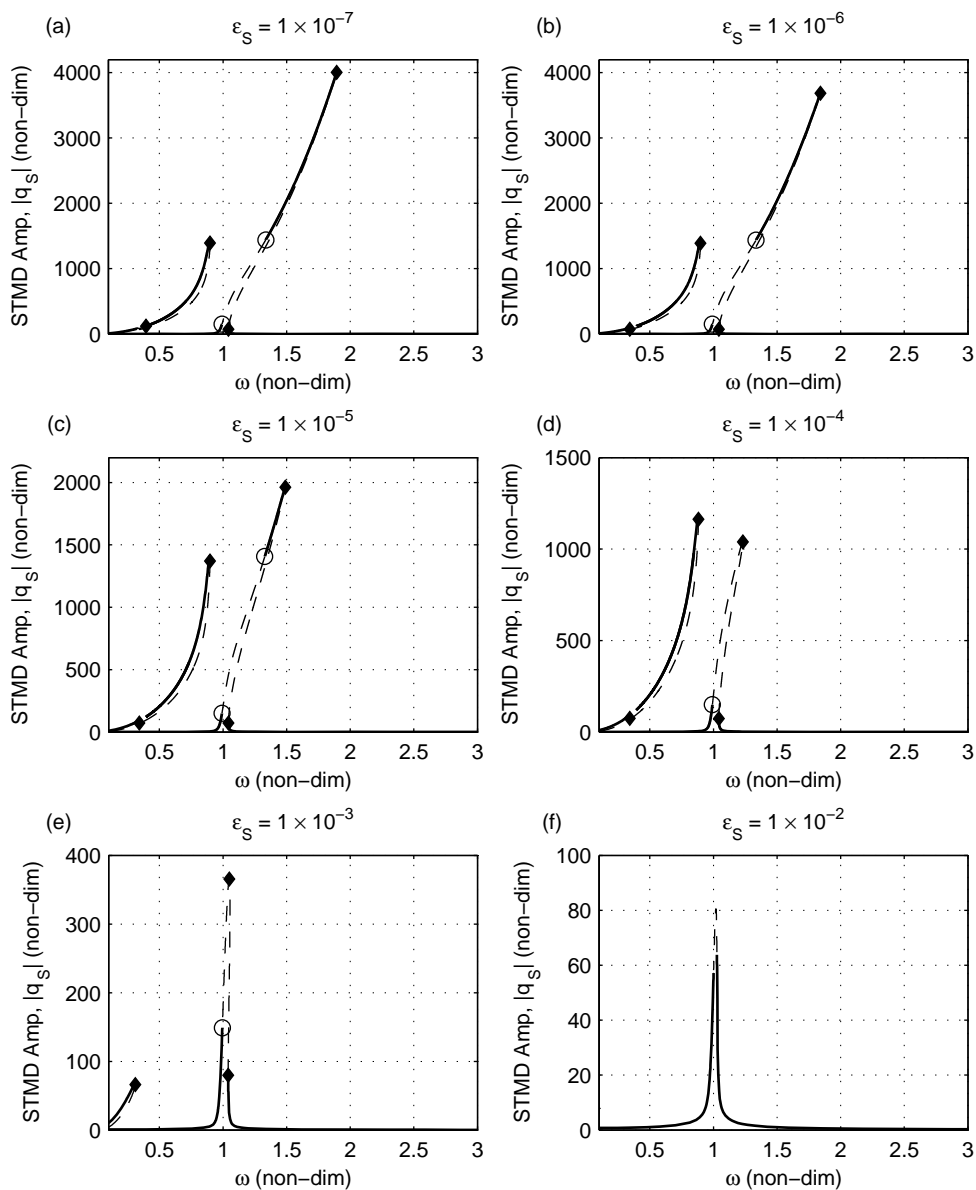


Figure 5.16: Frequency-response of the STMD within the PNS system at six STMD mass ratio values as labeled in (a)–(e); $\Omega = 0$, $\hat{\gamma}_N = 0.002$, $\Omega_N = 0.09$, $F = 0.35$, $\phi = 0$. Limit point (\diamond) and torus (\circ) bifurcation points are marked.

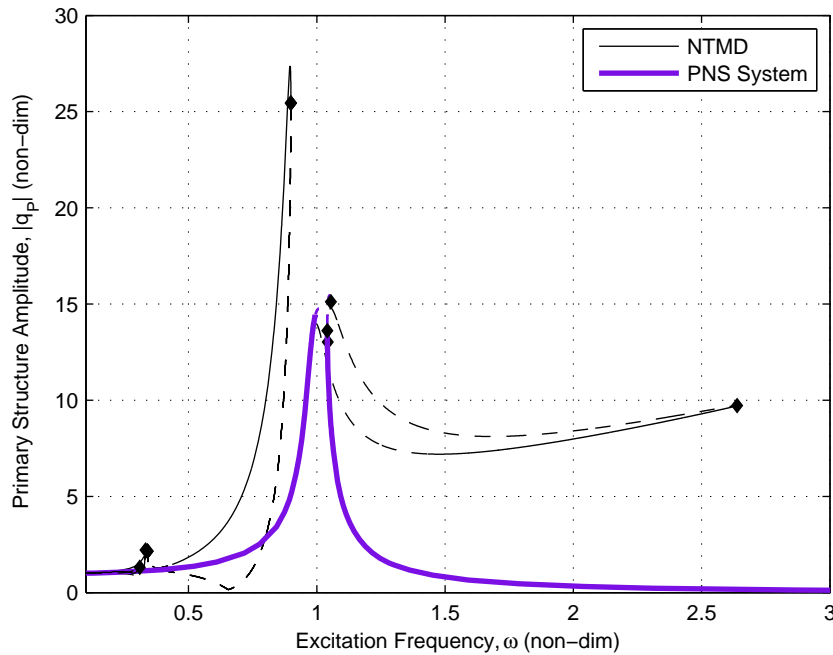


Figure 5.17: Frequency-response of the PN system (thin) and of the PNS system with $\epsilon_S = 1 \times 10^{-3}$ (thick); $\Omega = 0$, $\hat{\gamma}_N = 0.002$, $\Omega_N = 0.09$, $F = 0.35$, $\phi = 0$.

more clearly illustrate the performance benefits of the series STMD, Fig. 5.17 displays the response of the PNS system with $\epsilon_S = 1 \times 10^{-3}$ superimposed with the response of the PN system.

Based in the results presented in Figs. 5.14–5.16, it is also noted that since the effect of the STMD is to reduce the motion of the NTMD, a negative consequence resulting from large values of the STMD mass ratio is that response amplitudes in the neighborhood of the primary resonance are increased. On the other hand, smaller STMD mass ratios require a larger operating range. An STMD mass ratio which achieves a balance between these two considerations is therefore preferable.

Figure 5.18 is a bifurcation diagram presented to more clearly illustrate the transition from a state where multiple coexisting solutions are present to a state containing only a single solution, as the STMD mass ratio ϵ_S is increased. The results correspond to a frequency of $\omega = 0.85$, which is close to the peak amplitude but not high

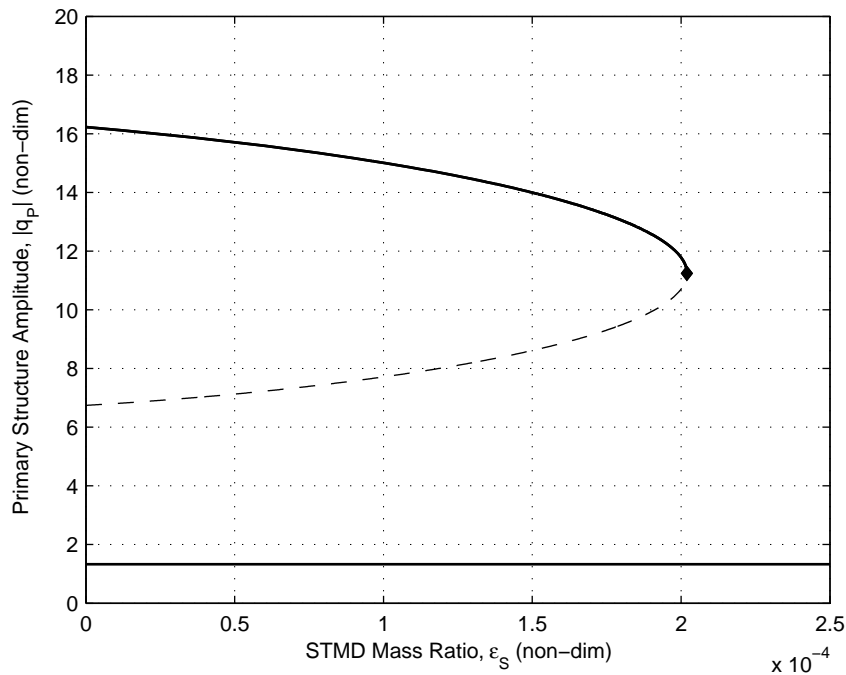


Figure 5.18: Bifurcation diagram illustrating the disappearance of the high amplitude solution at an STMD mass ratio of $\epsilon_S = 2 \times 10^{-4}$, at a frequency of $\omega = 0.85$.

enough to fall outside the upper boundary of the region due to a shift in the range of $B_{\omega < 1}$ corresponding to the parameter changes. The amplitudes of the high and low solutions match the results presented in Fig. 5.14. A limit point bifurcation at $\epsilon_S = 2 \times 10^{-4}$ corresponds to the disappearance of the high amplitude solution, indicating the smallest mass ratio value that can completely eliminate the constraint attractor. In particular, the bifurcation diagram helps to verify that the high amplitude solution is eliminated for larger ϵ_S values, rather than missed by the numerical techniques.

As discussed in Chapter 1, a more complete dynamic analysis requires identification of the type and magnitude of all existing solutions (attractors) as well as the distribution of the basins corresponding to each attractor. Considering the PNS system, the former was accomplished in Figs. 5.14–5.18. The latter is now presented in Fig. 5.19, which illustrates two-dimensional cross-sections of the basins of attraction

of the primary structure at various values of the STMD mass ratio. The layout is organized such that the system parameter values are the same between corresponding panels in Fig. 5.19 and Figs. 5.14–5.16, allowing for a direct comparison. Also, recall that the basin portrait for the PN system illustrated in Fig. 5.9(a) uses the same primary structure and NTMD parameter values. In the present figure, a higher resolution of 201^2 is used in order to provide sufficient clarity to observe any subtle changes that may occur. The phase portraits of each attractor (solid) are superimposed on the basin portraits in Fig. 5.19 in place of the integrity measures used in Fig. 5.9, which better illustrates the disappearance of the high amplitude solution.

Although a small decrease in PS response amplitude is observed with increasing STMD mass ratio from 1×10^{-7} to 1×10^{-5} , negligible change is observed in the basin portraits, indicating that while the STMD does have a small influence on the amplitude of the response in this region, it does not influence the relative strength of each attractor. A key observation from Fig. 5.19 is that the significant increase in system integrity occurs between $\epsilon_S = 1 \times 10^{-5}$ and 1×10^{-4} . Subsequent simulation results (not shown) refine the estimate of the transition point to be $\epsilon_S = 5 \times 10^{-5}$, an order of magnitude lower than the mass ratio needed to completely eliminate the solution, as indicated by Fig. 5.18. This demonstrates that while a mass ratio value of $\epsilon_S > 2 \times 10^{-4}$ is necessary to eliminate the existence of the high amplitude $B_{\omega < 1}$ solution, a value as small as $\epsilon_S = 5 \times 10^{-5}$ can increase the relative strength of the low amplitude attractor enough that the primary structure is not likely to exhibit the high amplitude response under reasonable operating conditions.

The results presented in this section have demonstrated that the STMD can effectively reduce the response amplitude of the NTMD, decreasing the effective nonlinearity and eliminating the high amplitude solution branch observed in the PN system response. It is understood, however, that the motivation behind designing an absorber with a strong cubic nonlinearity is that under certain conditions the absorber

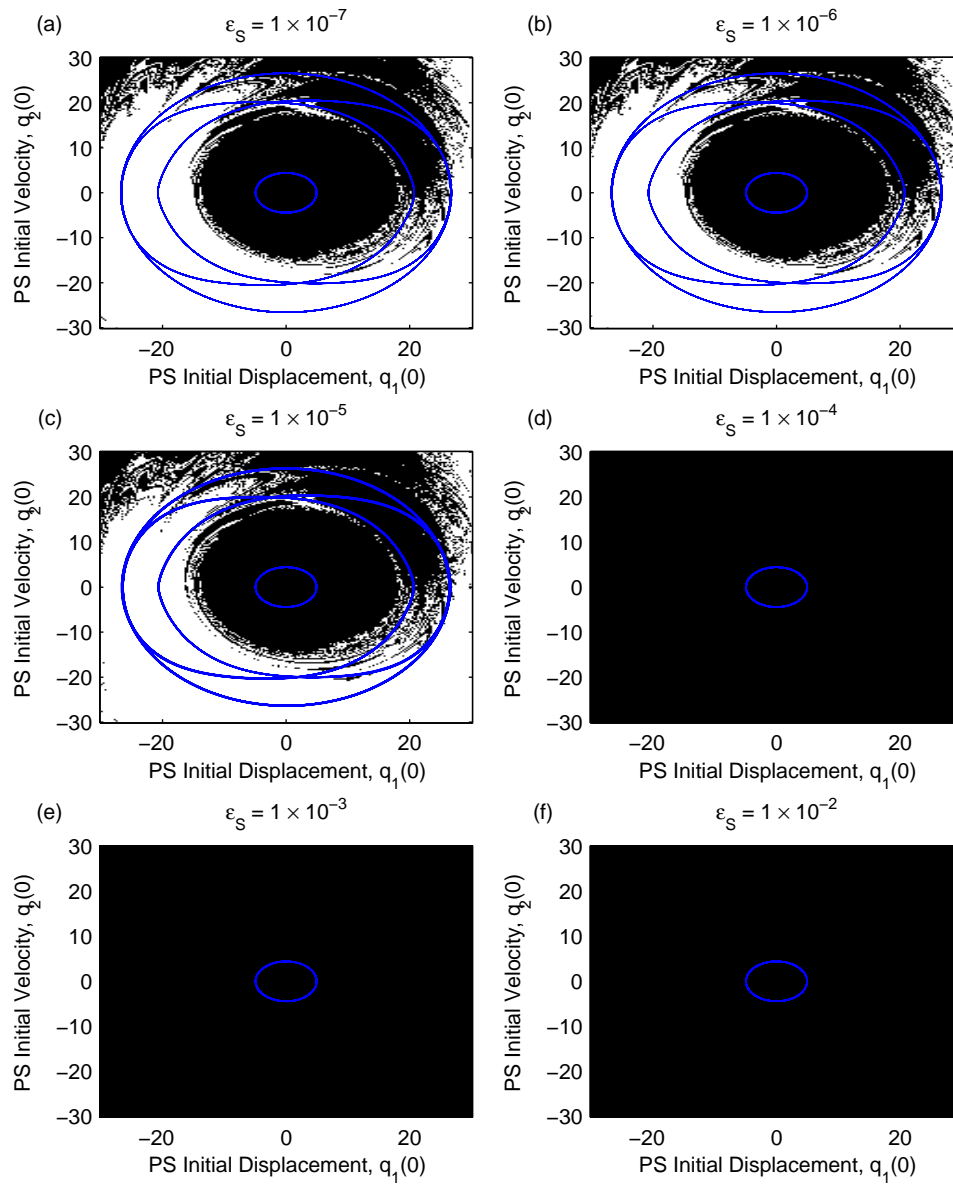


Figure 5.19: Basin of attraction versus the primary structure initial position and velocity for the series STMD system with $\epsilon_S =$ (a) 1×10^{-6} , (b) 1×10^{-5} , (c) 1×10^{-4} , (d) 1×10^{-3} , (e) 1×10^{-2} and (f) 1×10^{-1} , $\Omega = 0$. Phase portraits for the low and high amplitude solutions are illustrated in grey.

is capable of energy pumping—irreversible wide-band energy transfer from the primary structure to NTMD. The use of an STMD to limit the motion of an NTMD and minimize the effects of the nonlinearity under *all* conditions would therefore be impractical, resulting in an unnecessarily complicated system from which no better performance could be expected than by using a simple TMD.

Considering both the unique attenuation characteristics of the NTMD under certain conditions and the complex and potentially dangerous response that can exist under alternate conditions, the intended application of the STMD is to be used as a safety device which can be activated and deactivated as necessary. Deactivating the STMD, in the proposed context, refers to restricting the displacement of the STMD relative to the NTMD such that the NTMD and STMD act as a single mass. This can be accomplished by a number of mechanisms, for example by using actuators to physically hold and release the SMTD, or by tuning the stiffness of the STMD to a large enough value such that its natural frequency is significantly higher than the excitation frequency and any anticipated harmonics of the system.

Figures 5.20 and 5.21 demonstrate the capability of the series STMD absorber to act as an added protective device against unwanted transitions into the high amplitude response regime. At all times, the total mass ratio of absorbers in the system $\epsilon_N + \epsilon_S = 0.1$, or 10% of the primary structure. By instantaneously changing the dynamic model between a two-DOF PN system with $\epsilon_N = 0.1$ and a three-DOF PNS system with $\epsilon_N = 0.09$ and $\epsilon_S = 0.01$ —using the state of the NTMD to define the initial conditions for the STMD, the numerical model emulates the performance within the proposed application. The former model represents the case where the STMD is deactivated, fixed to the NTMD (denoted as “STMD OFF”). In the latter model, the STMD is activated, free to move independently of the NTMD (denoted as “STMD ON”).

In Fig. 5.20, the time response of the system with the STMD OFF is compared to that with the STMD ON as a shock of magnitude $F_{Sh} = 11$ is superimposed with

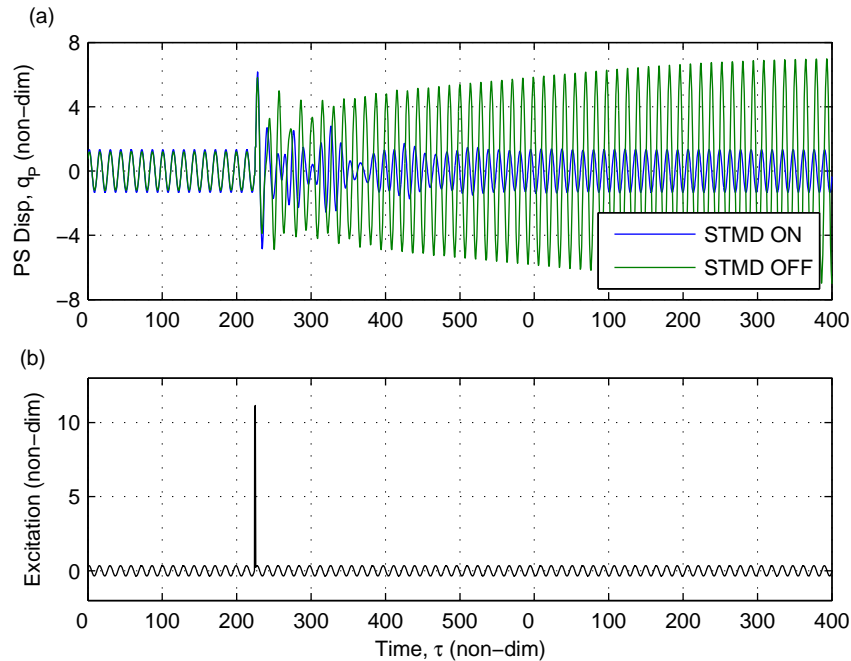


Figure 5.20: Primary structure response (a) and excitation (b) versus time with STMD deactivated (blue) and STMD activated (green) as an impulse-like force is applied to the structure.

the harmonic force of magnitude $F = 0.35$. It is observed that when the STMD is activated, the system recovers from the shock and returns to the low amplitude solution branch while the system with STMD OFF transitions to the high amplitude solution. In Fig. 5.21, the primary structure is initially exhibiting a high amplitude solution with the STMD OFF. When the STMD is released (STMD ON), the primary structure promptly transitions to the low amplitude solution. This demonstration illustrates the potential of the STMD as a protective device for a NES, the motivation for the proposed research for the strong nonlinearity problem.

5.5 Summary of Results

In this Chapter, the dynamic behavior and integrity of the two-DOF system consisting of the primary structure and NTMD (the PN system) was compared with that

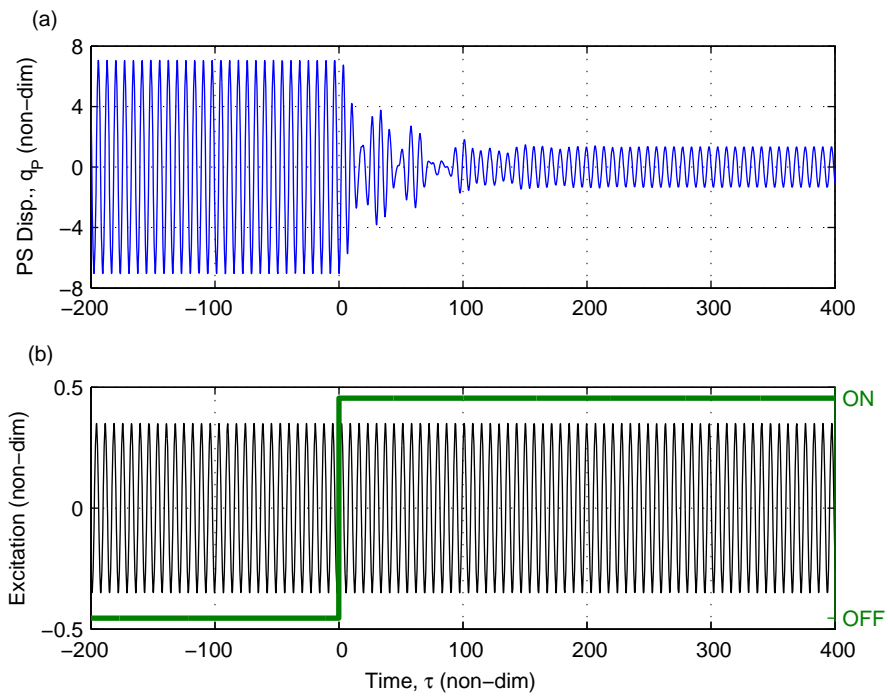


Figure 5.21: Primary structure response (a) and excitation (b) versus time illustrating a high-to-low amplitude transition corresponding to a change between STMD deactivated (OFF) and STMD activated (ON).

of the three-DOF system in which an additional STMD component is added in series (the PNS system). Here, the cubic stiffness nonlinearity in the NTMD is “strong”, meaning that the parameter values are similar to those that would be used to achieve energy pumping. A series of initial numerical simulations were used to determine the regions of parameter space within which the system behavior met two criteria: (1) multiple stable solutions coexist within the range of expected operating conditions and (2) the NTMD outperforms an optimally tuned linear TMD based on one or more performance measures. Based on the results from these initial simulations in addition to frequency-response curves constructed using continuation techniques, four combinations of system parameter values corresponding to two NTMD damping values and two linear frequency ratio values were selected for the global analysis of the PN system.

The global analysis of the PN system presented in Sections 5.2 and 5.3 accomplishes what Gendelman, a key author in the field, identified as a much-needed study in his recent review of nonlinear absorbers [40]. A total of 576 basin portraits were constructed by using the parallelized multi-degrees-of-freedom cell mapping method (PMDCM) to map over 5.9×10^6 response trajectories. From this data erosion profiles were constructed, summarizing the system integrity for the four combinations of NTMD damping and the oscillator’s linear frequency ratio. The conclusions from the global analysis of the PN system are as follows:

- Using numerical integration and continuation techniques, a family of 13 additional Period-1 and higher-period solutions are discovered (Figs. 5.3 and 5.7), further demonstrating the complexity of the PN system response. Numerical integration results suggest that more unidentified solutions may also exist.
- The integrity of the safe solution within the higher-frequency bi-stable region $B_{\omega>1}$ is significantly higher than the integrity within the low-frequency bi-stable region $B_{\omega<1}$, indicating that the system is likely to only exhibit the safe, low

amplitude solution within $B_{\omega>1}$. As an example, the integrity factor (IF) corresponding to the $B_{\omega>1}$ basin portrait illustrated in Fig. 5.4 is 78% higher than the *highest* integrity factor observed within the $B_{\omega<1}$ region.

- Integrity values within the $B_{\omega<1}$ region were 20–40% higher across all measures for the case of zero NTMD damping when compared with a small non-zero NTMD damping, resulting in increased robustness to large excitation magnitudes (Fig. 5.11).
- A small linear stiffness coefficient $\Omega = 0.1$ resulted in no significant change to the integrity measures when compared with the case of zero linear stiffness. If other favorable response characteristics can be obtained by adding or removing the small linear stiffness component, the integrity will not be affected.
- Both the total hyper-volume (GIM) and the size of the compact center of the safe basin (IF) are larger at the frequency corresponding to the peak of the frequency-response (ω_p) than the midpoint of the bi-stable region (ω_m), but the distance from the attractor to the boundary of the constraint basin is generally unchanged. The corresponding local integrity measure (LIM) and impulse integrity measures (IIM $^{\pm}$) indicate that the system is no more robust to perturbations at ω_p than ω_m , despite the larger amplitude separation.
- The integrity of the safe basin is eliminated completely at a threshold excitation magnitude F (approximately $F > 0.85$ for $\hat{\gamma}_N = 0$ and $F > 0.6$ for $\hat{\gamma}_N = 0.002$). The integrity loss corresponds to a bifurcation in which the original constraint solution becomes unstable and is augmented by a new stable constraint branch which acts as a strong attractor, illustrated in Fig. 5.12.
- Under certain conditions, the PN system exhibits a chaotic response. Figure 5.13 illustrates the evidence of chaos and the transition from a periodic to

a chaotic response.

A summary of conclusions from the evaluation of the PNS system in Section 5.4 is given as follows:

- Numerical results demonstrated that an STMD with a mass as low as 0.005% of the primary structure can effectively eliminate convergence to the high amplitude solution within the $B_{\omega < 1}$ region, considering a reasonable range of operating conditions (Fig. 5.19).
- An STMD with a mass as low as 0.02% that of the primary structure can eliminate the existence of the high amplitude solution within the $B_{\omega < 1}$ region (Figs. 5.14–5.18). As a result, the complex and potentially dangerous response characteristics such as the jump phenomenon are not exhibited (Fig. 5.17).
- The benefit of using the STMD as a safety mechanism which can be activated and deactivated based on response conditions was demonstrated in Figs. 5.20 and 5.21. Implementing the STMD device in this manner allows the strongly nonlinear NTMD to serve its purpose as an energy pumping device while also providing protection against unwanted response behavior.

The results from Sections 5.2 and 5.3 identified that the response behavior of a strongly nonlinear absorber is more complex than previously anticipated and that the high amplitude attractors significantly influence the response behavior. These findings present the challenges that must be addressed before a strongly nonlinear absorber can be practically implemented. The results in Section 5.4 then demonstrated a solution—adding an STMD in series with the NTMD and PS—which successfully eliminates the complex high amplitude behavior. By implementing the STMD in a way that allows for intermittent operation, the energy pumping benefits can be utilized with the system protected from the high amplitude response behavior.

Chapter 6

Experimental Validation

In this section, the design, characterization, and response of a three-DOF experimental system are discussed. The experimental system consists of a large steel frame on rollers acting as the primary mass, a small aluminum frame on linear bearings acting as the secondary mass (NTMD), and an adjustable-length pendulum as the tertiary mass (STMD), as illustrated in Fig. 6.1. Following the convention used in Chapter 5, the two-DOF system consisting of the primary structure and NTMD will be used as a reference system and will frequently be referred to as the *PN system*. The response of the PN system will be compared with the response of the three-DOF system consisting of the primary structure, NTMD, and STMD—referred to as the *PNS system*.

The linear stiffness is achieved for the primary mass by a large steel tension and compression spring. To create an NTMD from the secondary mass, six linear springs are attached in such a manner that their geometry creates an approximately cubic restoring force versus the NTMD deflection. Linear stiffness in the NTMD is achieved by pre-tensioning the geometric springs. A rigid pendulum with an auxiliary torsional stiffness element and a manually-adjustable length is used as the STMD component. The pendulum is a passive absorber, but by adjusting the effective length of the

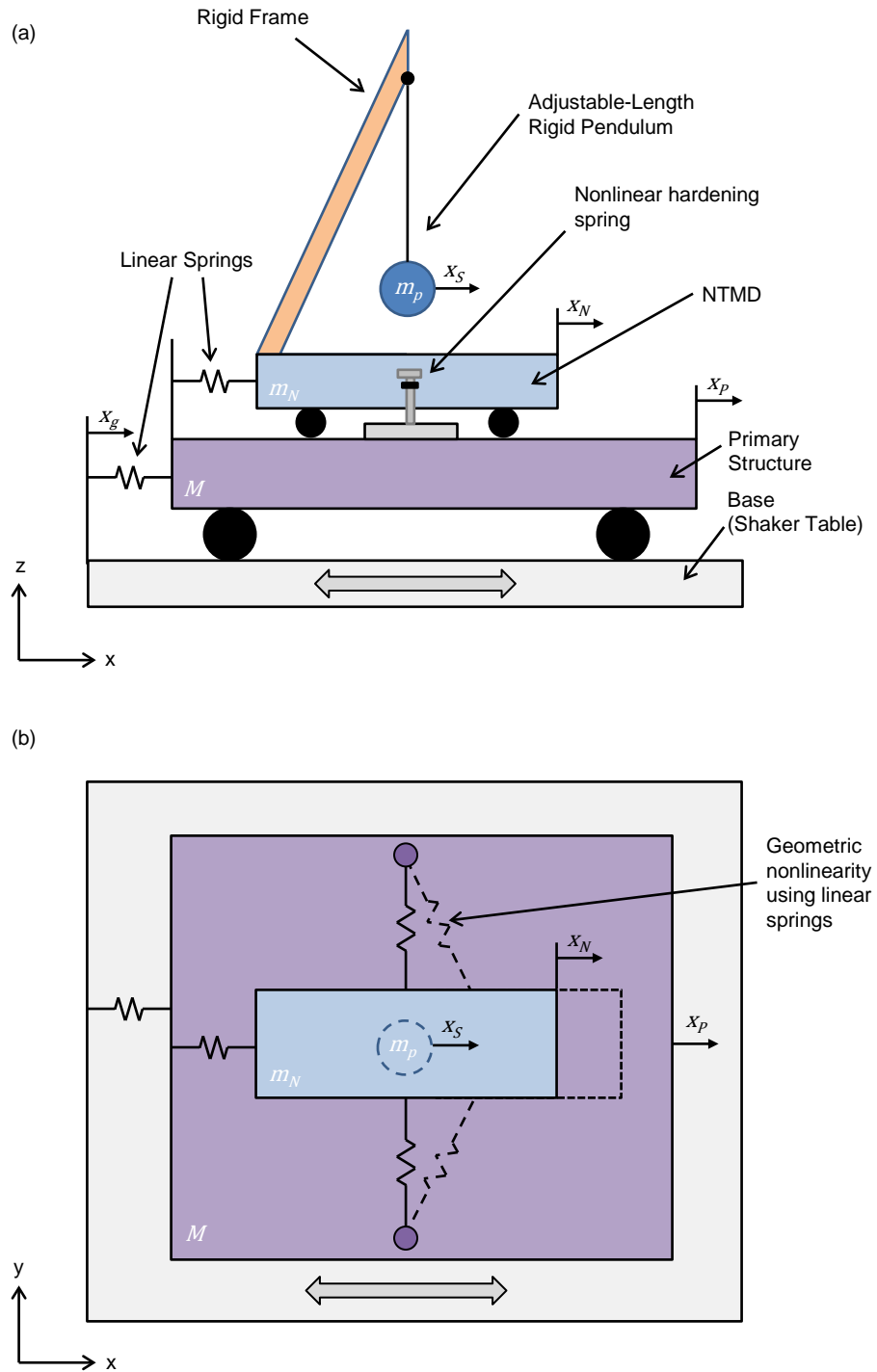


Figure 6.1: Schematic illustration of the experimental test setup: (a) side and (b) front view.

pendulum such that the natural frequency of the pendulum is equal to the excitation frequency at each data point the results accurately approximate the behavior of a semi-active device. For this reason, the adjustable-length pendulum is referred to as an STMD. Where applicable, the limitations of the manually-adjustable device to accurately represent the behavior of an STMD are discussed.

The purpose of the experimental tests are to validate the dynamic model used to obtain the numerical results in the preceding sections, to identify the presence of bi-stable regions where the primary structure is subject to exhibit a safe low amplitude or a dangerous high amplitude response, and to demonstrate the capability of the STMD to constrain the response to the safe low amplitude region.

In the first section, the equations of motion describing the experimental system are derived and the relationship between the dynamic model in this chapter and the model in Chapter 2 is explained. The constraints governing the design of the experimental system are discussed in the second section. In the third section, the design of the experimental components is presented and the parameter values are characterized. The experimental results illustrating the response behavior with and without the STMD are presented in the following section. In the final sections, a summary of the results is presented and the potential sources of error are discussed.

6.1 Equations of Motion

In this section, the governing equations of motion are derived for the experimental system consisting of a primary structure, NTMD and STMD. The key difference between the present dynamic model and the model derived in Chapter 2 is in the excitation term. In the experimental system, the excitation is achieved by harmonic ground displacement, as compared with the harmonic force directly applied to the primary structure in the Chapter 2 model. As a result, the effective excitation in the present

case is directly proportional to the base displacement amplitude and the square of the excitation frequency. In order to more closely match the constant excitation magnitude employed in the contrasting model, the base displacement amplitude can be modulated proportional to the square root of the excitation frequency, compensating for the frequency dependence.

The governing equations are easily obtained in their dimensional form by using the standard Newtonian or Lagrangian approach. In contrast with the matrix formulation used in Chapter 2, the equations in the present chapter are left in scalar form in order to better illustrate the coordinate transformation. Equations (6.1)–(6.3) describe the equations of motion.

$$\begin{aligned}
 M\ddot{x}_P(t) + c_1(\dot{x}_P(t) - \dot{x}_g(t)) + c_N(\dot{x}_P(t) - \dot{x}_N(t)) \\
 + k_1(x_P(t) - x_g(t)) + k_N(x_P(t) - x_N(t)) \\
 + \alpha_N(x_P(t) - x_N(t))^3 = 0,
 \end{aligned} \tag{6.1}$$

$$\begin{aligned}
 m_N\ddot{x}_N(t) + c_N(\dot{x}_N(t) - \dot{x}_P(t)) + c_S(\dot{x}_N(t) - \dot{x}_S(t)) \\
 + k_N(x_N(t) - x_P(t)) + k_S(x_N(t) - x_S(t)) \\
 + \alpha_N(x_N(t) - x_P(t))^3 = 0,
 \end{aligned} \tag{6.2}$$

$$m_S\ddot{x}_S(t) + c_S(\dot{x}_S(t) - \dot{x}_N(t)) + k_S(x_S(t) - x_N(t)) = 0. \tag{6.3}$$

Similar to the nomenclature used throughout the previous chapters, x_P , x_N , and x_S represent the displacement of the primary structure, NTMD, and STMD, respectively, relative to an inertial reference frame. The displacement of the base relative to an inertial reference frame is denoted by x_g ¹. Again, derivatives with respect to

¹“Base” refers to the element undergoing harmonic displacement to which the primary structure is coupled through a linear spring. In the experimental system this element is a hydraulically-actuated plate acting as the base of the structure. In seismic applications, the ground surface acts as this base element. The nomenclature throughout this chapter follows the convention of denoting parameters related to the base, or “ground”, motion by the letter g rather than b .

time t are denoted by an over-dot ($\dot{}$) and derivatives with respect to non-dimensional time τ by a the prime symbol (\prime).

In order to express the equations of motion in terms of the coordinates of interest, a new set of coordinates is introduced, defined as

$$g_P(t) = x_P(t) - x_g(t), \quad (6.4)$$

$$p_N(t) = x_N(t) - x_P(t), \quad (6.5)$$

$$n_S(t) = x_S(t) - x_N(t). \quad (6.6)$$

Therefore, g_P represents the displacement of the primary structure relative to the base, p_N the displacement of the NTMD relative to the primary structure, and n_S the displacement of the STMD relative to the NTMD. It follows from Eqns. (6.4)–(6.6) that

$$\dot{g}_P(t) = \dot{x}_P(t) - \dot{x}_g(t), \quad \ddot{g}_P(t) = \ddot{x}_P(t) - \ddot{x}_g(t), \quad (6.7)$$

$$\dot{p}_N(t) = \dot{x}_N(t) - \dot{x}_P(t), \quad \ddot{p}_N(t) = \ddot{x}_N(t) - \ddot{x}_P(t), \quad (6.8)$$

$$\dot{n}_S(t) = \dot{x}_S(t) - \dot{x}_N(t), \quad \ddot{n}_S(t) = \ddot{x}_S(t) - \ddot{x}_N(t). \quad (6.9)$$

Assuming that the base motion is harmonic, x_g can be described as $x_g(t) = X_g \sin(\omega_g t)$, where X_g and ω_g are the amplitude and frequency of the base displacement, respectively. The velocity and acceleration of the base are therefore expressed as

$$\dot{x}_g(t) = \omega_g X_g \cos(\omega_g t), \quad (6.10)$$

$$\ddot{x}_g(t) = -\omega_g^2 X_g \sin(\omega_g t), \quad (6.11)$$

Substituting Eqns. (6.4)–(6.9) and (6.11) into Eqns. (6.1)–(6.3) and rearranging then gives

$$\ddot{g}_P(t) + \frac{c_1}{M} \dot{g}_P(t) - \frac{c_N}{M} \dot{p}_N(t) + \frac{k_1}{M} g_P(t) - \frac{k_N}{M} p_N(t) - \frac{\alpha_N}{M} p_N(t)^3 = \omega_g^2 X_g \sin(\omega_g t), \quad (6.12)$$

$$\begin{aligned} \ddot{p}_N(t) - \frac{c_1}{M} \dot{g}_P(t) + \frac{c_N}{m_N} \dot{p}_N - \frac{c_S}{m_N} \dot{n}_S(t) - \frac{k_1}{M} g_P(t) \\ + \frac{k_N}{M} p_N(t) - \frac{k_S}{m_N} n_S(t) + \frac{\alpha_N}{M} p_N(t)^3 + \frac{c_N}{m_N} \dot{p}_N(t) \\ + \frac{k_N}{m_N} p_N(t) + \frac{\alpha_N}{m_N} p_N(t)^3 = 0, \end{aligned} \quad (6.13)$$

$$\begin{aligned} \ddot{n}_S(t) + \frac{c_S}{m_N} \dot{n}_S(t) + \frac{k_S}{m_N} n_S(t) - \frac{c_N}{m_N} \dot{p}_N(t) \\ - \frac{k_N}{m_N} p_N(t) - \frac{\alpha_N}{m_N} p_N(t)^3 + \frac{c_S}{m_S} \dot{n}_S(t) + \frac{k_S}{m_S} n_S(t) = 0. \end{aligned} \quad (6.14)$$

Employing the same design parameters defined in Eqn. (2.16) results in

$$\ddot{g}_P(t) + 2\gamma_1\omega_1\dot{g}_P(t) - 2\epsilon_N\gamma_N\omega_2\dot{p}_N(t) + \omega_1^2g_P(t) \quad (6.15)$$

$$-\epsilon_N\omega_2^2p_N(t) - \epsilon_N\omega_N^2p_N(t)^3 = \omega_g^2X_g \sin(\omega_g t),$$

$$\ddot{p}_N(t) - 2\gamma_1\omega_1\dot{g}_P(t) + 2\epsilon_N\gamma_N\omega_2\dot{p}_N(t) - 2\frac{\epsilon_S}{\epsilon_N}\gamma_S\omega_S\dot{n}_S(t) \quad (6.16)$$

$$\begin{aligned} -\omega_1^2g_P(t) + \epsilon_N\omega_2^2p_N(t) - \frac{\epsilon_S}{\epsilon_N}\omega_S^2n_S(t) + \epsilon_N\omega_N^2p_N(t)^3 \\ + 2\gamma_N\omega_2\dot{p}_N(t) + \omega_2^2p_N(t) + \omega_N^2p_N(t)^3 = 0, \end{aligned}$$

$$\ddot{n}_S(t) + 2\frac{\epsilon_S}{\epsilon_N}\gamma_S\omega_S\dot{n}_S(t) + \frac{\epsilon_S}{\epsilon_N}\omega_S^2n_S(t) - 2\gamma_N\omega_2\dot{p}_N(t) \quad (6.17)$$

$$\begin{aligned} -\omega_2^2p_N(t) - \omega_N^2p_N(t)^3 + 2\gamma_S\omega_S\dot{n}_S(t) \\ + \omega_S^2n_S(t) = 0, \end{aligned}$$

Non-dimensionalizing with respect to time is again accomplished by introducing the non-dimensional scaled-time parameter τ ,

$$t = \frac{\tau}{\omega_1}, \quad (6.18)$$

$$\frac{d}{dt} = \omega_1 \frac{d}{d\tau}, \quad (6.19)$$

$$\frac{d}{dt^2} = \omega_1^2 \frac{d}{d\tau^2}, \quad (6.20)$$

Substituting Eqns. (6.18)–(6.20) into Eqns. (6.15)–(6.17) gives

$$\omega_1^2 g_P''(\tau) + \omega_1 (2\gamma_1 \omega_1) g_P'(\tau) - \omega_1 (2\epsilon_N \gamma_N \omega_2) p_N'(\tau) \quad (6.21)$$

$$+ \omega_1^2 g_P(\tau) - \epsilon_N \omega_2^2 p_N(\tau) - \epsilon_N \omega_N^2 p_N(\tau)^3 = \omega_g^2 X_g \sin\left(\frac{\omega_g}{\omega_1} \tau\right),$$

$$\omega_1^2 p_N''(\tau) - \omega_1 (2\gamma_1 \omega_1) g_P'(\tau) + 2\omega_1 (1 + \epsilon_N) \gamma_N \omega_2 p_N'(\tau) \quad (6.22)$$

$$- 2\omega_1 \left(\frac{\epsilon_S}{\epsilon_N} \gamma_S \omega_S\right) n_S'(\tau) - \omega_1^2 g_P(\tau) + (1 + \epsilon_N) \omega_2^2 p_N(\tau) \\ - \frac{\epsilon_S}{\epsilon_N} \omega_S^2 n_S(\tau) + (1 + \epsilon_N) \omega_N^2 p_N(\tau)^3 = 0,$$

$$\omega_1^2 n_S''(\tau) + 2\omega_1 \left(\frac{\epsilon_S}{\epsilon_N} \gamma_S \omega_S\right) n_S'(\tau) + \frac{\epsilon_S}{\epsilon_N} \omega_S^2 n_S(\tau) \quad (6.23)$$

$$- 2\omega_1 (\gamma_N \omega_2) p_N'(\tau) - \omega_2^2 p_N(\tau) - \omega_N^2 p_N(\tau)^3 \\ + 2\omega_1 (\gamma_S \omega_S) n_S'(\tau) + \omega_S^2 n_S(\tau) = 0,$$

Then, by defining new variables to relate the various frequency parameters,

$$\Omega = \frac{\omega_2}{\omega_1} \text{ (unitless)} \quad (6.24)$$

$$\Omega_N = \frac{\omega_N}{\omega_1} \left(\frac{\text{sec}^{-1} \text{ft}^{-1}}{\text{sec}^{-1}} = \text{ft}^{-1} \right) \quad (6.25)$$

$$\Omega_g = \frac{\omega_g}{\omega_1} \text{ (unitless)} \quad (6.26)$$

$$\Omega_S = \frac{\omega_S}{\omega_1} \text{ (unitless)}, \quad (6.27)$$

and introducing the new coordinates $r_i(\tau)$,

$$r_1(\tau) = g_P(\tau), \quad (6.28)$$

$$r_2(\tau) = g'_P(\tau), \quad (6.29)$$

$$r_3(\tau) = p_N(\tau), \quad (6.30)$$

$$r_4(\tau) = p'_N(\tau), \quad (6.31)$$

$$r_5(\tau) = n_S(\tau), \quad (6.32)$$

$$r_6(\tau) = n'_S(\tau), \quad (6.33)$$

the first-order equations of motion governing the primary structure, NTMD, and STMD system are expressed as

$$r'_1(\tau) = r_2(\tau), \quad (6.34)$$

$$\begin{aligned} r'_2(\tau) = & 2\epsilon_N\gamma_N\Omega r_4(\tau) + \epsilon_N\Omega^2 r_3(\tau) + \epsilon_N\Omega_N^2 r_3(\tau)^3 - 2\gamma_1 r_2(\tau) \\ & - r_1(\tau) + \Omega_g^2 X_g \sin(\Omega_g \tau), \end{aligned} \quad (6.35)$$

$$r'_3(\tau) = r_4(\tau), \quad (6.36)$$

$$\begin{aligned} r'_4(\tau) = & 2\frac{\epsilon_S}{\epsilon_N}\gamma_S\Omega_S r_6(\tau) + \frac{\epsilon_S}{\epsilon_N}\Omega_S^2 r_5(\tau) - 2(1 + \epsilon_N)\gamma_N\Omega r_4(\tau) \\ & - (1 + \epsilon_N)\Omega^2 r_3(\tau) - (1 + \epsilon_N)\Omega_N^2 r_3(\tau)^3 + 2\gamma_1 r_2(\tau) + r_1(\tau), \end{aligned} \quad (6.37)$$

$$r'_5(\tau) = r_6(\tau), \quad (6.38)$$

$$\begin{aligned} r'_6(\tau) = & -2\left(1 + \frac{\epsilon_S}{\epsilon_N}\right)\gamma_S\Omega_S r_6(\tau) - \left(1 + \frac{\epsilon_S}{\epsilon_N}\right)\Omega_S^2 r_5(\tau) \\ & + 2\gamma_N\Omega r_4(\tau) + \Omega^2 r_3(\tau) + \Omega_N^2 r_3(\tau)^3. \end{aligned} \quad (6.39)$$

6.2 Constraints

As with any real-world implementation, physical constraints limit the range of achievable parameters. Within this section, design constraints based on displacement, mass, and frequency are discussed.

Displacement

An existing structure consisting of a steel frame on rollers is used for the primary structure, with a linear bearing and rail guide added in order to maintain alignment. The maximum range of motion allowed by linear bearings in the primary structure and the range allowed by the bearings in the NTMD component are each about ± 4 in (10 cm). Displacement amplitudes of the primary structure relative to the base $|g_P|$, the NTMD relative to the primary structure $|p_N|$, and the STMD relative to the NTMD $|n_S|$ are dependent on the particular choice of design parameters. However, based on the results from Chapter 5 and other preliminary numerical tests, the displacements of each at the peak resonant condition are generally in the ratio of $|g_P|/|p_N| \approx 2$ and $|g_P|/|n_S| \approx 1$. Therefore, the displacement of the PS is not expected to be a limiting factor, and the first design constraint is the limit of the NTMD displacement determined by the maximum range of the linear bearings: $|p_N| \leq 4$ in (10 cm).

An adjustable-length pendulum device is used as the STMD component. In order to most accurately represent the dynamic system, the angular deflection of the pendulum θ_S must be constrained to within an approximately linear range, $|\theta_S| \leq 30$ deg ($\pi/6$ rad), resulting in a restoring force within 25% of the true value. When possible, displacements amplitudes are kept within $|\theta_S| \leq 20$ deg ($\pi/9$ rad) resulting in a restoring force within 11% of the true value.

Mass

The mass of the primary structure is measured to be 326 lb (148 kg). It is estimated that additional components will increase the mass to approximately 350 lb (159 kg), forming the lower design limit. If necessary, the mass of the primary structure can be increased by adding one or both of two available steel plates. Based on a rough estimate of the volume of each plate and an average steel density, the mass of plates A and B are estimated to be $m_A = 0.412 \text{ ft}^3 \times 490 \text{ lb/ft}^3 \approx 200 \text{ lb}$ (90.7 kg) and $m_B = 2.391 \text{ ft}^3 \times 490 \text{ lb/ft}^3 \approx 1170 \text{ lb}$ (531 kg), respectively. Therefore, the mass of the primary structure is constrained to the approximate range of 350 lb (159 kg) $\leq M \leq 1720 \text{ lb}$ (780 kg).

As discussed in Chapter 5, a realistic upper limit for the mass of an absorber for structural applications is $\epsilon_N = 0.1$, forming the upper limit for the NTMD mass. Consequences of selecting a much smaller value for the mass ratio include an increase in the effective damping of the NTMD, a larger range of motion required to achieve nonlinear effects, and an increase in the amplitude ratio $|g_P|/|p_N|$ —resulting in a smaller available range for the primary structure. In order to minimize the influence of these factors but still give some design flexibility, a lower limit of $\epsilon_N = 0.05$ is selected.

Numerical results indicate that an STMD mass ratio as low as 0.001 can effectively eliminate the high amplitude solution. However, considering the target range for the primary structure and NTMD, the corresponding lateral STMD displacements would be on the order of $|n_S| = 20 \text{ in}$ (51 cm), resulting in a minimum pendulum length of $20/\sin(30 \text{ deg}) = 40 \text{ in}$ (1.0 m). Instead, a mass ratio value of $m_S \geq 0.01$ is targeted, limiting the expected range of motion to the much more reasonable range of $|n_S| < 2 \text{ in}$ (5 cm).

Frequency

Excitation is achieved by harmonic base displacement of the Rice University shaker table, constructed using an MTS hydraulic pump and actuator system [133]. The base displacement amplitudes required in order to achieve the prescribed displacement limits for the dynamic system are on the order of $X_g = 0.1$ in (2.5 mm), well within the capabilities of the shaker table. The dynamic properties of the shaker table itself do, however, impose a constraint on the natural frequency of the primary structure. Based on a published analysis of the shaker table behavior under various loading conditions, a flexible payload up to 450 lb (200 kg) is not expected to interfere with the shaker table transfer function as long as the natural frequency of the payload is less than 20 Hz [133]. Imposing a factor of safety of 2 due to the uncertainty regarding the effect of the second and third degrees-of-freedom of the payload on the shaker table, a constraint of $\omega_1 \leq 10$ Hz is selected.

The natural frequency of the STMD component must, at minimum, be adjustable over the frequency range where bi-stable behavior is present for the primary structure and NTMD. Based on numerical results, a bi-stable region generally occurs between $\omega_1/2$ and ω_1 and between ω_1 and $2\omega_1$. The numerical results presented in Chapter 5 indicated that the integrity of the system is much lower in the lower-frequency bi-stable region. Therefore, the experimental results will be focused on the lower-frequency bi-stable region and so the frequency ratio of the STMD must be adjustable over the minimum range of $0.5 \leq \Omega_S \leq 1$.

6.3 Design and Characterization

In this section, the process used to select components to build the experimental system is discussed. For quick reference, Table 6.1 summarizes the design constraints discussed in Section 6.2. Dimensional parameter values are targeted to match the

Table 6.1: Summary of design constraints for the experimental system based on physical limitations of space, size, and frequency.

Parameter	Constraint
Displacement amplitude of NTMD relative to PS, $ p_N $	$ p_N \leq 4$ in (10 cm)
Angular displacement amplitude of STMD, $ \theta_S $	$ \theta_S \leq 30$ deg ($\pi/6$ rad)
Mass of primary structure, M	$350 \text{ lb} \leq M \leq 1720 \text{ lb}$
...	$(159 \text{ kg} \leq M \leq 780 \text{ kg})$
Mass ratio of NTMD, ϵ_N	$0.05 \leq \epsilon_N \leq 0.1$
Mass ratio of STMD, ϵ_S	$\epsilon_S \geq 0.01$
Natural frequency of primary structure, ω_1	$\omega_1 \leq 10$ Hz (63 rad/s)
Tuning ratio of STMD, Ω_S (minimum range)	$0.5 \leq \Omega_S \leq 1.0$

non-dimensional parameter values from the key results in Chapter 5, namely $\Omega_N^* = 0.09$, $F = 0.6$. Within this chapter, a star (*) is used to denote the target parameter values, distinguishing them from the actual parameter values measured in Section 6.3.

6.3.1 Primary Structure

Since the damping ratio is defined as $\gamma_i = c_i/(2\omega_i m_i) = c_i/(2k_i^{1/2} m_i^{1/2})$, it is anticipated that maintaining a reasonably small damping ratio will be challenging, particularly for the small NTMD and STMD components. Larger values of mass and stiffness for these components will decrease the effects of damping. On the other hand, increasing the mass of the primary structure by adding plates *A* and/or *B* would require additional engineering to attach the plates to the existing frame and would increase the challenge of designing components sufficiently robust to the larger forces that would result. Therefore, the system is designed for a target primary mass of $M^* = 350 \text{ lb} = 10.88 \text{ slug}$ (159 kg), with the contingency plan that if damping ratios are too high to achieve the expected behavior the additional plates will be used.

In order to satisfy the design constraints, a 5 in (13 cm) tempered steel spring with a nominal rate of $k_1^* = 391.5 \text{ lbf/in} = 4698 \text{ lbf/ft}$ (68 560 N/m) is selected to couple the primary structure to the base. The linear range of the spring allows for



Figure 6.2: Linear spring component consisting of a 5 in (13 cm) tempered steel compression spring welded to two telescoping steel housing pieces.

a maximum deflection of 2.05 in (5.21 cm) and therefore does not further limit the displacement constraints. The expected natural frequency is therefore

$$\omega_1^* = \sqrt{\frac{k_1^*}{M^*}} = \sqrt{\frac{4698 \text{ lbf/ft}}{10.88 \text{ slug}}} = 20.78 \frac{\text{rad}}{\text{s}} = 3.31 \text{ Hz}, \quad (6.40)$$

which satisfies the constraint on the value of ω_1 .

The linear spring component, illustrated in Fig. 6.2, consists of the 5 in tempered steel spring welded to two steel housing pieces, each turned from $2\frac{3}{4}$ in (7 cm) steel rods. The housing pieces telescope to allow 2 in (5 cm) of travel for tension or compression in the spring, and include breathing holes to minimize damping. A $\frac{1}{2}$ in (13 mm) rod end is secured to each end of the housing in order to mount the spring to the primary structure and base.

The actual linear spring rate is tested by coupling the primary structure to a fixed

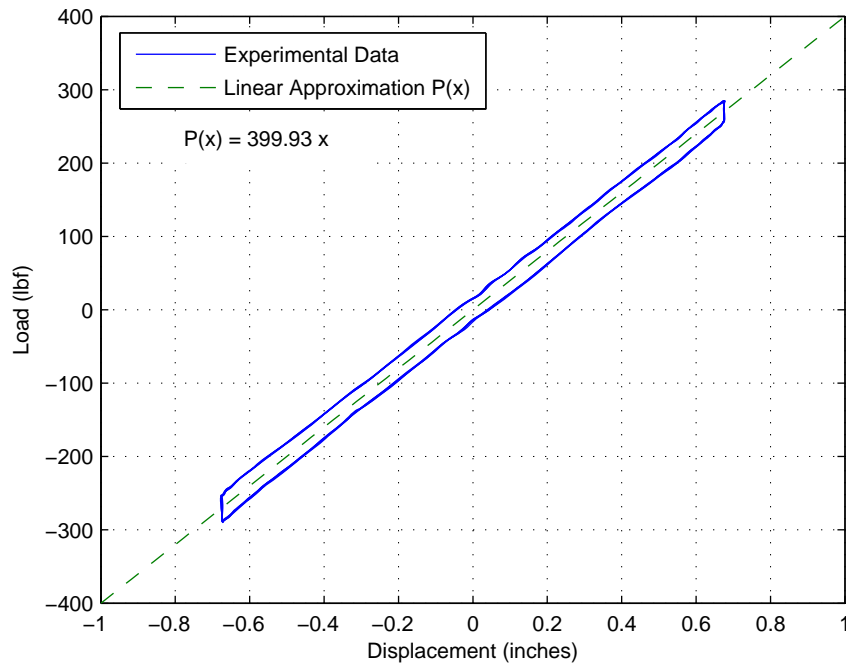


Figure 6.3: Load measured in the primary spring versus displacement of the primary structure relative to the base.

reference frame using a load cell and applying a harmonic base displacement at a frequency of 0.1 Hz (0.6 rad/s), the lowest output frequency possible from the controller. Displacement of the base relative to the primary structure—equal to the deflection of the spring—is measured using an LX-PA-10 linear variable displacement transducer (LVDT). Figure 6.3 illustrates the measured load versus spring deflection and a first order least squares approximation of the spring rate. Based on the characterization results, the actual linear spring rate is $k_1 = 399.9 \text{ lbf/in} = 4799 \text{ lbf/ft} (70\,030 \text{ N/m})$.

In order to characterize the damping ratio γ_1 , the structure is first excited near the fundamental frequency, then the excitation is removed and the local maxima of the decaying free oscillations are measured. The results from five separate tests, shown in Fig. 6.4, are averaged in order to improve accuracy. Based on the average decay between adjacent local maxima, the logarithmic decrement is calculated to be $\delta = 0.280$. The primary structure damping ratio is then calculated to be

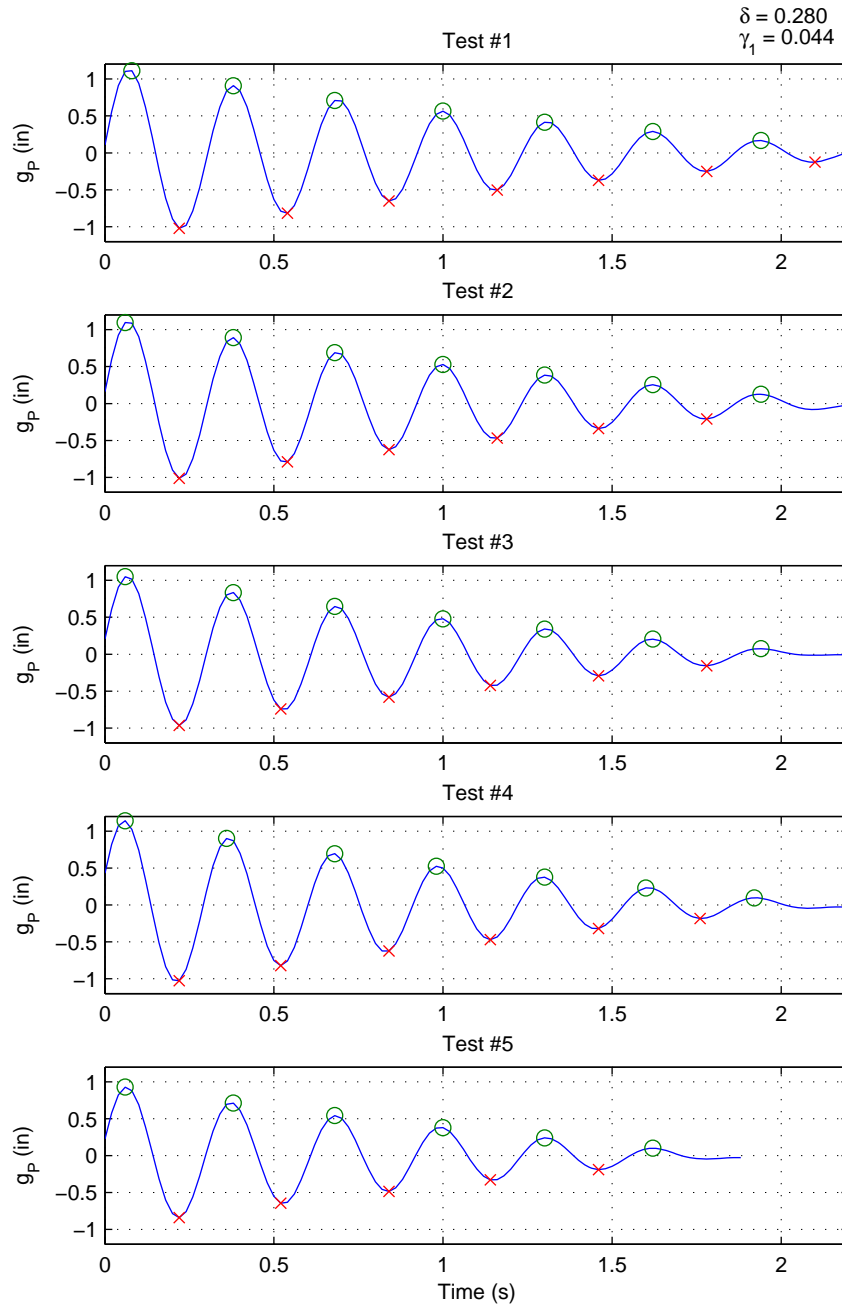


Figure 6.4: Primary structure displacement versus time (solid) and the corresponding local minima (\times) and maxima (\circ) of the decaying free oscillations.

$$\gamma_1 = \frac{1}{\sqrt{1 + \left(\frac{2\pi}{\delta}\right)^2}} = \frac{1}{\sqrt{1 + \left(\frac{2\pi}{0.280}\right)^2}} = 0.044. \quad (6.41)$$

Considering the initial mass of the primary structure frame and the combined weight of all added components, the actual mass of the primary structure is measured to be $M = 367.0$ lb (166.5 kg), resulting in a natural frequency of $\omega_1 = 3.265$ Hz (20.51 rad/s).

6.3.2 NTMD

Initial construction of the NTMD frame and spring mounts resulted in an NTMD mass of approximately 21.3 lb (9.66 kg), corresponding to a mass ratio of $21.3/367.0 = 0.058$. This mass ratio is within the range of target values, and therefore $\epsilon_N^* = 0.058$ is used to calculate the target parameter values. Mounting holes are also added to the NTMD to allow additional weights to be secured in order to achieve a mass ratio of up to 0.1.

In order to achieve behavior similar to the numerical results in Chapter 5, the target nonlinearity is $\Lambda^* = F^*\Omega_N^* = 0.045$. A maximum displacement of g_p^{max} is targeted in order to achieve the target nonlinearity well before reaching the displacement limits of the system. Based on the results of the numerical simulations, a gain of approximately 12 is experienced between the base displacement and primary structure displacement at resonance conditions, so $F^* = g_p^{max}/12 = 0.007$ ft (2 mm). Therefore, the target nonlinear coefficient is $\Omega_N^* = \Lambda^*/F^* = 6.48$ ft⁻¹ (21.3 m⁻¹).

Since $\omega_N = \Omega_N \omega_1$, the corresponding dimensional coefficient is calculated as follows,

$$\begin{aligned}
\alpha_N^* &= (\Omega_N^* \omega_1^*)^2 m_N^* \\
&= \left(6.48 \text{ ft}^{-1} \times 20.51 \frac{\text{rad}}{\text{s}} \right)^2 \times 0.6618 \text{ slug} \\
&= 11\,690 \frac{\text{lbf}}{\text{ft}^3} \left(1\,836 \frac{\text{kN}}{\text{m}} \right). \tag{6.42}
\end{aligned}$$

The nonlinear restoring force f_N versus lateral displacement of the NTMD p_N resulting from two tension springs of length l with linear stiffness coefficient k_g and pretension P , initially perpendicular to the NTMD is given by

$$f_N = 2k_g p_N + \frac{2p_N(P - k_g l)}{\sqrt{l^2 + p_N^2}}, \tag{6.43}$$

adapted from Gourdon *et al.* [46]. A Taylor series expansion of Eqn. (6.43) then gives

$$f_N \approx \frac{2P}{l} p_N + \frac{k_g l - P}{l^3} p_N^3 + O(p_N^5). \tag{6.44}$$

Since most real extension springs require some small initial preload and therefore are not linear in the neighborhood of zero, the target geometric spring parameters are calculated based on an initial stretch of $l_p = 1/8 \text{ in} = 1/96 \text{ ft}$ (3 mm). This results in a preload of $P = k_g l_p$. Therefore, at the target pretension the nonlinear coefficient is $\alpha_N = k_g (l - l_p) l^{-3}$, and the target spring rate for the geometric springs becomes

$$k_g^* = \frac{\alpha_N^* l^3}{l - l_p}. \tag{6.45}$$

The spring rate versus length prescribed by Eqn. (6.45) is larger than that of most available extension springs. Therefore, the system is designed to be used with three pairs of extension springs in parallel, requiring only one third of the spring rate for each pair. Figure 6.5 illustrates the target spring rate—one third of Eqn. (6.45) based on using three parallel springs—versus the nominal length of

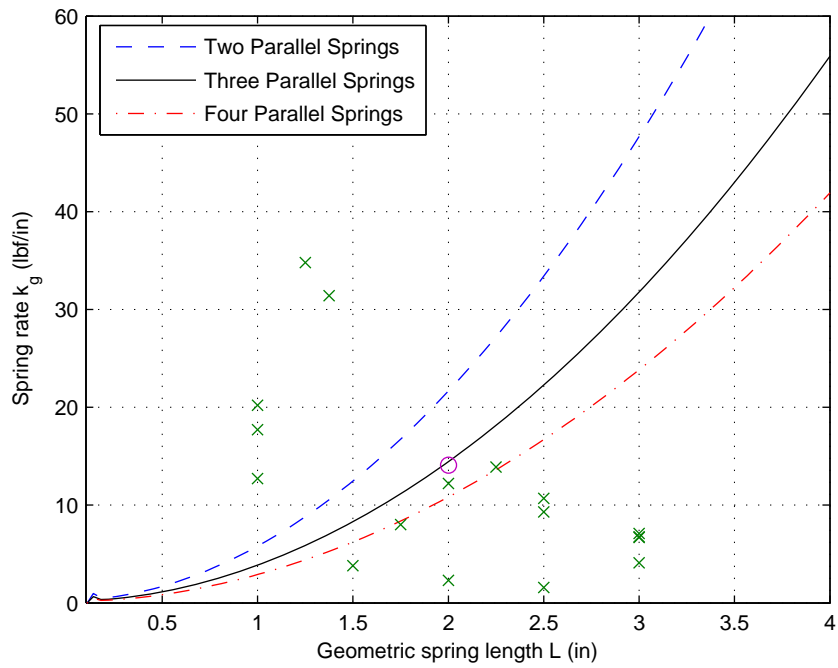


Figure 6.5: Spring rate required to achieve desired nonlinear coefficient (based on number of parallel springs) versus nominal spring length. Markers indicate spring rate and length properties of the purchased spring (\circ) other available springs (\times).

the springs. Two additional curves indicate the target spring rate based on using two and four parallel springs, for reference. Example spring rate/length combinations corresponding to a few of the available springs are each marked with an ‘×’. In general, the largest available spring rate is inversely proportional to the length. However, the shorter springs often have a very limited usable range. The spring selected for the NTMD, marked with an ‘○’, is 2 in long with a spring rate of $k_g^* = 14.10 \text{ lbf/in} = 1.175 \text{ lbf/ft} (17.15 \text{ N/m})$. The maximum deflection of the spring is 1.82 in (4.62 cm), larger than would be experienced in the expected operating conditions.

Of course, the required preload also introduces a linear stiffness coefficient. According to Eqn. (6.44), a corresponding linear spring rate of $k_N^* = 2P/l = 2k_g l_p/l = 43.3 \text{ lbf/ft} (632 \text{ N/m})$ is expected, corresponding to a linear stiffness coefficient of

$$\Omega^* = \frac{\omega_N^*}{\omega_1} = \frac{1}{\omega_1} \sqrt{\frac{k_N^*}{m_N^*}} = 0.394, \quad (6.46)$$

is expected. Although a near-zero linear coefficient would most closely match the values from the previous chapter, numerical simulations indicate that the key response characteristics will still be present for all linear stiffness coefficient values $\Omega \leq 0.8$.

Photographs of the NTMD attached to the primary structure (the PN system) are presented in Fig. 6.6. The nonlinear force-deflection profile for the NTMD is obtained experimentally by fixing a load cell and slowly pushing and pulling the NTMD by hand as the deflection is measured by an LVDT. Since the spring force introduced by the LVDT mechanism is large enough to influence the system on the scale of the NTMD, an identical LVDT is added to the opposite side of the structure, canceling out the spring force.

Figure 6.7 illustrates the load applied to the NTMD versus displacement. The dashed line represents a third order least squares approximation, closely resembling the trend of the experimental data. Based on the least squares approximation, the

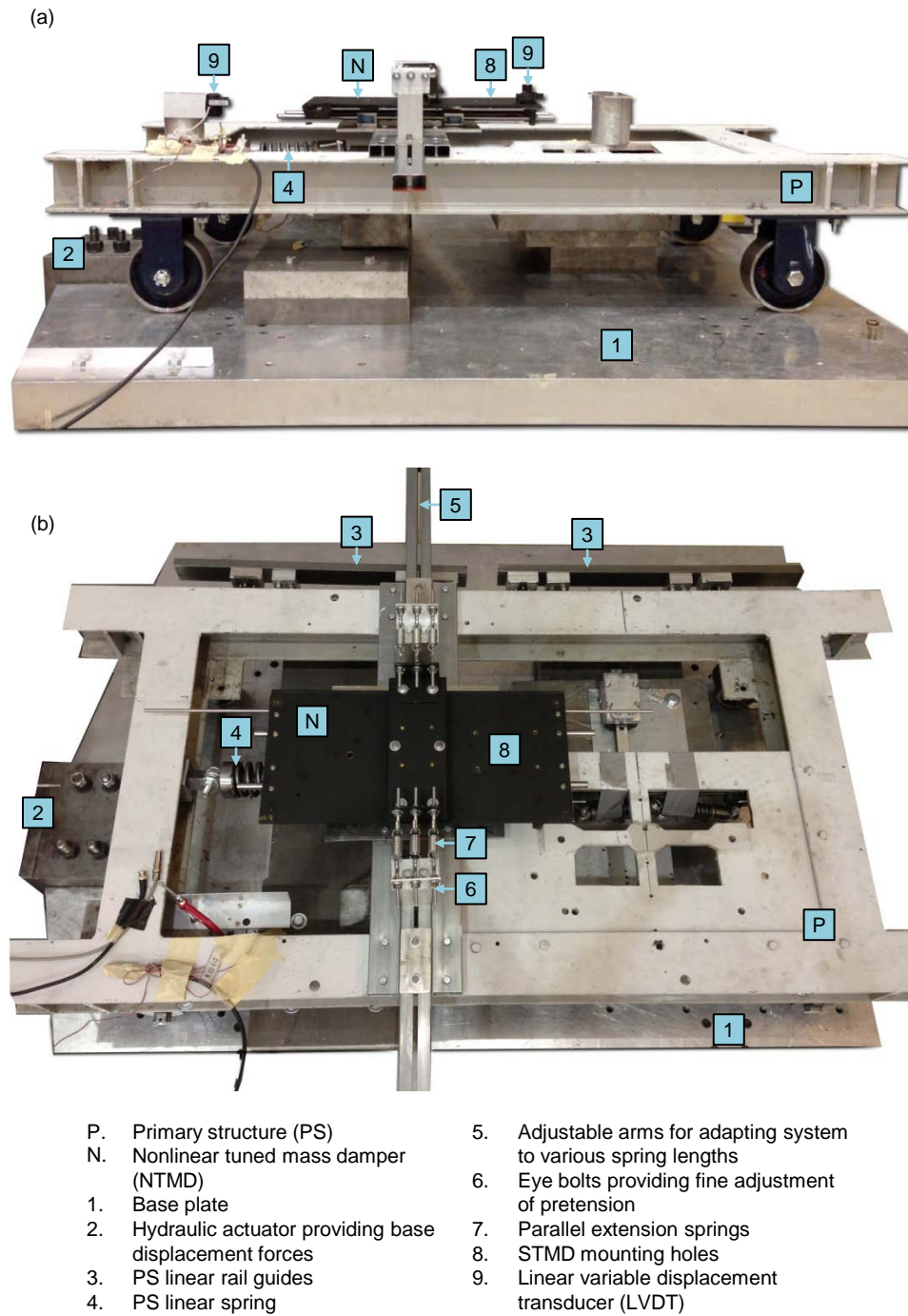


Figure 6.6: Experimental test setup for primary structure and NTMD (PN System): (a) side and (b) top view.

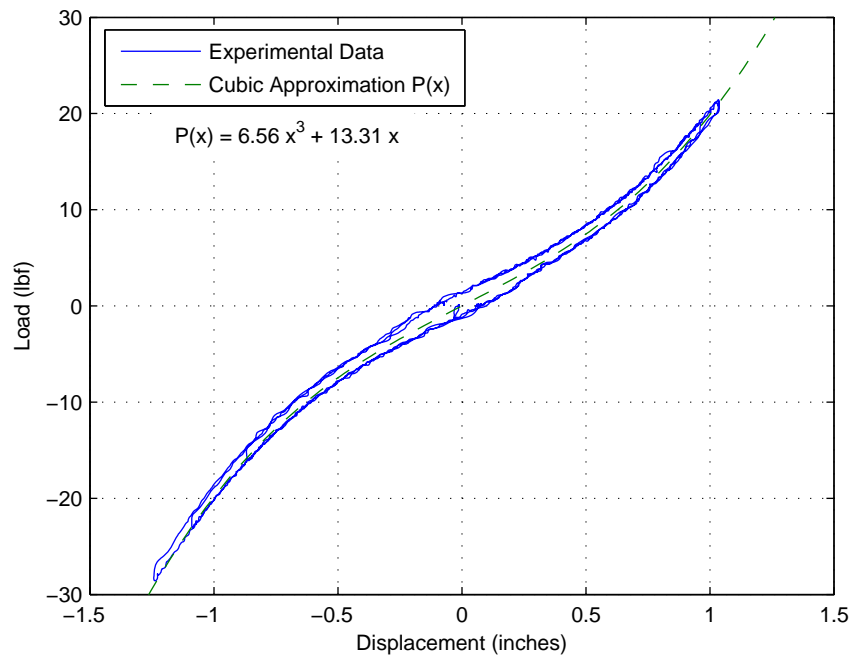


Figure 6.7: Applied load versus deflection of the NTMD component (solid) and a third-order least squares approximation (dashed) indicating the linear and nonlinear spring rate coefficients.

actual nonlinear stiffness coefficient is,

$$\alpha_N = 6.560 \frac{\text{lbf}}{\text{in}^3} = 11\,340 \frac{\text{lbf}}{\text{ft}^3} \left(1\,781 \frac{\text{kN}}{\text{m}^3} \right), \quad (6.47)$$

and the actual linear stiffness coefficient is,

$$k_N = 13.31 \frac{\text{lbf}}{\text{in}} = 159.7 \frac{\text{lbf}}{\text{ft}} \left(2.331 \frac{\text{kN}}{\text{m}} \right). \quad (6.48)$$

Finally, the NTMD damping ratio is determined by using the procedure outlined in Section 6.3.1. In an attempt to isolate the damping characteristics of the NTMD's linear bearings, the nonlinear springs are temporarily replaced with two opposing linear compression springs so that the decay of the free oscillations can be measured. The natural frequency of the NTMD with the linear springs is estimated to be $\omega_d = 9.3$ rad/s. From the experimental data, shown in Fig. 6.8, the logarithmic decrement is calculated to be $\delta = 0.463$. The damping ratio corresponding to the linear spring configuration is therefore $\zeta = \left(1 + \left(\frac{2\pi}{\delta} \right)^2 \right)^{-1/2} = 0.073$. Assuming a constant damping coefficient, the NTMD damping parameter is then calculated as

$$\hat{\gamma}_N = \zeta \frac{\omega_d}{\omega_1} = 0.033. \quad (6.49)$$

It is noted that the temporary linear spring configuration used to test the NTMD damping was subject to friction forces between the long springs and the mounting rail. The estimated damping ratio therefore represents an upper-limit, with the understanding that the actual damping ratio may be somewhat lower.

6.3.3 STMD

Equation (6.50) is the linearized equation of motion governing the free response of a pendulum consisting of a narrow rod and point mass with an auxiliary torsion spring, expressed in terms of the horizontal displacement n_S between the STMD and NTMD.

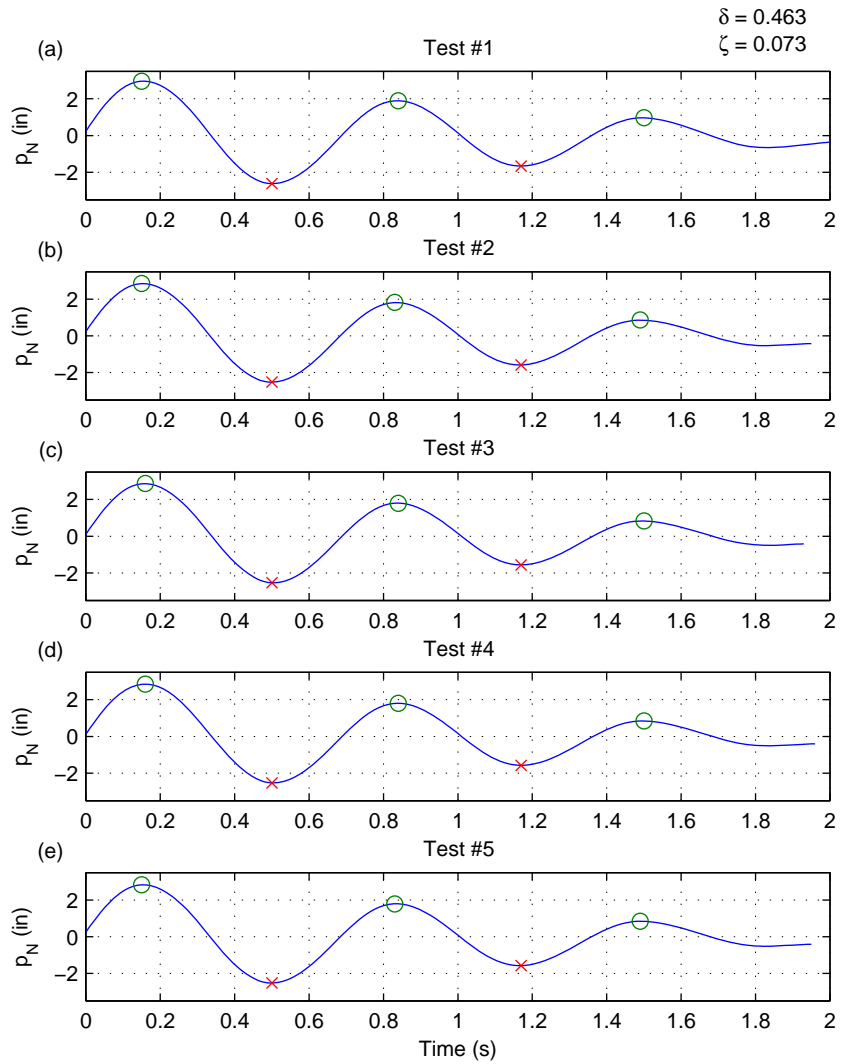


Figure 6.8: NTMD displacement versus time (solid) and the corresponding local minima (\times) and maxima (\circ) of the decaying free oscillations.

$$m_S \ddot{n}_S(t) + k_S n_S(t) = 0. \quad (6.50)$$

The effective mass m_S and effective stiffness k_S are expressed in terms of the mass of the pendulum m_p , length of the rod L , offset distance d_{cm} between the clamp and the center of mass of the rod, acceleration of gravity g , mass of the rod m_r , and torsional stiffness of the auxiliary spring k_{tor} as

$$m_S = \frac{m_p}{\left(d_{cm} + \frac{L}{2}\right)^2} \left(\frac{L^2}{12} + d_{cm}^2 \right) + m_p, \quad (6.51)$$

and

$$k_S = \frac{g}{d_{cm} + \frac{L}{2}} \left(m_r \frac{d_{cm}}{d_{cm} + \frac{L}{2}} + m_p \right) + \frac{k_{tor}}{\left(d_{cm} + \frac{L}{2}\right)^2}. \quad (6.52)$$

The STMD design must satisfy three design constraints from Table 6.1: $|\theta_S| \leq 30$ deg, $\epsilon_S \geq 0.01$, and $0.5 \leq \Omega_S \leq 1$. The design procedure will be to select parameters that satisfy the natural frequency constraint for the smallest acceptable mass ratio, $\epsilon_S^* = 0.01$, at a nominal offset distance of $d_{cm}^* = L/4$, half the distance between the center and the end of the rod. Then, if the angular displacement constraint is not satisfied, the target mass ratio value will be increased and the process repeated.

A mass ratio of $\epsilon_S^* = 0.01$ corresponds to an effective STMD mass of $m_S^* = \epsilon_S^* M = 3.67$ lb = 0.114 slug (1.67 kg). Therefore, to satisfy the mass constraint Eqn. (6.51) becomes

$$m_S^* = \frac{m_p^*}{\left(d_{cm}^* + \frac{L}{2}\right)^2} \left(\frac{L^2}{12} + (d_{cm}^*)^2 \right) + m_p^* = 0.114 \text{ slug}, \quad (6.53)$$

Figure 6.9 illustrates the effective mass versus total rod length for three values of pendulum mass m_p . The horizontal dashed line represents the target effective mass, $m_S = m_S^*$. It is clear that over the given range of rod length, the effective mass

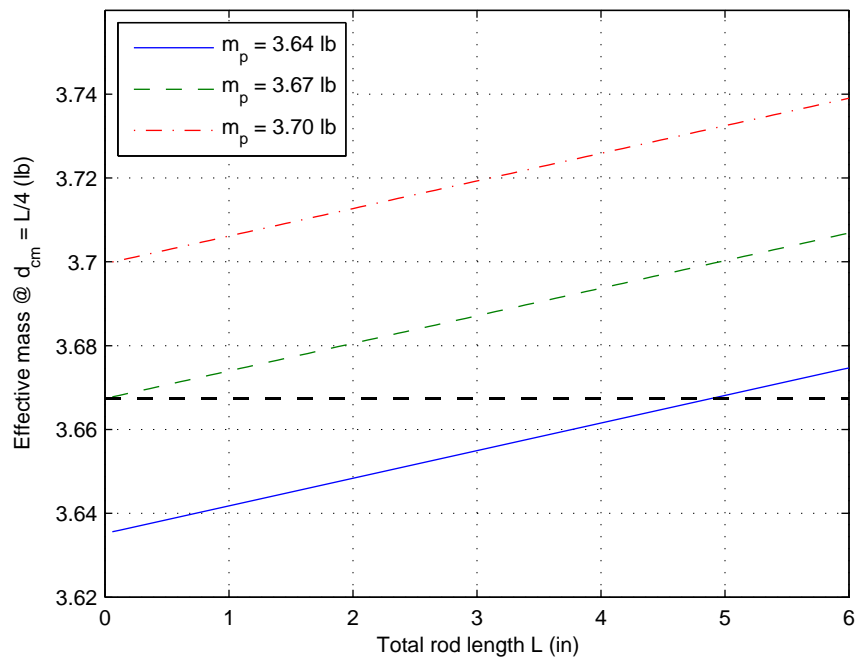


Figure 6.9: Effective STMD mass versus total rod length for a pendulum mass of 3.64 lb (solid), 3.67 lb (dashed), and 3.70 lb (dash-dot).

is closely related to the mass of the pendulum m_p , with little dependence on rod length L . Solving Eqn. (6.53) for m_p^* gives the expression which relates the required pendulum mass to the rod length,

$$m_p^* \text{ (slug)} = 0.115 - 0.002L. \quad (6.54)$$

Many of the key numerical results have been focused on the peak of the detached branch, which typically occurs at a frequency near $0.89 \times \omega_1$. Design parameters are selected such that the corresponding tuning ratio $\Omega_S^* = 0.89$ is achieved at the nominal offset distance, $d_{cm}^* = L/4$. The adjustable frequency range is then determined by substituting other values of d_{cm} in order to ensure that the frequency constraint is met.

The target natural frequency is therefore $\omega_S^* = \Omega_S^* \omega_1 = 18.25$ rad/s. By combining Eqns. (6.51) and (6.52), the target natural frequency is achieved when

$$\omega_S^* = \sqrt{\frac{k_S^*}{m_S^*}} = \sqrt{\frac{12k_{tor}^* + 6g \left((L + 2d_{cm}^* m_p^* + 2d_{cm}^* m_r^*) \right)}{3(L + 2d_{cm}^*)^2 m_p^* + (L^2 + 12(d_{cm}^*)^2) m_r^*}} = 18.25 \frac{\text{rad}}{\text{s}}, \quad (6.55)$$

In the initial design stages, a clamp with an inner diameter of 15 mm, approximately 0.049 ft, was selected to secure the pendulum rod. Assuming that the rod is machined from aluminum with a density of $\rho = 4.97$ slug/ft³ (2 560 kg/m³), the mass of the rod versus length is expressed as

$$m_r^* \text{ (slug)} = \pi \left(\frac{0.049 \text{ ft}}{2} \right)^2 L \times 4.97 \text{ slug/ft}^3 = 9.37 \times 10^{-3} L. \quad (6.56)$$

Figure 6.10 illustrates the natural frequency of the STMD ω_S versus total rod length for four values of auxiliary torsional stiffness k_{tor} . The horizontal dashed line represents the target natural frequency, $\omega_S = \omega_S^*$. The frequency dependence of the STMD demonstrated negligible change to variations to the pendulum mass, so the

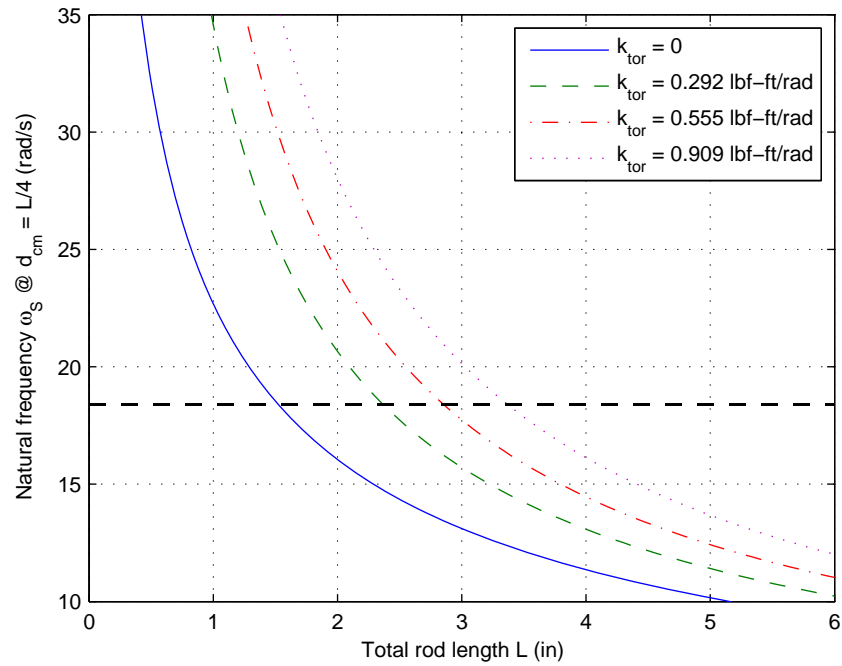


Figure 6.10: Natural frequency of the STMD versus total rod length for auxiliary torsional stiffness $k_{tor} = 0$ (solid), 0.292 lb-ft/rad (dashed), 0.555 lb-ft/rad (dash-dot), and 0.909 lb-ft/rad (dotted). The horizontal dashed line represents the natural frequency required to satisfy the design constraint.

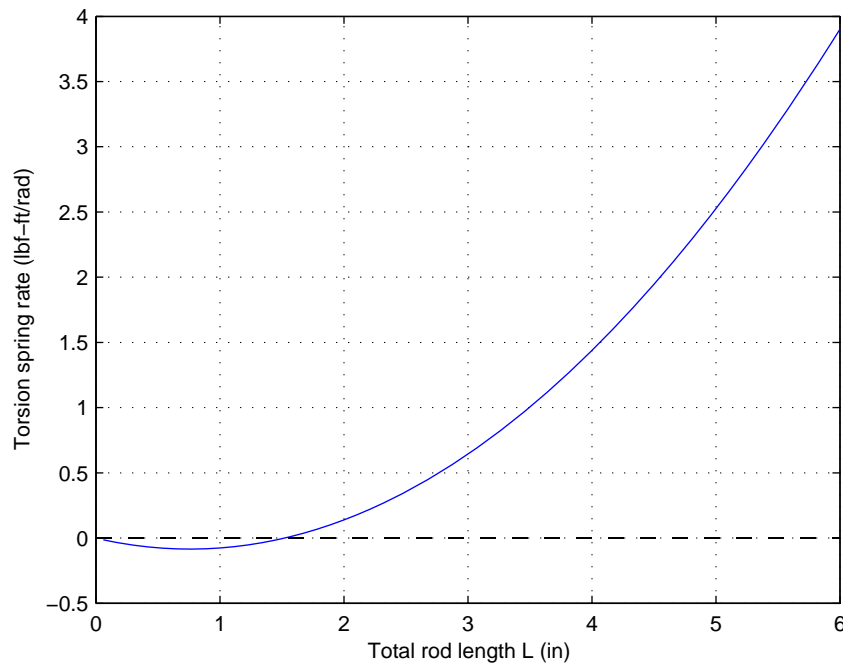


Figure 6.11: Auxiliary torsion spring rate versus total rod length required to satisfy the design constraint.

results shown correspond to the case of $m_p^* = m_s^*$. As expected, the auxiliary torsional stiffness increases the natural frequency. For the case of zero torsional stiffness, the corresponding rod length is only 1.5 in (3.8 cm), imposing a significant limitation on the lateral displacement range. By maximizing the auxiliary torsional stiffness within a reasonable range, the corresponding rod length increases and the lateral displacement range is increased.

Substituting Eqns. (6.54) and (6.56) and the nominal offset distance $d_{cm} = L/4$ into Eqn. (6.55) and solving for k_{tor}^* gives the torsional spring rate required to satisfy the frequency constraint versus the total rod length, plotted in Fig. 6.11. The zero intercept at $L = 1.5$ in (3.8 cm) indicates that no auxiliary torsion spring is needed for a rod length of 1.5 in (3.8 cm). The corresponding linear range and the range of achievable frequencies, however, would be limited.

In order to maximize the total rod length considering the available resources which

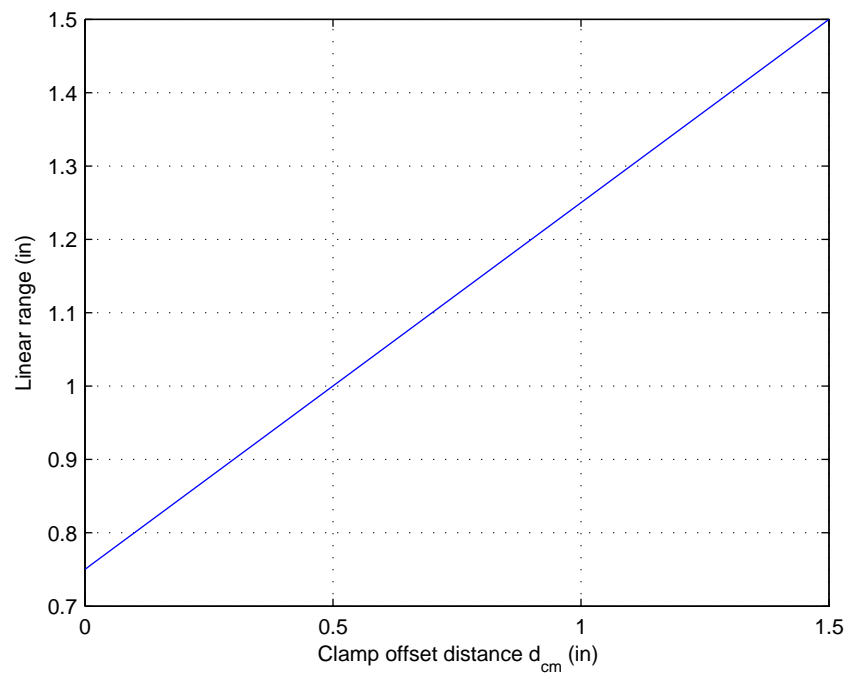


Figure 6.12: Linear range of the pendulum versus clamp offset distance at $k_{tor} = 0.682$ ft-lbf/rad.

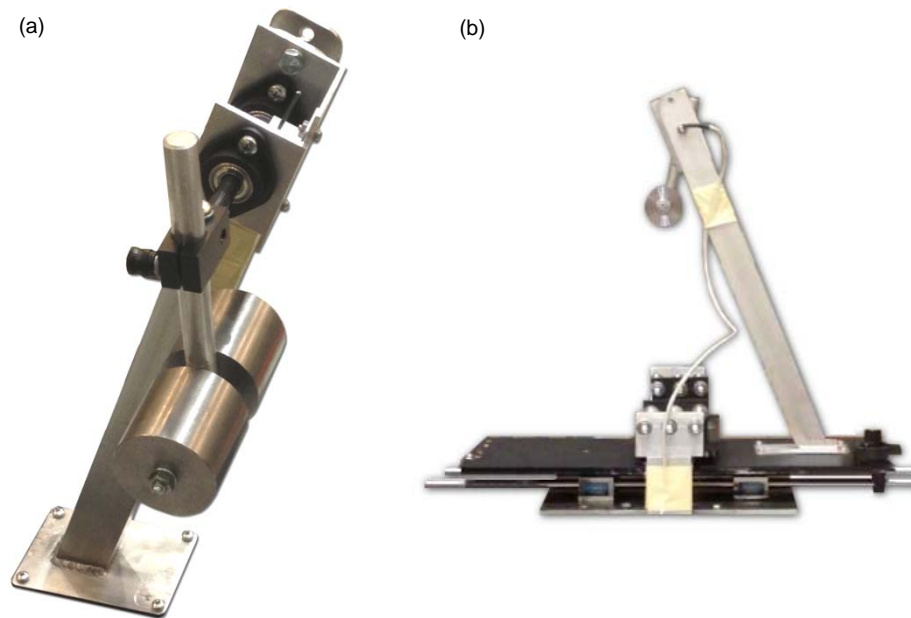


Figure 6.13: Photo of the (a) adjustable-length pendulum STMD and (b) STMD attached in series with the NTMD.

fit the size limitations of the application, an auxiliary spring with a published rate of $k_{tor}^* = 0.682 \text{ ft-lbf/rad}$ (0.925 N-m/rad) is selected. Figure 6.12 illustrates a simple estimate of the linear range of lateral motion $|n_S|$ versus the clamp offset distance d_{cm} based on the total rod length corresponding to the selected spring and the angular displacement constraint, $\theta_S \leq 30 \text{ deg}$. The results shown in Fig. 6.12 indicate an approximate linear range of $0.75 - 1.5 \text{ in}$ ($1.9 - 3.8 \text{ cm}$) and calculations using Eqns. (6.51) and (6.52) indicate an achievable frequency of up to 4.0 Hz (25 rad/s), both of which are expected to be large enough to observe most of the key results.

Photographs of the (a) adjustable-length pendulum STMD and (b) STMD attached in series with the NTMD are illustrated Fig. 6.13. The torsional springs are contained within the housing to which the two bearings are mounted (see Fig. 6.13(a)). The natural frequency of the STMD is adjusted by loosening the black rod clamp and changing the effective length of the pendulum. The encoder used to measure the an-

gular displacement of the STMD is in line with the rod clamp and bearings and is visible in Fig. 6.13(b).

In order to estimate the true spring rate of the selected torsion springs, a perpendicular force is applied to the end of the pendulum rod using the load cell and the resulting angular displacement is measured by the encoder. The corresponding moment load versus deflection curve obtained by combining the data from separate clockwise and counterclockwise tests is presented in Fig. 6.14 (solid). The best fit line calculated by a first-order least squares approximation appears as a dashed line. The slope of the best-fit line indicates an estimated spring rate of $k_{tor}^* = 1.240$ ft-lbf/rad (1.681 N-m/rad), nearly double the expected value. To compensate for the higher spring value, a longer pendulum rod is used ($L = 5.610$ in (14.2 cm)), providing the same frequency tuning capability as the original design but with the added benefit of a larger linear range.

By adjusting the STMD pendulum to various lengths, measuring the effective length with a pair of calipers and analyzing the corresponding frequency-response of the STMD to direct base excitation, the relationship between the length of the pendulum and natural frequency is determined. Figure 6.15 shows the numerical prediction using Eqn. (6.55) and the characterized spring rate value of $k_{tor}^* = 1.240$ ft-lbf/rad (1.681 N-m/rad) (solid) compared with the experimental data (\circ). By refining the estimate of the actual spring rate value to $k_{tor} = 1.6$ ft-lbf/rad (2.2 N-m/rad), a better fit numerical approximation is plotted (dashed). Based on results, the adjustable range of the natural frequency of the STMD is sufficient to satisfy the design constraint.

The STMD damping ratio is then calculated by analyzing the free response oscillations using the procedure outlined in Section 6.3.1. The response data from five tests is presented in Fig. 6.16. The logarithmic decrement is calculated to be $\delta = 0.3322$, and the damping ratio corresponding to the length of the pendulum used in the test is

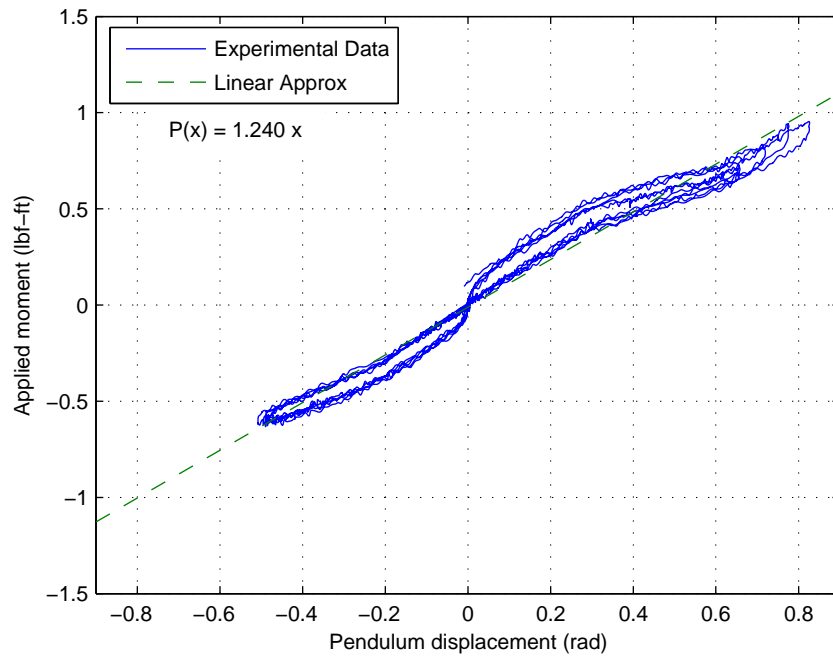


Figure 6.14: Applied moment versus angular displacement of the STMD pendulum component (solid) with zero added mass ($m_p = 0$) and a first-order least squares approximation (dashed) indicating the torsional spring rate k_{tor} .

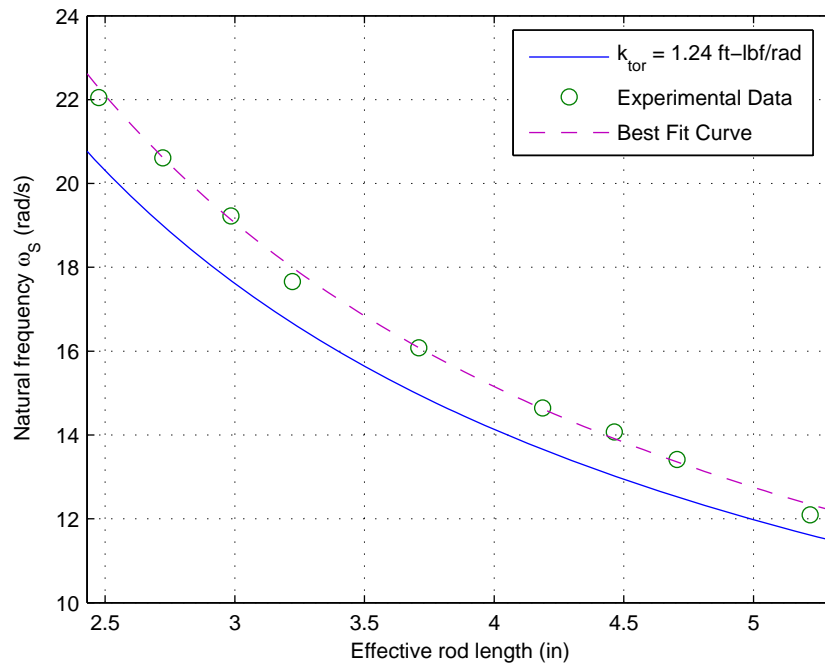


Figure 6.15: Natural frequency of the STMD versus effective length of the pendulum rod based on numerical predictions using the characterized torsion spring rate of $k_{tor}^* = 1.24$ ft-lbf/rad (solid), experimental data (\circ), and the numerical approximation best-fit to the experimental data by using a value of $k_{tor} = 1.6$ ft-lbf/rad (dashed).

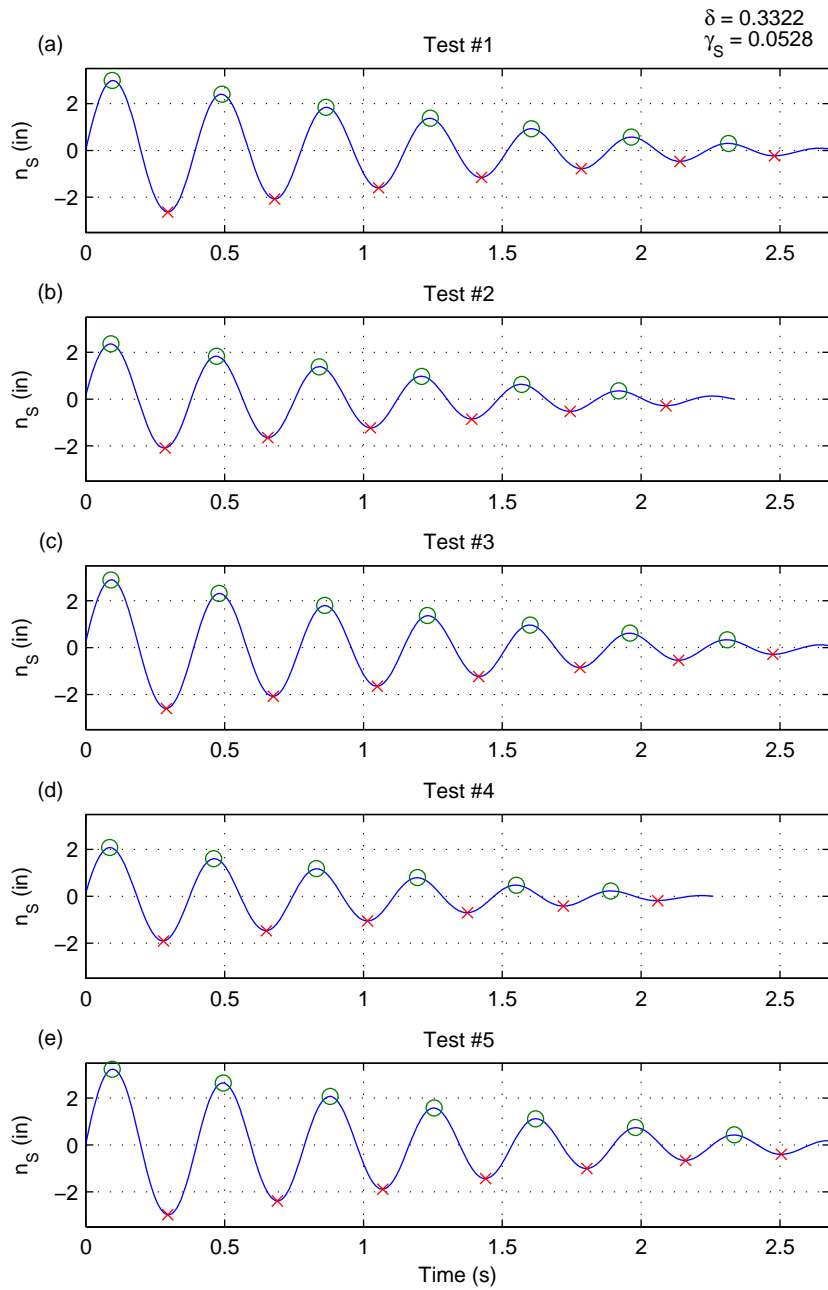


Figure 6.16: STMD lateral displacement versus time (solid) and the corresponding local minima (\times) and maxima (\circ) of the decaying free oscillations.

Table 6.2: Experimental system parameters (dimensional).

Parameter	Value
Mass of primary structure (PS), M	367.0 lb (166.5 kg)
Linear stiffness coefficient of PS, k_1	399.9 lbf/in (70.04 kN/m)
Natural frequency of PS, ω_1	3.265 Hz (20.51 rad/s)
Damping coefficient of PS, c_1	20.82 lbf-s/ft (303.8 N-s/m)
Mass of NTMD frame, m_f	22.00 lb (9.980 kg)
Linear stiffness coefficient of NTMD, k_N	13.31 lbf/in (2.331 kN/m)
Nonlinear stiffness coefficient of NTMD, α_N	6.560 lbf/in ³ (1 781 kN/m ³)
NTMD nonlinear stiffness parameter, Ω_N	0.5230 in ⁻¹ (20.59 m ⁻¹)
Damping coefficient of NTMD, c_N	0.9338 lbf-s/ft (13.63 N-s/m)
Torsional stiffness coefficient of STMD, k_{tor}	1.240 lbf-ft/rad (1.681 N-m/rad)
Length of pendulum rod, L	5.610 in (0.4675 m)
Mass of A-frame supporting pendulum, m_a	1.696 lb (0.7693 kg)
Mass of pendulum rod, m_r	0.1522 lb (0.06904 kg)
Mass of pendulum, m_p	3.444 lb (1.562 kg)
Effective Mass of STMD m_S (Nominal)	3.492 lb (1.584 kg)
Effective Mass of STMD (Variable)	± 0.002 lb (± 0.001 kg)
Damping coefficient of STMD, c_S	0.1949 lbf-s/ft (2.844 N-s/m)

$\zeta = \left(1 + \left(\frac{2\pi}{\delta}\right)^2\right)^{-1/2} = 0.0528$. Assuming a constant damping coefficient, the STMD damping parameter is then calculated as

$$\hat{\gamma}_S = \zeta \frac{\omega_d}{\omega_1} = 0.04375. \quad (6.57)$$

A summary of the experimental parameter values determined from the characterization tests is presented in Table 6.2. Table 6.3 lists the values of the corresponding non-dimensional design parameters.

6.4 Experimental Results

Before investigating the performance of the STMD, the behavior of the reference system consisting of the primary structure and NTMD is first characterized. For these initial experiments, the NTMD consists of the frame only, such that $m_N = m_f$.

Table 6.3: Experimental system parameters (non-dimensional).

Parameter	Value
Damping ratio of primary structure, γ_1	0.04447
Mass ratio of NTMD frame, ϵ_f	0.05995
Linear frequency ratio of NTMD, Ω	0.7451
NTMD damping parameter, $\hat{\gamma}_N$	0.03327
Mass ratio of A-frame supporting pendulum, ϵ_a	0.00462
Effective mass ratio of STMD ϵ_S (Nominal),	0.00952
Effective mass ratio of STMD (Variable)	$\pm 7 \times 10^{-6}$
STMD damping parameter, $\hat{\gamma}_S$	0.04375

Figures 6.17 and 6.18 illustrate the frequency response of the primary structure and NTMD, respectively, for the two-DOF reference system at four different base amplitudes: (a) $X_g = 0.04$ in (1.0 mm), (b) $X_g = 0.05$ in (1.3 mm), (c) $X_g = 0.06$ in (1.5 mm), and (d) $X_g = 0.07$ in (1.8 mm). Experimental results (\circ) are compared with stable solutions obtained using numerical continuation methods (solid) and numerical integration methods (\cdot). Unstable solutions and bifurcation points identified by using the numerical continuation methods are represented by dashed lines and diamond markers, respectively. This convention is followed throughout the remainder of the chapter.

The results from the numerical continuation and numerical integration methods match closely. Both methods clearly illustrate the bi-stable regions, responsible for the hysteresis and jump phenomena in the system. In addition to confirming the accuracy of the continuation methods, the close match verifies the non-dimensionalization, since the numerical integration uses the dimensional form of the equations of motion and the continuation methods use the non-dimensional form. The only discrepancy between the results from the two numerical methods is observed in the neighborhood of $\Omega_g = 1$ for $X_g = 0.06$ in (1.5 mm) and 0.07 in (1.8 mm). Here, the solution branch identified with the continuation methods becomes unstable and, as expected, the re-

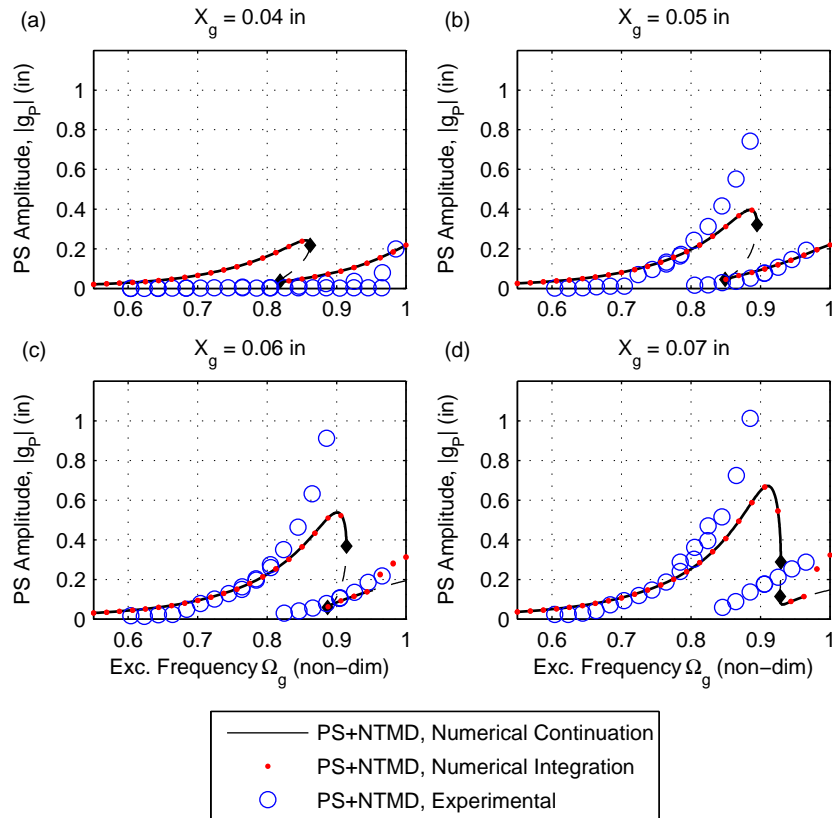


Figure 6.17: Frequency response of the primary structure for the PN system at four excitation amplitudes: (a) $X_g = 0.04$ in, (b) $X_g = 0.05$ in, (c) $X_g = 0.06$ in, and (d) $X_g = 0.07$ in. NTMD mass ratio $\epsilon_N = 6.0\%$.

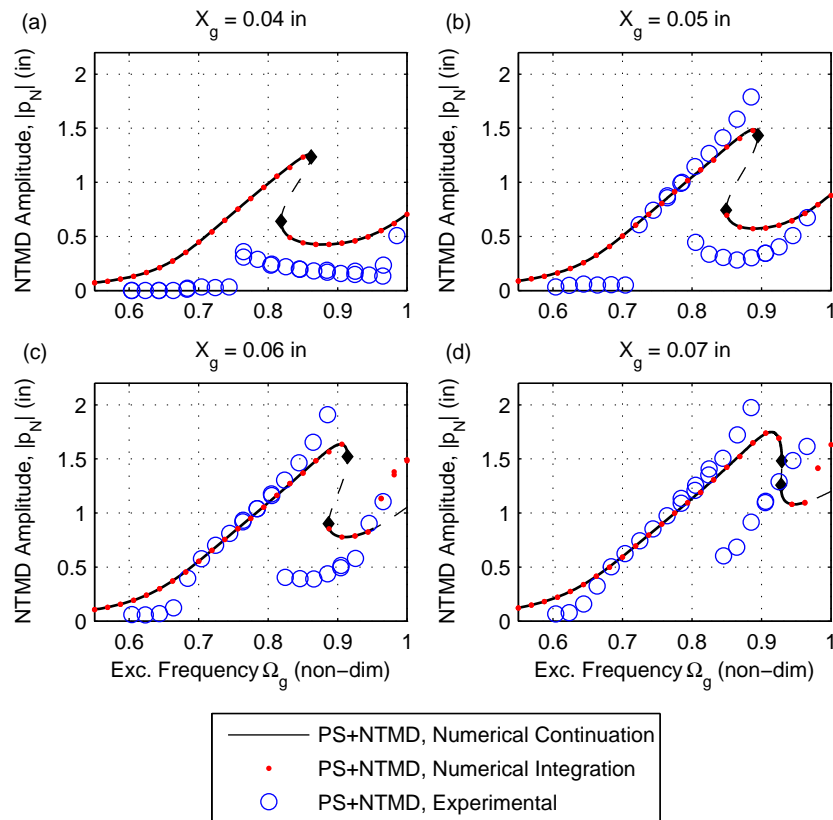


Figure 6.18: Frequency response of the NTMD for the PN system at four excitation amplitudes: (a) $X_g = 0.04$ in, (b) $X_g = 0.05$ in, (c) $X_g = 0.06$ in, and (d) $X_g = 0.07$ in. NTMD mass ratio $\epsilon_N = 6.0\%$.

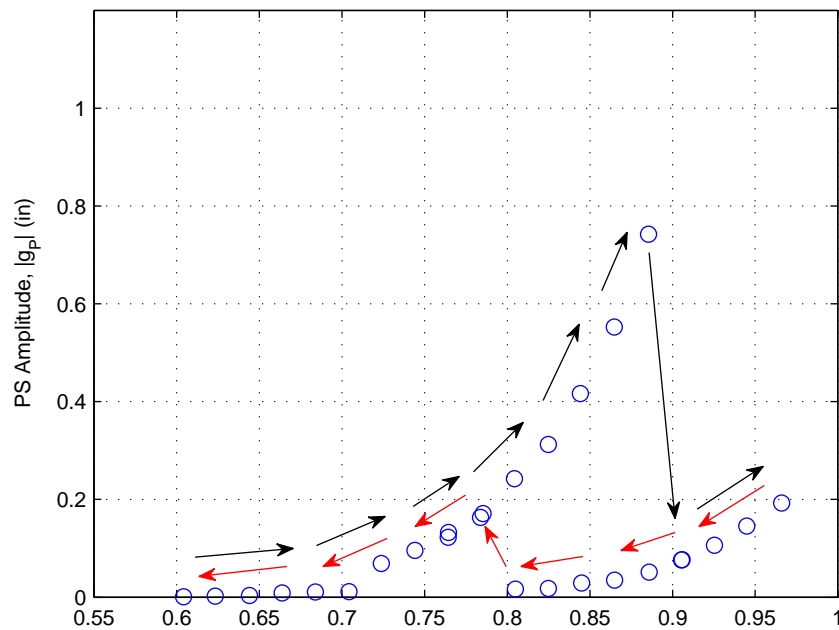


Figure 6.19: Frequency response of the primary structure for the PN system illustrating the hysteresis in the amplitudes of the experimental system obtained during a low-to-high frequency sweep (black arrows) and a high-to-low frequency sweep (red arrows).

sults obtained from numerical integration converge to a different solution, potentially higher-period or quasi-periodic. Since the continuation methods are more computationally efficient and provide a more complete view of the predicted solutions, all numerical results presented in the remainder of the chapter will be produced using these methods, unless otherwise noted.

The experimental results display similar behavior as the numerical results, following the same qualitative trends. The bi-stable regions are clearly observed from the experimental data. In general, incrementally increasing the excitation frequency results in a response that follows the higher-amplitude branch until a high-to-low amplitude jump is experienced in the neighborhood of the bifurcation point marking the edge of the bi-stable region. Conversely, the response follows the lower-amplitude

branch when incrementally decreasing the excitation frequency, followed by a low-to-high amplitude jump. This hysteretic behavior is illustrated in Fig. 6.19. Larger excitation magnitudes increase the effective nonlinearity and result in a larger peak in the high amplitude branch of both the primary structure and NTMD response.

Some quantitative differences are observed between the experimental and numerical results. First, response amplitudes corresponding to $X_g = 0.04$ in (Figs. 6.17 and 6.18) are lower than expected. This is believed to be a result of the energy in the system being too small to overcome the near-static friction forces, which are larger than the kinetic friction forces. In the neighborhood of the high amplitude peak, on the other hand, the experimental results exhibit larger amplitudes than expected. This behavior suggests that the damping in the primary structure and/or NTMD is somewhat lower than the results of the characterization tests indicated, or that the damping in the system may be nonlinear. Finally, the frequencies corresponding to the high-to-low and low-to-high jump phenomena are offset from the numerical predictions. This behavior could result from a number of mechanisms, including error between idealized controller output and the actual base response or insufficient time allowed to converge to a solution due to a slowly changing transient response being misinterpreted as steady-state behavior. Regardless, of the small quantitative discrepancy, the experimental results are able to capture the key behavior. A more complete description of the potential sources of error and the corresponding effects on the experimental data is given in Section 6.6.

In a similar manner, the force response profiles of the primary structure and NTMD at four different excitation frequencies: (a) $\Omega_g = 0.77$, (b) $\Omega_g = 0.85$, (c) $\Omega_g = 0.90$, and (d) $\Omega_g = 0.95$, is presented in Figs. 6.20 and 6.21, respectively. Consistent with the discussion of the frequency response results in Figs. 6.17 and 6.18, the experimental response follows the trends predicted by using the numerical methods. In the force response case, incrementally increasing the excitation amplitude results in

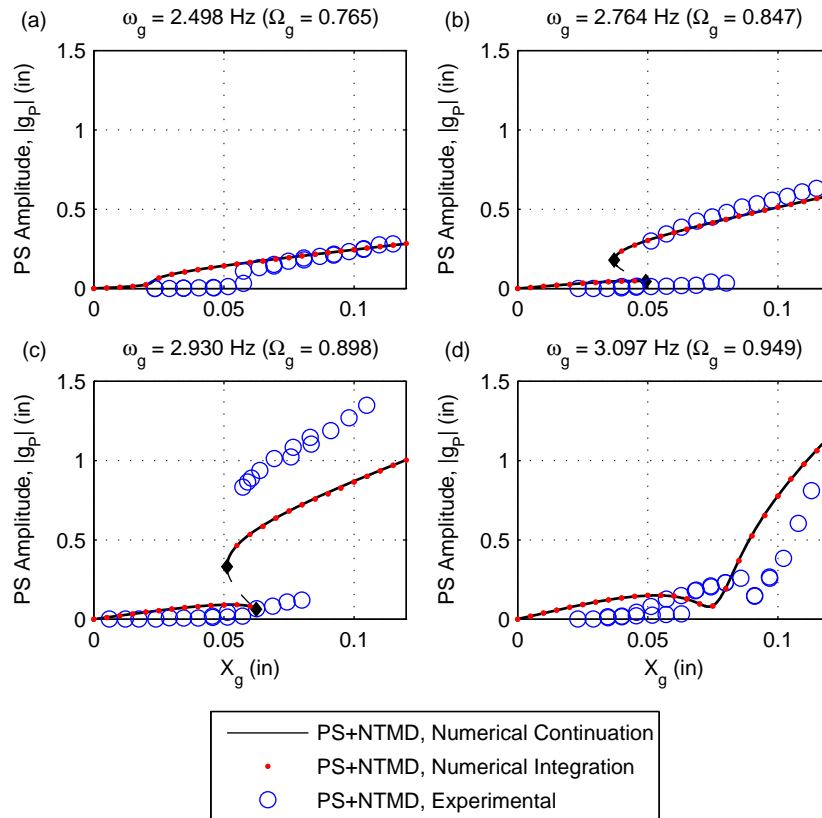


Figure 6.20: Force response of the primary structure for the PN system at four excitation frequencies: (a) $\Omega_g = 0.77$, (b) $\Omega_g = 0.85$, (c) $\Omega_g = 0.90$, and (d) $\Omega_g = 0.95$. NTMD mass ratio $\epsilon_N = 6.0\%$.

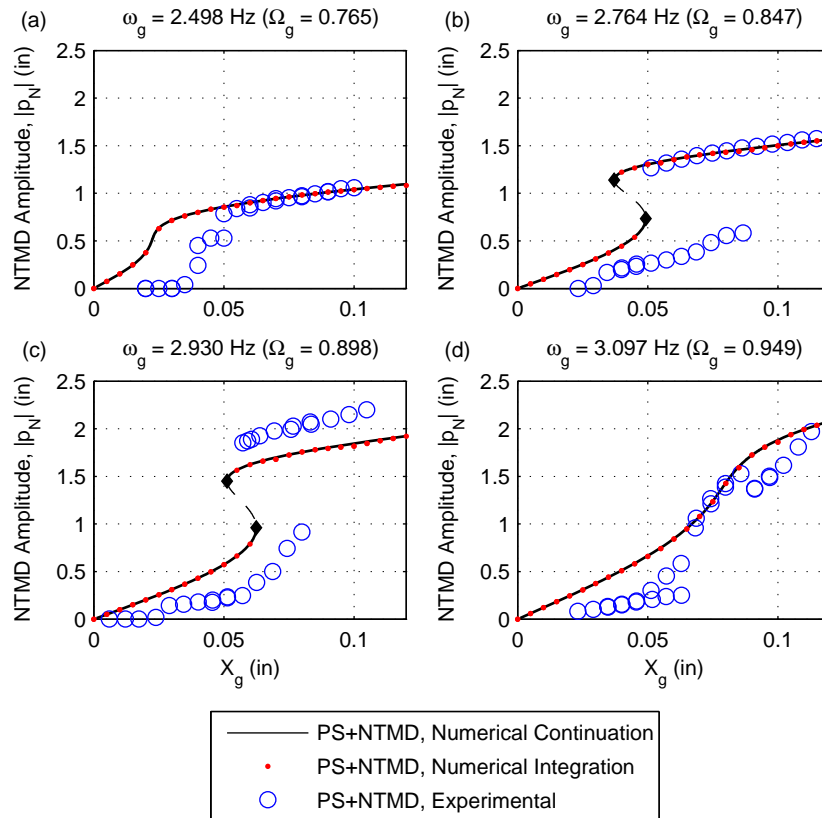


Figure 6.21: Force response of the NTMD for the PN system at four excitation frequencies: (a) $\Omega_g = 0.77$, (b) $\Omega_g = 0.85$, (c) $\Omega_g = 0.90$, and (d) $\Omega_g = 0.95$. NTMD mass ratio $\epsilon_N = 6.0\%$.

a response which follows the low amplitude solution branch and then exhibits a low-to-high amplitude jump. Incrementally decreasing the excitation amplitude leads to the opposite behavior: a high amplitude response and a high-to-low amplitude jump. In the case of $\Omega_g = 0.77$ and $\Omega_g = 0.95$, panels (a) and (d), numerical results predict only a single stable solution. Similar behavior is observed from the corresponding experimental results, exhibiting only low-magnitude jumps and a narrow region resembling hysteretic behavior, both of which could be artifacts of a slowly-decaying transient.

Based on the results observed in Figs. 6.20–6.18 as well as known characteristics of nonlinear systems, it would be possible that a real-world system with a similar nonlinearity could be operating safely within design constraints, but could quickly transition to a potentially dangerous high amplitude response. Due to the relatively large linear stiffness coefficient in the experimental system, both the low and high amplitude response belong to the same solution curve, and are easily observed by modulating the excitation frequency or magnitude. In the case of a near-zero linear stiffness coefficient, however, the high amplitude solution can become detached (see, *e.g.* Fig. 5.2). In this case, it is possible for a system to exhibit a safe, low amplitude response over a broad range of forcing frequencies, only to abruptly transition to a high amplitude solution upon experiencing an impulse.

Figure 6.22 shows the time-series response of the (a) base excitation, (b) primary structure, and (c) NTMD, illustrating a transition from a low to high amplitude response as the result of a small impulse to the primary structure. The time values have been shifted such that the impulse occurs at $t = 0$. Prior to the impulse ($t \ll 0$), the experimental system is brought to a steady-state low amplitude response within the bi-stable region. The excitation signal at the controller is then held constant for the remainder of the simulation, although by examining Fig. 6.22(a) it is observed that the reaction forces from the primary structure do have a small influence on the mea-

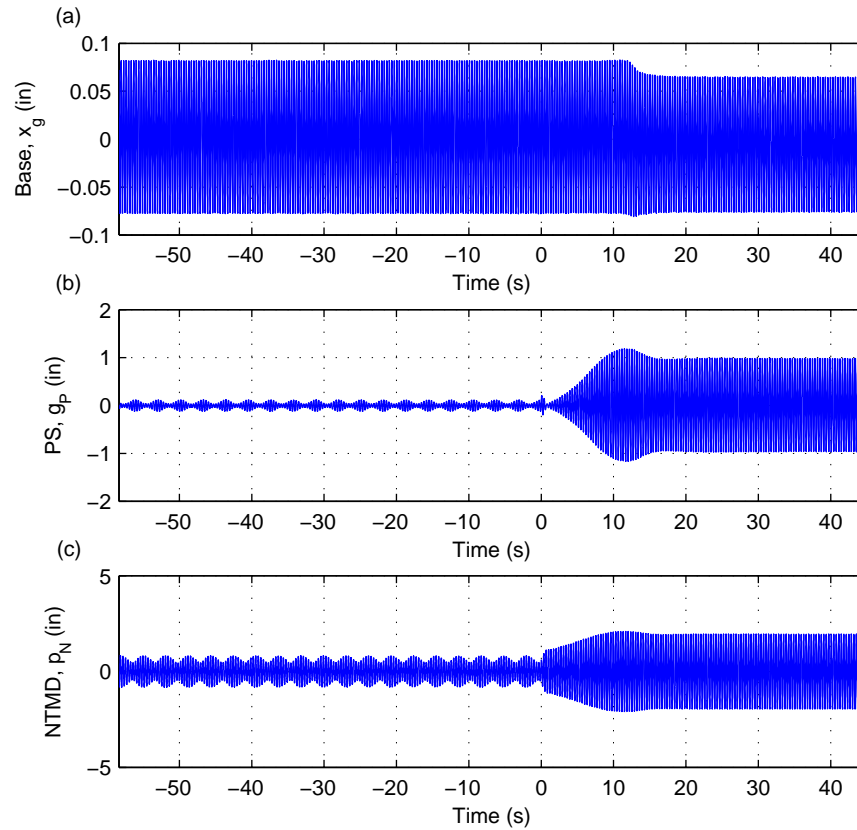


Figure 6.22: Time series response of the (a) base excitation, (b) primary structure, and (c) NTMD illustrating an abrupt transition from a low to high amplitude solution resulting from a small impulse applied to the primary structure at $t = 0$.

sured base response. The low amplitude response resembles the strongly modulated near-periodic response characteristic of systems with a cubic coupling nonlinearity. The impulse was applied by striking the primary structure with a small brass hammer, providing a small enough force that no visible change in the velocity of the primary structure is observed, but initiating a transition to the high amplitude response, an increase of 800% for the primary structure. The results presented in Fig. 6.22 demonstrate the potential danger of transitioning to a high amplitude response within a bi-stable region due to an impulse. The experiments verify the similar numerical results presented in Chapter 5. In the remainder of this section, the performance benefits of adding an auxiliary STMD are explored.

The adjustable-length pendulum STMD is now added in series with the primary structure and NTMD. The response of the PS+NTMD+STMD (PNS) system will be compared with the response of the PS+NTMD (PN) system presented in Figs. 6.17–6.18 ($m_N = m_f + m_a$), representing the performance benefits of retrofitting an STMD to an existing nonlinear absorber. In addition, the PNS response will be compared with new results which illustrate the response of the PN system with a larger NTMD mass such that the mass of the NTMD in the PN system ($m_N = m_f + m_a + m_r + m_p$) is equal to the total mass of the absorber components in the PNS system ($m_N = m_f + m_a$). Since the performance of a vibration absorber is often improved with added mass, this comparison will better isolate the performance benefits of the STMD from other response changes corresponding with a larger absorber.

The frequency tuning of the STMD within the experimental system is accomplished by manually adjusting the length of the pendulum, providing an accurate representation of the steady-state dynamics of the system. Other available systems such as the SAIVS [84] or ALP [95] incorporate actuators to tune the frequency in real-time during operation. However, adjustments to the STMD in the experimental system can only be made when the system is at rest. The force response therefore

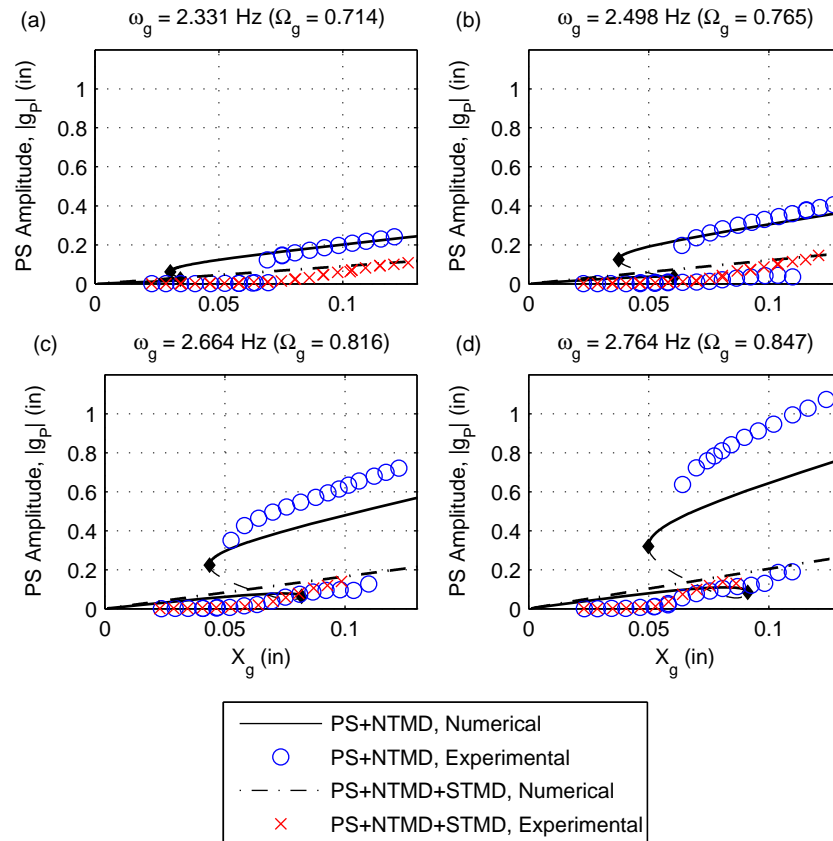


Figure 6.23: Force response of the primary structure for the PN system (numerical: solid/dashed, experimental: \odot) compared with the PNS system (numerical: dash-dot, experimental: \times) at four excitation frequencies: (a) $\Omega_g = 0.71$, (b) $\Omega_g = 0.77$, (c) $\Omega_g = 0.82$, and (d) $\Omega_g = 0.85$. Total mass ratio in each system is 7.4%.

provides a more accurate representation of the performance of the PNS system and would be able to identify any potential hysteretic behavior. Frequency response results are also presented to provide a more complete view of the expected behavior, with the understanding that each data point corresponds to a steady-state response resulting from zero-valued initial conditions.

Figures 6.23, 6.24, and 6.25 illustrate the force response of the primary structure, NTMD, and STMD, respectively, at four excitation frequencies where multiple solutions are expected for the PN system: (a) $\Omega_g = 0.71$, (b) $\Omega_g = 0.77$, (c) $\Omega_g = 0.82$, and (d) $\Omega_g = 0.85$. The solid/dashed lines and \odot markers represent the numerical

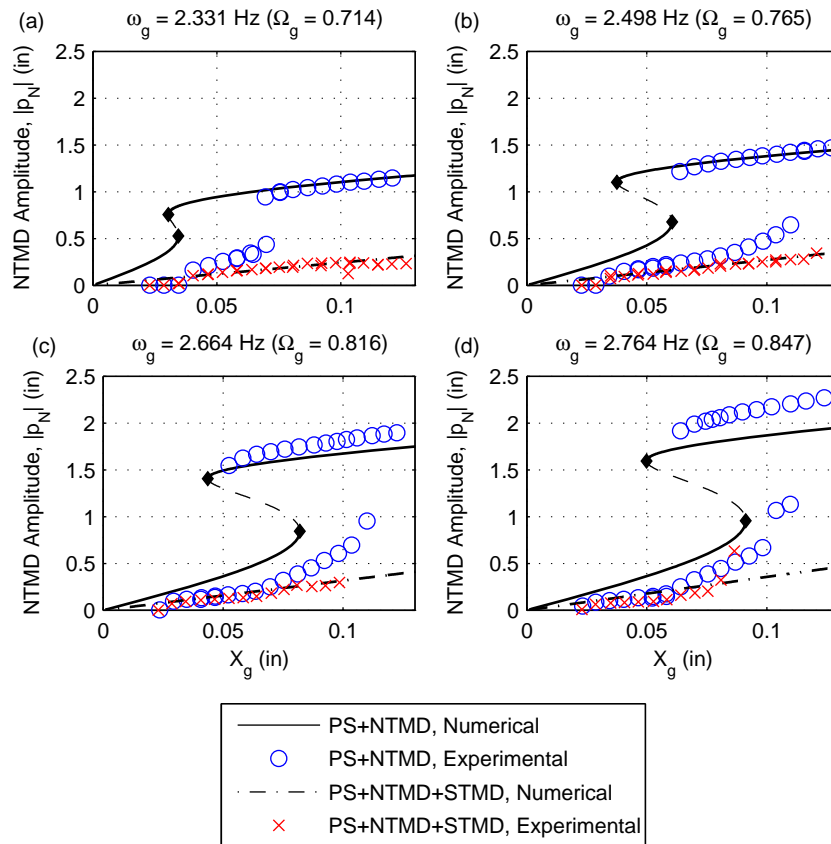


Figure 6.24: Force response of the NTMD for the PN system (numerical: solid/-dashed, experimental: (○)) compared with the PNS system (numerical: dash-dot, experimental: (×)) at four excitation frequencies: (a) $\Omega_g = 0.71$, (b) $\Omega_g = 0.77$, (c) $\Omega_g = 0.82$, and (d) $\Omega_g = 0.85$. Total mass ratio in each system is 7.4%.

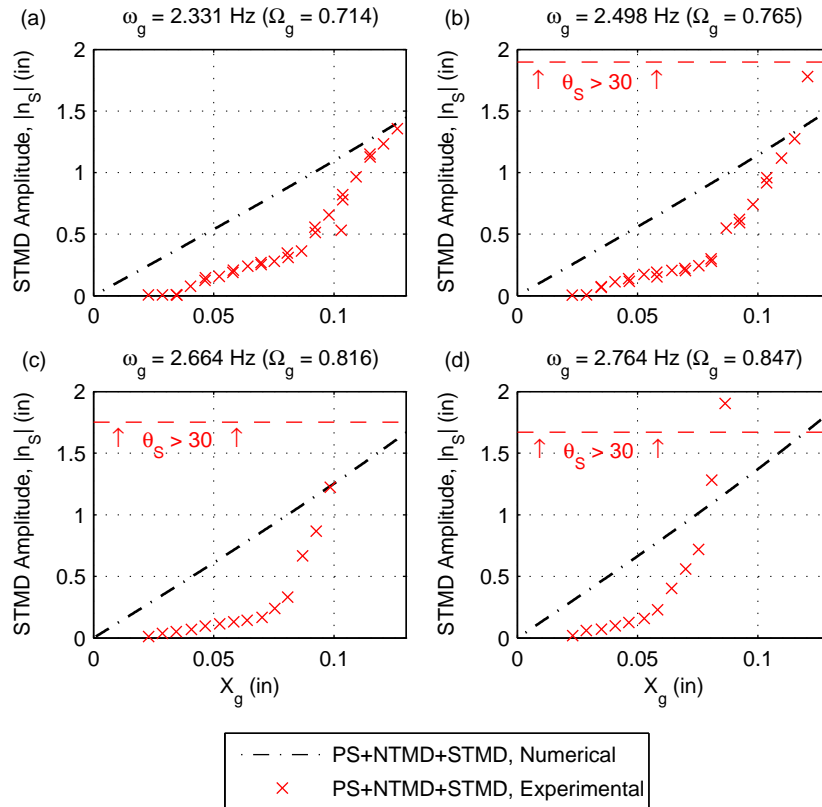


Figure 6.25: Force response of the STMD for the PNS system at four excitation frequencies: (a) $\Omega_g = 0.71$, (b) $\Omega_g = 0.77$, (c) $\Omega_g = 0.82$, and (d) $\Omega_g = 0.85$. Total mass ratio is 7.4%.

and experimental results for the PN system with $m_N = m_f + m_a + m_r + m_p$ and the dash-dot and (\times) markers represent the numerical and experimental results for the PNS system with $m_N = m_f + m_a$, respectively. The experimental simulations were aborted in cases where the angular displacement of the STMD exceeded the design range of ± 30 deg—marked by a red dashed line in Fig. 6.25, resulting in a smaller base amplitude range at the two larger frequencies, panels (c) and (d).

Consistent with the numerical data, the experimental results show that the STMD is capable of eliminating the high amplitude response and the corresponding bi-stable range and jump phenomena. As a result, the primary structure and NTMD continue to exhibit a low amplitude response which slowly increases proportional to the excitation magnitude until the linear range of the STMD is exceeded. The addition of the SMTD therefore creates a more predictable response where no potentially dangerous amplitude jumps are observed.

The frequency response of the PN and PNS systems at four excitation magnitudes: (a) $X_g = 0.04$ in (1.0 mm), (b) $X_g = 0.05$ in (1.3 mm), (c) $X_g = 0.06$ in (1.5 mm), and (d) $X_g = 0.07$ in (1.8 mm) are compared in Figs. 6.26 (PS), 6.27 (NTMD), and 6.28 (STMD). Line and marker styles denoting the numerical and experimental results of each follow the convention used in the force response plots. As previously noted, the force response profiles provide a better means by which to directly compare the performance of the two systems, so experimental results for the PN system are limited to only one case, used only to verify the response changes due to the added mass when compared with the results in Figs. 6.17 and 6.18.

The experimental data agrees with the numerical results, showing no response amplitudes in the neighborhood of the high amplitude solution branch observed in the PN system. The STMD limits the motion of the NTMD, reducing the effective nonlinearity and resulting in a primary structure response in the neighborhood of the low amplitude PN solution. It is noted that for the larger excitation magnitudes

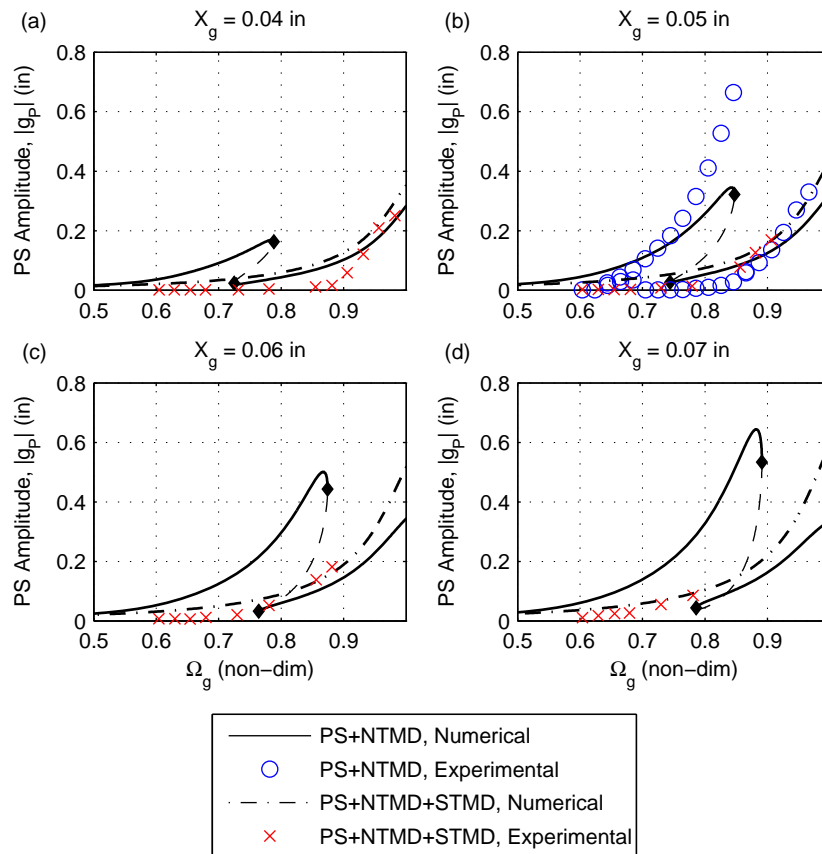


Figure 6.26: Frequency response of the primary structure for the PN system (numerical: solid/dashed, experimental: (○)) compared with the PNS system (numerical: dash-dot, experimental: (×)) at four excitation amplitudes: (a) $X_g = 0.04$ in, (b) $X_g = 0.05$ in, (c) $X_g = 0.06$ in, and (d) $X_g = 0.07$ in. Total mass ratio in each system is 7.4%.

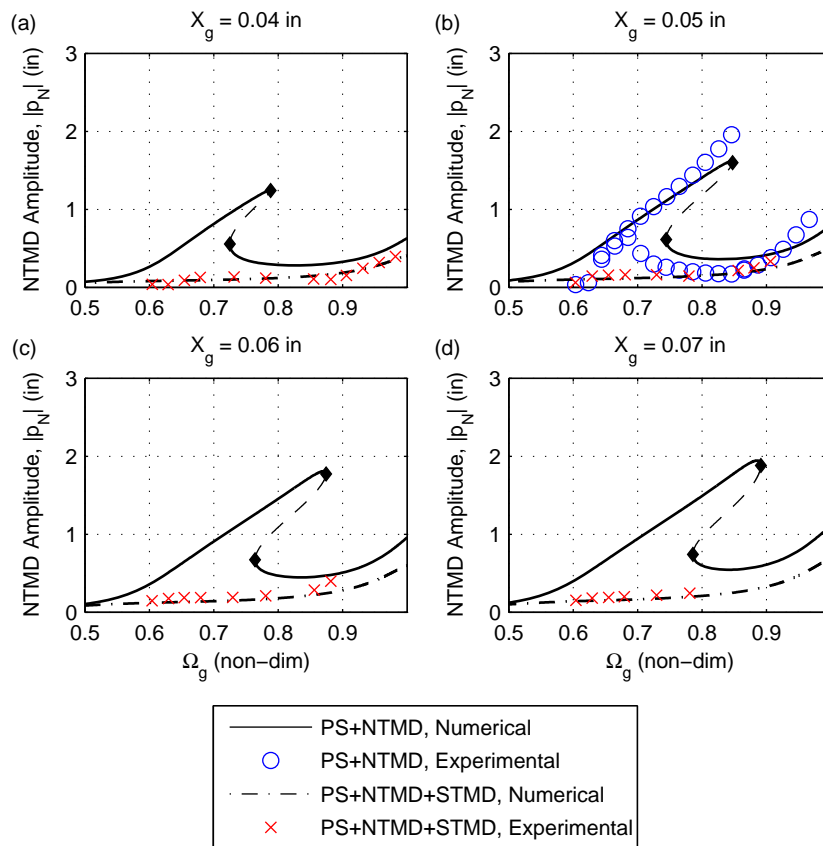


Figure 6.27: Frequency response of the NTMD for the PN system (numerical: solid/-dashed, experimental: (○)) compared with the PNS system (numerical: dash-dot, experimental: (×)) at four excitation amplitudes: (a) $X_g = 0.04$ in, (b) $X_g = 0.05$ in, (c) $X_g = 0.06$ in, and (d) $X_g = 0.07$ in. Total mass ratio in each system is 7.4%.

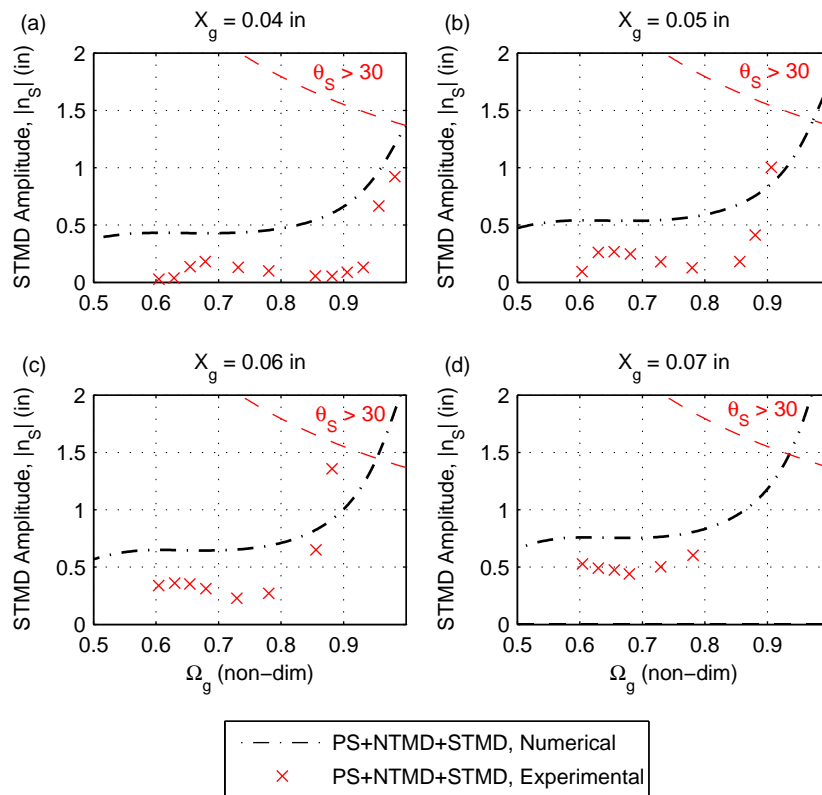


Figure 6.28: Frequency response of the STMD for the PNS system at four excitation amplitudes: (a) $X_g = 0.04$ in, (b) $X_g = 0.05$ in, (c) $X_g = 0.06$ in, and (d) $X_g = 0.07$ in. Total mass ratio is 7.4%.

(particularly (c) and (d)), the numerical results predict a much larger PNS response near the fundamental frequency ($\Omega_g = 1$) than the PN response. In this region, the nonlinearity in the NTMD improves the performance of the system. This can be easily avoided by intentionally detuning or deactivating the STMD when the response enters this region. The idea of activating and deactivating the STMD will be discussed later in this section.

The frequency response and force response figures provide a broad representation of the expected response of the PNS system under a variety of excitation conditions. It is also helpful to illustrate the time domain response corresponding to excitation conditions which lead to a low-to-high amplitude transition for the PN system but where the PNS system response experiences no abrupt transition and maintains a low amplitude response under similar conditions. The low-to-high transition was easily accomplished by impacting the primary structure, as shown in Fig. 6.22. Considering the available resources, however, it would be difficult to reproduce similar impacts in each structure and therefore an alternate method of illustrating this behavior is used.

Figure 6.29 illustrates the time series response of the (a) base excitation, (b) primary structure, and (c) NTMD in the PN system as the excitation magnitude is gradually increased to a maximum of $X_g \approx 0.12$ in (3.0 mm) then gradually decreased and held constant at $X_g = 0.06$ in (1.5 mm). The tuning frequency is $\Omega_g = 0.765$, corresponding to the data presented in Figs. 6.23(b)–6.25(b). At $t = 38$ s, corresponding to an excitation amplitude of approximately $X_g = 0.11$ in (2.8 mm) a clear transition from a low to high amplitude response is observed in the primary structure. Although the excitation amplitude is subsequently decreased and held constant for $t > 65$ s at nearly half of its peak value, the response of the primary structure and NTMD remain at a high amplitude indefinitely.

In comparison, Fig. 6.30 illustrates the response of the (a) base excitation, (b) primary structure, (c) NTMD, and (d) STMD under similar excitation conditions. It

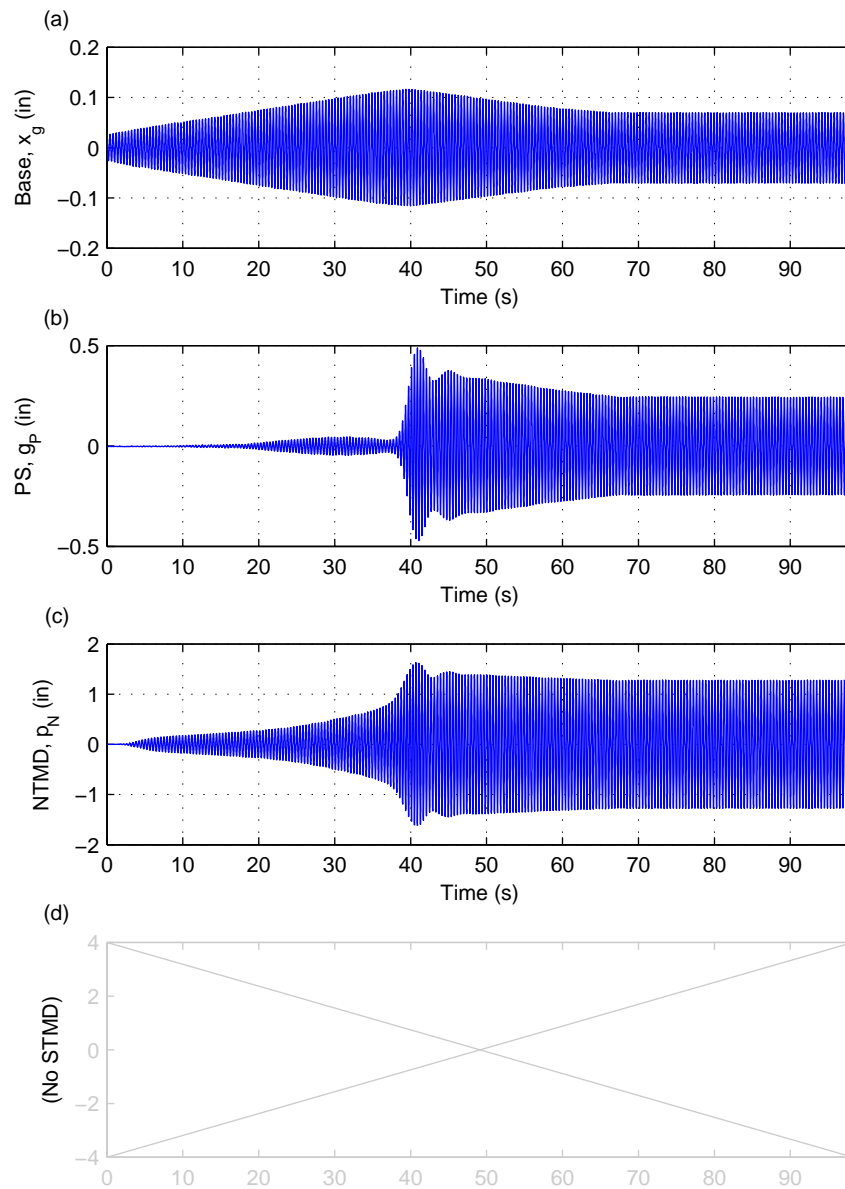


Figure 6.29: Time series response of the excitation and each component in the PN system as the excitation amplitude is gradually increased, decreased, then held constant.

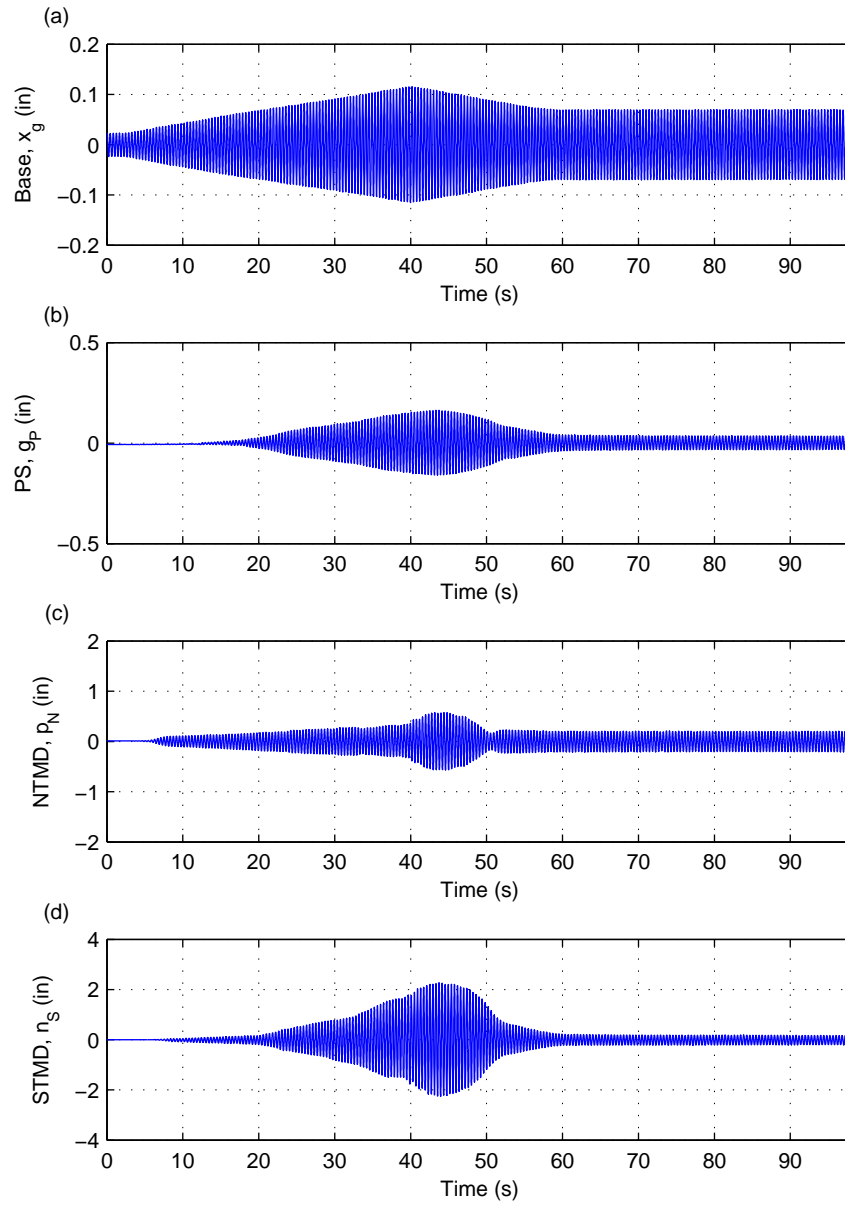


Figure 6.30: Time series response of the excitation and each component in the PNS system as the excitation amplitude is gradually increased, decreased, then held constant.

is noted that the excitation amplitude is modulated manually and therefore the two signals illustrated in Figs. 6.29(a) and 6.30(a) are not completely identical, but the signals are expected to be sufficiently similar to accurately compare the behavior of the two systems. In the PNS system, Fig. 6.30, the amplitudes of the PS, NTMD, and STMD increase and decrease proportionally with the excitation amplitude. The peak primary structure amplitude in the PNS system is 0.16 in (4.1 mm), compared with the peak value of 0.50 in (13 mm) for the PN system. The PNS system displays no hysteretic behavior and returns to an amplitude of 0.04 in (1.0 mm), which is 86% less than the corresponding amplitude of 0.24 in (6.1 mm) for the PN system. These results help to demonstrate that under the same conditions that would cause an abrupt and potentially dangerous increase in the response amplitude of the primary structure for the PN system, the PNS system exhibits a predictable, low amplitude response.

As discussed in Chapter 5, to implement both a strongly nonlinear TMD and a semi-active TMD under all response conditions would be impractical, since the STMD acts primarily to minimize the effects of the NTMD. Instead, the proposed implementation is to use the STMD as a safety device in order to harness the favorable effects of the NTMD while also protecting against a high amplitude response. In order to conclude the experimental study, a demonstration of the STMD performance under conditions resembling the proposed application is presented. Figure 6.31 illustrates the time series response of the (a) base excitation, (b) primary structure, (c) NTMD, and (d) STMD as the STMD motion is constrained and then released. The displacement $n_S(t)$ is calculated from the measured angular displacement $\theta_S(t)$ by using the effective length L and correcting for an offset shift between the disabled and enabled state.

For $t < 0$, the STMD is effectively deactivated by using a dowel pin extending through the pendulum rod and mounting frame, illustrated in Fig. 6.32. A small

STMD amplitude of $|n_S| = 0.38$ in (0.97 cm) is observed as a result of manufacturing the pin housing with sufficient clearance to allow for the dowel pin to be quickly removed during operation. Regardless, the dowel pin succeeds at constraining the motion of the pendulum enough that the effect of the STMD is negligible for $t < 0$.

The large amplitude motion observed in the deactivated state ($t < 0$) is the result of a short-term excitation amplitude increase causing a low-to-high amplitude transition. At $t = 0$, the pin is removed, allowing for the full range of pendulum displacement and activating the STMD. As a result, the system quickly transitions to a low amplitude response where it remains indefinitely. This experiment demonstrates one simple mechanism for activating/deactivating the device, and more importantly verifies that the deactivated STMD has a negligible effect on the PN system. Then, upon activation, the STMD is capable of quickly attenuating the system response.

6.5 Summary of Results

The experimental results presented in this chapter have successfully demonstrated three key points, summarized as follows.

- The qualitative agreement between the experimental data and the numerical results observed in Figs. 6.17–6.21 and 6.23–6.28 verifies that the dynamic model used in Chapters 5–6 accurately predicts the key response behavior. Qualitative discrepancies between the results are generally small and may be the result of a number of factors discussed in Section 6.6. Furthermore, the close match between the results obtained using numerical integration and a dimensional model and those obtained using numerical continuation and a non-dimensionalized model demonstrates the agreement between the methods and validates that no errors were made in the non-dimensionalization.
- The coexistence of multiple stable solutions and the associated hysteretic be-

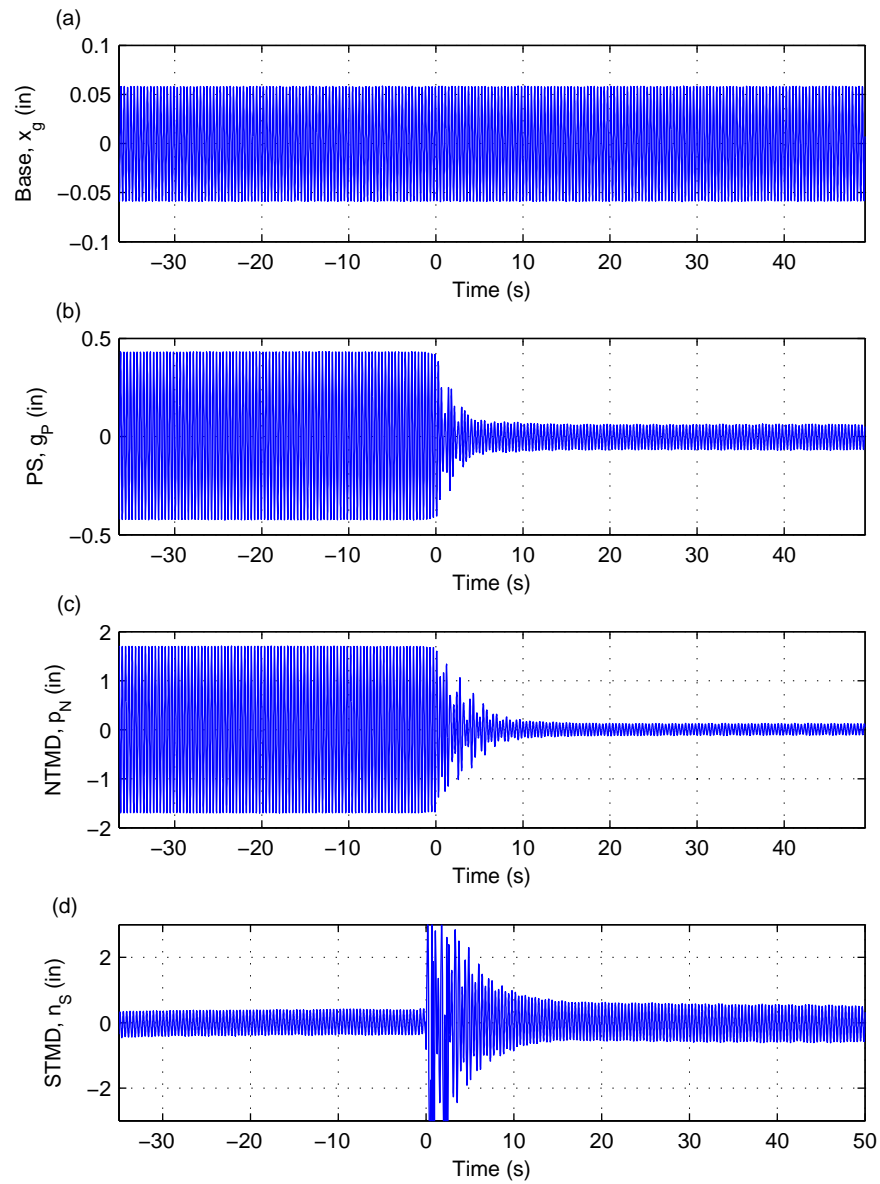


Figure 6.31: Time series response of the excitation and each component in the PNS system with the pendulum motion constrained for $t < 0$ to deactivate the STMD and free for $t \geq 0$, activating the STMD and attenuating the response.

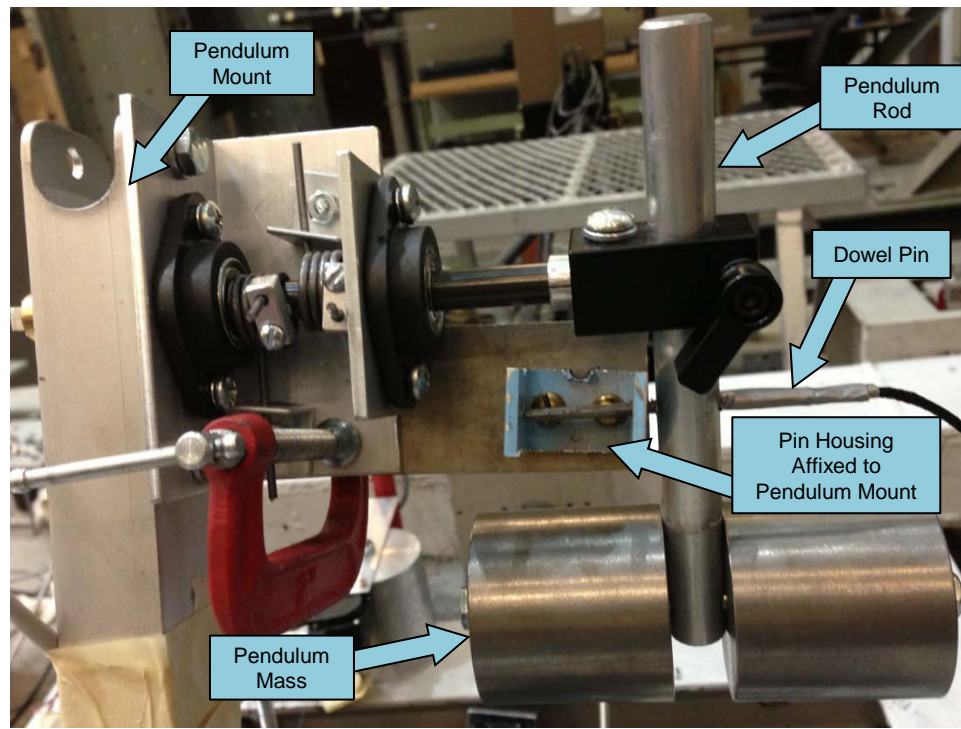


Figure 6.32: Mechanism used to fix the displacement of the STMD, consisting of a dowel pin inserted through the pendulum rod into a bracket which is clamped to the pendulum mount.

havior and jump phenomenon are successfully observed from the experimental results (*e.g.* Figs. 6.20–6.21). In addition, it is shown that a short-term perturbation can transition the response from the low amplitude to the high amplitude solution (Fig. 6.22). These results demonstrate the potentially dangerous and unpredictable behavior that can result in the NTMD system and form the motivation for the series STMD investigated in the present thesis.

- By using an adjustable-length pendulum STMD with an effective mass of only 1% of the primary structure mass, no bi-stability is observed in the experimental and numerical data, indicating successful elimination of the associated complex response transitions and attenuating the primary structure response (Figs. 6.23–6.28). Furthermore, by using a dowel pin to temporarily constrain the angular deflection of the STMD, the concept of deactivating and activating the STMD is illustrated (Fig. 6.31), allowing for the favorable characteristics of the NTMD to be utilized while using the STMD as a safety device in the event of a low-to-high amplitude transition.

6.6 Potential Sources of Error

The experimental results presented within Section 6.4 effectively displayed key behavior characteristics and demonstrated a qualitative agreement with the results obtained using numerical integration and continuation methods. The qualitative discrepancies between the experimental and numerical results were generally small, and may be the result of a number of factors. This section identifies a number of mechanisms that may have contributed to the qualitative discrepancies, organized from greatest to least potential effect on the measured response.

6.6.1 Nonlinear Viscous Damping

The damping ratios of the PS, NTMD, and STMD were calculated in Sections 6.3.1–6.3.3 by using the logarithmic decrement corresponding to adjacent local maxima of the decaying free response. In a system with ideal linear damping, the logarithmic decrement would be consistent indicating an exponential decay. However, in the characterization test results, the value of the logarithmic decrement increased as the amplitudes decayed, indicating that the effective damping ratio is lower at high amplitudes and higher at low amplitudes. The damping ratio presented in Table 6.3 for each structure was calculated by averaging the results from the adjacent peaks. For the primary structure, the characterized damping ratios actually ranged from $\gamma_1 = 0.038$ – 0.049 based on free response amplitudes ranging from 1.0 in (2.5 cm) to 0.3 in (0.7 cm). Since actual response amplitudes ranged from $0 \leq |g_P| < 2$, an even larger variation of the damping ratio can be expected. Similar behavior was observed during the characterization of the NTMD component.

Some of the nonlinear damping behavior may be attributed to energy in the system being too small at very low amplitudes to overcome the near-static friction forces, which are larger than the kinetic friction forces. The results presented in Figs. 6.17(a)

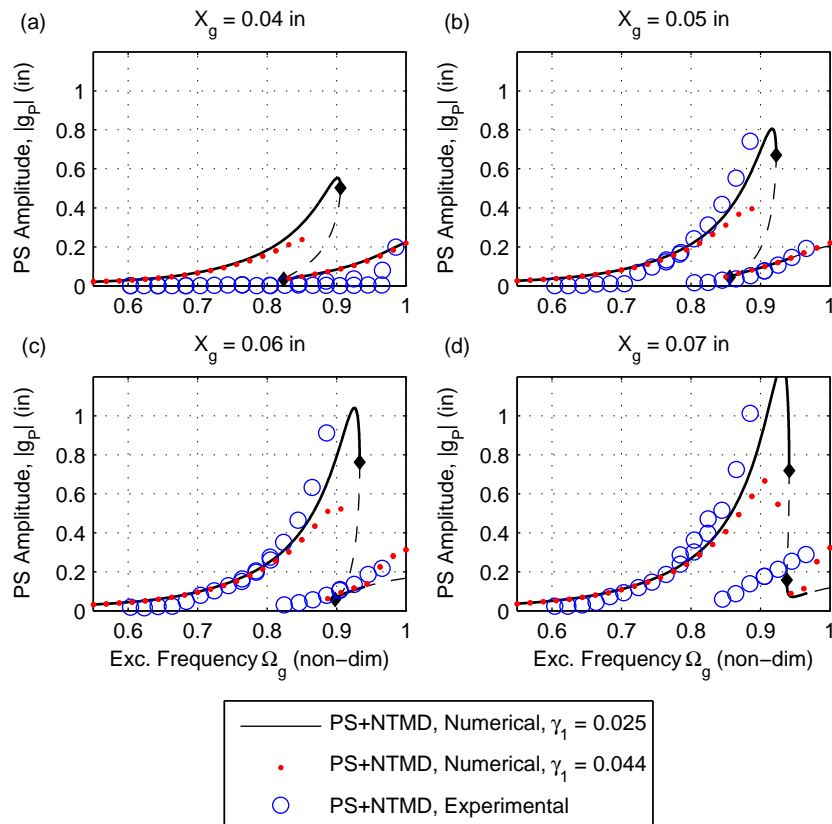


Figure 6.33: Frequency response of the primary structure for the PN system highlighting the effects of PS damping in the numerical results with the experimental data.

and 6.20(a), for example, support this conclusion—the primary structure response amplitudes remain near zero when a small non-zero response is expected. Another mechanism that may contribute to the observed nonlinear damping behavior is the breathing mechanisms in the linear spring, illustrated in Fig. 6.2. The purpose of the breathing holes and flattened shaft are to minimize the nonlinear stiffness effects that would result from air being compressed in the piston-like spring guide during normal operation. However, the breathing mechanisms introduce additional damping from the friction forces resulting from the air flow, the effects of which may be assumed to be nonlinear.

Figure 6.33 illustrates the influence of the damping in the primary structure on

the predicted numerical response. The numerical integration (\cdot) and experimental (\circ) results correspond to the data presented in Fig. 6.17. Numerical continuation results using a damping ratio of $\gamma_1 = 0.025$, 43% less than the characterized value are displayed using solid and dashed lines. A better agreement with the experimental data in the neighborhood of the detached resonance peak is observed for the lower damping ratio. A decrease in the damping ratio of the NTMD produces a similar increase in the primary structure response amplitudes. The damping ratio values obtained by averaging the results from the characterization tests were sufficient in order to qualitatively verify the key behavior using numerical simulations. A quantitative agreement could be obtained by introducing nonlinear damping terms into the numerical model and conducting a series of additional characterization tests to predict the corresponding parameter values.

6.6.2 Non-Ideal Excitation

Based on the results of the shaker table characterization tests published in Ref. [133], the total mass of the PNS system was believed to be small enough to have a negligible influence on the shaker dynamics. When the experimental system was oscillating at low amplitude, no influence from the system response on the shaker dynamics was observed. However, for high amplitude oscillations the reaction forces were not negligible, and the phase offset of the primary structure response relative to the shaker resulted in a decrease of the base displacement amplitude. This behavior can be observed in Fig. 6.22(a), for example. In this case, the controller output was configured to produce a constant base amplitude of 0.07 in (1.8 mm) throughout the test. However, before and after the low-to-high PS amplitude jump the measured base amplitude was 0.08 in (2.0 mm) and 0.07 in (1.8 mm), respectively, a decrease of 13%. An error in the identified base amplitude values would result in a lateral shift of force-response data points and could modify the shape or amplitude of a frequency-

response curve. As an attempt to compensate for the effects of this behavior, all force-response data points were plotted using the measured base amplitudes rather than the controller set-point amplitude.

6.6.3 Transient Response

The experimental data points were obtained by monitoring the response signal as the transient behavior decayed and calculating the response amplitudes after 10–30 seconds of observing behavior resembling steady state conditions. In some cases, however, the high-to-low and low-to-high response transitions occurred after long periods (60+ seconds) of what appeared to be a steady state response. The slow transitions in these regions can be attributed to a non-hyperbolic response at the bifurcation point [57]. After this behavior was identified, efforts were made to dedicate more time to letting the transient decay in the neighborhood of a predicted bifurcation. Still, the values of some experimental data points in the vicinity of the jump transitions may be misrepresentative of the true steady state behavior due to a very slowly decaying transient. This behavior could contribute to the wider range of the bi-stable regions observed in the experimental data when compared with the numerical data.

6.6.4 Component Degradation

Due to the large peak stresses and fatigue that the system is exposed to during a dynamic test, the potential for degradation or failure of components is anticipated. Over the course of the experimental tests, the following observations were made, presented in chronological order. Loose ball bearings were observed near the linear bearings of the NTMD, as illustrated in Fig. 6.34, after completing the dynamic characterization tests for the NTMD component. No corresponding changes to the performance of the NTMD were observed. Figure 6.35 illustrates wear within the STMD component due to contact between the torsional spring attachment piece and

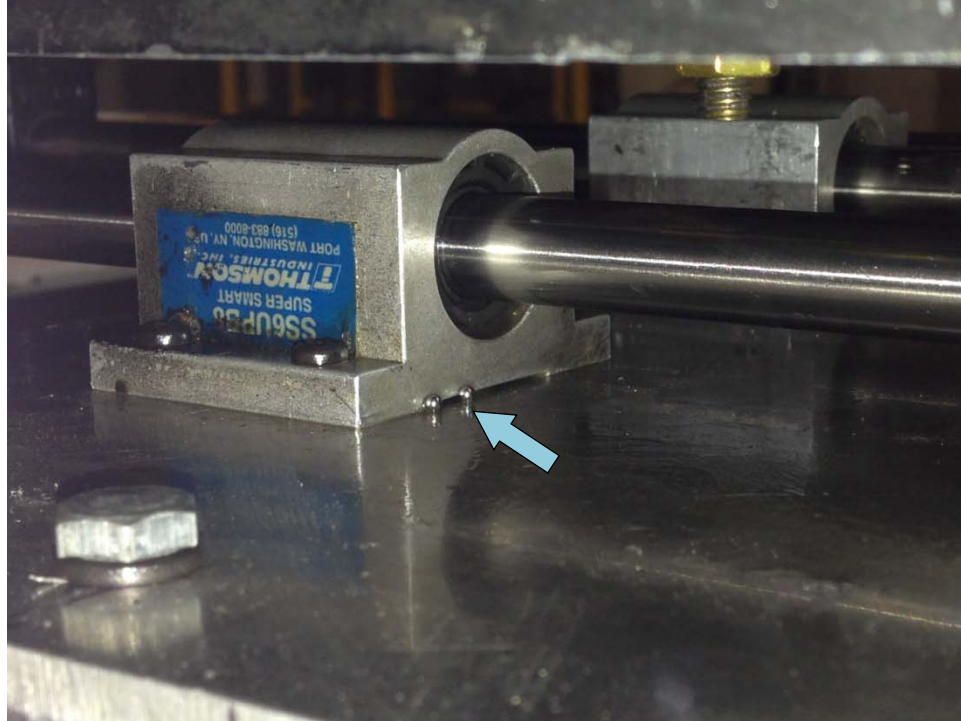


Figure 6.34: Loose ball bearings observed under the NTMD, indicating degradation of the linear bearing components.

the mounting plate. The components were initially separated but later came in to contact following an axial drift of the shaft component, which could contribute to a gradually increasing STMD damping ratio over the span of the experimental tests. Upon completion of all experimental tests, a crack in one of the welds in the linear spring component was discovered, shown in Fig. 6.36. No indication of damage was present in the other five welds of the spring component.

6.6.5 Sensor Limits

Throughout the course of the experimental study, much care was taken to ensure that the operating conditions were well within the limits defined by the various sensors that were used. If the sensor limits are exceeded, errors may be introduced into the measured data. Evidence of these errors are observed in the angular displacement

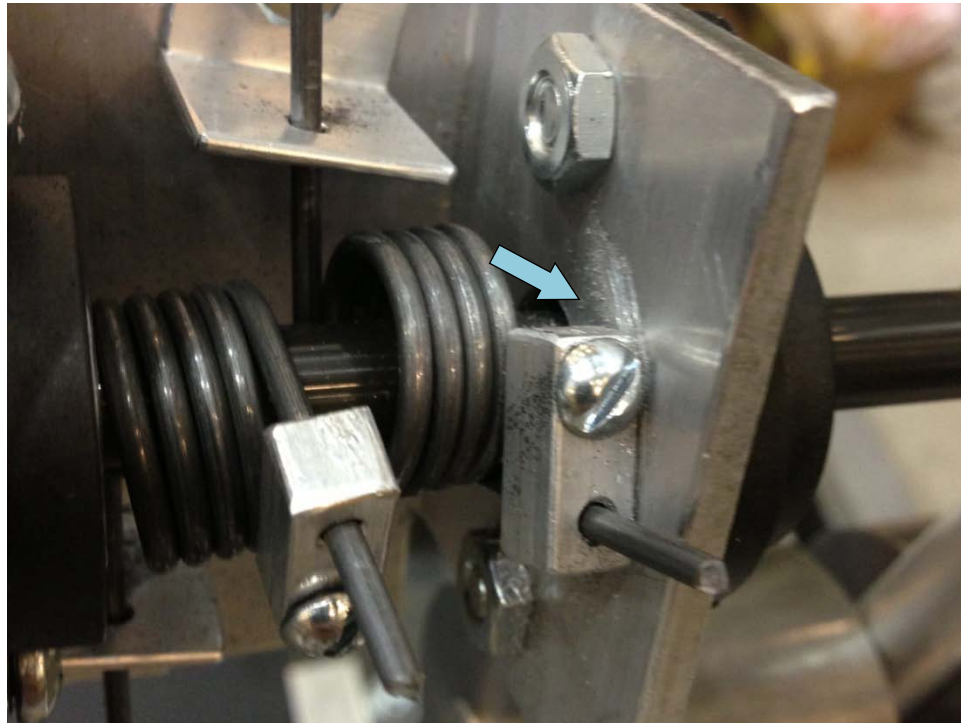


Figure 6.35: Wear within the STMD component due to contact between the torsional spring attachment and mounting plate.



Figure 6.36: Failure of one of the six welds in the linear spring component discovered upon completion of the experimental tests.

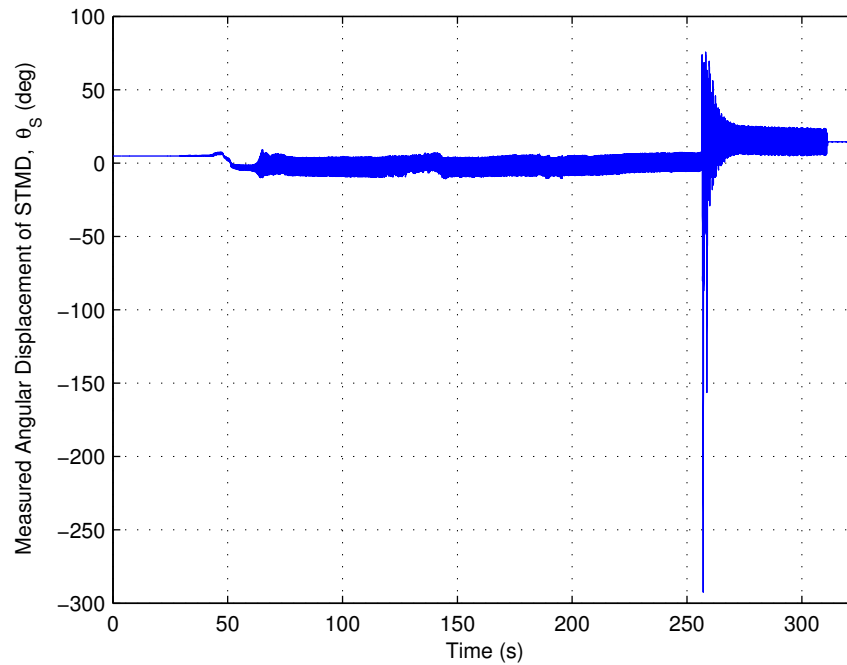


Figure 6.37: Angular displacement signal versus time corresponding to the dowel pin experiment, with no offset correction.

signal from the dowel pin experiment at the end of Section 6.4. The angular displacement signal is obtained by multiplying the voltage signal from the encoder by a constant calibration coefficient and is displayed in Fig. 6.37. Two indications of measurement error are present: sudden shifts in the RMS signal value and unreasonably high-valued peak displacements. The small RMS shifts observed in the present results can be attributed to physical settling of the dowel pin within the housing during the initial excitation (*e.g.* $t = 45$ s) and failed attempts to remove the pin during operation (*e.g.* $t = 130$ s). The large RMS shift observed at $t = 255$ s can be attributed to a relative displacement between the rod clamp and aluminum shaft or between the aluminum shaft and encoder, resulting from the large-amplitude oscillations.

The unreasonably high-valued peak displacements can be attributed to sensor error resulting from radial forces in excess of the 1 lbf (4.4 N) limit prescribed by the manufacturer. As illustrated in Fig. 6.32, the aluminum rod is mounted on two

flanged bearings in order to minimize the radial forces acting on the encoder (hidden from view behind the pendulum mount). However, during the dowel pin experiment the mounting screws on the outside bearing came loose and the encoder was exposed to large radial forces resulting from the weight and inertia of the pendulum. Based on physical observation of the displacement amplitudes from a video recording of the experiment, the actual peak displacement was no larger than $\pm 100^\circ$. With the exception of the large amplitudes measured within $0 < t < 5$, the shift-corrected signal presented in Fig. 6.31(d) provides an accurate representation of the physical observations.

6.6.6 Other Error Mechanisms

Other potential sources of error include nonlinear STMD behavior, coexisting solutions, and characterization errors. It is well understood that a linear approximation for the restoring force of a pendulum absorber is only valid in the neighborhood of the stable equilibrium ($\theta_S = 0$). In order to minimize the influence of nonlinearity in the STMD, simulations were aborted when large angular displacements were experienced ($\theta_S > 30^\circ$). In Chapter 5, a family of coexisting Period-1 and higher-period solutions were identified in a system similar to the experimental setup (see Fig. 5.7). It is possible that some of the experimental data points correspond with a different solution branch than the numerical results. This, however, is unlikely since the main low and high Period-1 solution branches are expected to be much stronger attractors as demonstrated by the results of Chapter 5. Finally, small errors may have been introduced as a result of human error or the limited precision and accuracy of the sensors used to characterize the system parameters.

Chapter 7

Concluding Remarks

In conclusion, the present chapter reviews a summary of contributions and describes proposed future work based on the results of the thesis. For a comprehensive overview of results, the reader is referred to the corresponding summary at the end of each chapter. The results within this thesis:

- Demonstrated numerically that a small semi-active tuned mass damper can be used to restore the attenuation performance of a linear absorber which has been detuned by a hardening nonlinearity,
- Developed the PMDCM algorithm, which improves upon the efficiency of the MDCM method—an important tool used for the global dynamic analysis of higher-dimensional systems—without compromising accuracy,
- Conducted a global dynamic analysis of a primary structure and a strongly nonlinear tuned mass damper in order to determine the strength of the coexisting attractors,
- Discovered a family of additional solutions and evidence of chaotic response behavior,

- Demonstrated numerically and experimentally that a small semi-active tuned mass damper can be used to protect a structure and a strongly nonlinear tuned mass damper from complex, high amplitude response behavior.

7.1 Summary of Contributions

In Chapter 3, it was demonstrated that a small semi-active tuned mass damper (STMD) can be used to effectively restore the performance of a system consisting of a linear primary structure (PS) and an optimally tuned absorber that has developed a weak nonlinearity (NTMD). By combining the results of a linear Laplace domain analysis and a nonlinear perturbation solution, an approximate analytical expression was derived to describe how the nonlinearity detunes the linear absorber and compromises the attenuation performance of the absorber. The results of a numerical study then demonstrated that a small STMD coupled to the NTMD in a series configuration can limit the motion of the NTMD to an approximately linear range, achieving similar performance to the PS and optimally tuned linear absorber for both wide-band harmonic and random excitation. The results using a single degree-of-freedom (DOF) system such as the present structure can often be extended to multi-DOF systems [17]. These findings could eventually lead to a solution of retrofitting with a small STMD device as a cost-efficient alternative to a complete system replacement in the event that a real-world linear absorber develops a hardening stiffness due to component degradation, operation outside of the intended range, or other means.

In Chapter 4, the parallelized multi-degrees-of-freedom cell mapping (PMDCM) method was developed. The theoretical basis of the PMDCM method is based on the multi-degrees-of-freedom cell mapping (MDCM) method, which is one of the only cell mapping methods that is able to efficiently analyze multi-DOF systems. The PMDCM method overcomes a major shortfall of the MDCM method—namely, the

sequential nature of the MDCM algorithm which limits the ability to utilize parallel computing resources. In contrast, the author's new PMDCM algorithm is capable of simultaneously executing certain time-intensive tasks, resulting in an efficiency gain over MDCM that is proportional to the number of available processors. By using a quad-core CPU, the PMDCM method was demonstrated to reduce the total computation time by 93% when compared with the MDCM method. Furthermore, the results obtained using the PMDCM method were observed to be even more accurate than using the MDCM method: 0.04% versus 0.11% error in the global integrity measure, respectively, when compared with the "true" solution obtained using the grid of starts (GOS). The PMDCM therefore improves upon one of the tools most suitable for higher-dimensional cell mapping, an important analysis used to determine the safety of nonlinear dynamic systems [98].

A global dynamic analysis of the two degrees-of-freedom system consisting of a primary structure and a strongly nonlinear tuned mass damper (NTMD) was presented in Chapter 5. The results of the analysis directly address the need identified by Gendelman in his 2011 review for a thorough study of the relative strength of each coexisting attractor [40]. By using numerical continuation and integration methods, a family of new Period-1 and higher-period solutions were discovered that had been overlooked in previous works [59]. Under certain conditions, chaotic response behavior was also observed. Chaotic response behavior has been identified in studies of related systems (*e.g.* [2, 62]), but to the knowledge of the author has not yet been identified in the present system. These results uncovered additional challenges that must be addressed before strongly nonlinear absorbers can be practically implemented.

As a potential solution, it was proposed that an STMD be attached in series with the strongly nonlinear NTMD and PS in order to use the STMD as a safety device, disabling the STMD to allow for the energy pumping capabilities to be utilized and enabling to prevent a high amplitude response. It was demonstrated numeri-

cally (Chapter 5) and experimentally (Chapter 6) that the complex and potentially dangerous nonlinear behavior could be minimized and the high amplitude attractors eliminated by adding an STMD many orders of magnitude smaller than the PS, resulting in a single low amplitude attractor. The full performance of the strongly nonlinear system, including an analysis of how the STMD affects the energy pumping capabilities, is reserved for future studies.

7.2 Future Work

In this section, a list of ideas for proposed future research is presented. These ideas are based on the results presented within this thesis and other related developments by the author. When available, preliminary results or a more detailed description are included.

7.2.1 Chaos in the PN System

In Chapter 5 it was demonstrated that the PN system is capable of exhibiting a Period-3 response and the exponential divergence of nearby trajectories, both of which are characteristics of chaotic systems. Chaotic response behavior has been previously identified in related systems (*e.g.* [2, 62]), but to the knowledge of the author it has not yet been identified in the present system. A targeted study of chaotic attractors and conditions leading to chaotic behavior could be used to provide a more conservative estimate of safe operating limits for a linear oscillator-nonlinear absorber system.

7.2.2 Control Algorithm Development

The present thesis focused on the dynamics of the PNS system response in order to evaluate the attenuation capability of the series STMD. A future study dedicated to the control of the PNS system would be helpful in order to more accurately evaluate

the performance of a practical system. A complete study would include a description of the control algorithm, an investigation of any negative behavior attributed to a time delay or other effects, and an evaluation of the performance of the control system under random excitation. Additional development of the method used to activate and deactivate the series STMD, a more thorough evaluation of the transient response, and an evaluation of the energy pumping capability of the PNS system are also needed. In addition to standard control methods, Rega and Lenci's methods for controlling basin erosion could also be explored as a means to enlarge the safe operating range of the PNS system [99, 100].

7.2.3 Smart Nonlinear Energy Sink (SNES)

The present thesis demonstrated that a small series STMD could be used as a safety mechanism allowing for the energy pumping capabilities of a strongly nonlinear absorber or nonlinear energy sink to be realized while allowing the system to quickly recover in the event of a high amplitude response. As an alternative approach, a novel semi-active system capable of smoothly transitioning from an essentially nonlinear cubic stiffness (allowing for energy pumping) to a linear stiffness (providing classical attenuation capabilities) is proposed. This device will be referred to hereafter as the *smart nonlinear energy sink* (SNES).

A common configuration used to produce an essentially nonlinear absorber consists of two linear springs with zero pretension attached perpendicular to the direction of absorber deflection, as illustrated in Fig. 1.5. In the smart nonlinear energy sink, an electromechanical actuator is used in order to change the location of the fixed ends of the springs—referred to hereafter as the *end posts*—relative to the absorber. The path of the end post movement is defined such that a smooth transition is obtained from an equilibrium position with the springs perpendicular to the direction of the absorber deflection to a position parallel to the direction of the absorber deflection.

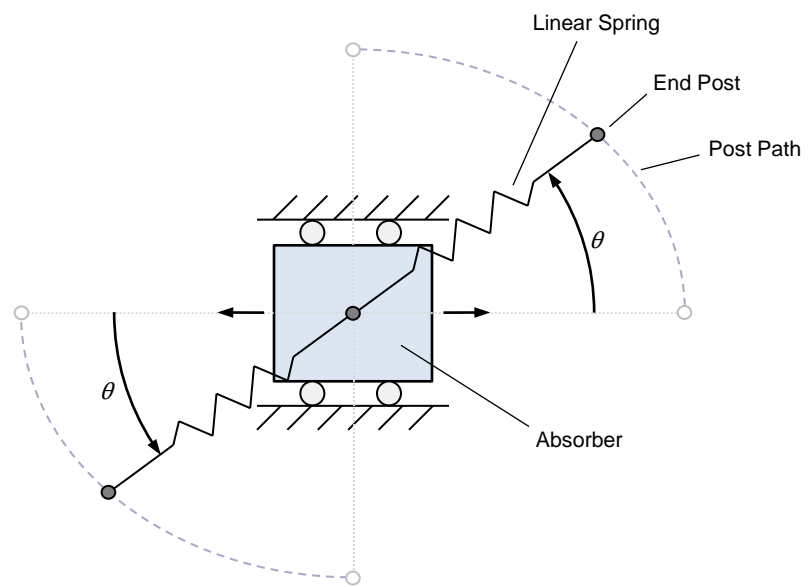


Figure 7.1: Schematic illustration of the proposed smart nonlinear energy sink (SNES) system.

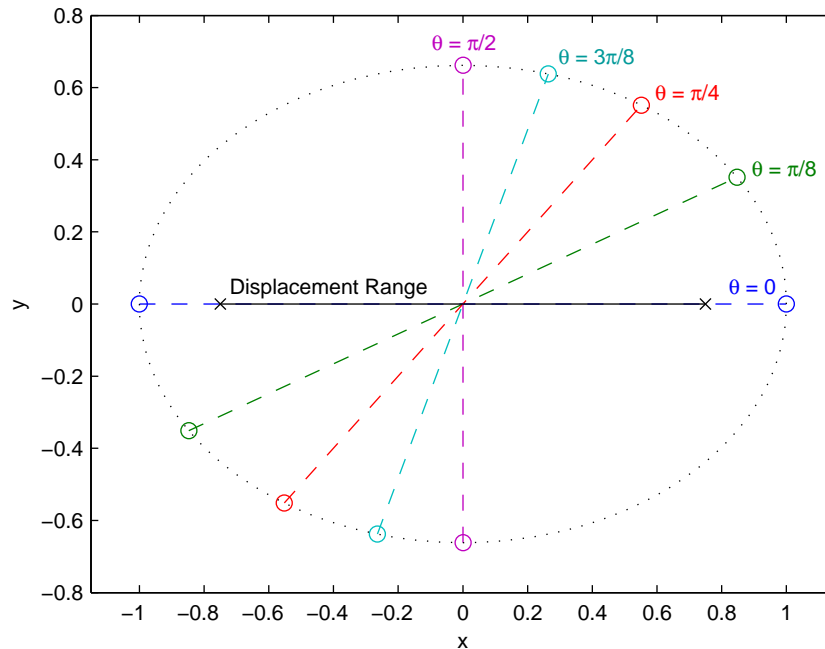


Figure 7.2: Elliptical path followed by the spring end posts as the rotation angle θ is increased in the proposed SNES system.

A schematic of the proposed SNES with an elliptical post path is illustrated in Fig. 7.1. Analytical equations based on the geometry of the SNES system at five values of the post rotation angle (θ) as illustrated in Fig. 7.2 are used to determine the force-deflection characteristics of the system, displayed in Fig. 7.3. Force and deflection values are non-dimensionalized based on the geometry of the system. As the post rotation angle is increased from $\theta = 0$ to $\pi/2$, the force-deflection profile smoothly transitions from a linear to an essentially nonlinear—approximately cubic—relationship. Increasing the eccentricity of the ellipse increases the ratio of nonlinear to linear stiffness coefficients at the expense of requiring a larger spring deflection range. Alternate post paths may prove to be favorable over an elliptical path.

A similar transition from an essentially nonlinear to a linear force-deflection profile may also be achieved using other mechanisms. The geometry of the SAIVS device (see Fig. 1.8) may produce similar characteristics for large deflections. Furthermore, it

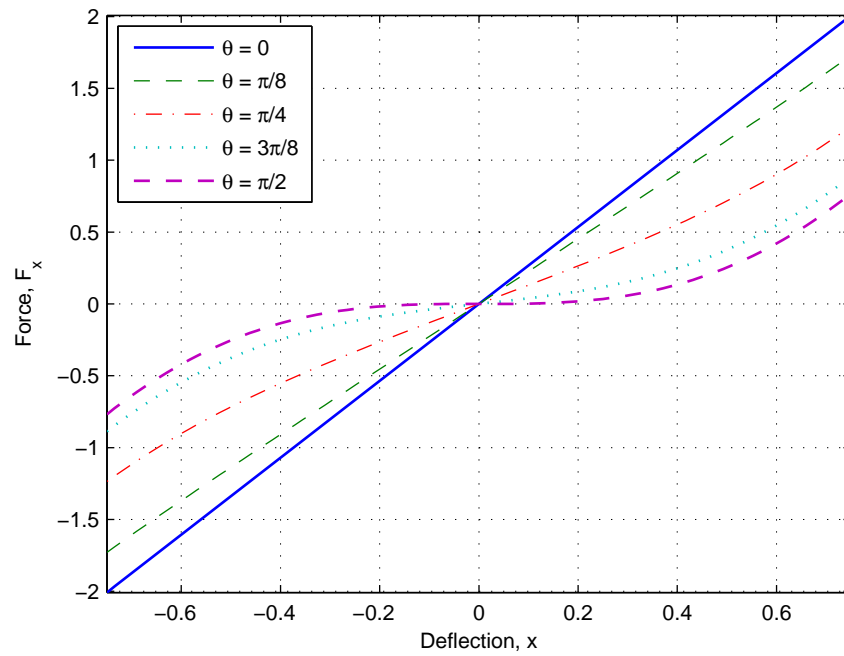


Figure 7.3: An example of the smooth transition from an essentially nonlinear to a linear force-deflection profile as the post rotation angle θ is increased in the proposed SNES system.

may be possible to incorporate principles of the SAIVS device into the SNES in order to achieve some control over the linear stiffness characteristics. A simpler device that introduces only linear post movement in order to adjust the pretension of the springs could be used to control the ratio of nonlinear to linear stiffness coefficients according to Eqn. (6.44). The lesser degree of control offered by this alternative device may be sufficient to control transitions to high amplitude attractors.

7.2.4 Mapping Using a Variable or Adaptive Cell Size

The dimensions of the cells (the “step size”) within cell mapping methods determine the efficiency of the method and the accuracy of the results, with a tradeoff between the two. It is known that the lowest accuracy is generally observed at the basin boundaries, particularly at fractal basin boundaries, motivating the use of a very small step size when studying these regions. The accuracy of the results may be less influenced by the step size within other regions of cell-state space. Based on this behavior, a cell mapping method using a variable or adaptive step size may be able to improve both efficiency and accuracy over current methods. For a variable step size, a meshing algorithm could be developed—similar to commercial finite element analysis software—in order to determine the boundaries of rectangular or arbitrarily-shaped cells in a way that maximizes efficiency and accuracy for the current system. Alternatively, a method could be developed to modify the step size during processing in order to adapt to different conditions.

7.2.5 Accurate and Efficient Integrity Measure Calculation

The local integrity measure (LIM) provides one of the most useful estimates of the integrity of a dynamic system. As described in Section 1.2.3, the LIM is the normalized radius of the largest hyper-sphere (circle in two dimensions) that is centered on the safe attractor and entirely contained within the safe basin. The only straightfor-

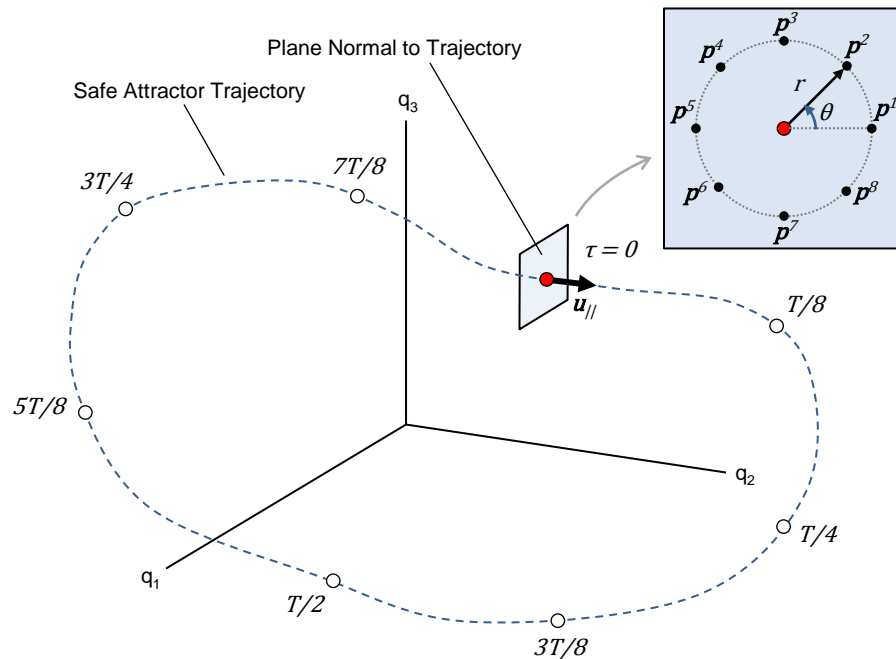


Figure 7.4: Illustration of a targeted algorithm used to accurately and efficiently calculate the local integrity measure (LIM).

ward method to obtain the true value of the LIM would be to construct the *entire* N -dimensional basin, an extremely inefficient, often practically impossible task. In practice, the LIM is typically estimated as the minimum value calculated from a limited number of two-dimensional basin portraits at different phase offset values. This approach provides an efficient estimate but is likely to overlook key out-of-plane behavior—regions where the safe attractor trajectory is closer to the basin boundary than observed in the limited number of portraits—which would result in an overestimate of the system integrity.

The accurate and efficient calculation of the LIM can only be accomplished by using an algorithm specifically designed for that purpose. One proposed solution is illustrated in Fig. 7.4 and described by the following steps.

1. Use numerical integration or other means to obtain the steady-state trajectory

of the safe periodic attractor over one response period T in N -dimensional state-space.

2. Identify the coordinates of points along the safe attractor, denoted hereafter as the *nodes*, at evenly spaced time intervals over the response period, $\tau \in [0, T)$. Eight nodes are displayed in Fig. 7.4. A much larger number of nodes is recommended in order to improve the accuracy of the results.
3. Starting with the first node, $\tau = 0$, determine the unit vector parallel to the trajectory at the node, \mathbf{u}_{\parallel} .
4. Define a new spherical-type coordinate system normal to \mathbf{u}_{\parallel} and of dimension $N-1$ with the origin centered on the node. In the three-dimensional example system illustrated in Fig. 7.4, the new coordinate system is a two-dimensional plane with polar coordinates r and θ . The coordinate system for a general N dimensional system would be hyper-spherical with the coordinates $r, \theta_1, \dots, \theta_{N-2}$.
5. Starting with a small value of r , identify a set of points $\mathbf{p}^1, \dots, \mathbf{p}^K$ located at r and combinations of a grid of k values of each angular coordinate θ_i , with $i = 1, \dots, N-2$, and $K = k(N-2)$. Determine the corresponding basins to which trajectories initiated from each point \mathbf{p}^j converge, $j = 1, \dots, K$. This can be accomplished using straightforward integration such as the grid of starts (GOS) method or by using cell mapping methods. For example, a modified version of the PMDCM method could be used where the set Z of cells to analyze is defined by the set of cells containing each \mathbf{p}^j , determined by using an analogous expression to Eqn. (1.7).
6. Incrementally increase the value of r and repeat Step 5 until one of the \mathbf{p}^j converges to the constraint attractor. Denote the corresponding radius as the local minimum radius r_{min}^* .

7. Repeat Steps 3–6 for each node. Denote the global minimum radius as r_{min} , the minimum radius from any of the nodes to a point converging to the constraint basin. The computation time can be minimized by aborting further computations and moving on to the next node whenever the radius r corresponding to \mathbf{p}^j exceeds r_{min} , even if no trajectories converging to the constraint basin have been located for that node.
8. After all nodes have been processed, the local integrity measure is equal to the value of r_{min} normalized by any characteristic length.

The key output from the proposed algorithm is a single scalar value, the local integrity measure, which is directly related to the safety of the dynamic system [98]. Of course, as with any analytical tool, visual output is helpful in order to more easily interpret the results. Three plots that could be used to summarize the results of the analysis and supplement the scalar LIM value output are discussed here and illustrated in Fig. 7.5. The first, Fig. 7.5(a), is a plot of the local radius corresponding to each node— r_{min}^* versus τ —with the minimum of the curve representing the global radius r_{min} used to calculate the LIM. This plot helps to identify whether the system is sensitive to perturbations at a specific time within the response period or is sensitive to perturbations over the entire response period. Note that in order for this curve to be plotted a value for r_{min}^* must be calculated at each node, which would require more calculations than the process recommended in Step 7. The second proposed plot, displayed in Fig. 7.5(b), is the value of the angular coordinates of the point corresponding to the local r_{min}^* for each node— θ_i versus τ . This plot illustrates the sensitivity of the system to perturbations in each of the global coordinates. Finally, with a slight modification to the listed steps a third plot could be constructed. The third proposed plot, illustrated in Fig. 7.5(c), is the value of the local minimum radii in specific directions of the original Cartesian coordinate system at each node—for example the positive and negative q_2 direction, q_2 versus τ . Assuming that q_2

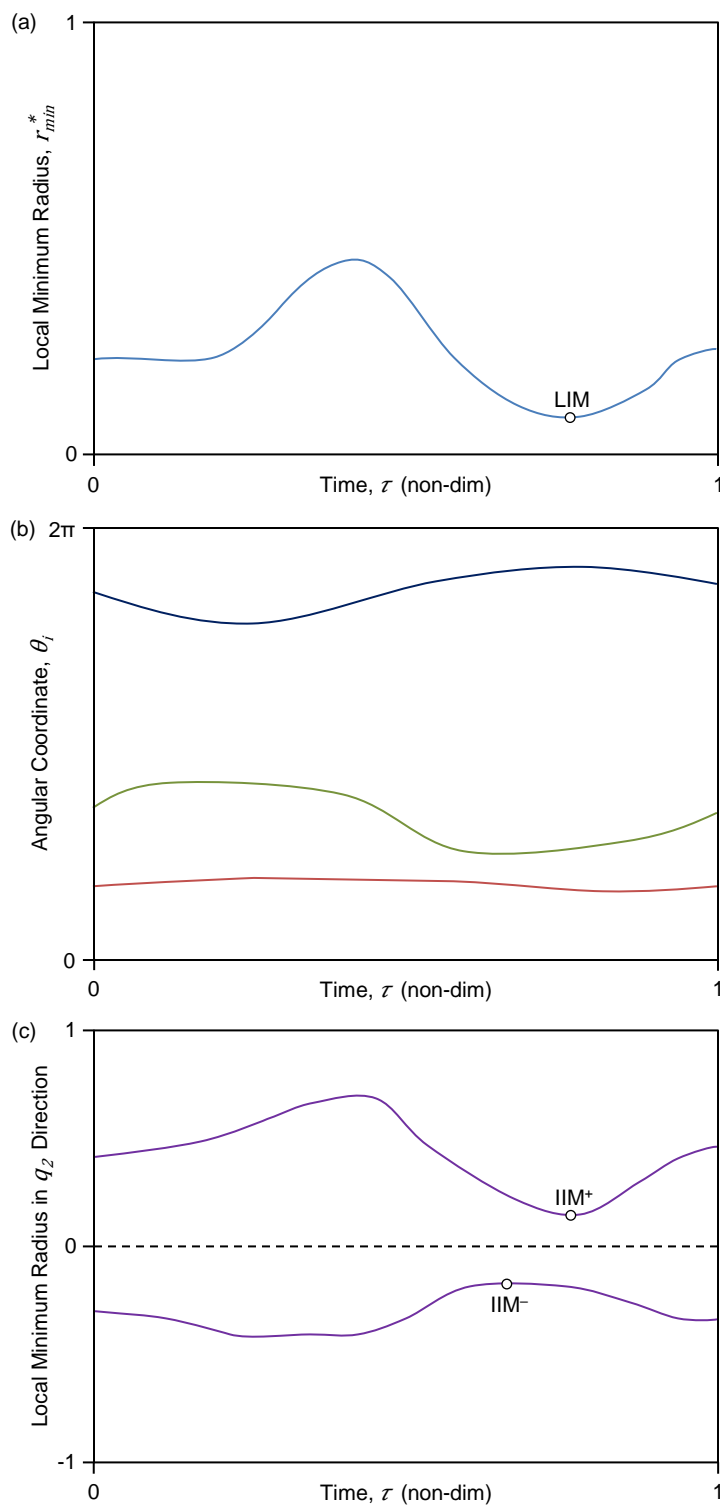


Figure 7.5: Three examples of proposed output plots from a targeted algorithm used to accurately and efficiently calculate the local integrity measure (LIM).

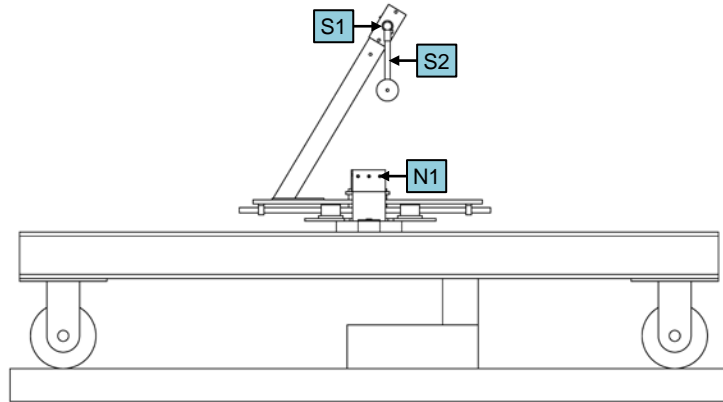
represents a velocity of a component in the dynamic system, the minimum of the absolute value of each curve represents the impulse integrity measures (IIM $^{\pm}$). This plot requires small additions to be made to the steps listed above, but demonstrates that the algorithm can be easily expanded to more accurately and efficiently calculate other integrity measures.

Appendix A

Experimental System Components

This section presents a description of some of the key components used in the experimental system from Chapter 6. Figure A.1 is a CAD illustration of the experimental system from an (a) top and (b) side perspective. Figure A.2 is a detail view of the pendulum assembly from a line-of-sight normal to the pendulum mount. In each figure, alphanumeric labels are used to denote different components. Technical details regarding each component are presented in the remainder of the section, organized by the label numbers.

(a)



(b)

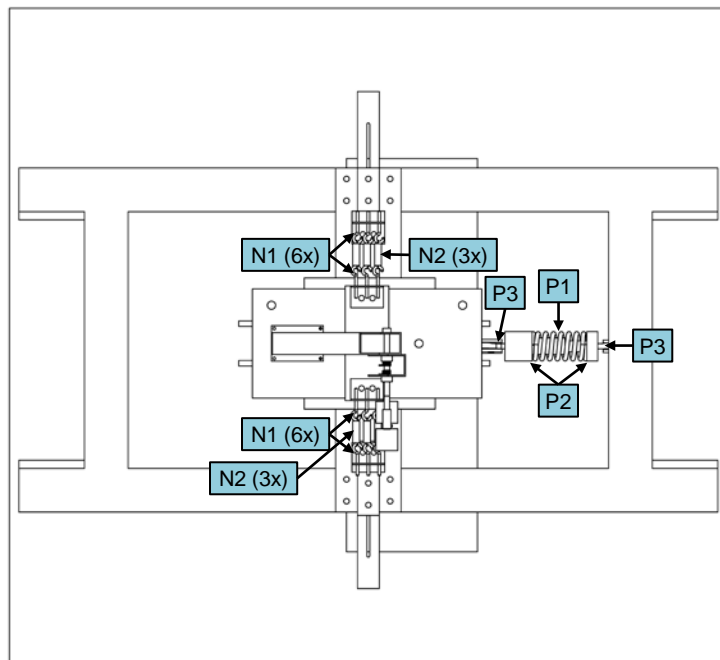


Figure A.1: CAD illustration of the full experimental setup from the (a) top and (b) side view. Labels denote system components.

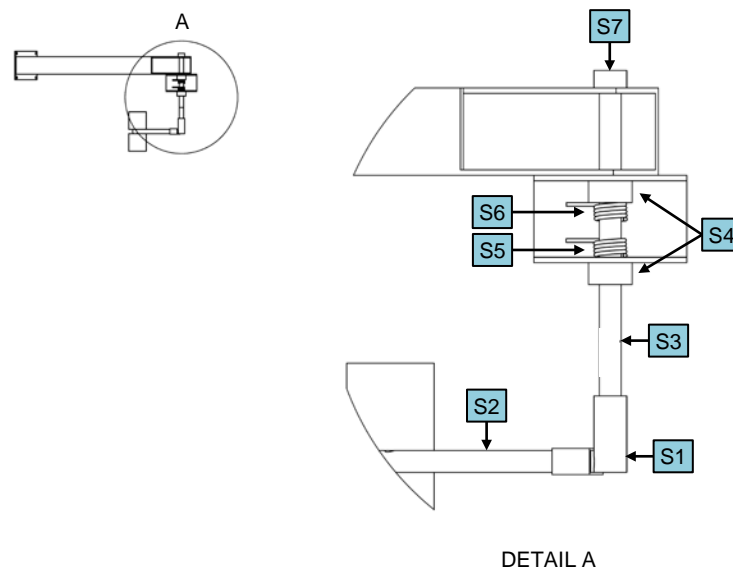


Figure A.2: CAD illustration of adjustable-length pendulum (STMD) assembly. Labels denote system components.

(P1) Tempered Steel Compression Spring

Specifications	
Part Number:	96485K211
Distributor:	McMaster-Carr
Material:	Tempered Steel
End Finish:	Closed and Ground
Spring Rate:	391.50 lbf/in
Maximum Load:	804.00 lbf

(P2) Steel Rod

Specifications	
Part Number:	8920K82
Distributor:	McMaster-Carr
Material:	Type 1018 Carbon Steel
Diameter:	2-3/4 in
Length:	12 in
Hardness:	Rockwell B70
Yield Strength:	54,000 psi

(P3) Ball Joint Rod End

Specifications	
Part Number:	60645K161
Distributor:	McMaster-Carr
Material (Housing):	Zinc-Plated Steel
Material (Ball):	Chrome-Plated Steel
Maximum Ball Swivel:	± 20 deg
Static Radial Load Capacity:	10,046 lbf

(N1) Steel Eyebolt

Specifications	
Part Number:	9490T4
Distributor:	McMaster-Carr
Material:	Zinc-Plated Steel
Type:	Open-Eye

(N2) Precision Extension Spring

Specifications	
Part Number:	9432K118
Distributor:	McMaster-Carr
Material:	Zinc-Plated Steel Music Wire
Diameter (Spring):	0.625" \pm 0.015"
Diameter (Wire):	0.069"
Length Inside Ends:	2.00 in
Extended Length:	3.68 in
Spring Rate:	14.10 lbf/in
Minimum Load:	2.00 lbf
Maximum Load:	25.71 lbf

(S1) 15mm Rod Clamp

Specifications	
Part Number:	15mm-Single-RodClamp-4
Distributor:	CoolLCD
Material:	Aluminum
Clamp ID:	0.59 in(15 mm)
Thread Size:	1/4"-20

(S2) Aluminum Rod

Specifications	
Part Number:	4634T19
Distributor:	McMaster-Carr
Material:	Type 6061 Aluminum
Diameter:	0.59 in(15 mm)
Straightness Tolerance:	$\pm 0.0125''/\text{ft}$
Length:	6 ft
Hardness:	90 Brinell
Yield Strength:	35,000 psi

(S3) Ceramic Coated Aluminum Shaft

Specifications	
Part Number:	1031K71
Distributor:	McMaster-Carr
Material (Shaft):	Type 6061 Aluminum
Material (Finish):	0.002" Ceramic Coating
Diameter:	3/8 in
Straightness Tolerance:	± 0.001 " / ft
Surface Hardness:	Rockwell C70

(S4) Miniature Flange-Mounted Ball Bearing

Specifications	
Part Number:	4575N35
Distributor:	McMaster-Carr
Material (Bearing):	Type 440C Stainless Steel
Material (Housing):	PEEK
Bearing Type:	Sealed
For Shaft Diameter:	3/8 in
Dynamic Load Capacity:	749 lbf
Max. Angular Velocity:	32,000 RPM

(S5) Left-Handed Torsion Spring

Specifications	
Part Number:	9271K587
Distributor:	McMaster-Carr
Material:	Steel Music Wire
Maximum Deflection:	90 deg
Length at Max. Deflection:	0.455 in
Number of Coils:	4.25
Spring Rate:	0.682 ft-lbf/rad

(S6) Right-Handed Torsion Spring

Specifications	
Part Number:	9271K653
Distributor:	McMaster-Carr
Material:	Steel Music Wire
Maximum Deflection:	90 deg
Length at Max. Deflection:	0.455 in
Number of Coils:	4.25
Spring Rate:	0.682 ft-lbf/rad

(S7) Absolute Magnetic Shaft Encoder

Specifications	
Part Number:	MA3-A10-125-B
Distributor:	US Digital
Material (Shaft):	Stainless Steel
Material (Bushing):	Brass
Interface:	10-bit Analog
Shaft Diameter:	1/8 in
Type:	Ball Bearing/Free Spinning
Sensor:	Non-Contacting Magnetic Single Chip
Sampling Rate:	2.6 kHz
Sensor Range:	360 deg
Power Supply:	5 V
Signal Range:	0.015 – 4.987 V
Maximum Vibration (5Hz to 2kHz):	20 g
Angular Accuracy:	±1.0 deg
Max. Angular Velocity:	15,000 RPM
Max. Shaft Loading:	1 lbf

Appendix B

Experimental Equipment, Sensors, and Calibration Data

The procedure used to calibrate the sensors and the corresponding data is presented as follows.

B.1 Load Cell

The load cell is calibrated in compression by using 10 lb plates to apply known loads to the sensor. The applied load versus measured signal voltage is plotted in Fig. B.1. A first order least squares approximation is used to determine the best-fit line and the corresponding calibration coefficient: 59.6075 lbf/V. No tests are conducted to calibrate the load cell in tension, but based on the published data sheet and the highly linear compression data, the calibration coefficient is assumed to be accurate over the full range of the sensor.

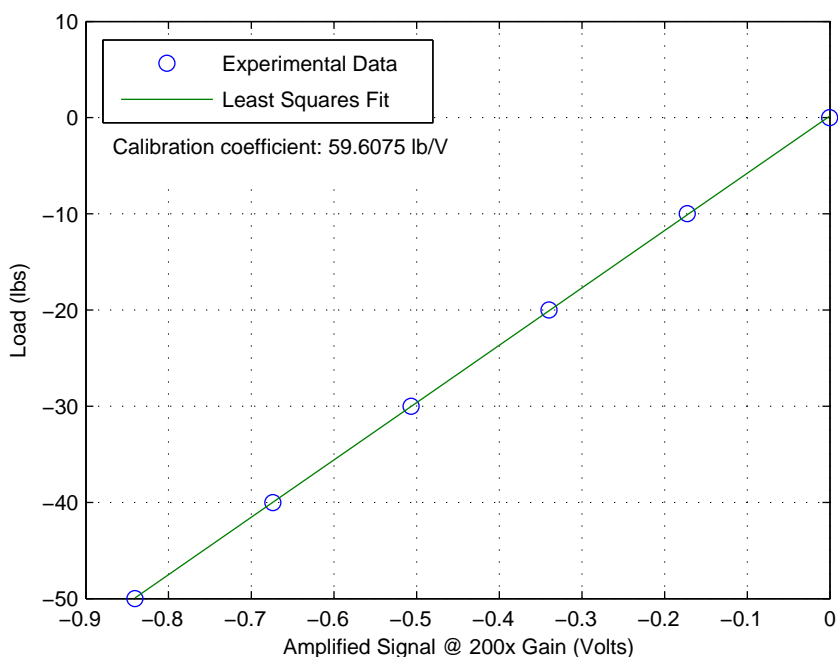


Figure B.1: Applied load versus load cell output voltage, and best fit line indicating calibration coefficient.

B.2 LVDT

The LVDT is calibrated by using a digital caliper to measure the exact displacement of the sensor at various points within the range of the sensor. The applied displacement versus measured signal voltage is plotted in Fig. B.2. A first order least squares approximation is used to determine the best-fit line and the corresponding calibration coefficient: 4.5207 in/V.

B.3 Encoder

The published calibration of the encoder is checked by using a digital incline meter to measure the exact angular displacement of the pendulum at various points within the range of the pendulum. The angular displacement versus measured signal voltage is plotted in Fig. B.3. A first order least squares approximation is used to determine

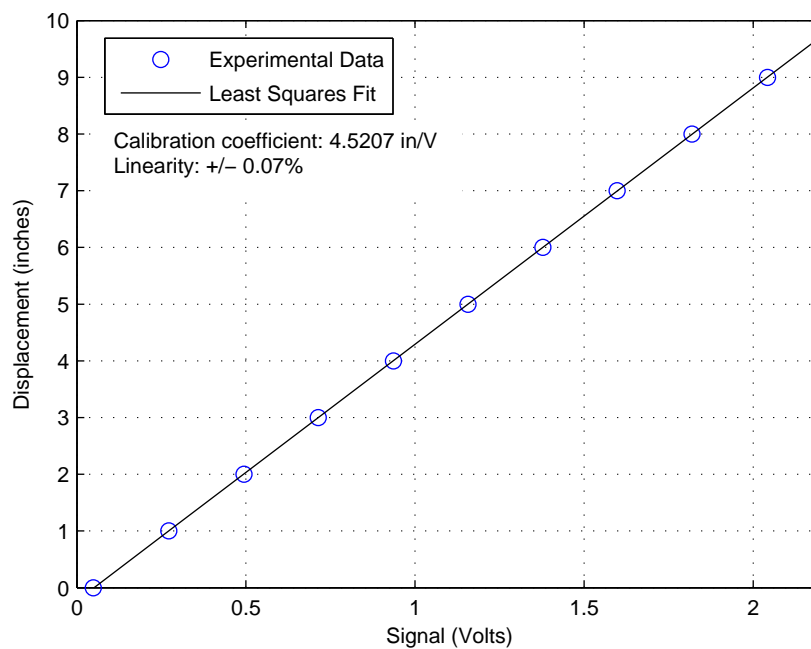


Figure B.2: Applied displacement versus LVDT output voltage, and best fit line indicating calibration coefficient.

the best-fit line and the corresponding calibration coefficient: 74.025 deg/V, which agrees with the published value.

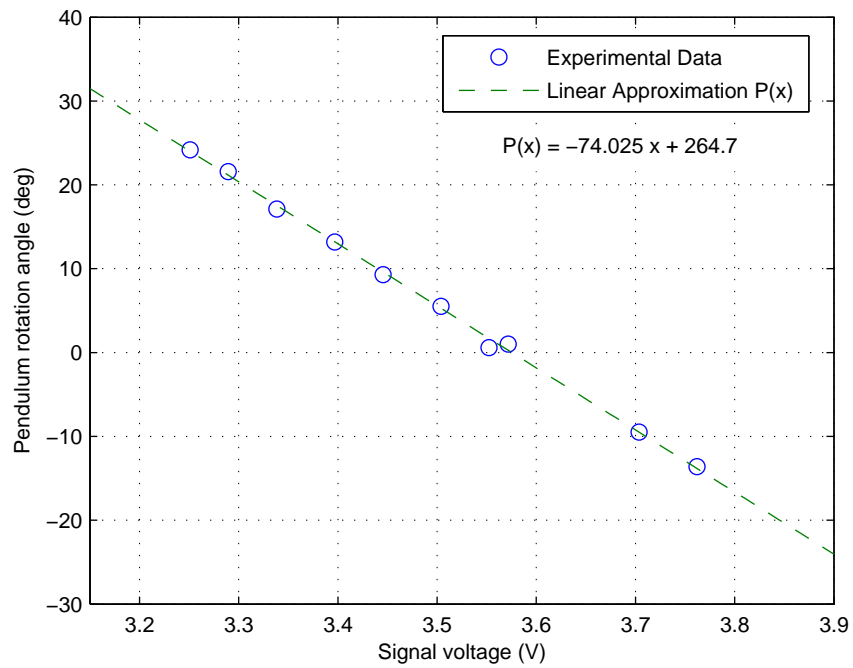


Figure B.3: Rotation angle of the STMD pendulum versus encoder output voltage, and best fit line indicating calibration coefficient.

Appendix C

Selected Code

Example MATLAB code for a PMDCM analysis of the two-DOF system consisting of the primary structure and NTMD (the PN system) is presented. The main body of the PMDCM algorithm is given in Section C.1, and the subroutines in Sections C.2–C.8. The equations of motion for the PN system are defined in Section C.9. Sections C.10 and C.11 present additional scripts used to calculate the basins from the group number array output of the PMDCM algorithm and identify the steady state time series trajectories corresponding to each of the basins, respectively.

C.1 PMDCM Algorithm

```
1 function [pc,b] = ParallelMDCM.PNsystem
2
3 % An example of the Parallelized Multi-DOF Cell Mapping (PMDCM)
4 % algorithm for determining the basin of attraction of a N-DOF,
5 % 2N-dimensional system applied to a 2-DOF system consisting of a
6 % linear primary structure and NTMD
7
8 % SYSTEM PARAMETERS: %%%%%%%%%%%%%%%%%%%%%%%%%%%%%%%%%%%%%%%%%%%%%%%%%%%%%%%%%%%%%%%%%%%%%%%%%%
9
10 GI      = 0.02;
11 GNhat  = 0.02;
12 EPN    = 0.1;
```

```

13 OMN    = 0.1;
14 F      = 0.35;
15 OMI    = 0.1;
16
17 OM     = 0.88;
18
19 % SIMULATION PARAMETERS: %%%%%%%%%%%%%%%%%%%%%%%%%%%%%%%%%%%%%%%%%%%%%%%%%%%%%%%%%%%%%%%%%%%%%%%%%%
20
21 % The limits for each of the generalized coordinates are defined below.
22 % The dimensions corresponding to the two rows with different limits
23 % are used to define the dimensions of the subspace sigma (X and Y
24 % assigned in order). The rest of the rows are taken as fixed
25 % values. If more than two rows have different limits, an error is
26 % returned.
27 Q_lims = [-30  30;
28           -30  30;
29           0   0;
30           0   0];
31 ssP = 16; % Number of steady state periods to compare - determines max
32           % periodicity that can be identified
33 aTol = 0.20; % Percent difference between amplitudes must meet this
34           % tolerance for solutions to be considered the same
35 nstpp = 20; % Number of integration steps per period
36
37 Nper = 20; % Number of periods used for cell imaging
38 MAX = 50; % Maximum number of cells under processing
39
40 Ns = 100; % Number of cells in the set to simultaneously integrate
41
42 %%%%%%%%%%%%%%%%%%%%%%%%%%%%%%%%%%%%%%%%%%%%%%%%%%%%%%%%%%%%%%%%%%%%%%%%%%
43
44 PARAMS = [GI;GNhat;EPN;OMN;F;OMI;OM]; % Array used to pass values to EOM
45
46 per = 2*pi/OM; % Period used for cell imaging (freq in rad/s)
47 dt = per/nstpp; % Time per integration step
48
49 N = size(Q_lims,1); % Number of dimensions in the system
50 Nchaos = 0; % Initialize Nchaos
51
52 % Define sigma and upper and lower cell limits based on limits defined
53 % for generalized coordinates. Redefine cell spacing if necessary:
54 sigma = zeros(1,2); sigc = 0;
55 for r = 1:N
56     if Q_lims(r,1) ≠ Q_lims(r,2)
57         sigc = sigc + 1;
58         switch sigc
59             case 1
60                 sigma(1) = r;
61                 n_X = (Q_lims(r,2)-Q_lims(r,1))/h(r) + 1;

```



```

111         fxdidx = Q_lims(d,1)/h(d); % Index of fixed coordinate
112         if rem(fxdidx,1) ≠ 0 % If fxdidx is not integer valued
113             warning(['Cell index is not integer valued using'...
114                     'given spacing'])
115             display(['Given spacing in Q',num2str(d),' = ',...
116                     num2str(h(d))])
117             fxdidx = round(fxdidx); % New index
118             h(d) = Q_lims(d,1)/fxdidx;
119             % Define new spacing based on integer index
120             display(['Using spacing in Q',num2str(d),' = ',...
121                     num2str(h(d))])
122             pause(5)
123         end
124         Z(:,d) = fxdidx; % Set index in column d
125     end
126 end
127
128 %%%%%%%%%%%%%%%%%%%%%%%%%%%%%%%%%%%%%%%%%%%%%%%%%%%%%%%%%%%%%%%%%%%%%%%%%
129
130 % INITIALIZATION %%%%%%%%%%%%%%%%%%%%%%%%%%%%%%%%%%%%%%%%%%%%%%%%%%%%%%%%%%%%%%%%%%%%%%%%%
131 Ng = 0; % Number of periodic groups
132 ri = 2; % Index of the smallest valued row that has not been processed
133
134 Zs = [Z(1,:);zeros(Ns-1,N)]; % Initialize set of cells to integrate
135 op = (2:Ns); % All rows in Zs need to be populated except first
136 Ks = [1;zeros(Ns-1,1)]; % Vector of K values corresp to each element
137 Ls = [1;zeros(Ns-1,1)]; % Longest trajectory — values will be
138     % different than Ks if ADDTOG is called
139 inds = [1;zeros(Ns-1,1)]; % Array of pos in pc of cells in current seq
140 pc = Z(1,:); % Initialize pc
141 g = -1; % Initialize g
142 Gchk = zeros(1,Ndim); % Array to store cells believed to be nearby the
143     % attractor for each group number – to be used for
144     % post processing
145 %%%%%%%%%%%%%%%%%%%%%%%%%%%%%%%%%%%%%%%%%%%%%%%%%%%%%%%%%%%%%%%%%%%%%%%%%
146
147 while length(find(Ls≥0)) ≥ 1
148
149     % SUBROUTINE POPZs %%%%%%%%%%%%%%%%%%%%%%%%%%%%%%%%%%%%%%%%%%%%%%%%%%%%%%%%%%%%%%%%%%%%%%%%%
150
151     Nop = length(op); % Number of open locations
152
153     for o = 1:Nop
154         r = op(o); % Current row
155         if ri ≤ M % If there are remaining cells to process
156             B = 1;
157             while B == 1;
158                 z = Z(ri,:); % Temp variable to check whether cell has
159                     % been processed

```

```

160         ri = ri + 1; % Increment ri
161         [B,I] = SCAN(z,pc); % Determine if temp variable z has
162             % been processed
163     end
164     Zs(r,:) = z; % Replace one row of cell indices with indices
165             % of a cell that needs to be processed
166     Ks(r) = 1; % Reset number of elements in current seq
167     Ls(r) = 1; % Reset length of current sequence
168     [pc,g,inds] = UPDATE(Ks,pc,I,inds,g,Ns);
169     pc(I,:) = z; % 2D array of all cells processed or processing
170     g(I) = -r; % Group number
171     inds(r,Ks(r)) = I; % Array of position in pc of cells in
172             % current sequence
173     elseif ri > M % If all cells have been processed
174         Ks(r) = 0;
175         Ls(r) = -1; % Marking this cell to be ignored
176         Zs(r,:) = zeros(1,N);
177     end
178 end
179
180 %%%%%%%%%%%%%%%%%%%%%%%%%%%%%%%%%%%%%%%%%%%%%%%%%%%%%%%%%%%%%%%%%%%%%%%%%%%
181
182 % Image Ns cells in parallel:
183 Zs = PARIMG(Zs,h,per,Nper,PARAMS,N,Ns,dt);
184
185 % SUBROUTINE SCAN/PROC %%%%%%%%%%%%%%%%%%%%%%%%%%%%%%%%%%%%%%%%%%%%%%%%%%%%%%%%%%%%%%%%%%%%%%%%%%%
186
187 for r = 1:Ns
188     z = Zs(r,:); % Take one element from set of cell images
189     [B,I] = SCAN(z,pc); % Determine if cell has been processed
190             % (if z exists in pc)
191     if B == 1; % If z exists in pc
192         if (Ls(r) > 0) && (Ls(r) ≤ MAX)
193             if g(I) ≥ 0 % Trajectory maps to a periodic group that
194                 % has already been processed
195                 g = OLDG(g,Ks(r),I,inds,r); % Old group number
196                 Ls(r) = 0; % Set to zero to indicate that a new cell
197                     % can be placed in row r
198             elseif g(I) == -r; % Current trajectory repeats itself
199                 [Ng,g] = NEWG(Ng,g,Ks(r),inds,r); % New group number
200                 Ls(r) = 0; % Set to zero to indicate that a new cell
201                     % can be placed in row r
202             elseif g(I) < 0; % Trajectory maps to another trajectory
203                 % that is in progress
204                 [Ks,inds,g] = ADDTOG(g,Ks,I,inds,r);
205                 % Combine elements from two trajectory
206                 % sequences
207                 Ls(r) = 0; % Set to zero to indicate that a new cell
208                 % can be placed in row r

```

```

209         end
210     end
211     else
212         if (Ls(r) > 0) && (Ls(r) < MAX)
213             % If cell has not been processed and MAX number of cells
214             % has not been reached
215             [pc,g,inds] = UPDATE(Ks,pc,I,inds,g,Ns); % Update arrays
216             Ks(r) = Ks(r) + 1; % Increment number of cells in array
217             Ls(r) = Ls(r) + 1; % Increment length of sequence
218             pc(I,:) = z; % Add cell to array of cells pc
219             g(I) = -r; % Set corresponding group number
220             inds(r,Ks(r)) = I; % Array of position in pc of cells in
221                 % current sequence
222         end
223     end
224 end
225
226 %%%%%%%%%%%%%%%%%%%%%%%%%%%%%%%%%%%%%%%%%%%%%%%%%%%%%%%%%%%%%%%%%%%%%%%%%
227
228 % SUBROUTINE POSTSP %%%%%%%%%%%%%%%%%%%%%%%%%%%%%%%%%%%%%%%%%%%%%%%%%%%%%%%%%%%%%%%%%%%%%%%%%
229
230 nonc = find(Ls ≥ MAX); % Indices of cells that have not converged
231                 % in MAX number of iterations
232
233 for i = 1:length(nonc)
234     r = nonc(i);
235     [Ks,pc,inds,g] = CHAOS(Ks,pc,I,z,inds,g,r,Ns);
236                 % CHAOS subroutine
237     Nchaos = Nchaos + 1; % Increment counter
238     Ls(r) = 0; % Set to zero to indicate that a new cell
239                 % can be placed in row r
240 end
241
242 op = find(Ls == 0); % Constructs a vector of indices corresponding
243                 % to cell locations (rows) in Zs that need to be
244                 % replaced
245
246 %%%%%%%%%%%%%%%%%%%%%%%%%%%%%%%%%%%%%%%%%%%%%%%%%%%%%%%%%%%%%%%%%%%%%%%%%
247
248 end
249
250 % Construct basins and attractor trajectories:
251 [b,p,Qarray,QeachG] = ...
252     ConstructBasins(g,h,per,ssP,PARAMS,Ndim,aTol,Gchk,nstpp);
253 % Qarray stores SS response time histories for each of the gen coords
254 % First dimension: Basin number
255 % Second dimension: Generalized coordinate
256 % Third dimension: Time step
257 end

```

C.2 PARIMG Subroutine

```

1 function newZs = PARIMG(Zs,h,per,Nper,PARAMS,Ndim,Ns,dt)
2
3 h_mat = diag(h);
4 Cs = Zs*h_mat; % 2-D array describing location of cell centers
5               % rows = each cell in parallel cell set Zs
6               % columns = location in each dimension
7
8 [~,Qs] = ode45(@(t,q)ParallelEOM(t,q,PARAMS,Ndim,Ns),...
9               (0:dt:Nper*per),Cs);
10
11 Es = reshape(Qs(end,:),Ns,Ndim); % Construct an array of end points in
12                                % each dimension (cols) for each cell
13                                % (rows) by reshaping the row vector at
14                                % the end of the trajectory array
15
16 newZs = floor(Es*diag(1./h) + 1/2); % Array of indices of mapped cells
17
18 end

```

C.3 SCAN Subroutine

```

1 function [BIsTrue,I] = SCAN(z,pc)
2
3 TC = (1:1:size(pc,1)); % Vector of row numbers in pc left to check
4 stop = 0;
5
6 while stop == 0
7
8     Nleft = length(TC); % Number of rows left to scan
9
10    cw_idx = floor(Nleft/2)+1; % Index of TC representing approx center
11    cw = pc(TC(cw_idx),:); % Cell in PC to compare with z
12
13    if Nleft ≠ 1
14        switch comparetwo(z,cw);
15            case 1 % z < cw
16                TC = (TC(1):1:TC(cw_idx-1));
17            case 2 % z = cw
18                stop = 1;
19                BIsTrue = 1;
20                I = TC(cw_idx);
21            case 3 % z > cw
22                if cw_idx+1 ≤ Nleft
23                    TC = (TC(cw_idx+1):1:TC(end));
24                else
25                    stop = 1;
26                    BIsTrue = 0;
27                    I = TC(cw_idx)+1;
28                end
29            end
30    else
31        switch comparetwo(z,cw);
32            case 1 % z < cw
33                stop = 1;
34                BIsTrue = 0;
35                I = TC(cw_idx);
36            case 2 % z = cw
37                stop = 1;
38                BIsTrue = 1;
39                I = TC(cw_idx);
40            case 3 % z > cw
41                stop = 1;
42                BIsTrue = 0;
43                I = TC(cw_idx)+1;
44        end

```


C.4 UPDATE Subroutine

```

1 function [pc,g,inds] = UPDATE(Ks,pc,I,inds,g,Ns)
2
3 Npc = size(pc,1);
4
5 pc(I+1:Npc+1,:) = pc(I:Npc,:);
6 g(I+1:Npc+1) = g(I:Npc);
7
8 for r = 1:Ns
9     for c = 1:Ks(r)
10        if inds(r,c) ≥ I
11            inds(r,c) = inds(r,c) + 1;
12        end
13    end
14 end
15
16 end

```

C.5 CHAOS Subroutine

```

1 function [Ks,pc,inds,g] = CHAOS(Ks,pc,I,z,inds,g,r,Ns)
2
3 [pc,g,inds] = UPDATE(Ks,pc,I,inds,g,Ns);
4 Ks(r) = Ks(r) + 1;
5
6 pc(I,:) = z;
7 inds(r,Ks(r)) = I;
8
9 for i=1:Ks(r)
10    g(inds(r,i)) = 0;
11 end
12
13 end

```

C.6 NEWG Subroutine

```

1 function [Ng,g] = NEWG(Ng,g,K,inds,r)
2

```

```

3 Ng = Ng + 1;
4 for i = 1:K
5     g(inds(r,i)) = Ng;
6 end
7
8 end

```

C.7 OLDG Subroutine

```

1 function g = OLDG(g,K,I,inds,r)
2
3 for i = 1:K
4     g(inds(r,i)) = g(I);
5 end
6
7 end

```

C.8 ADDTOG Subroutine

```

1 function [Ks,inds,g] = ADDTOG(g,Ks,I,inds,r)
2
3 from = r; % Index of sequence containing cells to be moved
4 to = -g(I); % Index of sequence where cells are to be moved to
5
6 for c = 1:Ks(from)
7     inds(to,Ks(to)+c) = inds(from,c); % Move cells into encountered
8                                     % sequence
9     g(inds(from,c)) = g(I);
10 end
11
12 Ks(to) = Ks(to)+Ks(from);
13
14 end

```

C.9 Parallelized EOM

```

1 function [dq] = Parallel_EOM(t, q, PARAMS, Ndim, Ns)
2
3 GI      = PARAMS(1);
4 GNhat   = PARAMS(2);
5 EPN     = PARAMS(3);
6 OMN     = PARAMS(4);
7 F       = PARAMS(5);
8 OMI     = PARAMS(6);
9 OM      = PARAMS(7);
10
11 dq = zeros(Ns*Ndim, 1);
12
13 q1 = q(1:Ns);
14 q2 = q(Ns+1:2*Ns);
15 q3 = q(2*Ns+1:3*Ns);
16 q4 = q(3*Ns+1:4*Ns);
17
18 dq(1:Ns) = q2;
19 dq(Ns+1:2*Ns) = - 2*GI*q2 - q1 + EPN*OMI^2*(q3-q1) ...
20                + EPN*OMN^2*(q3-q1).^3 ...
21                + 2*EPN*GNhat*(q4-q2) + F*sin(OM*t);
22 dq(2*Ns+1:3*Ns) = q4;
23 dq(3*Ns+1:4*Ns) = -OMI^2*(q3-q1) - 2*GNhat*(q4-q2) - OMN^2*(q3-q1).^3;
24
25 end

```

C.10 Construct Basins From PMDCM Output

```

1 function [b,p,Qarray,QeachG] = ConstructBasins(g,h,per,ssP,PARAMS,...
2           Ndim,aTol,Gchk,nstpp)
3
4 b = zeros(size(g)); % Vector of basin numbers for each cell
5 p = zeros(size(g)); % Vector of periodicity for each cell
6
7 Nb = 0; % Number of basins
8 Ng = max(g);
9
10 dt = per/nstpp; % Time required per step
11
12 Qarray = NaN*zeros(1,Ndim,nstpp*ssP);
13 % Qarray stores SS response time histories at each basin for each of
14 % the gen coords
15 % First dimension: Basin number
16 % Second dimension: Generalized coordinate
17 % Third dimension: Time step
18
19 QeachG = NaN*zeros(Ng,Ndim,nstpp*ssP);
20 % QeachG stores SS response time histories at each group for each of
21 % the gen coords
22 % First dimension: Group number
23 % Second dimension: Generalized coordinate
24 % Third dimension: Time step
25
26 gCounts = zeros(1,Ng); % Number of cells belonging to each group
27 gInds = NaN*zeros(length(g),Ng); % Indices of cells belonging to each
28 % group
29
30 for cell = 1:length(g)
31     if g(cell) ≠ 0;
32         gCounts(g(cell)) = gCounts(g(cell)) + 1;
33         gInds(gCounts(g(cell)),g(cell)) = cell;
34     end
35 end
36 lastrow = max(gCounts);
37 gInds(lastrow+1:end,:) = []; % Delete trailing rows
38
39 clc
40 display('Constructing basins...')
41
42 for gnum = 1:Ng
43
44     z = Gchk(gnum,:);

```

```

45 IC = h.*z;
46 [~,Q,pernum] = SSsoln(h, IC, dt, per, ssP, PARAMS);
47
48 L = nstpp*ssP;
49 Qnow = Q';
50 QeachG(gnum,1:Ndim,1:L) = Qnow; % Archive trajectory information
51
52 Idx_Amp = zeros(0,2); % Vector of indices of the group numbers that
53 % current trajectory matches and average dists
54 MinAmps = NaN; % Smallest average distance outside of the tolerance
55
56 for gchk = 1:Nb % At each group number that has been previously
57 % stored
58
59 Qchk(1:Ndim,1:L) = Qarray(gchk, :, :); % Extract trajectory data
60 % from Qarray
61 AmpDiff = abs(max(Qchk(1, :)) - max(Qnow(1, :)));
62 % Difference between the PS amplitudes of each trajectory
63 BiggerAmp = max([max(Qchk(1, :)), max(Qnow(1, :))]);
64 % The larger of the two amplitudes
65 AmpPDiff = AmpDiff/BiggerAmp; % Percent difference between the
66 % two amplitudes
67
68 if AmpPDiff ≤ aTol % Trajectory matches previously identified
69 % trajectory
70 row = size(Idx_Amp,1)+1;
71 Idx_Amp(row,1) = gchk; % Add index to vector of matches
72 Idx_Amp(row,2) = AmpPDiff; % Add avg dist to vector of
73 % matches
74 else
75 MinAmps = min([AmpPDiff, MinAmps]);
76 end
77
78 end
79
80 if size(Idx_Amp,1) == 1; % Matches a single trajectory
81 gmatch = Idx_Amp(1,1); % Matching group number
82 display(['Group ', num2str(gnum), ' → Basin ', ...
83 num2str(gmatch), ' :: Normalized Distance = ', ...
84 num2str(Idx_Amp(1,2))])
85 for idx = 1:gCounts(gnum)
86 b(1,gInds(idx,gnum)) = gmatch;
87 p(1,gInds(idx,gnum)) = pernum;
88 end
89 elseif length(Idx_Amp) == 2; % Matches multiple trajectories
90 [~,closest] = min(Idx_Amp(:,2)); % Returns index of Imatch
91 % corresponding to closest solution match
92 gmatch = Idx_Amp(closest,1); % Closest matching group number
93 display(['Group ', num2str(gnum), ' → Basin ', ...

```

```

94         num2str(gmatch), ' :: Normalized Distance = ', ...
95         num2str(Idx_Amp(closest,2))]
96     display('WARNING: Multiple identical trajectories located.')
97     display('Consider reducing tolerance value.')
98     for idx = 1:gCounts(gnum)
99         b(1,gInds(idx,gnum)) = gmatch;
100        p(1,gInds(idx,gnum)) = pernum;
101     end
102     else % New basin located
103         Nb = Nb + 1; % Increment number of basins located
104         display(['Group ', num2str(gnum), ' → Basin ', ...
105                num2str(Nb), ' :: Closest Distance to Other', ...
106                'Trajectory = ', num2str(MinAmps)])
107         Qarray(Nb,1:Ndim,1:L) = Qnow;
108
109         for idx = 1:gCounts(gnum)
110             b(1,gInds(idx,gnum)) = Nb;
111             p(1,gInds(idx,gnum)) = pernum;
112         end
113     end
114
115
116 end
117
118 end

```

C.11 Steady State Solution Information

```

1 function [Q_less_h,Q_fxd_stp,pernum] = SSsoln(h,IC,fxd_dt,per,ssP,...
2         PARAMS)
3
4 % Outputs:
5 % Q_less_h — Array containing the coordinates of the points in the
6 %             ss solution with a maximum step size no greater than the
7 %             minimum spacing defined in h
8 % Q_fxd_stp — Array containing the coordinates of the points in the
9 %             steady state solution with a fixed step size defined by
10 %            fxd_dt
11 % pernum — Periodicity of the identified solution
12
13 % PARAMETERS %%%%%%%%%%%%%%%%%%%%%%%%%%%%%%%%%%%%%%%%%%%%%%%%%%%%%%%%%%%%%%%%%%%%%%%%%%
14 tmn = 0.5; % Minimum tolerance, expressed as a fraction of hmin
15 tmx = 1.0; % Maximum tolerance, expressed as a fraction of hmin
16 initper = 200; % Initial number of periods before iterations
17 maxper = 1000; % Maximum number of periods including iterations
18 %%%%%%%%%%%%%%%%%%%%%%%%%%%%%%%%%%%%%%%%%%%%%%%%%%%%%%%%%%%%%%%%%%%%%%%%%%
19
20 display('Calculating safe basin solution...')
21
22 % The largest step in the solution should be less than or equal to
23 % the smallest step size in any of the dimensions in h
24 hmin = min(h); % Smallest step size which defines the upper bound for
25 %             solution step size
26
27 Ndim = length(h);
28 tolmin = tmn*hmin; % Define minimum tolerance
29 tolmax = tmx*hmin; % Define maximum tolerance
30 minerr = 100*tolmin; % Initialize minimum error well above tolerance
31 err_vec = minerr*ones(1,ssP); % Vector to check last nchk periods
32 Q_lastN = zeros(ssP,Ndim); % Array of previous Q values
33 [~,Q] = ode45(@(t,q)ParallelEOM(t,q,PARAMS,Ndim,1),[0 initper*per],IC);
34 % Initial run for 200 periods
35 totper = initper;
36 t_lims = [(initper-1)*per initper*per];
37 while (minerr > tolmin) && (totper <= maxper)
38     IC = Q(end,:); % Reset IC
39     t_lims = t_lims + per; % Increment time vector to run for
40 %                         % another per
41     totper = totper + 1;
42     Q_lastN(2:ssP,:) = Q_lastN(1:ssP-1,:);
43     Q_lastN(1,:) = IC;
44     [~,Q] = ode45(@(t,q)ParallelEOM(t,q,PARAMS,Ndim,1),t_lims,IC);

```

```

45     Qnow = Q(end,:);
46     for p = 1:ssP
47         diff = Q_lastN(p,:) - Qnow;
48         err_vec(p) = sqrt(diff*diff'); % Vector norm
49     end
50     minerr = min(err_vec);
51 end
52
53 if minerr ≤ tolmin
54     indx = find(err_vec ≤ tolmax); % In case multiple periods satisfy
55                                     % tolmax
56     pernum = indx(1);
57     display(['Period ', num2str(pernum), ' solution located'])
58 else
59     warning(['No periodic solution located within given tolerance'...
60             'and time'])
61     pernum = ssP;
62 end
63
64 t_lims(1) = t_lims(1) - (pernum-1)*per; % Update start time
65 IC = Q_lastN(pernum,:); % Update IC
66 [T,Q] = ode45(@(t,q)ParallelEOM(t,q,PARAMS,Ndim,1),t_lims,IC);
67
68 dt = per/10;
69 maxstp = 100*hmin; % Used to enter the while loop the first time
70 nrefine = 0; % To avoid an infinite loop
71 while (maxstp ≥ hmin) && (nrefine ≤ 100)
72     dt = dt/2;
73     Tint = t_lims(1):dt:t_lims(2);
74     Qint = interp1(T,Q,Tint);
75     maxstp = 0; % Initialize max step
76     for stp = 2:length(Tint)
77         diff = Qint(stp,:) - Qint(stp-1,:);
78         dist = sqrt(diff*diff'); % Vector norm
79         maxstp = max([maxstp dist]);
80     end
81     nrefine = nrefine + 1;
82 end
83
84 if maxstp < hmin
85     display(['Step size tolerance achieved using dt = ', num2str(dt)])
86 else
87     warning('Step size tolerance not achieved')
88 end
89
90 Q_less_h = Qint;
91 % Q_less_h now represents an array of coordinates spanning the ss
92 % solution with step size less than or equal to the cell spacing
93

```

```

94 Tint = t_lims(1):fxd_dt:t_lims(2);
95 Qint = interp1(T,Q,Tint);
96 nstpp = per/fxd_dt;
97 nrep = ssP/pernum; % Number of times to repeat the trajectory to fill
98                 % array
99
100 if rem(nrep,1) == 0 % If nrep is an integer
101     Q_fxd_stp = repmat(Qint(1:end-1,:),nrep,1);
102 else
103     Q_fxd_stp = zeros(nstpp*ssP,Ndim);
104     integrep = floor(nrep);
105     r = (ssP-integrep*pernum)*nstpp+1;
106     Q_fxd_stp(r:end,:) = repmat(Qint(1:end-1,:),integrep,1);
107                                     % Repeat an integer # of times
108     qidx = size(Qint,1)-1;
109     while r ≥ 1 % Fill in remaining values
110         Q_fxd_stp(r,:) = Qint(qidx,:);
111         r = r - 1; qidx = qidx - 1;
112     end
113 end
114
115 end

```

Appendix D

Analytical Expressions

This section summarizes the procedure used to derive Eqn. (3.3) and explicitly lists the components of the key arrays. Starting with the 2-DOF version of Eqn. (2.23), a coordinate transformation is applied by introducing the new coordinates

$$\mathbf{y}(\tau) = \mathbf{P}\mathbf{z}(\tau), \quad (\text{D.1})$$

where \mathbf{P} is the matrix of eigenvectors of \mathbf{K} , and

$$P_{(1,1)} = \frac{\Omega^2 - \epsilon_N \Omega^2 - 1 + \sqrt{(-\Omega^2 - \epsilon_N \Omega^2 - 1)^2 - 4\Omega^2}}{2\Omega^2}, \quad (\text{D.2})$$

$$P_{(1,2)} = \frac{\Omega^2 - \epsilon_N \Omega^2 - 1 - \sqrt{(-\Omega^2 - \epsilon_N \Omega^2 - 1)^2 - 4\Omega^2}}{2\Omega^2}, \quad (\text{D.3})$$

$$P_{(2,1)} = P_{(2,2)} = 1. \quad (\text{D.4})$$

Substituting into the EOM and pre-multiplying by the inverse of \mathbf{P} , denoted as \mathbf{P}^{-1} , we obtain

$$\mathbf{z}''(\tau) + \mathbf{P}^{-1}\mathbf{C}\mathbf{P}\mathbf{z}'(\tau) + \mathbf{P}^{-1}\mathbf{K}\mathbf{P}\mathbf{z}(\tau) + \mathbf{P}^{-1}\tilde{\mathbf{n}}(\mathbf{z}(\tau)) = \mathbf{P}^{-1}\mathbf{g}(\tau). \quad (\text{D.5})$$

Or, defining $\tilde{\mathbf{C}} = \mathbf{P}^{-1}\mathbf{C}\mathbf{P}$, $\tilde{\mathbf{K}} = \mathbf{P}^{-1}\mathbf{K}\mathbf{P}$, $\tilde{\mathbf{n}}(\mathbf{z}(\tau)) = \mathbf{P}^{-1}\tilde{\mathbf{n}}(\mathbf{z}(\tau))$, and $\tilde{\mathbf{g}}(\tau) = \mathbf{P}^{-1}\mathbf{g}(\tau)$,

$$\mathbf{z}''(\tau) + \tilde{\mathbf{C}}\mathbf{z}'(\tau) + \tilde{\mathbf{K}}\mathbf{z}(\tau) + \tilde{\mathbf{n}}(\mathbf{z}(\tau)) = \tilde{\mathbf{g}}(\tau). \quad (\text{D.6})$$

The components of the damping matrix $\tilde{\mathbf{C}}$ are expressed as

$$\tilde{C}_{(1,1)} = \frac{\gamma_1 (\Omega^2 (1 - \epsilon_N) - 1 + \xi_1) - \Omega\gamma_N (\Omega^2 (1 + \epsilon_N^2) - 1 - \xi_1 + \epsilon_N (2\Omega^2 + 1 - \xi_1))}{\xi_2}, \quad (\text{D.7})$$

$$\tilde{C}_{(1,2)} = -\frac{(\Omega\gamma_1 - \gamma_N) (1 + \xi_2 - \xi_3)}{\Omega\xi_2}, \quad (\text{D.8})$$

$$\tilde{C}_{(2,1)} = -\frac{(\Omega\gamma_1 - \gamma_N) (\Omega^2 (1 - \epsilon_N) - 1 + \xi_2)}{\Omega\xi_2}, \quad (\text{D.9})$$

$$\tilde{C}_{(2,2)} = \frac{\gamma_1 (1 + \xi_1 - \xi_3) + \Omega\gamma_N (\Omega^2 (1 + \epsilon_N^2) - 1 + \xi_1 + \epsilon_N (1 + 2\Omega^2 + \xi_1))}{\xi_2}. \quad (\text{D.10})$$

The stiffness matrix is diagonal, with

$$\tilde{K}_{(1,1)} = \frac{-1 + 2\Omega^2 - \Omega^4 - 2\Omega^2\epsilon_N - 2\Omega^4\epsilon_N - \Omega^4\epsilon_N^2 + \xi_2 (1 + \xi_3)}{2\xi_2}, \quad (\text{D.11})$$

$$\tilde{K}_{(2,2)} = \frac{(\xi_1 - 4\Omega^2) (1 + \xi_3)}{2\xi_2}. \quad (\text{D.12})$$

Finally, the components of the nonlinear and excitation vectors are given by

$$\tilde{\mathbf{n}}_{(1)} = -\frac{(\xi_3 - \xi_2 - 1) \Omega_N^2 ((\xi_3 - \xi_1 + 1) z_1[\tau] + (\xi_3 + \xi_1 + 1) z_N[\tau])^3}{16\Omega^6 \xi_2}, \quad (\text{D.13})$$

$$\tilde{\mathbf{n}}_{(2)} = \frac{(\xi_3 + \xi_2 - 1) \Omega_N^2 ((\xi_3 - \xi_1 + 1) z_1[\tau] + (\xi_3 + \xi_1 + 1) z_N[\tau])^3}{16\Omega^6 \xi_2}, \quad (\text{D.14})$$

and

$$\tilde{\mathbf{g}}(\tau) = \left\{ \begin{array}{c} \frac{F\Omega^2}{\xi_2} \cos(\omega\tau) \\ -\frac{F\Omega^2}{\xi_2} \cos(\omega\tau) \end{array} \right\}, \quad (\text{D.15})$$

where the following terms are used as shorthand,

$$\xi_1 = \sqrt{(-1 + \Omega^2)^2 + 2(\Omega^2 + \Omega^4) \epsilon_N + \Omega^4 \epsilon_N^2}, \quad (\text{D.16})$$

$$\xi_2 = \sqrt{-4\Omega^2 + (1 + \Omega^2 + \Omega^2 \epsilon_N)^2}, \quad (\text{D.17})$$

$$\xi_3 = \Omega^2 (1 + \epsilon_N). \quad (\text{D.18})$$

Bibliography

- [1] F. Lim, M. Cartmell, A. Cardoni, and M. Lucas, “A preliminary investigation into optimising the response of vibrating systems used for ultrasonic cutting”, *Journal of Sound and Vibration*, **272** (2004) 1047–1069.
- [2] S. Narayanan and K. Jayaraman, “Control of chaotic oscillations by vibration absorber”, in *Proceedings of the Structural Vibration and Acoustics Conference*, American Society of Mechanical Engineers, Design Engineering Division, Montreal, Quebec, Canada, (1989) 391–394.
- [3] C. Sun, R. Eason, S. Nagarajaiah, and A. Dick, “Hardening Duffing oscillator attenuation using a nonlinear TMD, a semi-active TMD and multiple TMD”, *Journal of Sound and Vibration*, **332** (2013) 674–686.
- [4] A. Kareem, T. Kijewski, and Y. Tamura, “Mitigation of motions of tall buildings with specific examples of recent applications”, *Wind and Structures, an International Journal*, **2** (1999) 201–251.
- [5] P. Watts, “On a method of reducing the rolling of ships at sea”, *Transactions of the Institution of Naval Architects*, **24** (1883) 165–190.
- [6] H. Frahm. “Device for damping vibrations of bodies”. United States Patent No. 989,958, 1911.

- [7] J. Ormondroyd and J. Den Hartog, “The theory of the dynamic vibration absorber”, *Transactions of the ASME*, **50** (1928) A9–A22.
- [8] A. Srinivasan, “Analysis of parallel damped dynamic vibration absorbers”, *Journal of Engineering for Industry*, **91** (1969) 282–287.
- [9] V. Borowski, H. Denman, D. Cronin, S. Shaw, J. Hanisko, L. Brooks, D. Mikulec, W. Crum, and M. Anderson, “Reducing vibration of reciprocating engines with crankshaft pendulum vibration absorbers”, *SAE (Society of Automotive Engineers) Transactions*, **100** (1991) 376–382.
- [10] D. Thompson, “A continuous damped vibration absorber to reduce broad-band wave propagation in beams”, *Journal of Sound and Vibration*, **311** (2008) 824–842.
- [11] J. Den Hartog, *Mechanical Vibrations*. Dover Publishing, 1934.
- [12] J. Brock, “A note on the damped vibration absorber”, *Journal of Applied Mechanics*, **13** (1946) A–284.
- [13] S. Crandall and W. Mark, *Random vibration in mechanical systems*. Academic Press, New York and London, 1963.
- [14] P. Wirsching and G. Campbell, “Minimal structural response under random excitation using the vibration absorber”, *Earthquake Engineering and Structural Dynamics*, **2** (1974) 303–312.
- [15] R. Jacquot and D. Hoppe, “Optimal random vibration absorbers”, *Journal of the Engineering Mechanics Division*, **99** (1973) 612–616.
- [16] G. Warburton, “Optimum absorber parameters for various combinations of response and excitation parameters”, *Earthquake Engineering and Structural Dynamics*, **10** (1982) 381–401.

- [17] F. Sadek, B. Mohraz, A. Taylor, and R. Chung, “A method of estimating the parameters of tuned mass dampers for seismic applications”, *Earthquake Engineering and Structural Dynamics*, **26** (1997) 617–635.
- [18] C. Liu and C. Chang, “A method for vibration absorber tuning based on baseline frequency response functions”, *Proceedings of the Institution of Mechanical Engineers, Part C: Journal of Mechanical Engineers, Part D: Journal of Automobile Engineering*, **221** (2007) 1071–1078.
- [19] I.I. Bykhovsky, *Fundamentals of Vibration Engineering*. Robert E. Krieger, 1980.
- [20] Y. Gupta and A. Chandrasekaran, “Absorber system for earthquake excitations”, in *Proceedings of the 4th world conference on earthquake engineering*, Santiago, Chile, (1969).
- [21] D. Manikanahally and M. Crocker, “Vibration analysis of hysteretically damped mass-loaded beams”, *Journal of Sound and Vibration*, **132** (1989) 177–197.
- [22] D. Manikanahally and M. Crocker, “Experimental investigation of minimization of the dynamic response of mass-loaded beams using vibration absorbers”, *Journal of the Acoustical Society of America*, **93** (1993) 1896–1907.
- [23] L. Sun, Y. Fujino, B. Pacheco, and P. Chaiseri, “Modeling of Tuned Liquid Damper (TLD)”, *Journal of Wind Engineering and Industrial Aerodynamics*, **43** (1992) 1883–1894.
- [24] T. Igusa and K. Xu, “Vibration control using multiple tuned mass dampers”, *Journal of Sound and Vibration*, **175** (1994) 491–503.

- [25] L. Zuo and S. Nayfeh, “The two-degree-of-freedom tuned-mass damper for suppression of single-mode vibration under random and harmonic excitation”, *Transactions of the ASME*, **128** (2006) 56–65.
- [26] L. Zuo, “Effective and robust vibration control using series multiple tuned-mass dampers”, *Journal of Vibration and Acoustics*, **131** (2009) 1–11.
- [27] X. Tang and L. Zuo, “Regenerative semi-active control of tall building vibration with series tmds”, in *Proceedings of the American Control Conference*, Baltimore, MD, USA, (2010).
- [28] X. Tang and L. Zuo, “Passive, active and semi-active series tuned mass dampers”, *Proceedings of SPIE: The International Society for Optical Engineering*, **7643** (2010) 76432P.
- [29] R. Roberson, “Synthesis of a nonlinear dynamic vibration absorber”, *Journal of the Franklin Institute*, **254** (1952) 205–220.
- [30] L. Pipes, “Analysis of a nonlinear dynamic vibration absorber”, *Journal of Applied Mechanics*, **20** (1953) 515–518.
- [31] F. Arnold, “Steady state behavior of systems provided with nonlinear dynamic vibration absorbers”, *Journal of Applied Mechanics*, **22** (1955) 487–492.
- [32] H. Kojima and H. Saito, “Forced vibrations of a beam with a non-linear dynamic vibration absorber”, *Journal of Sound and Vibration*, **88** (1983) 559–568.
- [33] A. Soom and M.-S. Lee, “Optimal design of linear and nonlinear vibration absorbers for damped systems”, *Journal of Vibration, Acoustics, Stress, and Reliability in Design*, **105** (1983) 112–119.
- [34] H. Rice and J. McCraith, “Practical non-linear vibration absorber design”, *Journal of Sound and Vibration*, **116** (1987) 545–559.

- [35] I. Jordanov and B. Cheshankov, “Optimal design of linear and non-linear dynamic vibration absorbers”, *Journal of Sound and Vibration*, **123** (1988) 157–170.
- [36] J. Hunt and J.-C. Niessen, “The broadband dynamic vibration absorber”, *Journal of Sound and Vibration*, **83** (1982) 573–578.
- [37] A. Nayfeh, D. Mook, and S. Sridhar, “Nonlinear analysis of the forced response of structural elements”, *Journal of the Acoustical Society of America*, **55** (1974) 281–291.
- [38] A. Nayfeh and D. Mook, *Nonlinear oscillations*. Wiley Interscience, New York, 1986.
- [39] S. Nayfeh and A. Nayfeh, “Energy transfer from high to low-frequency modes in a flexible structure via modulation”, *Journal of Vibration and Acoustics*, **116** (1994) 203–207.
- [40] O. Gendelman, “Targeted energy transfer in systems with external and self-excitation”, *Proceedings of the Institution of Mechanical Engineers, Part C: Journal of Mechanical Engineering Science*, **225** (2011) 2007–2043.
- [41] O. Gendelman, “Transition of energy to a nonlinear localized mode in a highly asymmetric system of two oscillators”, *Nonlinear Dynamics*, **25** (2001) 237–253.
- [42] O. Gendelman, L. Manevitch, A. Vakakis, and R. M’Closkey, “Energy pumping in nonlinear mechanical oscillators: Part I — dynamics of the underlying Hamiltonian systems”, *Journal of Applied Mechanics*, **68** (2001) 34–41.
- [43] A. Vakakis and O. Gendelman, “Energy pumping in nonlinear mechanical oscillators ii: Resonance capture”, *Journal of Applied Mechanics*, **68** (2001) 42–48.

- [44] A. Vakakis, “Inducing passive nonlinear energy sinks in linear vibrating systems”, *Journal of Vibration and Acoustics*, **123** (2001) 324–332.
- [45] E. Gourdon and C. Lamarque, “Energy pumping with various nonlinear structures: Numerical evidences”, *Nonlinear Dynamics*, **40** (2005) 281–307.
- [46] E. Gourdon, N. Alexander, C. Taylor, C. Lamarque, and S. Pernot, “Nonlinear energy pumping under transient forcing with strongly nonlinear coupling: Theoretical and experimental results”, *Journal of Sound and Vibration*, **300** (2007) 522–551.
- [47] X. Jiang, D. McFarland, L. Bergman, and A. Vakakis, “Steady state passive nonlinear energy pumping in coupled oscillators: Theoretical and experimental results”, *Nonlinear Dynamics*, **33** (2003) 87–102.
- [48] P. Malatkar and A. Nayfeh, “Steady-state dynamics of a linear structure weakly coupled to an essentially nonlinear oscillator”, *Nonlinear Dynamics*, **47** (2007) 167–179.
- [49] A. Vakakis and L. Bergman, “Rebuttal of “steady state dynamics of a linear structure weakly coupled to an essentially nonlinear oscillator” by P. Malatkar and A.H. Nayfeh”, *Nonlinear Dynamics*, **53** (2008) 167–168.
- [50] P. Malatkar and A. Nayfeh, “Authors’ response to the rebuttal by A.F. Vakakis and L.A. Bergman of Steady state dynamics of a linear structure weakly coupled to an essentially nonlinear oscillator”, *Nonlinear Dynamics*, **53** (2008) 169–171.
- [51] O. Gendelman, E. Gourdon, and C. Lamarque, “Quasiperiodic energy pumping in coupled oscillators under periodic forcing”, *Journal of Sound and Vibration*, **294** (2006) 651–662.

- [52] O. Gendelman and Y. Starosvetsky, “Quasiperiodic response regimes of linear oscillator coupled to nonlinear energy sink under periodic forcing”, *Journal of Applied Mechanics*, **74** (2007) 325–331.
- [53] Y. Starosvetsky and O. Gendelman, “Attractors of harmonically forced linear oscillator with attached nonlinear energy sink II: optimization of a nonlinear vibration absorber”, *Nonlinear Dynamics*, **51** (2008) 47–57.
- [54] D. Quinn, O. Gendelman, G. Kerschen, T. Sapsis, L. Bergman, and A. Vakakis, “Efficiency of targeted energy transfers in coupled nonlinear oscillators associated with 1:1 resonance captures: Part I”, *Journal of Sound and Vibration*, **311** (2008) 1228–1248.
- [55] T. Sapsis, A. Vakakis, O. Gendelman, L. Bergman, G. Kerschen, and D. Quinn, “Efficiency of targeted energy transfers in coupled nonlinear oscillators associated with 1:1 resonance captures: Part II”, *Journal of Sound and Vibration*, **325** (2009) 297–320.
- [56] Y. Starosvetsky and O. Gendelman, “Vibration absorption in systems with a nonlinear energy sink: Nonlinear damping”, *Journal of Sound and Vibration*, **324** (2009) 916–939.
- [57] A. Nayfeh and B. Balachandran, *Applied nonlinear dynamics*. Wiley-VCH, Weinheim, 2004.
- [58] J. Shaw, S. Shaw, and A. Haddow, “On the response of the non-linear vibration absorber”, *International Journal of Non-Linear Mechanics*, **24** (1989) 281–293.
- [59] N. Alexander and F. Schilder, “Exploring the performance of a nonlinear tuned mass damper”, *Journal of Sound and Vibration*, **319** (2009) 445–462.

- [60] G. Gatti, I. Kovacic, and M. Brennan, “On the response of a harmonically excited two degree-of-freedom system consisting of a linear and a nonlinear quasi-zero stiffness oscillator”, *Journal of Sound and Vibration*, **329** (2010) 1823–1835.
- [61] G. Gatti, M. Brennan, and I. Kovacic, “On the interaction of the responses at the resonance frequencies of a nonlinear two degrees-of-freedom system”, *Physica D*, **239** (2010) 591–599.
- [62] A. Savadkoochi, L. Manevitch, and C. Lamarque, “Analysis of the transient behavior in a two dof nonlinear system”, *Chaos, Solitons and Fractals*, **44** (2011) 450–463.
- [63] R. Haxton and A. Barr, “The autoparametric vibration absorber”, *Journal of Engineering for Industry*, **49** (1972) 119–125.
- [64] M. Cartmell and J. Lawson, “Performance enhancement of an autoparametric vibration absorber by means of computer control”, *Journal of Sound and Vibration*, **177** (1994) 173–195.
- [65] H. Hatwal, A. Mallik, and A. Ghosh, “Non-linear vibrations of a harmonically excited autoparametric system”, *Journal of Sound and Vibration*, **81** (1982) 153–164.
- [66] S. Oueini, A. Nayfeh, and J. Pratt, “A nonlinear vibration absorber for flexible structures”, *Nonlinear Dynamics*, **15** (1998) 259–282.
- [67] A. Vyas, A. Bajaj, and A. Raman, “Dynamics of structures with wideband autoparametric vibration absorbers: Theory”, *Proceedings of the Royal Society A: Mathematical, Physical and Engineering Sciences*, **460** (2004) 1547–1581.

- [68] J. Spencer, B.F. and M. Sain, “Controlling buildings: A new frontier in feedback”, *IEEE Control Systems Magazine*, **17** (1997) 19–35.
- [69] J. Yao, “Concept of structural control”, *ASME Journal of the Structural Division*, **98** (1972) 1567–1574.
- [70] R. Lund, “Active damping of large structures in winds”, in *ASCE Convention*, (1979).
- [71] J. Chang and T. Soong, “Structural control using active tuned mass dampers”, *Journal of the Engineering Mechanics Division*, **106** (1980) 1091–1098.
- [72] T. Kobori, N. Koshika, K. Yamada, and Y. Ikeda, “Seismic-response-controlled structure with active mass driver system. part 1: design”, *Earthquake Engineering and Structural Dynamics*, **20** (1991) 133–149.
- [73] Y. Ikeda, K. Sasaki, M. Sakamoto, and T. Kobori, “Active mass driver system as the first application of active structural control”, *Earthquake Engineering and Structural Dynamics*, **30** (2001) 1575–1595.
- [74] J. Spencer, B.F. and S. Nagarajaiah, “State of the art of structural control”, *Journal of Structural Engineering*, **129** (2003) 845–856.
- [75] T. Yamada, T. Kobori, and I. Nishimura, “Dynamic vibration absorber”, *Japan Patent Bureau*, **S63-156171** (1988).
- [76] I. Nishimura, T. Yamada, M. Sakamoto, and T. Kobori, “Control performance of active-passive composite tuned mass damper”, *Smart Materials and Structures*, **7** (1998) 637–653.
- [77] G. Housner, L. Bergman, T. Caughey, A. Chassiakos, R. Claus, S. Masri, R. Skelton, T. Soong, B. Spencer, and J. Yao, “Structural control: Past, present and future”, *Journal of Engineering Mechanics*, **123** (1997) 897–971.

- [78] A. Nishitani and Y. Inoue, “Overview of the application of active/semiactive control to building structures in Japan”, *Earthquake Engineering and Structural Dynamics*, **30** (2001) 1565–1574.
- [79] M. Feng and M. Shinozuka, “Use of a variable damper for hybrid control of bridge response under earthquake”, in *Proceedings of the U.S. National Workshop on Structural Control Research*, USC Publication No. CE-9013, (1990).
- [80] Z. Akbay and H. Aktan, “Actively regulated friction slip devices”, in *Proceedings of the 6th Canadian Conference on Earthquake Engineering*, (1991) 367–374.
- [81] S. Kannan, H. Uras, and H. Aktan, “Active control of building seismic response by energy dissipation”, *Earthquake Engineering and Structural Dynamics*, **24** (1995) 747–759.
- [82] H. Miller and J. Gartner, “Tunable, non-linear vibration absorber”, *American Society of Mechanical Engineers (Paper)*, **75-DET-9** (1975) 1–8.
- [83] P. Walsh and L. Lamancusa, “A variable stiffness vibration absorber for minimization of transient vibrations”, *Journal of Sound and Vibration*, **158** (1992) 195–211.
- [84] S. Nagarajaiah. “Structural vibration damper with continuously variable stiffness”. United States Patent No. 6,098,969, 2000.
- [85] S. Nagarajaiah and N. Varadarajan, “Short time Fourier transform algorithm for wind response control of buildings with variable stiffness TMD”, *Engineering Structures*, **27** (2005) 431–441.
- [86] S. Nagarajaiah and D. Mate, “Semi-active control of continuously variable stiffness system”, in *Proceedings of the 2nd World Conference on Structural Control*, volume 1, Kyoto, Japan, (1998) 397–405.

- [87] S. Nagarajaiah, V. Nadathur, and S. Sahasrabudhe, “Variable stiffness and instantaneous frequency”, in *Proceedings of the World Structures Congress*, ASCE, New Orleans, LA, (1999) 281–292.
- [88] N. Varadarajan and S. Nagarajaiah, “Wind response control of building with variable stiffness tuned mass damper using EMD/HT”, *Journal of Engineering Mechanics*, **130** (2004) 451–458.
- [89] S. Nagarajaiah and E. Sonmez, “Structures with Semiactive Variable Stiffness Single/Multiple Tuned Mass Dampers”, *Journal of Structural Engineering*, **133** (2007) 67–77.
- [90] S. Nagarajaiah, “Adaptive passive, semiactive, smart tuned mass dampers: Identification and control using Empirical Mode Decomposition, Hilbert Transform, and Short-Term Fourier Transform”, *Structural Control and Health Monitoring*, **16** (2009) 800–841.
- [91] S. Sahasrabudhe and S. Nagarajaiah, “Effectiveness of variable stiffness systems in base-isolated bridges subjected to near-fault earthquakes: An experimental and analytical study”, *Journal of Intelligent Material Systems and Structures*, **16** (2005) 743–756.
- [92] S. Narasimhan and S. Nagarajaiah, “A STFT semiactive controller for base isolated buildings with variable stiffness isolation systems”, *Engineering Structures*, **27** (2005) 514–523.
- [93] S. Nagarajaiah and S. Sahasrabudhe, “Seismic response control of smart sliding isolated buildings using variable stiffness systems: An experimental and numerical study”, *Earthquake Engineering and Structural Dynamics*, **35** (2006) 177–197.

- [94] S. Nagarajaiah and S. Narasimhan, “Seismic control of smart base isolated buildings with new semiactive variable damper”, *Earthquake Engineering and Structural Dynamics*, **36** (2007) 729–749.
- [95] S. Nagarajaiah and D. Pasala, “Semi-active control of ASD device - Adaptive length pendulum dampers”, in *Proceedings of the 19th Analysis and Computation Specialty Conference*, Orlando, FL, (2010) 325–334.
- [96] E. Doedel, “AUTO: A program for the automatic bifurcation analysis of autonomous systems”, *Congressus Numerantium*, **30** (1981) 265–284.
- [97] E. Doedel and B. Oldeman, “AUTO-07p: Continuation and bifurcation software for ordinary differential equations”, Technical report, Concordia University, Montreal, Quebec, Canada, 2009.
- [98] P. Gonçalves, M. Frederico, G. Rega, and S. Lenci, “Global dynamics and integrity of a two-dof model of a parametrically excited cylindrical shell”, *Nonlinear Dynamics*, **63** (2011) 61–82.
- [99] G. Rega and S. Lenci, “Identifying, evaluating, and controlling dynamical integrity measures in non-linear oscillators”, *Nonlinear Analysis*, **63** (2005) 902–914.
- [100] G. Rega and S. Lenci, “Dynamical integrity and control of nonlinear mechanical oscillators”, *Journal of Vibration and Control*, **14** (2008) 159–179.
- [101] W. Szemplinska-Stupnicka and H. Troger, editors, *Engineering Applications of Dynamics of Chaos*, Chapter 1, 42–61, CISM Courses and Lectures No. 319. Springer Verlag, Wien - New York, 1991.
- [102] Z.-M. Ge and S.-C. Lee, “A modified interpolated cell mapping method”, *Journal of Sound and Vibration*, **199** (1997) 189–206.

- [103] B. Tongue, “On obtaining global nonlinear system characteristics through interpolated cell mapping”, *Physica D*, **28** (1987) 401–408.
- [104] C. Hsu, “Theory of cell-to-cell mapping dynamical systems”, *Journal of Applied Mechanics*, **47** (1980) 931–939.
- [105] C. Hsu and R. Guttalu, “Unravelling algorithm for global analysis of dynamical systems: An application of cell-to-cell mappings”, *Journal of Applied Mechanics*, **47** (1980) 940–948.
- [106] J. Sun and A. Luo, *Bifurcation and chaos in complex systems*, volume 1 of *Edited Series on Advances in Nonlinear Science and Complexity*. Elsevier, 2006.
- [107] B. Tongue and K. Gu, “Interpolated cell mapping of dynamical systems”, *Journal of Applied Mechanics*, **55** (1988) 461–466.
- [108] C. Hsu, “Probabilistic theory of nonlinear dynamical systems based on the cell state space concept”, *Journal of Applied Mechanics*, **49** (1982) 895–902.
- [109] C. Hsu, R. Guttalu, and W. Zhu, “Method of analyzing generalized cell mappings”, *Journal of Applied Mechanics*, **49** (1982) 885–894.
- [110] L. Virgin and C. Begley, “Grazing bifurcations and basins of attraction in an impact friction oscillator”, *Physica D*, **130** (1999) 43–57.
- [111] L. Xu, M. Lu, and Q. Cao, “Bifurcation and chaos of a harmonically excited oscillator with both stiffness and viscous damping piecewise linearities by incremental harmonic balance method”, *Journal of Sound and Vibration*, **264** (2003) 873–882.
- [112] B. Tongue and K. Gu, “A higher order method of interpolated cell mapping”, *Journal of Sound and Vibration*, **125** (1988) 169–179.

- [113] B. Tongue, “A multiple-map strategy for interpolated mapping”, *International Journal of Non-Linear Mechanics*, **25** (1990) 177–186.
- [114] J. van der Spek, C. de Hoon, A. de Kraker, and D. van Campen, “Parameter variation methods for cell mapping”, *Nonlinear Dynamics*, **7** (1995) 273–284.
- [115] M. Wiercigroch and B. Kraker, editors, *Applied nonlinear dynamics and chaos of mechanical systems with discontinuities*, volume 28 of *World Scientific Series on Nonlinear Science*, Chapter 4, 64–93. World Scientific, 2000.
- [116] D. van Campen, E. van de Vorst, J. van der Spek, and A. de Kraker, “Dynamics of a multi-DOF beam system with discontinuous support”, *Nonlinear Dynamics*, **8** (1995) 453–466.
- [117] J. van der Spek, D. van Campen, and A. de Kraker, “Cell mapping for multi degrees of freedom systems”, in *Proceedings of the 1994 International Mechanical Engineering Congress and Exposition*, volume 192, Chicago, IL, (1994) 151–159.
- [118] D. van Campen, A. de Kraker, R. Fey, E. van de Vorst, and J. van der Spek, “Long-term dynamics of non-linear MDOF engineering systems”, *Chaos, Solitons and Fractals*, **8** (1997) 455–477.
- [119] L. Crespo and J. Sun, “Stochastic optimal control of nonlinear systems via short-time Gaussian approximation and cell mapping”, *Nonlinear Dynamics*, **28** (2002) 323–342.
- [120] M. Soliman and J. Thompson, “Integrity measures quantifying the erosion of smooth and fractal basins of attraction”, *Journal of Sound and Vibration*, **135** (1989) 453–475.
- [121] S. Lenci and G. Rega, “Optimal control of nonregular dynamics in a Duffing oscillator”, *Nonlinear Dynamics*, **33** (2003) 71–86.

- [122] D. Inman, *Engineering vibration*. Prentice Hall, Inc., 1996.
- [123] S. Kelly, *Advanced vibration analysis*. CRC Press, 2007.
- [124] J. Den Hartog, *Mechanical vibrations*. McGraw Hill, 1947.
- [125] A. Yan, J. Teng, Z. Lu, and Q. Wang, “Effect of geometrical nonlinearity on the SAIVS device”, *Advances in Structural Engineering*, **11** (2008) 91–105.
- [126] P. Spanos and B. Zeldin, “Efficient iterative ARMA approximation of multivariate random processes for structural dynamics applications”, *Earthquake Engineering and Structural Dynamics*, **25** (1996) 497–507.
- [127] P. Spanos and B. Zeldin, “Monte Carlo treatment of random fields: A broad perspective”, *Applied Mechanics Reviews*, **51** (1998) 219–237.
- [128] M. Shinozuka and C.-M. Jan, “Digital simulation of random processes and its applications”, *Journal of Sound and Vibration*, **25** (1972) 111–128.
- [129] G. Deodatis and M. Shinozuka, “Auto-regressive model for nonstationary stochastic processes”, *Journal of Engineering Mechanics*, **114** (1988) 1995–2012.
- [130] Y. Lin and Y. Yong, “Evolutionary Kanai-Tajimi earthquake models”, *Journal of Engineering Mechanics*, **113** (1987) 1119–1122.
- [131] P. Spanos and I. Kougiumtzoglou, “Harmonic wavelets based statistical linearization for response evolutionary power spectrum determination”, *Probabilistic Engineering Mechanics*, **27** (2012) 57–68.
- [132] A. Alasty and R. Shabani, “Chaotic motions and fractal basin boundaries in spring-pendulum system”, *Nonlinear Analysis*, **7** (2006) 81–95.

- [133] T. Trombetti, J. Conte, and A. Durrani, “Correlation studies between analytical and experimental dynamic behavior of the Rice University shaking table”, Technical Report 49, Rice University, 1997.